NTNU

Norwegian University of
Science and Technology

Dual-Porosity Modeling of Tight Unconventionals

Ilina Yusra

Petroleum Engineering
Submission date: July 2018
Supervisor: Curtis Hays Whitson, IGP

Norwegian University of Science and Technology
Department of Geoscience and Petroleum

Abstract

Enhancing oil recovery in tight unconventional has been a great interest over the last decade. Huff-n-puff gas EOR becomes the most popular method among many alternatives, particularly after *EOG Resources, Inc.* claimed that they had succeeded implementing such method in the Eagle Ford shale.

Little information was released by EOG regarding the employed method as they affirmed such details are their proprietary. Instead, they provided that miscible displacement plays an important role to its success along with the utilization of existing wells. Approximately the incremental range of 30% to 70% is expected according to their simulation model if such method is exerted relative to not having it at all.

This study highlights the usage of dual-porosity approach as what EOG have done in their reservoir simulation model. Not only limited studies have covered this topic, but also none of them has discussed how it is implemented in tight unconventionals. The correct solution is given by single-porosity modeling (SPM) as it defines numerical equations for matrix and fracture blocks independently. Unlike SPM, dual-porosity modeling (DPM) accounts matrix and fracture system together within each grid block. Fracture properties are imposed as matrix boundary condition.

Simple model was carried to understand the behavior of DPM in tight unconventionals during two periods, namely depletion and gas injection. Subsequently, the results were compared to SPM along with the necessity to modify the model to preserve the reliability of the results. It is found that DPM can represent SPM results during depletion phase, although some modifications on matrix-fracture exchange transmissibilities (TEX) may be needed. In contrast, DPM yields overoptimistic performances during gas injection phase even with modifying TEX. In other words, DPM provides a misleading result from SPM when injection is acquainted.

Preface

This thesis is written in partial fulfillment of the requirements for TPG4920 Petroleum Engineering, Master Thesis in Reservoir Engineering, Department of Geoscience and Petroleum, Norwegian University of Science and Technology (NTNU). In addition, this report is corresponding to previous work done for TPG4560 Petroleum Engineering, Specialization Course (Yusra, 2017).

I wish to express my utmost gratitude towards my supervisor, Professor Curtis Hays Whitson for the opportunity given to me. All the learning and guidance he has given over the past year have been really helpful in deepen and enhancing reservoir engineering knowledge in both way practically and theoretically. It is such an honor being supervised and working with him.

I would also like to acknowledge Petrostreamz AS for Pipe-It license, Coats Engineering, Inc for SENSOR license and Tecplot, Inc. for Tecplot RS license.

My appreciation also goes to Wynda Astutik, Silvya Dewi Rahmawati and Mohamad Majzoub Dahouk, for helping me and giving me their insight not only on understanding Pipe-It but also on the project overall.

The greatest gratitude I would give to my other half, Rino Reynaldo for his endless support and patience hearing me complaining about everything. Without a doubt, I would never have finished this report if it was not because of him. Not to forget to mention my mom, my dad, my eight other siblings, Ammar, my little nephew, and Salsa, my little niece, for their constant pray and presence whenever I needed.

Trondheim, 30 June 2018

Ilina Yusra

Table of Contents

List of Figures

List of Tables

Chapter 1

Introduction

1.1 Background

Evidently, unconventional resources play an important role to total hydrocarbon production in the world for the past decade. Tight oil in particular has dominated around 50% of total U.S. production within that time range (U.S. Energy Information Administration, 2018a). Many have projected that the production will increase considerably over time along with the rapidly growing technology. Despite the splendid incremental, the recovered oil is considered only a small part of the total in-place. Additionally, the current issue with oil price has gotten the economical aspect to be the main key of its development. Determining an alternative solution that is able to provide optimal production in connection with promising returns has offered more challenges to the table.

Enhanced oil recovery (EOR) is believed to be the best approach for this matter to compensate low matrix permeability such altering the fluid and/or rock properties by the injectant. Kurtoglu (2013) explains that the current interest in the petroleum industry is to engage gas injection. It can be employed by two methods, continuous injection with two different injecting and producing wells, and cyclic injection process with single dedicated well for both injector and producer. The latter method is widely known as Huff-n-Puff gas EOR in tight unconventionals.

In May 2016, first successful EOR in the Eagle Ford shale were announced by *EOG Resources, Inc.*, one of the largest independent oil and gas companies in the United States (Thomas, Helms, Driggers, Trice, & Thomas, 2016). They believe that the accomplishment due to three factors that they analyzed for three years thoroughly started from laboratory experiments. The three factors are geologic characteristics, drilling planning and the amount of returns earned.

Eagle Ford offers a unique characteristic that support the gas injection in contact and becomes miscible with the reservoir oil thus able to escalate the recovered oil. Different shale characteristics may result in different production response, which further studies are required. EOG are planning to implement same method to the next step, 32-well pilot.

There was no additional drilling required upon the four successful pilot projects, implying that the EOR was empowered existing wells both to inject gas and to produce

oil. The wells were put on production for two-to-four years and closed for three-to-four months before producing more oil. Additionally, EOG reported that the operating cost are low due to the utilization of available produced gas as injectant and such method is expected to have long-term effect on Eagle Ford base production profile.

Taking into accounts the facts that they have shared, many have speculated that the method is related to huff-n-puff. Yet, when asked about it, EOG disinclined to share the proprietary details. They mentioned that the process followed miscible displacement and did not involve any thermal process. EOG emphasized that they tried to forecast the history matched production data from their initial four pilot projects with and without the application of EOR. Applying such method is suspected to increase the recovery factor to range of 30% until 70% according to their model (Thomas et al., 2016) compared to not having it at all. They utilized the dual-porosity approach to the reservoir model to account microfractures that may have formed naturally or induced after performing hydraulic fracture (Kazemi, Eker, Torcuk, & Kurtoglu, 2015).

Long-term additional production, low cost and high-return reserves which EOG acquired have prompted an enormous interest of oil industry players on EOR in tight unconventionals, peculiarly huff-n-puff. This will be a tremendous breakthrough in the history of tight unconventional reservoir production if found to be compatible to any other pilots.

The existence of so-called shattered rock volume region due to extensive micro- and macro-fractures allows us to use fractured reservoir concept. There are two different approaches to carry this matter to the reservoir simulation, by establishing single- or dual-porosity model (Coats, 1989). The latter approach is used by EOG for their reservoir simulation model. Single-porosity model accounts matrix and fracture characteristics independently, such that every numerical equation for each matrix and fracture blocks are solved separately (Cheng, 2010). This approach provides the correct solutions. On the other hand, dual-porosity model enables to value matrix and fracture system within each grid block. Despite providing simpler model and quick simulation time, dual-porosity approach should honor the result from single-porosity approach.

Limited studies have covered the application of single- and dual-porosity approach in simulation model, yet it has not been fully discussed how this implemented in tight unconventionals. The necessities to study dual-porosity modeling behavior in tight unconventional becomes substantial prior employing to the field-scale model. Although that EOG declared their findings as a game-changing event for their company, utilizing dual-porosity model without having a better understanding about the behavior can severely mislead the results.

1.2 Study Objective

The purpose of this study is to analyze the behavior of dual-porosity modeling (DPM) in tight unconventionals and to understand the interest of having this model in the simulation. Performances during two periods, which are depletion and gas injection, are presented in this study. In each of the period, sensitivity analyses are undertaken to discern the repercussions of having utilized this model. Further, the performances in each

period are examined and compared to single-porosity modeling (SPM), in order to assure reliable results. The necessity to modify the DPM such that having better correspondence with SPM is also considered.

1.3 Software Description

1.3.1 Sensor

System for Efficient Numerical Simulation of Oil Recovery, knows as Sensor, developed by Coats Engineering. It is a generalized 3D numerical model used by engineers to optimize oil and gas recovery processes through simulation of compositional and black oil fluid flow in single porosity, dual porosity, and dual permeability petroleum reservoirs (Coats Engineering, Inc., 2016). Coats Engineering believes that none of full-physics reservoir simulator contend sensor in terms of the speed and robustness. Sensor is used to run the model and its results subsequently be analyzed.

1.3.2 Pipe-It

Pipe-It is a unique integrated asset management (IAM) software that integrates models and optimizes petroleum assets (Petrostreamz AS, 2016). The developer, Petrostreamz AS, claims limitless number of applications can be chained together and run subsequently either in series or parallel. In other words, this software not only can launch any software, but also connect and compile data from different resources.

Upon this study, Pipe-It is employed to chain the whole workflow starting with the input data and ending with final result plot. By utilizing many features provided, for instance MapLinkz and Optimizer, scenarios and inputs could be changed instantly. This correlates peculiarly to perform sensitivity analysis without having all the data open manually one by one. Hence, reducing the time spent considerably.

1.3.3 GAWK

Gawk is acknowledged as the GNU operating system implementation of awk. It interprets a special-purpose programming language to handle simple jobs with just a few lines (Free Software Foundation, Inc., 2017). Generating task corresponds to many text files is attainable by utilizing this software. Author use GAWK to develop reservoir model and production schedule for the necessity of sensor input data.

1.3.4 Tecplot RS

In general, the reservoir simulators provide the results of the simulation in specific files filled with numbers depend on the total variables and time step run. Sensor produces output file (*.out*) along with other files if requested in the data set. The most common

requested files are *.61* and *.71*, however, the files could be expensive to be translated manually. Tecplot RS is one of the best tools to quickly validate and visualize the results with only just a few mouse clicks (Tecplot, Inc., 2018).

It is a powerful tool that helps the user to manage and analyze large amounts of simulation data developed by Tecplot, Inc. In addition, it has the ability to modify the results without harming the original result files. One can more easily elaborate the reservoir model as expected by employing this software. The author use Tecplot RS frequently not only to visualize XY, 2D and 3D solution but also to compare results from two or more scenarios.

Chapter 2

Literature Review

2.1 Tight Unconventionals

Shale is a fissile mudstone including not only silt with 4-60 μm and clay-size particles with less than 4 μm but also organic matter (Kazemi et al., 2015). Large overburden stress together with high temperature proper this organic material transforms to hydrocarbon components. The utilization of shale oil and tight oil is usually interchangeably, frankly, the two terms are different. Zou, Yang, and Cui (2013) imply shale oil to oil that are accumulated in a rich organic matters shale formation without any migration. Meanwhile, tight oil and gas refer to oil and gas in very low porosity and poor permeability formation that are preserved in sandstone, shale, siltstone, limestone, dolomite and even volcanic rocks after short-distance migration. The matrix permeability is less than 0.1 mD such that the oil cannot be retrieved using conventional techniques. Consequently, multi-stage hydraulic fracture has been widely applied to the horizontal well (Shoaib & Hoffman, 2009).

Despite the complexity of the rock combined with the difficulty of applied technology in tight unconventional, the incremental of its production in U.S. for the past two decades has been magnificent. Its enormous production has increased significantly four-fold compared to in 2010 as shown in Figure 2.1. Eagle Ford and Bakken formation are two of the largest tight unconventional resources in U.S. with 4 and 5 billion barrels reserves estimation, respectively (U.S. Energy Information Administration, 2018b). Eagle ford is located in the southwest Texas, while Baken is located in Eastern Montana and Western North Dakota. For Bakken formation, the most oil producing coming from the Middle Bakken member, which has been the main focus for horizontal drilling (Kurtoglu, 2013).

Though by employing multi-stage hydraulic fracture, oil recovery in tight oil is still considered very small (Shoaib & Hoffman, 2009). Identifying additional approach to increase oil recovery has been current interest of oil and gas players. Various studies are discussing on enhanced oil recovery in tight oil reservoir, particularly using huff-n-puff gas. Huff-n-Puff (HnP) is defined as one of EOR method that taking place at the same well and includes huff, soak and puff process. Huff refers to injecting gas, continued by waiting period to allow the gas interact with reservoir fluid causing the oil to swell, usually known as soak period. The process finishes with producing the reservoir fluid or

known as puff process (Kanfar, Ghaderi, Clarkson, Reynolds, & Hetherington, 2017). It is predicted that 10% of incremental oil recovery is obtained by employing huff-n-puff to tight unconventionals (Shoaib & Hoffman, 2009; Yu, Lashgari, & Sepehrnoori, 2014).

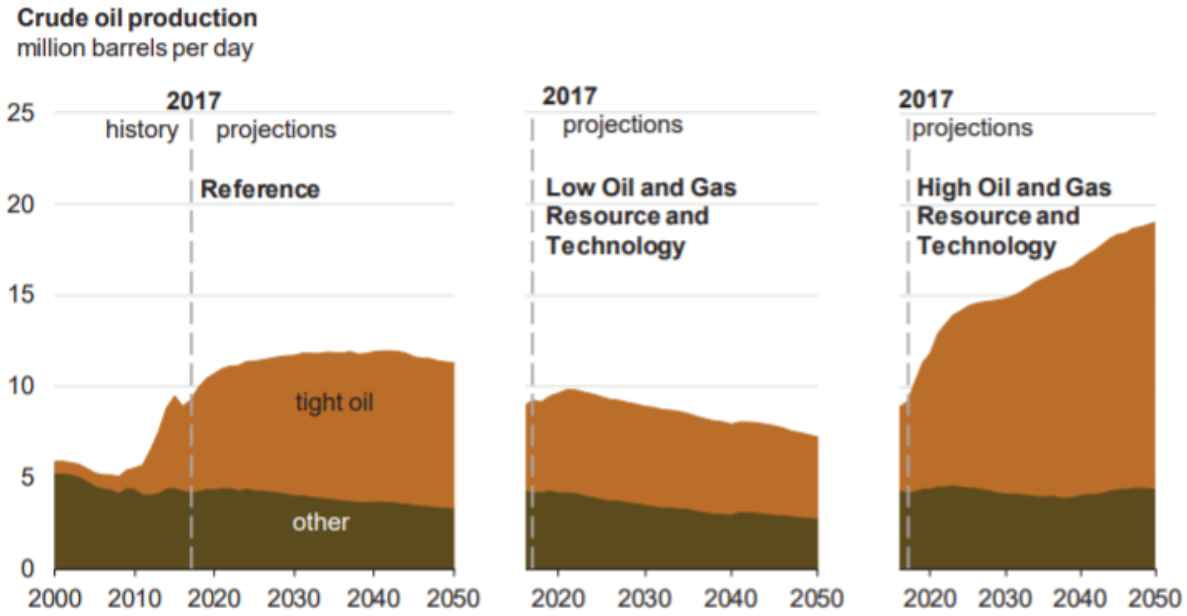

Figure 2.1: U.S. oil production and projection to 2050 (U.S. Energy Information Administration, 2018a).

2.2 Shattered Rock Volume

Multistage transverse hydraulic fractures in horizontal wells until now is considered to be the most effective method to access the reservoir pores of tight unconventionals (Kazemi et al., 2015). Generally, the range of horizontal segment length is 4000 to 1000 ft that consists up to 20-50 stages of stimulation process. In Eagle Ford and Bakken, the horizontal segments in average are 5000 ft and 9000 ft length, respectively.

Performing hydraulic fracture to tight reservoirs may result in *micro-* and *macrofracture* network (Kazemi et al., 2015). It becomes extensive in the adjacent hydraulic fractures region and less further away. Fracture porosity with range of 0.01-0.5 % is classified as macrofracture, whereas less than 0.01% is considered as microfracture. We refer this induced regions of fracture-matrix rock as *shattered rock volume* (SRV). Additionally, some microfractures may occur naturally in the matrix rock. For instance, this situation arises because of the fluid expansion force that caused by a large internal hydrostatic pressure during the formation of hydrocarbon components in shale. In other words, not only hydraulic fractures and matrix take place in near wellbore but also microfractures, either formed naturally or precipitate by hydraulic fracture. Having said that, these combinations create so-called dual-porosity environment.

Several studies were conducted to assure that the fluid performance near wellbore follows dual-porosity behavior (Kurtoglu, 2013; Kazemi et al., 2015). Kurtoglu (2013)

found that between core-measured and field-measured permeability of Bakken formation, there is a discrepancy of one order of magnitude. It implies to the role of micro-fracture system in Bakken formation in regard to the overall productivity. Therefore, the use of the fractured reservoir principle in a multi-stage hydraulic fracture tight unconventional is believed to be representative.

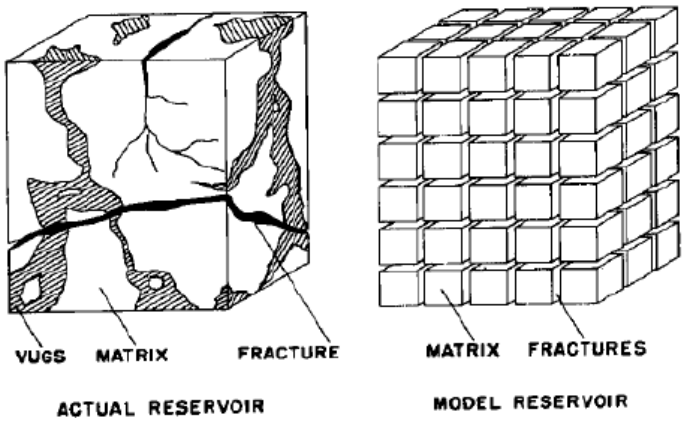

Figure 2.2: Fractured system (Warren & Root, 1963).

The concept of dual-porosity models first was introduced by Warren and Root (1963) as illustrated in Figure 2.2. Later in 1976, Kazemi, Merrill, Porterfield, and Zeman (1976) integrated the numerical simulation with this concept. Such application continues to grow ever since.

Fractured reservoir

Dual-porosity refers to the existence of the matrix porosity (ϕ_m) and the fracture porosity (ϕ_f) in correspondence to the total porosity (Golf-Racht, 1982). The subscript m and f simply explain matrix and fracture properties, respectively. Basically, the two terms are defined as follows;

$$\phi_m = \frac{volume\ voids\ of\ the\ matrix}{matrix\ bulk\ volume} \tag{1}$$

$$\phi_f = \frac{volume\ voids\ of\ the\ fracture}{total\ bulk\ volume} \tag{2}$$

The fluid is stored in rock storage, or known as *storage capacity*. Determining the total permeability in fractured reservoir is difficult due to fracture porosity dependency to the flow direction (Golf-Racht, 1982). In the case of vertical and horizontal flow as depicted in Figure 2.3, the total permeability is defined as;

$$\begin{aligned} k_{tv} &= k_m + k_f, \\ k_{th} &= k_m \end{aligned} \tag{3}$$

Total permeability is denoted by k_t with subscript of v and h imply vertical and horizontal. On the contrary, if the direction of the fracture is random, then total permeability is obtained by following darcy's equation as shown in Equation (4).

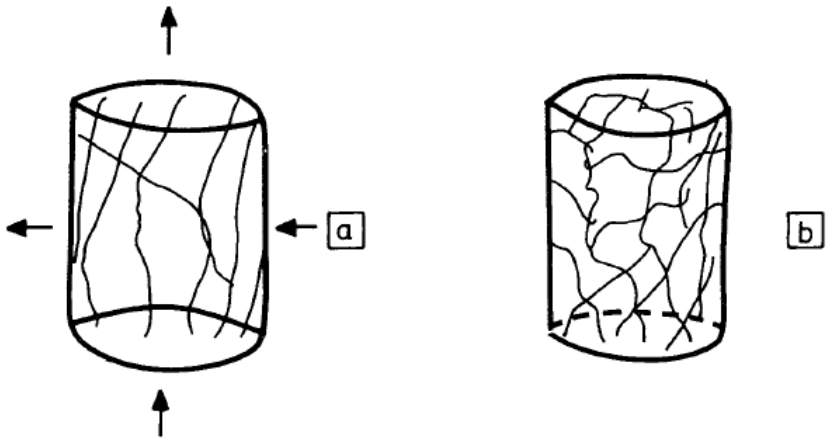

Figure 2.3: Flow direction illustration, (a)vertical or horizontal, (b)random direction (Golf-Racht, 1982).

$$k_t = \frac{Q \cdot \mu \cdot L}{A \cdot \Delta P} \tag{4}$$

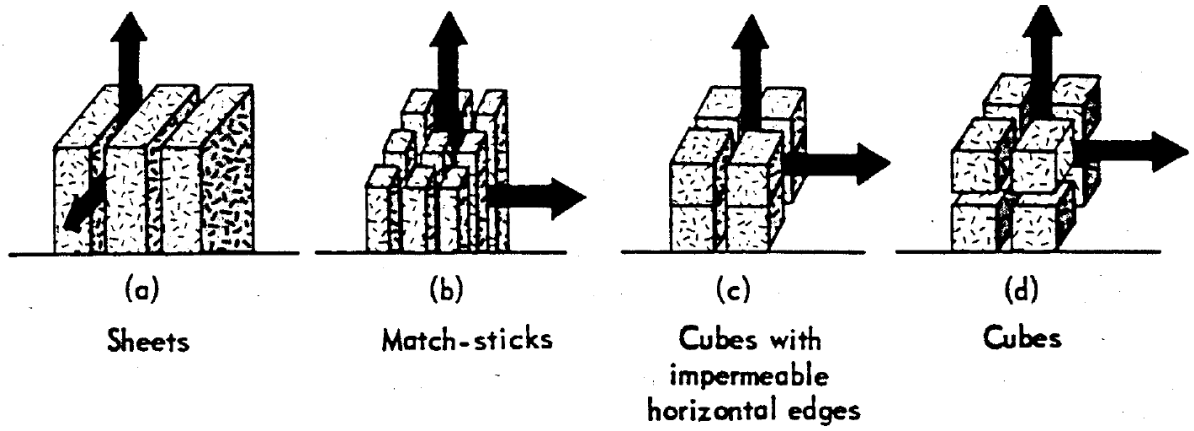

Figure 2.4: Matrix element shapes (Reiss, 1980).

The above equation works in standard international (SI) units. Where Q and μ represent oil production rate and oil viscosity, respectively. Model length is referred as L, model area is A and ΔP is pressure difference between upstream and downstream of the flow. Reiss (1980) shows that the relationship between porosity and permeability depends on geometrical system of the formation as illustrated in Figure 2.4. The arrows represent the possible flow directions.

1. Sheets: fracture separates matrix in parallel.
2. Match-sticks: matrix is separated by two orthogonal fracture planes.
3. Cubes with impermeable horizontal edges: three orthogonal fracture planes separate matrix, but thin stratification replaces the horizontal fracture.
4. Cubes: three orthogonal planes separate matrix equally.

Modeling fractured reservoir in numerical simulation is more difficult and complex than conventional reservoir, as one should take into account the presence of SRV. Coats

(1989) describes in his paper that the numerical simulation of dual-porosity reservoirs can be categorized into two main approaches of implicit numerical model, which are single-porosity and dual-porosity modeling. The model regards three different types of interblock flow which are; fracture-fracture flow between blocks in SRV and/or matrix+natural fracture region, matrix-matrix flow between blocks in matrix only region and matrix-fracture flow between blocks on the interface of matrix and fracture.

Single-porosity modeling (SPM)

Single-porosity modeling does not imply to formation with only single-porosity but refer to model the fracture and matrix explicitly. A reservoir is discretized into matrix and fracture blocks as single planar or network planar planes (Cheng, 2010). In other words, all equations in numerical simulation are solved for every blocks separately. Despite expensive simulation, this should give correct solutions.

The model equations in total are $2N_c + 4$, where N_c is number of components. It includes primary equations with respect to conservation of mass for N_c hydrocarbon components and water. In addition to primary equations, N_c equations of hydrocarbon phase equilibrium and three equations of hydrocarbon phase mol fractions and saturations. These equations are described in more detail in Coats (1980).

Dual-porosity modeling (DPM)

Herein, a reservoir is modeled by one or many blocks containing matrix and fracture system. Instead of describing matrix and fracture blocks explicitly, fracture properties are imposed as matrix boundary condition. The matrix cell size and shape can vary from block to block along the model. Subscript $x-$, $y-$ and $z-$ indicates properties along the $x-$, $y-$ and $z-$directions. The usage of Δ and DEL are implying to grid block size and interchangeable. If fracture spacings are expressed ℓ_x, ℓ_y and ℓ_z, then grid block volume (V_{bl}) and matrix block number (N_m) are defined :

$$V_{bl} \;=\; \Delta x\ \Delta y\ \Delta z \tag{5}$$

$$N_m \;=\; \frac{V_{bl} \cdot\ (1\ -\ \phi_f)}{\ell_x\ \cdot\ \ell_y\ \cdot\ \ell_z} \tag{6}$$

A grid block contains N_m matrix blocks. According to Coats (1989), the shape factor (σ) of matrix-fracture pressure difference and flow rate are determined by;

$$\sigma \;=\; 8\left(\frac{1}{{\ell_x}^2}\ +\ \frac{1}{{\ell_y}^2}\ +\ \frac{1}{{\ell_z}^2}\right) \tag{7}$$

In the absence of one particular fracture spacing, the term involving that fracture spacing in the above equation is omitted. For instance if ℓ_z is 0, then the third term $1/{\ell_z}^2$ is omitted.

The matrix-fracture flow is related to transfer of fracture-block fluids represented by *source/sink* function in the equation of conservation of mass. However, the term is not

fully understood and is the most difficult to be entitled accurately. Golf-Racht (1982) explains that some reservoir simulators entail that the source/sink function along with block-fracture transfer function is defined prior the simulation, either by core analysis or history matching. Others calculate the function internally. Sensor Reservoir Simulator (Coats Engineering, Inc., 2011) refers this function as matrix-fracture exchange coefficient or transmissibility (TEX). This term is what defining the oil production performance, following darcy's equation as written in Equation (8) and (9). Herein, the influence of diffusion to the performance is neglected, and left for future study.

$$TEX \;=\; 4\left(\frac{1}{{\ell_x}^2} \;+\; \frac{1}{{\ell_y}^2} \;+\; \frac{1}{{\ell_z}^2}\right) \Delta x\; \Delta y\; \Delta z_{matrix}\; (1 \;-\; \phi_f)\left(\frac{\phi_m}{\tau}\right) \tag{8}$$

$$q_{MF} \;=\; TEX\; (P_M \;-\; P_F) \tag{9}$$

TEX is expressed in $rb - cp/d - psi$ while k_x, k_y, k_z are matrix permeability along the x, y, z directions. Where τ refers to tortuosity with range of 1 to 4. P_M and P_F refer to pressure along the matrix and fracture cells, respectively. Sensor calculates TEX only for grid blocks with fractures, and it becomes zero for matrix only blocks. The accuracy of using dual-porosity modeling is evaluated in correspond to the correct results given by single-porosity simulation.

2.3 Gas Enhanced Oil Recovery

Initially, gas injection was propagated to maintain reservoir pressure such that preserving the oil production. Nowadays, together with the development of oil production over time, gas injection becomes one of most used enhanced oil recovery techniques. Generally, gas EOR has two types of injection namely miscible and immiscible injection. Miscible implies that the injectant gas *mixes* with oil whilst immiscible refers to the condition where injectant gas and oil do not form a single fluid that one could distinct these two fluids easily. The system covers two main recoveries, macroscopic and microscopic.

Macroscopic recovery process, or recognized as conformance, portrays areal and vertical (heterogeneity) sweep efficiency, along with well-completion intervals and regional flow gradient (Coats, Whitson, & Thomas, 2009). This particular process reckons the amount of hydrocarbon pore volume contacted by injectant gas, permeability in $x-$, $y-$ and $z-$direction heterogeneity and gravity segregation. Having one of permeability equals to zero reflects flow barrier.

Microscopic recovery process deals with pore-level size (Coats et al., 2009). The mechanism includes immiscible, with and without the necessity of vertical lift equilibrium (VLE), along with miscible. Coats, Dempsey, and Henderson (1971) explain that the term equilibrium here refer to neither uniform pressure nor uniform saturation. It relates to capillary-gravitation equilibrium in correspond with nonuniform saturation and pressure profile along vertical direction (z-axis). VLE becomes extensive in large vertical permeability, thin reservoir, low viscosity and high capillary and/or gravity forces along

with low rates of areal sweep (Coats et al., 1971). Practically, Coats (1989) shows that the utilization of VLE assumption provides more reliable result for a given number of layers as it allows fewer layers depicted transition zone saturation distributions.

Initiating gas injection to reservoir oil develops two possibilities of mechanism in regard to miscible process, namely vaporizing and condensing gas miscible drive. Vaporizing gas miscible drive denotes the process when enriched in-situ gas in intermediate components are developed by vaporization at sufficiently high pressure in oil reservoir (Stalkup, 1984). Likewise, condensing-gas miscible drive is when repeated enriched gas transforms into an oil that may become miscible with the injection gas. Additionally, Zick (1986) introduced an alternative mechanism that is combining the two mechanisms mentioned previously and later known as condensing/vaporizing mechanism. The mechanism does not establish a miscible condition, yet the results could be similar to miscible-like recoveries (≈95%). It develops a sharp near-miscible front, with a condensing mechanism ahead of the gas front while behind a gas front, a vaporizing mechanism occurs. Miscible displacement process is beneficial for small gravity force and/or unfavorable of relative permeability.

Generally speaking, only 10% of the displacement process by injecting gas is vaporizing gas drive mechanism with lean injectant gas of C_1 or N_2. Lean gases when used as injectant gas tend to vaporize intermediate hydrocarbons components (C_5 to C_{12}). Vaporizing-gas drive process takes place as the injectant gas and reservoir oil generate miscibility front at sufficiently high pressure, if and only if no free-gas saturation ahead of the front (Whitson & Brulé, 2000). Thus, the essential parameter determining vaporizing-gas miscible drive is pressure. One should bear in mind that the reservoir pressure should be kept above the dewpoint pressure, otherwise the retrograde condensation may arise. In other words, the mechanism gets more complex with more fluid phase ahead of the front.

Condensing/vaporizing mechanism could dominate 90% of the displacement process by injecting gas. Condensation happens when enriched gas first in contact with the reservoir oil such that forming lighter oil. This equilibrium gas moves ahead as it is more mobile than the oil. New fresh injection gas replaces the equilibrium gas and develops even lighter oil. Condensing-gas drive mechanism arises when this oil light enough to be miscible. Zick (1986) argues that this mechanism is highly unlikely occur as the injectant gas cannot be replace in the oil. He believes that the first few contacts are dominated by condensation of light intermediates that develops lighter oil, but when more contacts are made, vaporization of middle intermediates outweigh the mechanism in which the oil becomes heavier. He concludes that oil is unlikely becoming miscible with the gas.

Such perception makes sense because all the light intermediates component has condensed into the oil leaving nothing in the injectant gas during first few contacts. Subsequently, oil becomes saturated in light intermediates while it loses middle intermediate as they are stripped out by the mobile gas phase. These middle intermediates cannot be replaced by the light intermediates of injection gas. Saturation, densities and k-values calculated by an EOS slim-tube simulator when using enriched gas injection are depicted in Figure 2.5.

Zick (1986) defines five emerging regions by having condensing/vaporizing mechanism:

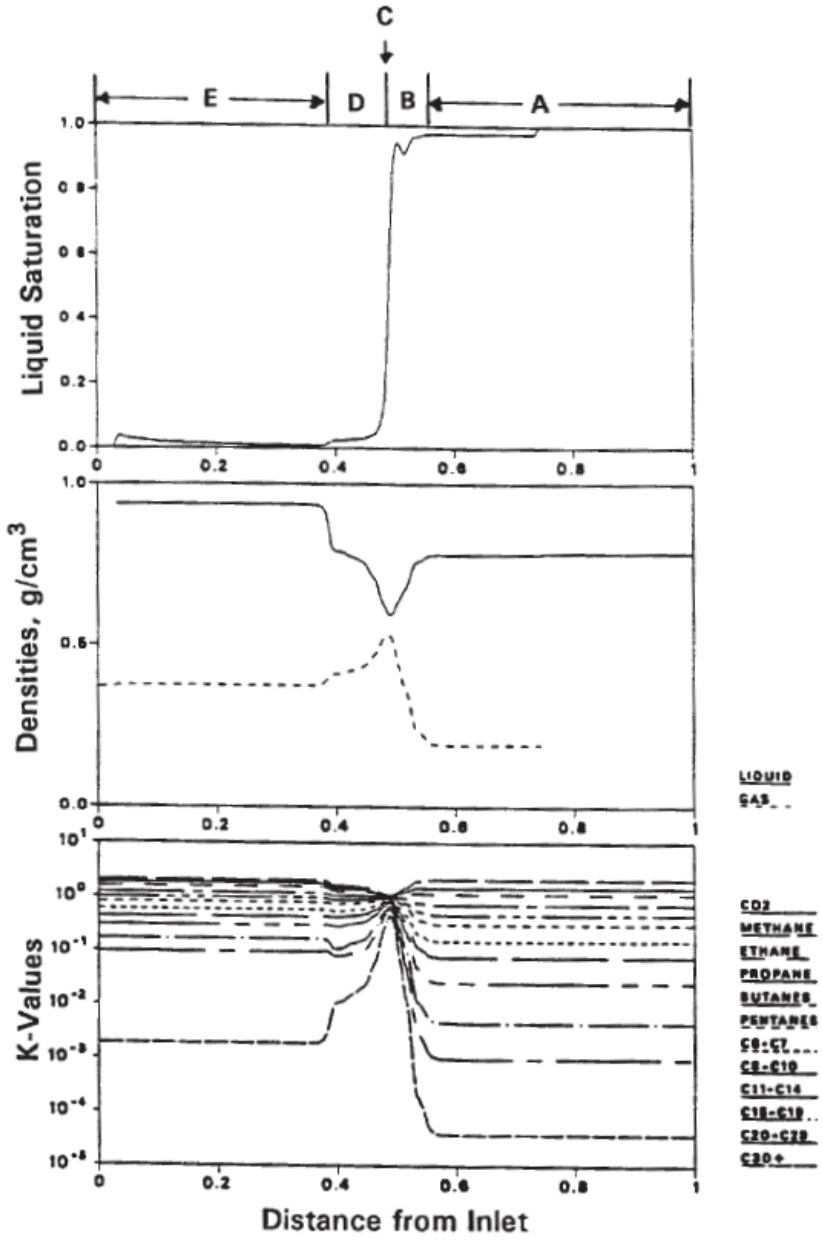

Figure 2.5: Calculated EOS slim-tube profiles for condensing/vaporizing mechanism of reservoir oil (Modified from Zick (1986) by Whitson and Brulé (2000)).

A. Reservoir oil

B. Two-phase front with condensation of intermediate components.

C. Sharp transition with near-miscible behavior. The dramatic changes toward B denotes significant condensation while toward D implies substantial vaporization of intermediate and heavy components.

D. Trailing front of enriched-gas that vaporizes middle-intermediate components.

E. Residual oil saturation is in equilibrium with the gas injectant.

Microscopic recovery processes become more complex and not fully understood for

fractured reservoirs, either naturally or artificially (induced) fractured (Uleberg & Kleppe, 1996). It involves gravity-capillary equilibrium, swelling, vaporization, imbibition and/or re-imbibition and diffusion that may induce interfacial tension gradients effect to the system.

The capillary continuity between matrix blocks may influence gravity segregation in fractured reservoir. Imbibition and re-imbibition are associated to gravity drainage of fractured reservoirs from a matrix block into a matrix block underneath. This effect has not adequately modelled in the reservoir simulator. Likewise, very low matrix permeability in tight unconventional may obscure the contribution of imbibition and/or re-imbibition.

The interfacial tension in pore-level recovery is highly affected by capillary pressure of gas and oil (P_{cgo}) and relative permeability of oil (k_{ro}) as well as residual oil saturation (S_{org}). Furthermore, it affects buckley-leverett displacement as explained by Hu, Whitson, and Yuanchang (1991).

Diffusion occurs due to the difference in concentration that allowing the molecules to move from a region with higher concentration to a region with lower concentration. Diffusion between the gas phase takes place in fracture cell whereas diffusion between the oil phase is in matrix cells. When the gas and oil surface are in equilibrium, component partitioning between gas and oil phase may also arise. For practical purpose, this study disregards the effect of diffusion considering that modeling one correctly is difficult.

Chapter 3

Model Description

3.1 Invariant Model Properties

A simple one-dimensional homogeneous case provided by *Coats Engineering* is carried out as a starting point. It is modeled in both single- and dual-porosity modeling for comparison purpose. Fracture and matrix relative permeability follow typical rock properties of unconventional reservoirs as shown in Figure 3.1 and Figure 3.2, respectively. *Equation-of-state* (EOS) properties utilize *spe5* example data set using *Peng-Robinson (1977)* with seven component as depicted in Table 3.1 and Table 3.2. Black oil table is generated based on this EOS as depicted in Appendix A.

Several modifications are performed to meet the objectives of the study. The number of grid along the z-direction is kept constant, which is one grid block. While for x-direction and y-direction, it would be decided after grid blocks number sensitivity is undertaken. Clearly, this enables the model becomes two-dimensional problem.

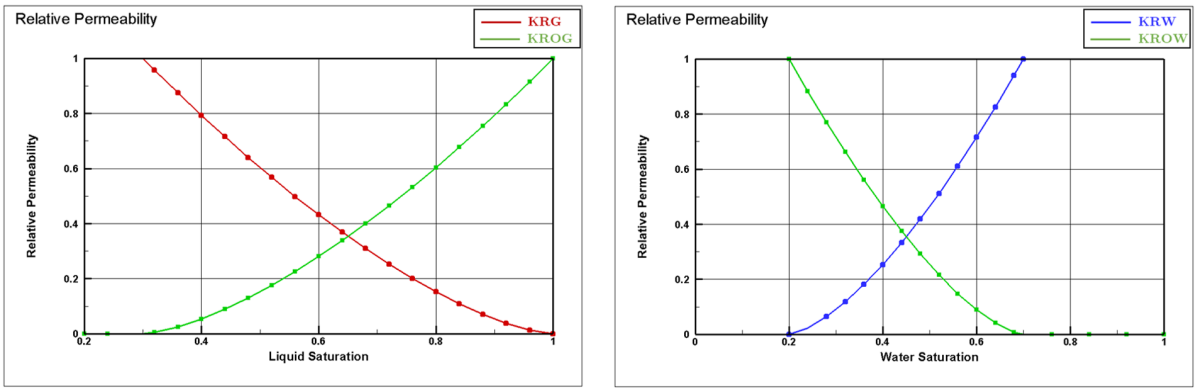

Figure 3.1: Matrix relative permeability.

Bakken shale is honored as analogue data. The study covers only a segment scale implying *hydraulic fracture-to-hydraulic fracture* assuming that each segment is identical and symmetrical. This *hydraulic fracture-to-hydraulic fracture* will be referred as *frac-to-frac* throughout the study. Subsequently, the reference model is modified following

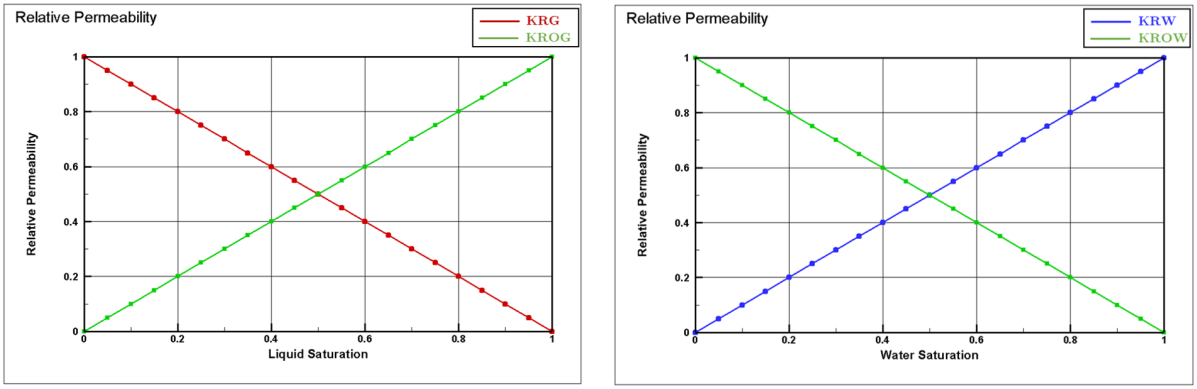

Figure 3.2: Fracture relative permeability.

Table 3.1: EOS properties using Peng-Robinson (1977)

Component	Molecular Weight M (lbm/lbmmol)	Critical Constants p_c (psia)	T_c (^oR)	Z_c	Acentric Factor ω	Parachor
CO_2	44.010	1071.331	548.46	0.274	0.2250	78.0
C_1	16.040	667.800	343.00	0.290	0.0130	71.0
C_3	44.100	616.300	665.70	0.277	0.1524	151.0
C_6	86.180	436.900	913.40	0.264	0.3007	271.0
C_{10}	142.290	304.000	1111.80	0.257	0.4885	431.0
C_{15}	206.000	200.000	1270.00	0.245	0.6500	631.0
C_{20}	282.000	162.000	1380.00	0.235	0.850	831.0

Table 3.2: Binary interaction parameters

	CO_2	C_1	C_3	C_6	C_{10}	C_{15}	C_{20}
CO_2	0.000	0.100	0.100	0.100	0.100	0.100	0.100
C_1	0.100	0.000	0.000	0.000	0.000	0.050	0.050
C_3	0.100	0.000	0.000	0.000	0.000	0.005	0.005
C_6	0.100	0.000	0.000	0.000	0.000	0.000	0.000
C_{10}	0.100	0.000	0.000	0.000	0.000	0.000	0.000
C_{15}	0.100	0.050	0.005	0.000	0.000	0.000	0.000
C_{20}	0.100	0.050	0.005	0.000	0.000	0.000	0.000

typical frac-to-frac length, likewise the model width and thickness (Figure 3.3). Details of general simulation setup used are summarized in Table 3.3. Production well is located in left boundary of the model ($i = 1$ and $j = 1$) with perforation point in the middle of the cell (20 ft from top of the reservoir).

It is important to ensure the reliability of the results when employing dual-porosity option. In other words, having another model to be compared with this model is obligatory. As explained previously, correct results are those obtained with single-porosity modeling for leastwise one matrix grid block. More matrix grid blocks actuates longer

CPU time and it becomes prohibitively expensive in the case of larger scale. Hereinafter, SPM simulation represents single matrix grid block of dual-porosity and is considered sufficient for this study. Fully implicit simulation is employed for all runs. The option of using either *Black Oil* or *EOS* (compositional) run will also be discussed upon this study.

Fractures are modeled by generating small-scale grids that are 0.01 ft wide and its length corresponds to fracture length. The way these fractures surrounding the matrix depends on matrix element shape. The matrix geometric scheme for the model used here follows *match-sticks* meaning that the matrix is separated by two orthogonal fracture planes which are in $x-$ and $y-$direction (Reiss, 1980).

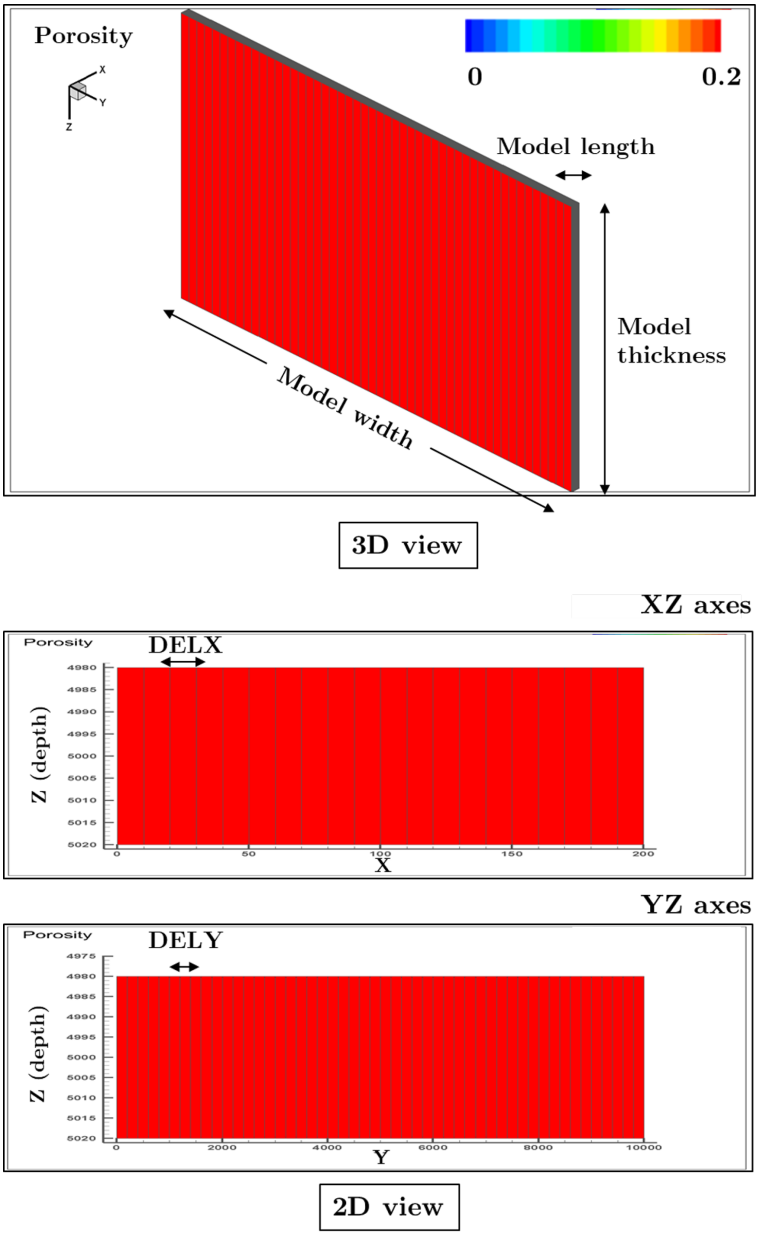

Figure 3.3: Model illustration in 3D and 2D view.

Unlike SPM, in DPM one grid contains both fracture and matrix without the needs of having them generated physically. Each grid is separated into two computational cells, a

matrix and a fracture cell. Sensor reservoir simulator models this by doubling the number of reservoir layers (Coats Engineering, Inc., 2011). If the fractured reservoir has n true layers, the input value of grid block along the $z-$axis (N_Z) is $2n$, which the first and second n layers correspond to matrix and fracture, respectively. Every properties that are assigned for first n layers belongs to matrix properties and for second n layers belongs to fracture properties. The dimension of each physical grid block are Δx, Δy and Δz as denoted in Figure 3.4. It contains many matrix blocks of dimensions ℓ_x, ℓ_y and ℓ_z that is separated by fracture.

Within the study, the behavior of dual-porosity modeling are analyzed in two different conditions, during depletion and huff-n-puff (gas injection) phase, separately. Some of the properties might be changed upon the analysis.

Table 3.3: General simulation setup

Parameter	Variable	Value	
Model length	L	200	ft
Model width	W	10000	ft
Model thickness	H	40	ft
Initial reservoir pressure	P_{Ri}	5000	psia
Reservoir temperature	T_R	160	^{o}F
Formation compressibility	c_f	4x10^{-6}	1/psi
Matrix properties			
Porosity	ϕ_m	0.2	
Permeability	k_m	200	nd
Fracture properties			
Porosity	ϕ_f	0.001	
Permeability	k_f	0.02	md
Width	f_w	0.01	ft
Water properties			
Formation volume factor	B_w	1.01	rb/stb
Density	ρ_w	63.05	lb/ft^3
Compressibility	c_w	3x10^{-6}	1/psi
Viscosity	μ_w	0.50	cp

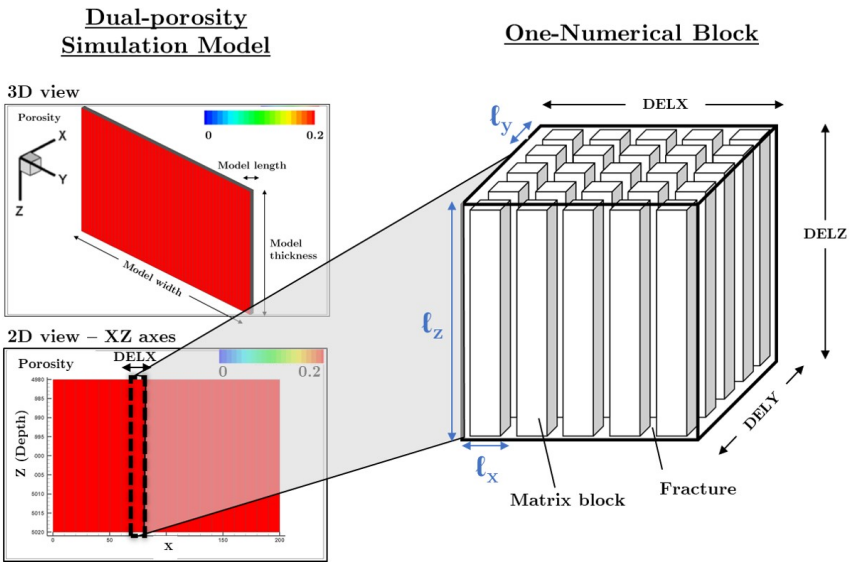

Figure 3.4: Dual-porosity model system.

3.2 Depletion Models

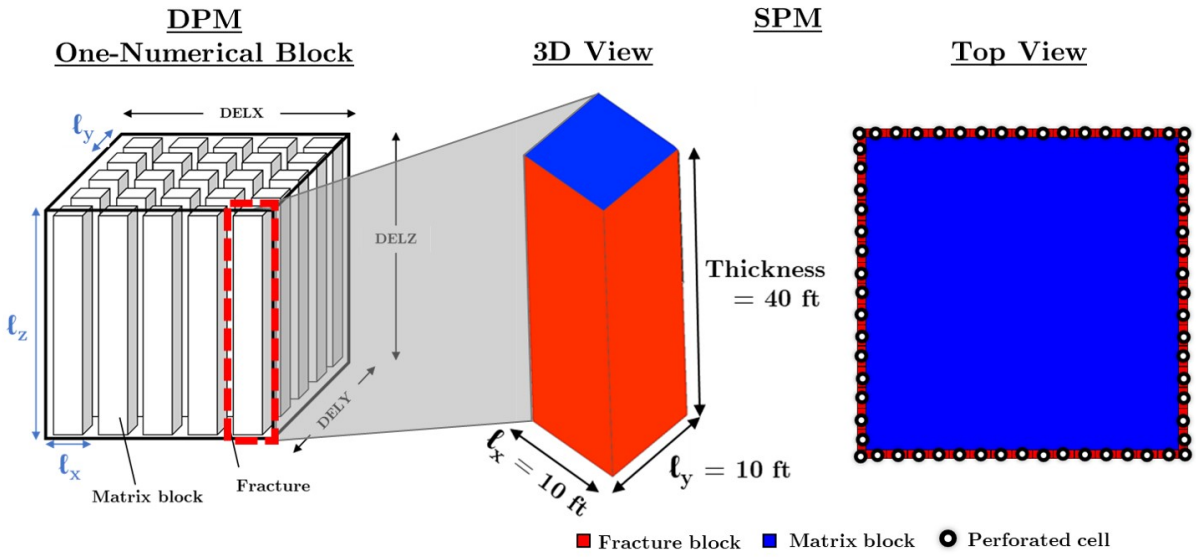

Figure 3.5: Built-in single-porosity model for depletion phase.

The dimension of single-porosity depends on the fracture spacing in correspond with the matrix geometric scheme. The model follows fracture along the x-axis and y-axis with no fracture lies along the z-axis as depicted in Figure 3.5. In this study, the dimension of single-porosity model in ℓ_x x ℓ_y x thickness is 10 x 10 x 40 ft. Later, ℓ_x and ℓ_y together with matrix permeability (k_m) are varied to capture the behavior in a wider range. Fracture grid blocks, represented by red color, surround the matrix blocks denoted by blue color.

The depletion phase takes place for 500 days and arbitrarily chosen to see the performance until the well stops to produce. The production is controlled by bottom-hole

Table 3.4: Simulation setup for depletion phase

Parameter	Variable	Value	
Model properties			
Matrix Permeability	k_m	200	nd
Schedule timing			
Depletion period	T_{dpl}	500	days
SENSOR time-step	DT	0.001	days
Production control			
Oil production rate	q_o	10^6	rb/d
Minimum bottom hole pressure during production	BHP_{prod}	2500	psia

Table 3.5: Grid properties for depletion phase

Parameter	Variable	Value	
Dual-Porosity			
Grid block in x-direction	N_x	4	
Grid block in y-direction	N_y	50	
Grid block in z-direction	N_z	1	
SRV length	L_{SRV}	200	ft
SRV width	W_{SRV}	10000	ft
SRV thickness	H_{SRV}	40	ft
Fracture spacing in x-direction	ℓ_x	10	ft
Fracture spacing in y-direction	ℓ_y	10	ft
Fracture spacing in z-direction	ℓ_z	0	ft
Single-Porosity			
Matrix block number in x-direction	N_{xm}	10	
Matrix block number in y-direction	N_{ym}	10	
Matrix block number in z-direction	N_{zm}	1	
SPM length	L_{SPM}	10	ft
SPM width	W_{SPM}	10	ft
SPM thickness	H_{SPM}	40	ft

pressure and is kept above the bubble-point to ensure no gas presents within the matrix blocks. In other words, preserving the single phase fluid system in the matrix. The setup during depletion phase are shown in Table 3.4 and Table 3.5.

In the interest of comparing DPM to SPM, both models should have the same setup. Identical model properties can be designed easily, however, careful consideration must be given when designing the production control. Since SPM represents to single matrix block, pressure in fracture blocks surrounding the matrix should have similar pressure as in fracture cells in single numerical block of DPM. This will be appointed as *fracture pressure* in this report. To avoid confusion, the employment of *fracture pressure* does not

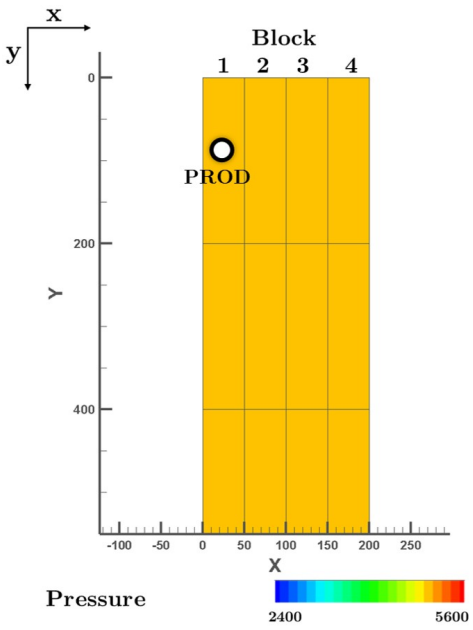

Figure 3.6: Dual-porosity model to be resembled with single-porosity model.

represent the pressure to crack and create a fissure, yet it refers to pressure along the fracture cells.

Three blocks are chosen to be compared with SPM, block number 1 (i=1, j=1), 2 (i=2, j=1) and 4 (i=4, j=1), as denoted in Figure 3.6. The concept is applied prior the comparison between both models as less interference due to production further away from wellbore. It simply says that the fracture pressure of the first block over time is highly unlikely to be the same with other blocks. For instance, prior comparing second block of DPM to SPM, fracture pressure as a function of time in second block of DPM are taken and set as production control in SPM. Doing it this way will ensure similar fracture pressure during depletion phase in both models.

3.3 Huff-n-Puff Gas EOR Models

The gas injection process is appointed as *huff* and the oil production process is referred as *puff*. The utilization of huff-n-puff (HnP) phase is interchangeable with gas injection phase in this study. Different simulation setup is employed when analyzing huff-n-puff gas EOR model. Unlike depletion phase, no sensitivity analysis are done related to matrix and fracture properties. Most of the results from depletion phase are carried to gas injection phase.

For instance, the selection of production and injection cycle period. It is decided to have 30 days of cycle period for both production and injection, whilst soak period is neglected for this particular case after scrutinizing production profile during depletion phase. The discussion is covered in Chapter 4 in more detail. The injection starts after 60 days of depletion phase and ends after 10 years. Both black oil and EOS run are compared in this phase. Simulation setup and grid properties are summarized in Table

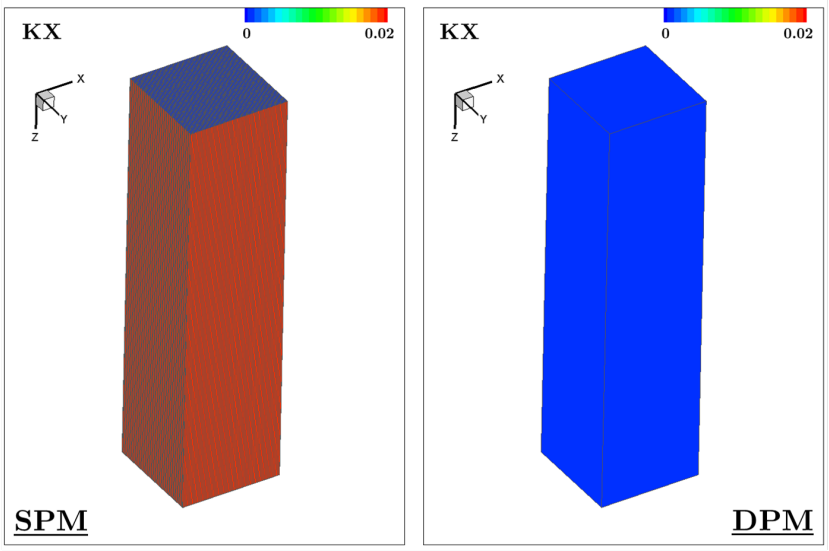

Figure 3.7: Built-in single-(left) and dual-(right) porosity model for huff-n-puff phase.

Table 3.6: Simulation setup for HnP Gas EOR phase

Parameter	Variable	Value	
Model properties			
Matrix Permeability	k_m	50	nd
Schedule timing			
Depletion period	T_{dpl}	60	days
HnP Gas EOR period	T_{inj}	3600	days
Injection cycle period	DT_{inj}	30	days
Soak cycle period	DT_{soak}	0	days
Production cycle period	DT_{prod}	30	days
Production and injection control			
Oil production rate	q_o	10^6	rb/d
Gas injection rate	q_{ginj}	10^6	rb/d
Minimum bottom hole pressure during production	BHP_{prod}	1000	psia
Injection pressure	P_{inj}	5000	psia

3.6 and Table 3.7, respectively.

Matrix permeability of 50 nd and fracture spacing of 10 ft are employed to honor predicted properties from Bakken shale reservoir. Such applications result in 10 x 10 x 40 ft dimension of SPM as length, width and thickness. In this particular section, DPM only has single physical grid block with single matrix block such that eliminating the existence of block 2, 3 and so on from depletion phase. Its dimensions correspond to SPM as illustrated in Figure 3.7. The provision of having this done is not only to minimize numerical error coming from number of grid blocks, but also to simplify the adjustment of identical fracture pressure in DPM and SPM.

Table 3.7: Grid properties for HnP Gas EOR phase

Parameter	Variable	Value	
Dual-porosity			
Grid block in x-direction	N_x	1	
Grid block in y-direction	N_y	1	
Grid block in z-direction	N_z	1	
SRV length	L_{SRV}	10	ft
SRV width	W_{SRV}	10	ft
SRV thickness	H_{SRV}	40	ft
Fracture spacing in x-direction	ℓ_x	10	ft
Fracture spacing in y-direction	ℓ_y	10	ft
Fracture spacing in z-direction	ℓ_z	0	ft
Single-porosity			
Matrix block number in x-direction	N_{xm}	75	
Matrix block number in y-direction	N_{ym}	75	
Matrix block number in z-direction	N_{zm}	1	
SPM length	L_{SPM}	10	ft
SPM width	W_{SPM}	10	ft
SPM thickness	H_{SPM}	40	ft

Chapter 4

Depletion Performance

Prior comparing DPM to SPM, it is needed to perform sensitivity analysis to minimize error caused by numerical dispersion and/or user misconception. Failing in ensuring the reliability of both models, SPM and DPM, could end up with misleading results. In this chapter, Table 3.4 and 3.5 are employed in addition to Table 3.3 as simulation input, unless otherwise stated.

4.1 Single-Porosity Model

Having depletion period of 60 days is considered sufficient for sensitivity analysis purpose in order to reduce CPU time. There are two sensitivities performed namely, connection cells and matrix grid block number sensitivity.

Connection cells sensitivity

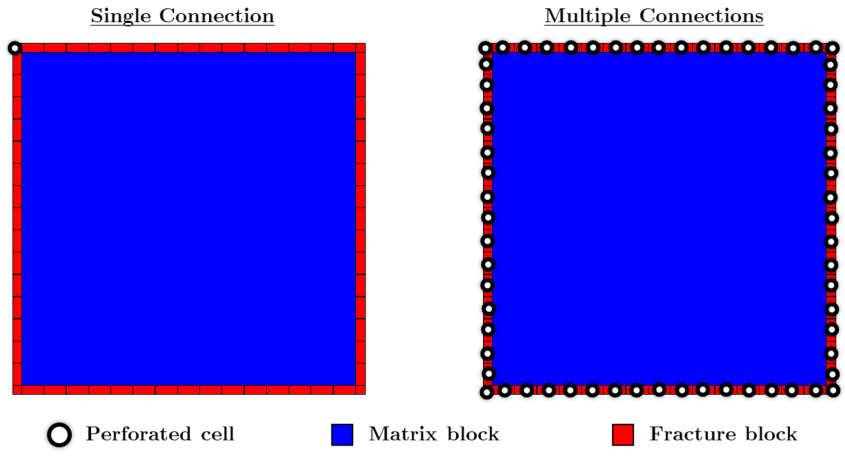

Figure 4.1: SPM - Sensitivity on number of connection cells.

Two ideas are carried for connection cells sensitivity, which are single and multiple connections as illustrated in Figure 4.1. First, single connection implies to only one

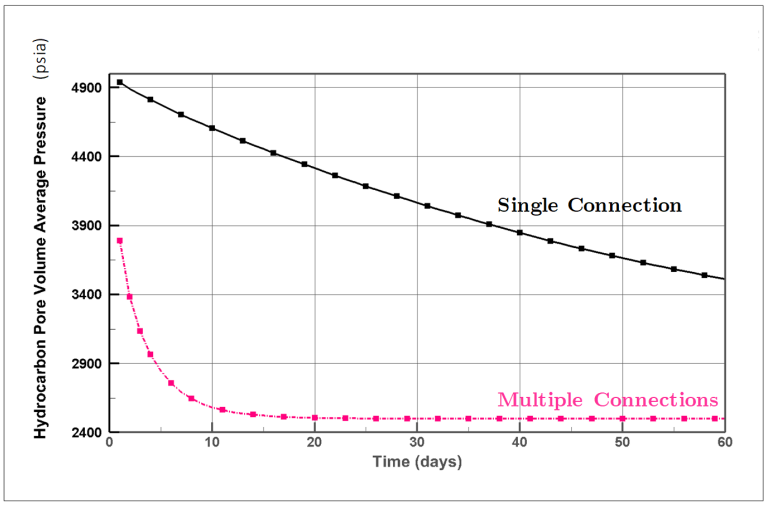

(a) Pressure profile

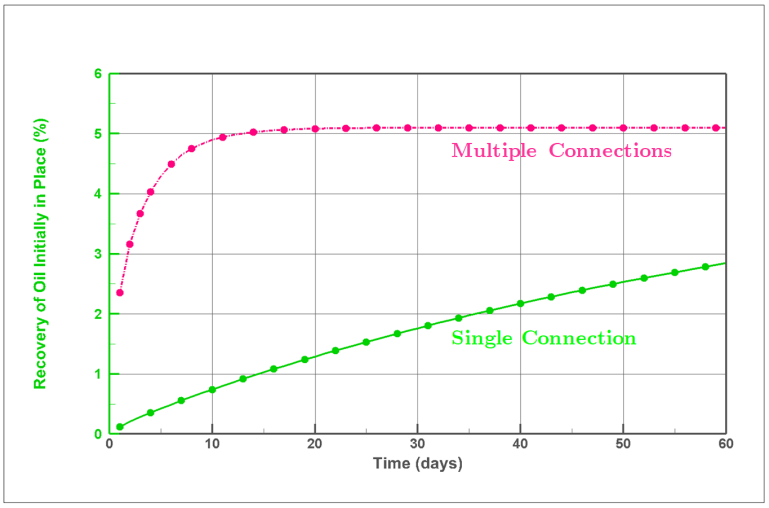

(b) Oil recovery factor profile

Figure 4.2: SPM - Perforation cells comparison after 60 days of production.

fracture cell that is connected to the wellbore. The other one is to connect all fracture cells to the wellbore later called multiple connections case.

Looking at Figure 4.2, it is notable that average reservoir pressure (P_{avg}) depletes immediately to BHP for the case of multiple connections. On the contrary, single connection case needs longer time to decrease it to BHP as P_{avg} is still at 3500 psia on day 60. The substantial difference is caused by different pressure gradient along the fracture grid blocks (ΔP_f). One could regard the findings by mapping the pressure along the fracture cells. Figure 4.3 shows the pressure map in j-cells at i=1.

Having all fracture cells connected to wellbore generates *infinite conductivity* behavior that is zero pressure drop in the fracture during production. In other words, pressure at the fracture cells equals to bottom hole pressure. It leads to depleting the matrix block symmetrically from the edges towards the center of the matrix as shown in Figure 4.4a.

Single connection case, contrarily to multiple connections case, has larger pressure

gradient along the fracture cells. The pressure propagates further away from the perforated cell. At the perforated cell (i,j,k = 1,1,1), there is no pressure discrepancy with respect to BHP, but further away, the pressure discrepancy becomes larger. It causes asymmetry pressure map such that nearest matrix cells to the wellbore are drained first. Figure 4.4b portray pressure map over 20 days of production.

Carrying larger pressure gradient along the fracture cells is not preferred as this does not reflect dual-porosity block behavior correctly. The fluid flow throughout the matrix is very slow considering very low permeability. Once the oil comes out and reaches the fracture cells, it flows immediately towards the wellbore given the fact that k_f is in orders of magnitude larger than k_m. Having said that, ΔP_f should be very little (≈ 0) such that infinite conductivity is obtained. Hereinafter, SPM will utilize multiple connections concepts for both sensitivity and comparison study in depletion and injection phase.

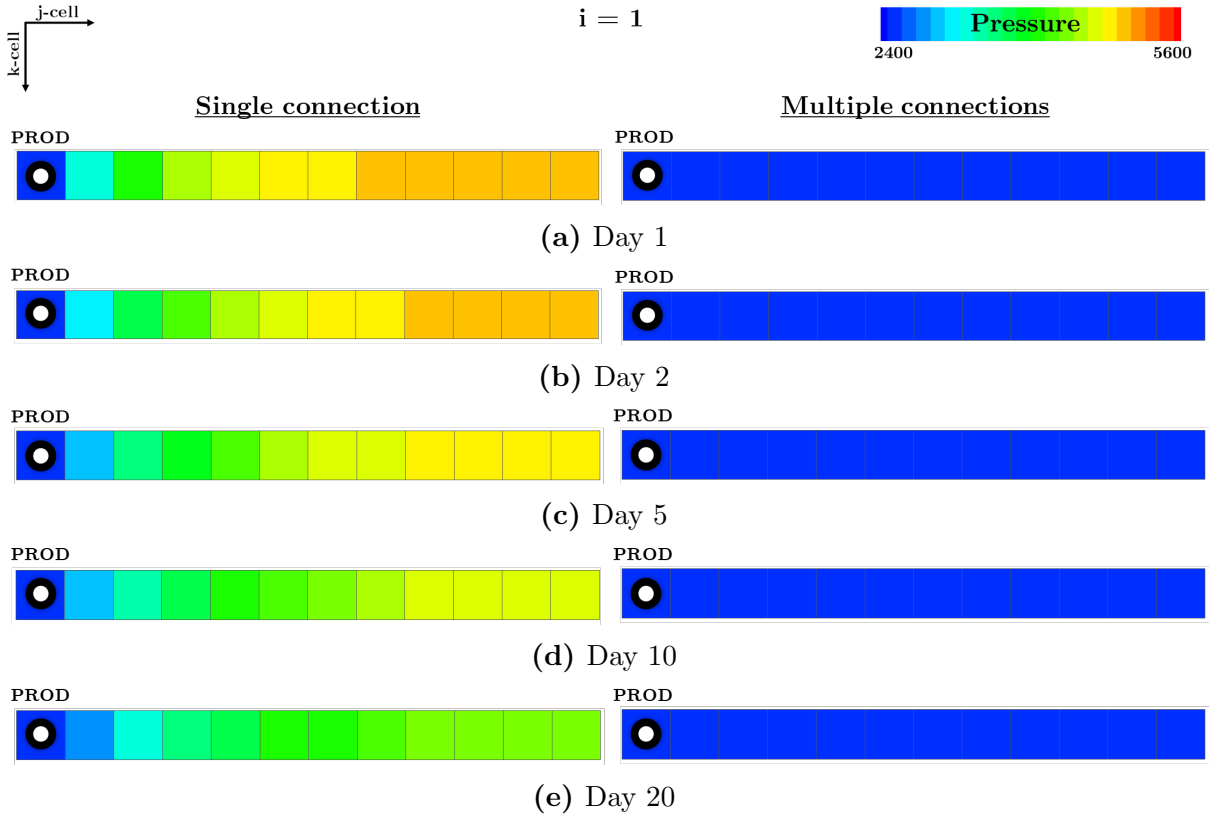

Figure 4.3: SPM - Pressure response over 20 days of production along the fracture cells (i=1).

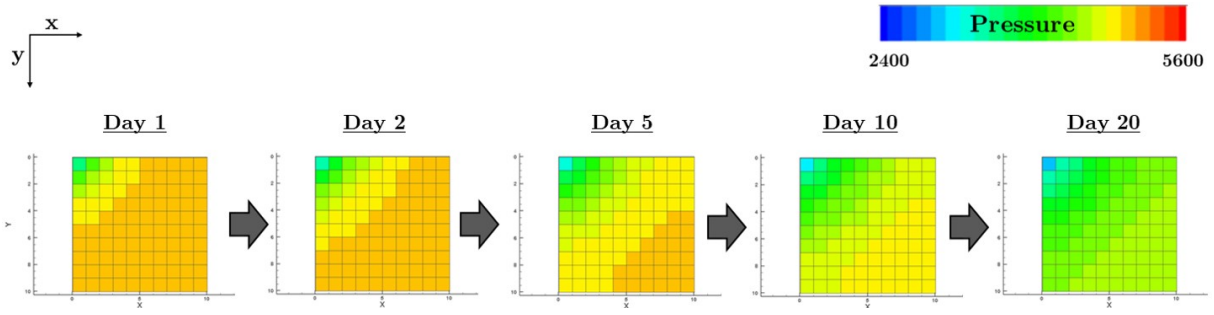

(a) Single connection

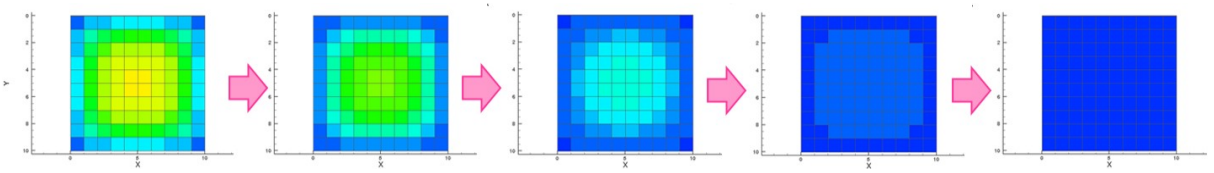

(b) Multiple connections

Figure 4.4: SPM - 2D view of pressure response over 20 days of production.

Matrix grid blocks number sensitivity

Most of reservoir simulators employ finite-difference formulation as the basis of the simulation. It discretizes the spatial segmentation of the model into smaller part so-called grid blocks. The discretization error is proportional to Δx^2 which is second order with respect to grid block size. For instance, it is expected to have global error of forth times higher when the grid block size is twice larger. In other words, the smaller grid blocks, the smaller error it would have. Yet, longer CPU time is unavoidable. It is necessary to find the optimum number of grid blocks that can compensate smaller error and faster CPU time.

Number of grid blocks in x- and $y-$direction are set to be equal, with single grid block in z-direction. The range of sensitivity starts from 1x1 (N_{xm}xN_{ym}) matrix grid block to maximum of 75x75 matrix grid blocks, due to the limitation of grid blocks number in *Sensor6k*.

Looking at the result plots portray in Figure 4.5, having 10x10 matrix grid blocks seems to be sufficient for 10 ft long of fracture spacing ($\ell_x = \ell_y = 10$ ft). It is considered quite reliable as increasing the matrix grid blocks number barely change the results. Despite the pressure and oil recovery factor for every case converge to the same value at the end of depletion phase, it has a fairly large amount of discrepancies for the first 40 days of production. Such error should be eliminated prior comparing SPM and DPM. Pressure response for several cases over 20 days of production is available in Figure 4.6. It is clear that 1x1 matrix grid block has a delayed pressure response. This happened given the fact that the larger the grid block size is, the longer time it needs to deplete.

Different fracture spacing is also contemplated for the study purpose following the estimated range in the Bakken shale reservoir. In that case, matrix grid block number sensitivity should be performed for every single case. The results are available in Table 4.1 and interested readers might find more detail results in Appendix B.

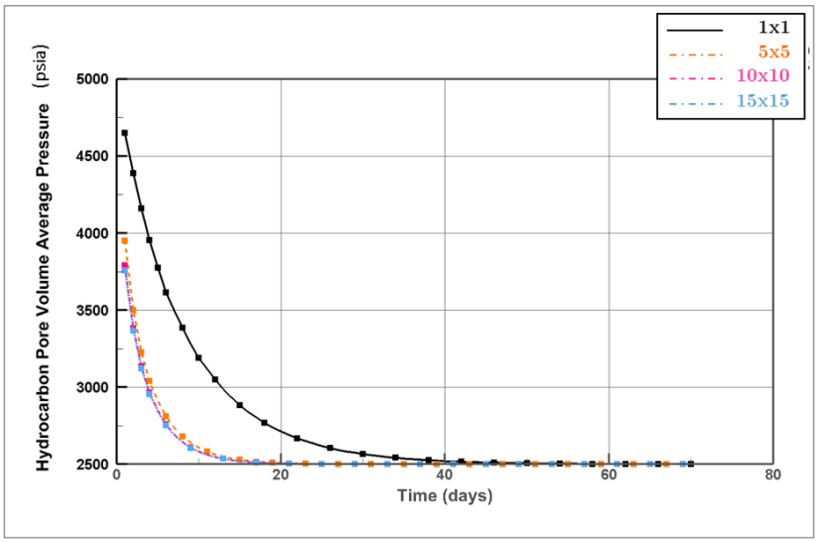

(a) Pressure profile

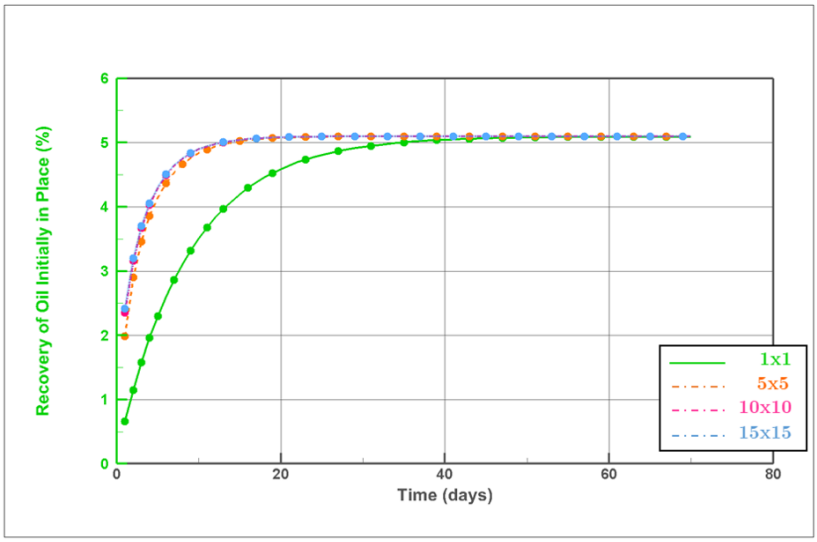

(b) Oil recovery factor profile

Figure 4.5: SPM - Matrix grid blocks number sensitivity - $\ell_x = 10$ ft.

Table 4.1: SPM - Matrix Block Number Sensitivity Results for Various Fracture Spacing

Fracture Spacing (ℓ_x)	Minimum Matrix Grid Blocks
1 ft	3x3
5 ft	5x5
10 ft	10x10
20 ft	10x10
50 ft	25x25

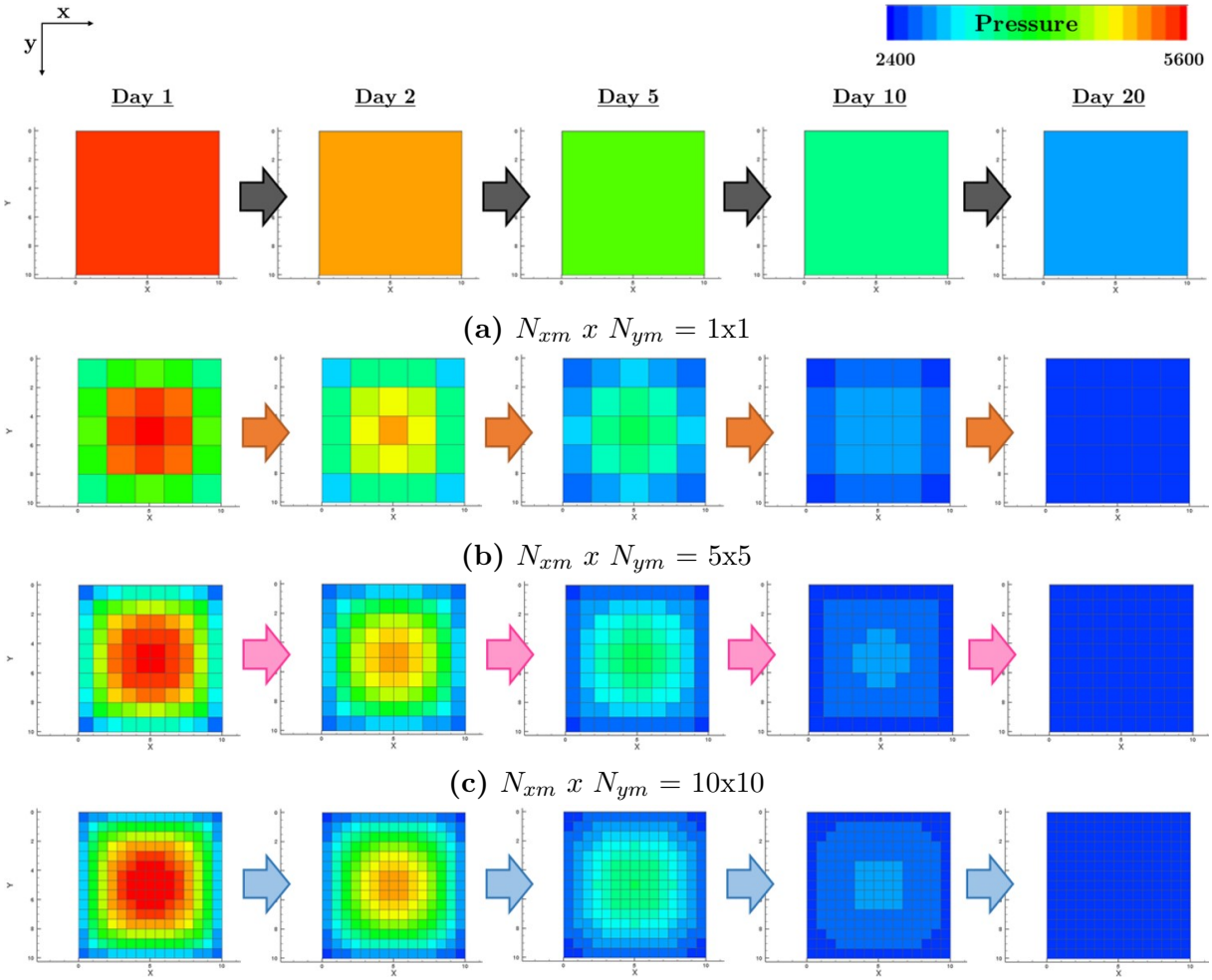

(a) $N_{xm}\ x\ N_{ym}$ = 1x1

(b) $N_{xm}\ x\ N_{ym}$ = 5x5

(c) $N_{xm}\ x\ N_{ym}$ = 10x10

(d) $N_{xm}\ x\ N_{ym}$ = 15x15

Figure 4.6: SPM - Matrix grid blocks number sensitivity - 2D view of pressure response (ℓ_x = 10 ft) over 20 days of production.

4.2 Dual-Porosity Model

Two sensitivity studies are performed namely, grid blocks number sensitivity (both along the x- and y-direction) and fracture spacing. For these sensitivity studies, 60 days simulation is considered sufficient.

Grid blocks number sensitivity

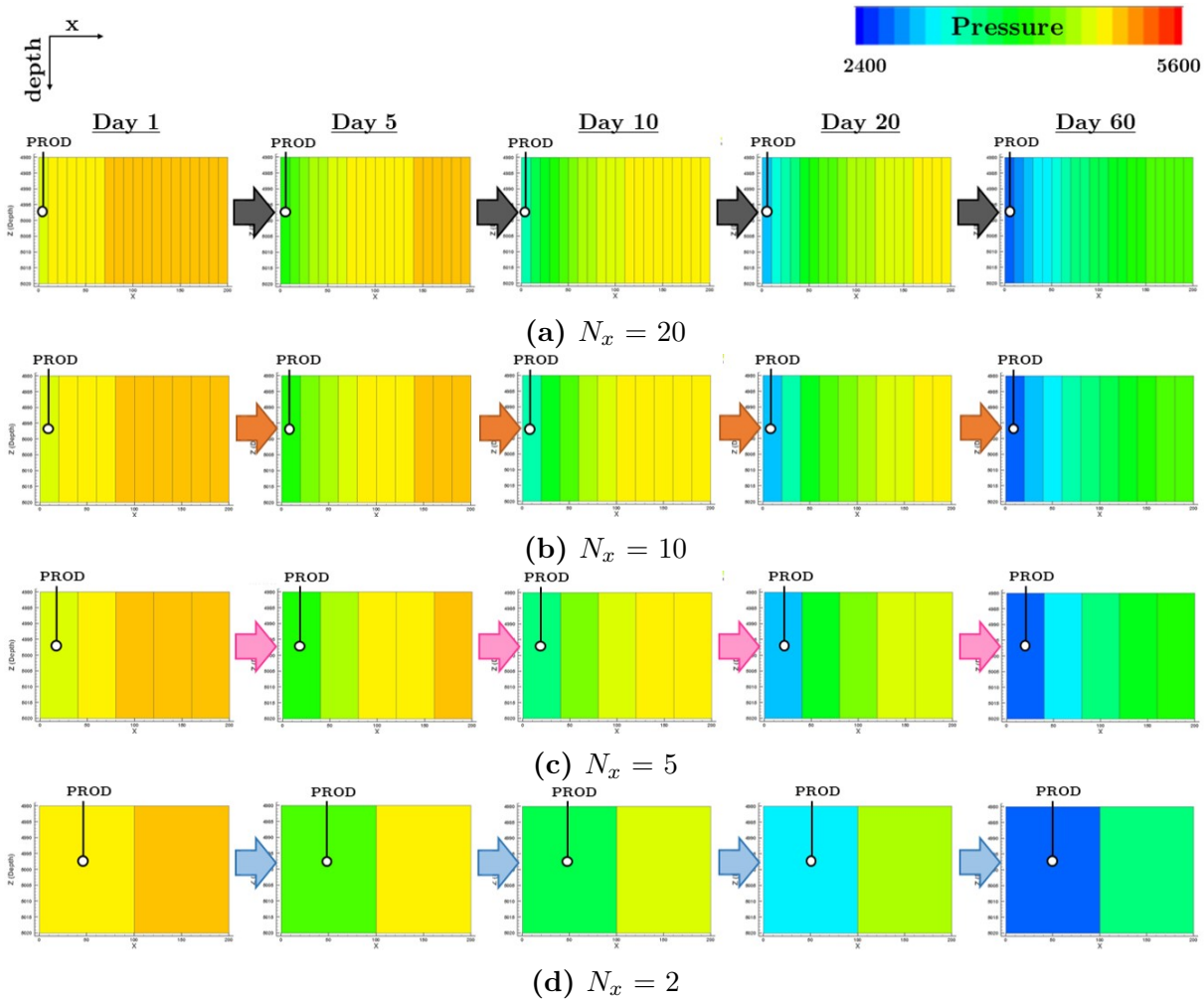

(a) $N_x = 20$

(b) $N_x = 10$

(c) $N_x = 5$

(d) $N_x = 2$

Figure 4.7: DPM - Grid blocks number sensitivity in x-direction - 2D view of pressure response over 20 days of production.

The grid blocks number in x-direction (N_x) is varied from 1 to 20 blocks. One block of N_z and N_y are set constant for this particular sensitivity. Unlike SPM, in DPM fluid flow follows the concept of *pseudosteady-state flow* (*PSS*) from the beginning, which is removing the transient flow. It implies that the reservoir behaves as a tank where the pressure at any point within a grid block decreases at the same constant rate. Having said that, the fracture pressure in the grid block where the well is located will immediately decline to well bottom hole pressure regardless of the grid block size. It moves further away from the wellbore that is creating pressure gradient along the reservoir. Larger number of grid blocks induces higher pressure gradient, yet reduces the numerical dispersion error as shown in Figure 4.7.

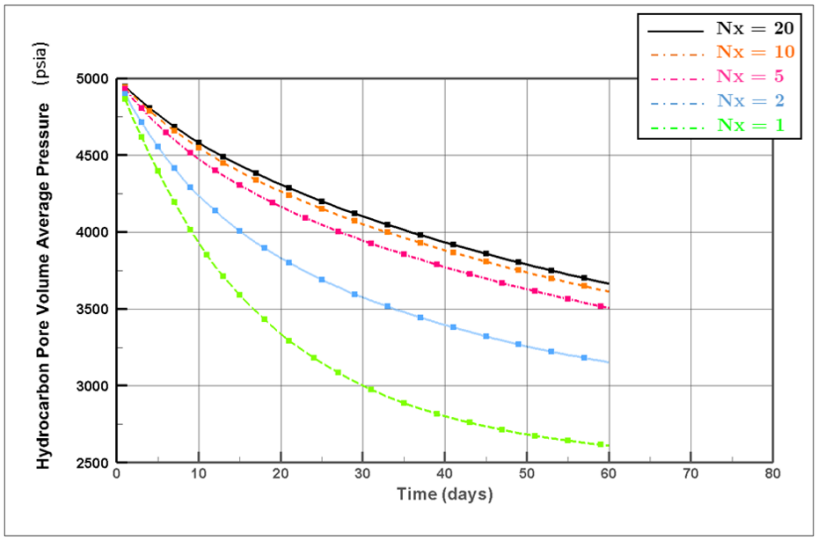

(a) Pressure profile

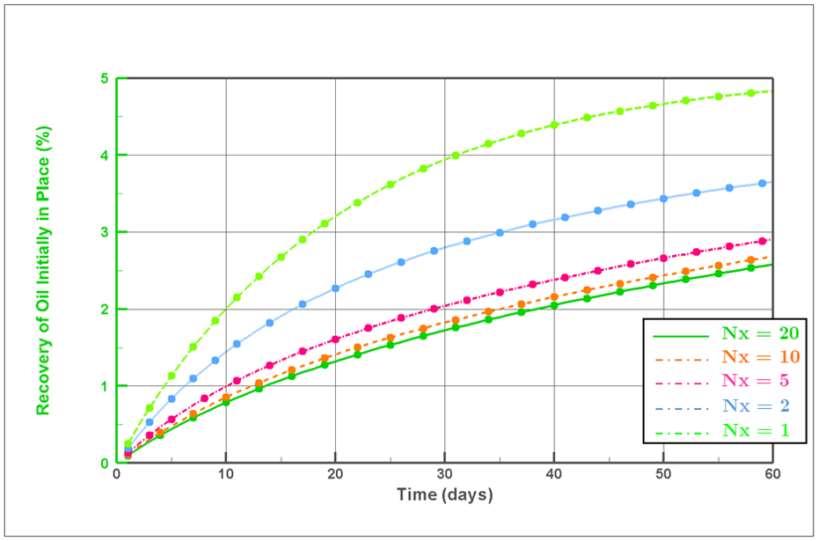

(b) Oil recovery factor profile

Figure 4.8: DPM - Grid blocks number sensitivity in x-direction performance profile (full model).

Looking at Figure 4.8, it is proven that decreasing grid blocks size evokes slower decline of P_{avg} along with smaller oil recovery. N_x=10 and N_x=20 have quite similar performance. This obtained because as the grid blocks size becomes smaller it reaches the convergent solution where the result does not change further.

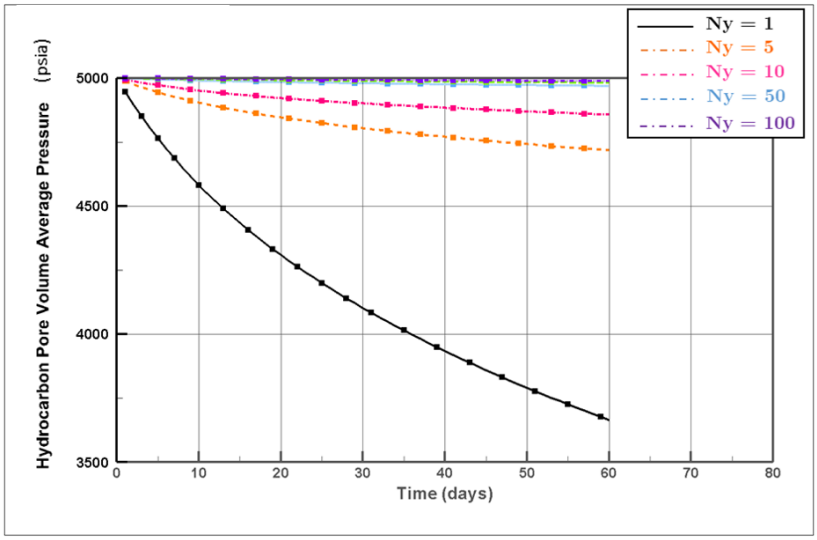

(a) Pressure profile

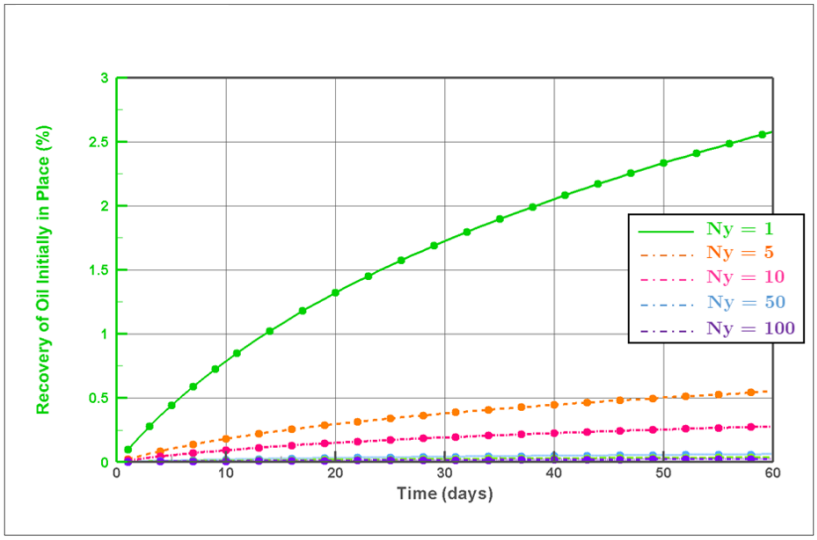

(b) Oil recovery factor profile

Figure 4.9: DPM - Grid blocks number sensitivity in y-direction performance profile (full model).

Similar profile performances are presumed for matrix grid blocks number sensitivity in y-direction as depicted in Figure 4.9 and Figure 4.10. The matrix grid blocks number is varied from 1 to 100 while N_x and N_z are set constant to 20 and 1 grid block, respectively. One should expect decreasing in recovered oil if the result has not converged to single solution yet, which for this specific case the single solution is 50.

In addition to that, changing the number of grid blocks while keeping the fracture spacing the same will also change the matrix-fracture exchange transmissibilities (TEX).

Calculated TEX for various matrix grid blocks number sensitivity are summarized in Table 4.2. As explained previously, this term is inversely proportional to number of matrix within one grid block of dual-porosity. It defines the oil production performance with respect to darcy's law. Higher TEX yields in higher oil rate, thus explaining more recovered oil in less grid blocks number. For instance, if N_x=2 then matrix cells can be calculated as follow;

$$
\begin{aligned}
DELX &= L \Big/ N_x \qquad\qquad = 200\ ft \Big/ 2 = 100\ ft \\
N_{matrix} &= \frac{DELX\ \cdot\ DELY}{\ell_x\ \cdot\ \ell_y} \\
&= \frac{100\ ft\ \cdot\ 10000\ ft}{10\ ft\ \cdot\ 10\ ft} \\
&= 10000
\end{aligned}
$$

Clearly, a better result is expected when exerting more grid blocks as it eliminates the numerical dispersion error. But then again, careful consideration should be taken, as more grid blocks generate larger CPU time. For DPM and SPM comparison (Section 4.3), N_x of 4 and N_y of 50 are carried out in order to capture the range of fracture spacing from 1 to 50 ft. It is decided given the fact that the grid block size should be larger or equal than fracture spacing ($\Delta x\ \geq\ \ell_x$). Thus, the contribution of grid blocks number that may cause different performance could be minimized.

Table 4.2: TEX as a Function of Grid Block Dimension

N_x	Ny	DELX (ft)	DELY (ft)	TEX (rb-cp/d-psi)
2	1	100	10000	0.7208
5	1	40	10000	0.2883
10	1	20	10000	0.1442
20	1	10	10000	0.0721
20	10	10	1000	0.0072
20	50	10	500	0.0014
20	100	10	100	0.0007

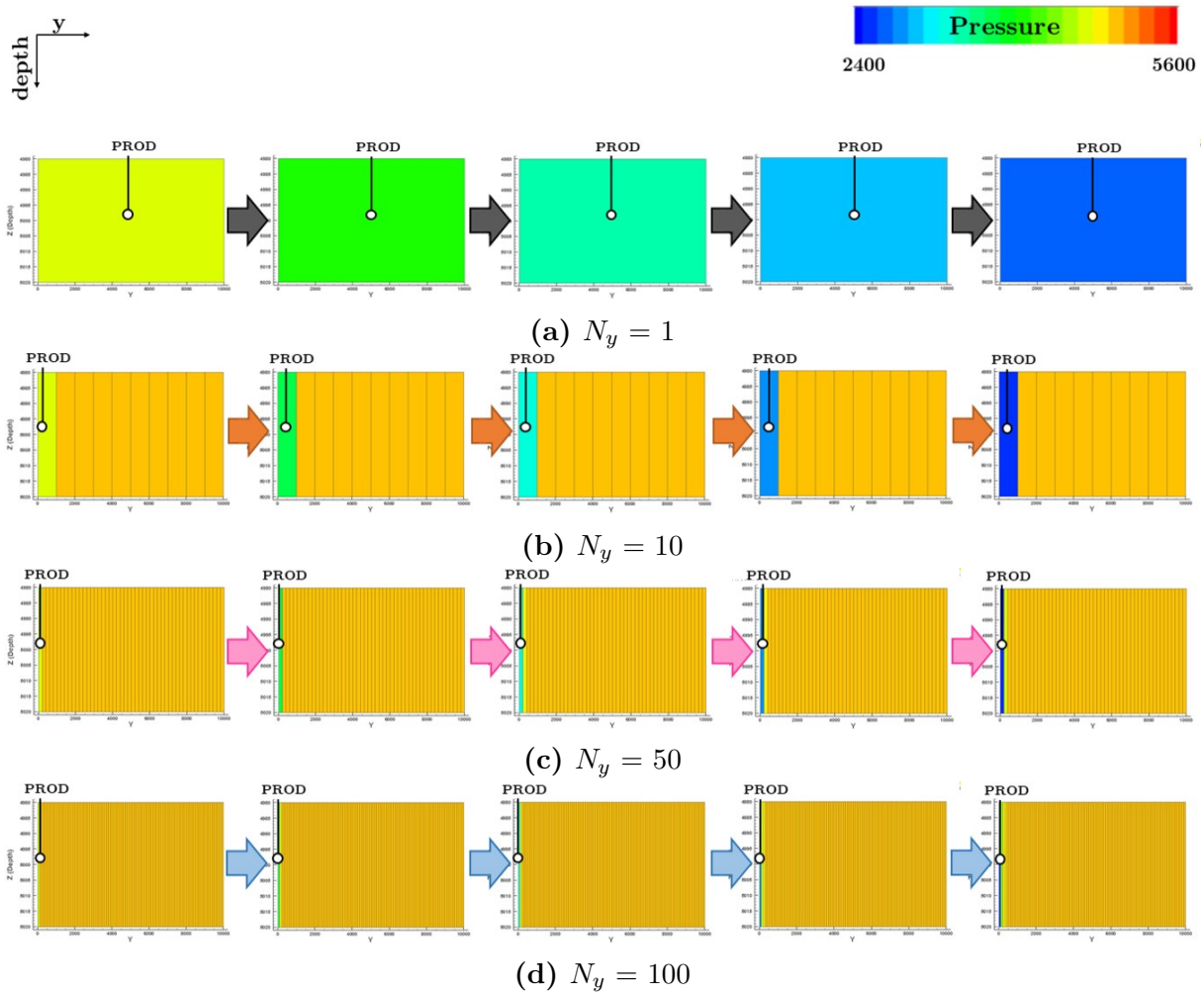

(a) $N_y = 1$

(b) $N_y = 10$

(c) $N_y = 50$

(d) $N_y = 100$

Figure 4.10: DPM - Grid blocks number sensitivity in y-direction - 2D view of pressure response over 20 days of production.

Fracture spacing sensitivity

Changing fracture spacing mainly affects number of matrix cells within one grid block of dual-porosity. Smaller fracture spacing generates more matrix cells thus, higher TEX and higher pressure drawdown. Both fracture spacing in x- (ℓ_x) and y-direction (ℓ_y) are set equal.

The results are shown in Figure 4.11. It is arguably that changing fracture spacing give quite similar performances. Nonetheless, there is still some differences among these three cases knowing the fact that smaller fracture spacing induces more extensive of SRV which theoretically gives more oil production.

Coats (1989) found that TEX is directly proportional to oil rate. Evidently, TEX is one of the most difficult processes to represent the behavior of DPM (Coats Engineering, Inc., 2016). Studying TEX would be discussed in more detail in this study, yet for this section, its relationship with matrix cells number is observed.

The same simulation condition is run multiple times with various scenarios of fracture spacing in three directions (ℓ_x, ℓ_y and ℓ_z). Here ℓ_y and ℓ_z are set equal and varied while

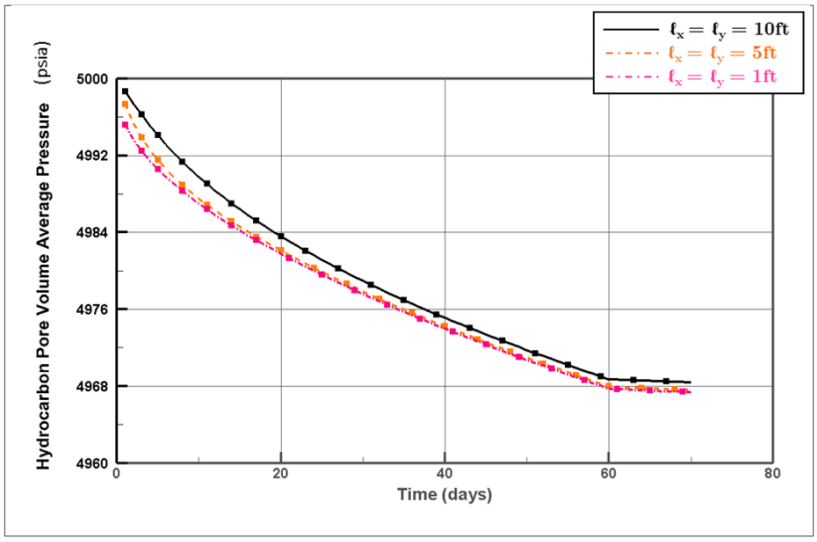

(a) Pressure profile

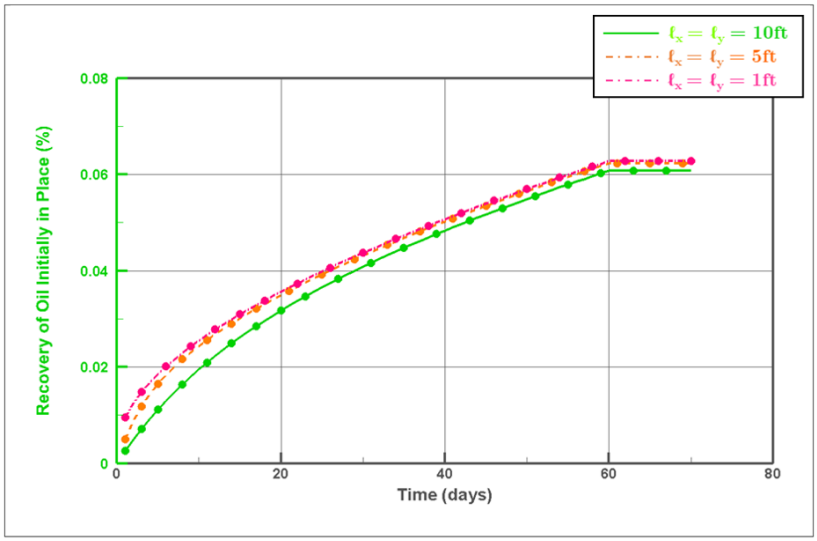

(b) Oil recovery factor profile

Figure 4.11: DPM - Fracture spacing sensitivity performance profile (full model).

ℓ_x is set constant. Several ℓ_x are analyzed. Unsurprisingly, the results are the same if ℓ_y or ℓ_z is chosen to be constant instead of ℓ_x.

The results are summarized in Figure 4.12. Certainly, TEX becomes larger when smaller ℓ_x is employed. The almost linear trendline is obtained when both ℓ_y and ℓ_z are larger than ℓ_x. When these fracture spacing are less than ℓ_x, TEX increase considerably resulting in two different trendline. Point where the change acquired is denoted in red dot, that is when all fracture spacing in three directions are identical. One might conclude that TEX does not have direct relationship with respect to all directions of fracture spacing. Yet, it does have direct relationship with the smallest fracture spacing, either in x-, y- or z-direction. As long as at least one of the fracture spacing is less than the others, that fracture spacing will determine how big the TEX.

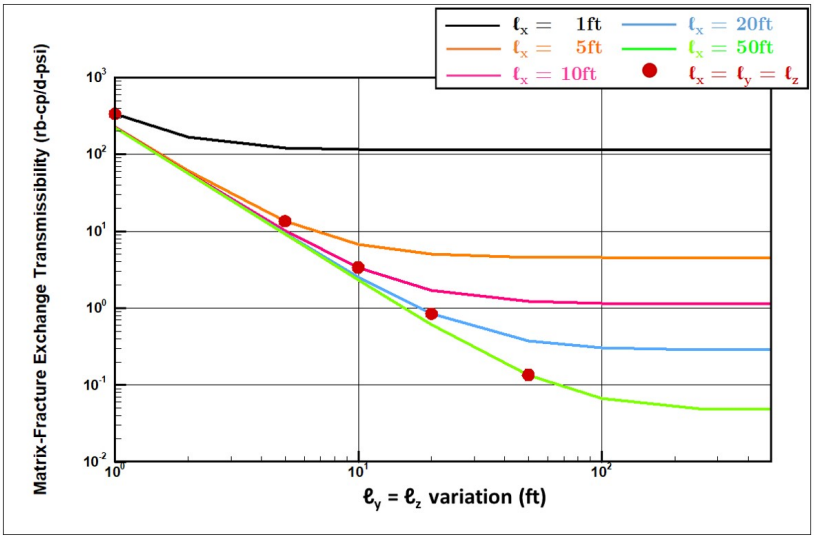

Figure 4.12: TEX variance of matrix block number.

4.3 Single- vs Dual-Porosity Model

In this section, SPM models multiple connections case such as providing infinite fracture conductivity with 10x10 matrix grid blocks (N_{xm} x N_{ym}). While for DPM, N_x and N_y are 4 and 50 grid blocks, respectively. These are selected as a result of previous sensitivity studies discussed in section 4.1 and 4.2.

Black Oil vs EOS run

Prior comparing DPM to SPM, the utilization of different run should be considered, which are black oil and EOS run. Several cases are employed, but only one of them is presented in this section. The equations need to be solved during simulation depend on number of components introduced to the model. There are only three components in black oil run namely, oil, gas and water. For EOS run, the components are N_2, CO_2, C_1, C_2, C_3, C_4, and as many as the user wants. Larger number of components implies more equations to be solved per grid block, which in most of the time can be expensive for EOS run. Generally speaking, EOS run has higher CPU time compared to black oil run.

Table 4.3: CPU time comparison between black oil and EOS runs

SPM		DPM	
EOS	BO	EOS	BO
285.25 s	48.91 s	0.16 s	0.16 s

Having a model with shorter CPU time is preferable, for this particular case Table 4.3 summarizes the result. Noticeably, utilizing DPM gives a great deal of having faster CPU time, with two to three orders of magnitude less than SPM in black oil and eos run. Although at a glance, using this model seems promising, eventually the reliability of the results would determine it.

For DPM the application of black oil and EOS run do not render any issue in regard

to CPU time. While for SPM, EOS run yields 5 times larger of CPU time than black oil run. The difference might even be substantial depending on the size and complexity of the model.

Unsurprisingly, SPM performance of black oil and EOS runs overlap each other both on pressure and recovered oil profile as denoted in Figure 4.13. Likewise for DPM, the results overlap one to another run as they are exactly alike. In conclusion, the utilization of black oil for depletion phase is considered an adequate approximation due to lower CPU time and giving almost equivalent performance to EOS run.

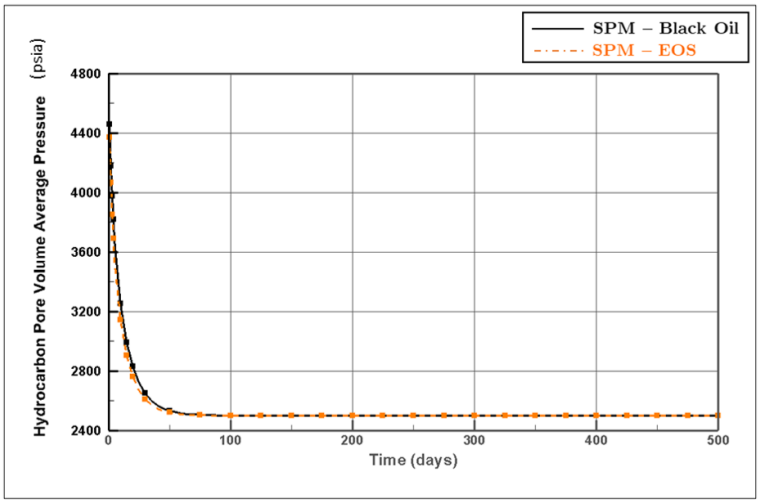

(a) Pressure profile

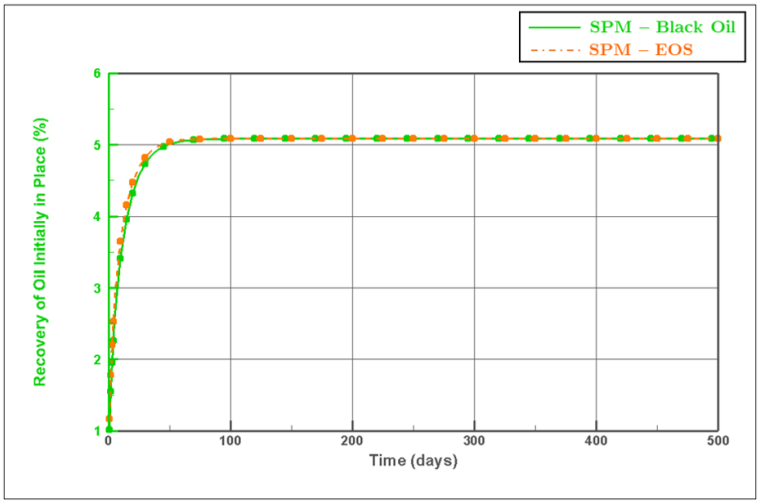

(b) Oil recovery factor profile

Figure 4.13: SPM performance comparison between black oil and EOS runs

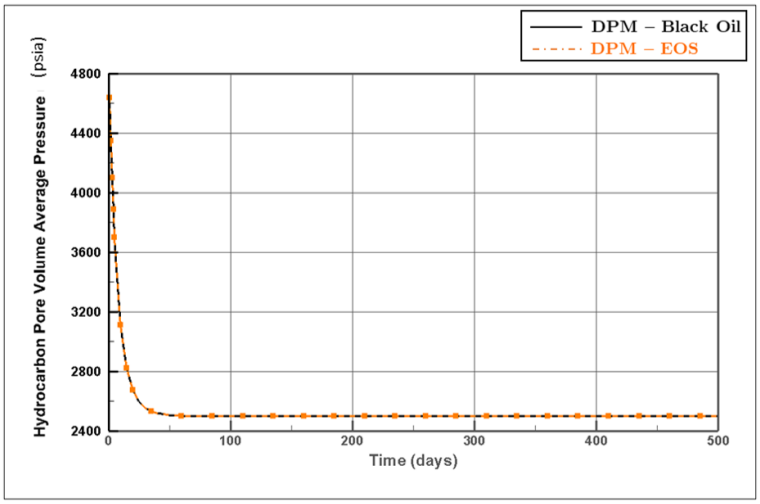

(a) Pressure profile

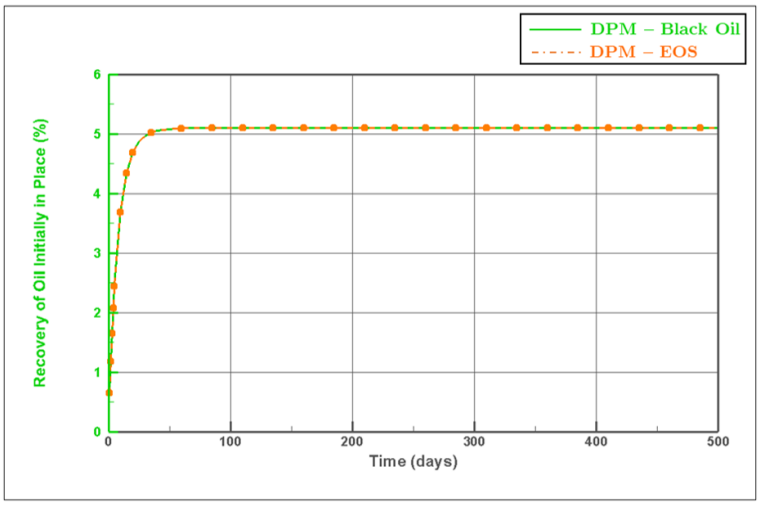

(b) Oil recovery factor profile

Figure 4.14: DPM performance comparison between black oil and EOS runs using default Sensor calculated TEX.

TEX modification

Several analysis are undertaken to preserve the behavior of different conditions of matrix permeability and fracture spacing. The fracture spacing is varied with range of 1 to 50 ft. The utilization of fracture spacing in this section, either ℓ_x or ℓ_y, can be interchangeable as the two are kept identical. Matrix permeability varies from the smallest, 10 nd (*nanodarcies*) to the largest, 1000 nd. For each combination of k_m and ℓ_x, three blocks are investigated one at a time. Detailed results for every case are summarized in Appendix B and are left for the interested readers.

The idea of comparing DPM to SPM is to have a more reliable results from DPM such that could follow the correct solution from SPM. After ensuring both models are in the same environment and setting, then first run is made. If by looking at the performance profiles (e.g. pressure and recovery factor) both models match, then one could say that the usage of DPM is adequate and indistinguishable with SPM. In the case of both

models have only slight agreement or nothing at all, minor modifications might have to be attempted.

The modification would only focus on changing TEX as it represents the fluid production rate. The main assumption of DPM is that the fluid is in PSS flow from the beginning. This may alter the accuracy of the performance in general, considering it eliminates transient behavior that captured by SPM. Sensor calculates TEX using Equation (8). To modify this number, a multiplier is chosen arbitrarily prior the simulation. If no agreement is found in both results, another multiplier is selected and the run is repeated. The acceptable TEX multiplier is when the performance profiles of DPM is sufficient enough that can represent performance of SPM without having to model one.

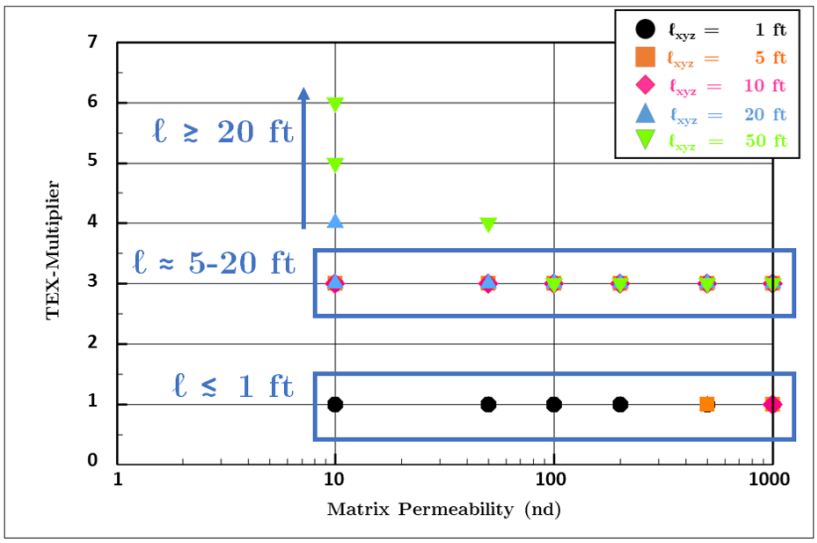

Figure 4.15: Summary of modified TEX Multiplier applied on DPM to have better agreement with SPM.

The selected TEX multipliers for various ℓ_x and k_m are summarized in Figure 4.15. Clearly from the results, DPM underperforms in every cases such that one should modify TEX to even higher value. Generally speaking, the selected TEX multiplier is 3 for most cases. There are some cases having different multiplier with the range of 1 to 6. This happened in correspondence with the loss of transient flow that may have major affection. Transient flow in matrix implies a larger pressure drawdown at the face of matrix and fracture cells, over time it moves further into the matrix. The behavior of PSS flow may eliminate this, given the fact that the pressure drawdown in the matrix and fracture are uniform at any point.

The interesting part is that modifying DPM is not necessary in the case of very small fracture spacing together with very high matrix permeability. Almost all points from 1 ft fracture spacing are placed with TEX multiplier of 1. As the fracture spacing becomes bigger, the TEX multiplier becomes larger. Employing larger matrix permeability reduces the number of TEX multiplier as the fluid flows easily from the matrix cells towards the fracture cells. Additionally, higher matrix permeability yields faster transient flow period, reaching PSS flow instantly.

In conclusion, as fracture spacing becomes smaller or matrix permeability becomes

higher then TEX is smaller. Likewise, larger TEX is expected when having larger fracture spacing along with smaller matrix permeability.

Single matrix grid block

Arguably, the number of matrix cells within a single DPM block may have some contributions to the performance such one could not produce similar performance to SPM. To verify that, one single matrix block of DPM is generated and is compared with SPM, resulting in identical model for two different principles. The model properties follow one of the cases arbitrarily, which in this case is combination of 10 ft fracture spacing and 50 nd of matrix permeability.

The performance results before and after applying TEX multiplier are depicted in figure 4.16. Clearly, DPM underperforms in the early times of production, that is when transient flow dominates flow regime in SPM. The transient flow effect is well illustrated in Figure 4.16c. It assumes that the flow acts as infinite acting reservoir without encountering any boundaries. It usually happens for a relatively short period after the production started, that caused some pressure disturbance in the adjacent wellbore. As explained previously, it is needed to minimize this error by modifying its TEX. The closest performance is achieved by having multiplier of 3. The result is in accordance with the previous finding.

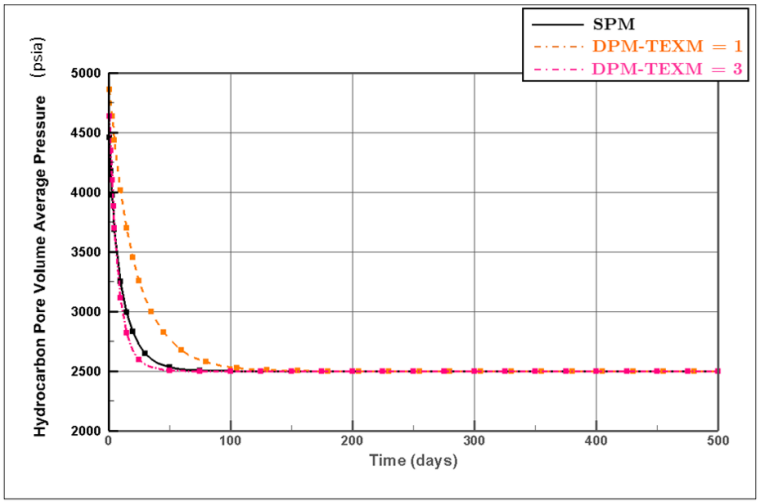

(a) Pressure profile

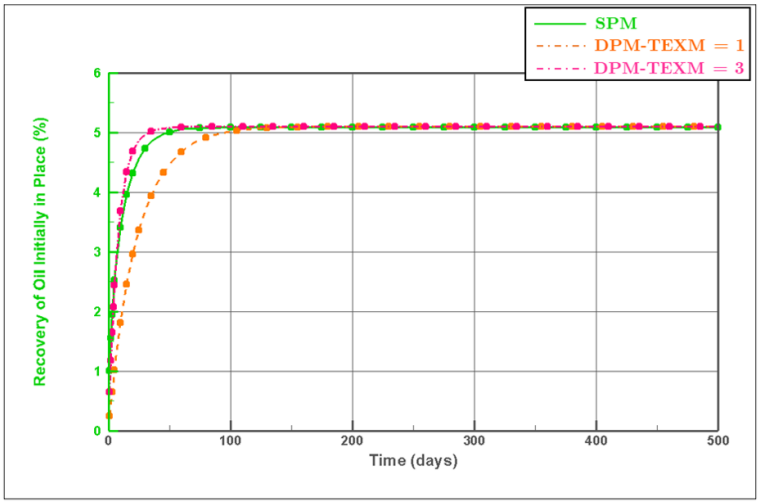

(b) Oil recovery factor profile

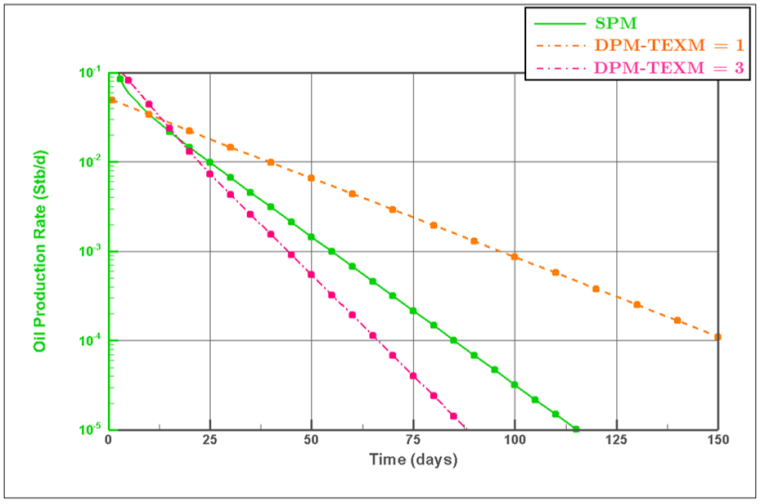

(c) Oil production rate profile

Figure 4.16: Single matrix block performance profile after applying modified TEX multiplier.

Recommended huff-n-puff cycle period

Broadly speaking, the oil recovery factor stops at approximately 5%. In a relatively short time, the pressure reaches minimum bottomhole pressure and by that time one cannot produce more oil from the matrix. The maximum oil recovery is acknowledged as ultimate oil recovery. In order to improve the recovery, injection gas EOR is performed to the model in addition to study its behavior during injection phase, which will be discussed in the next chapter. Choosing the appropriate cycle time for both injection and production becomes necessary prior the study.

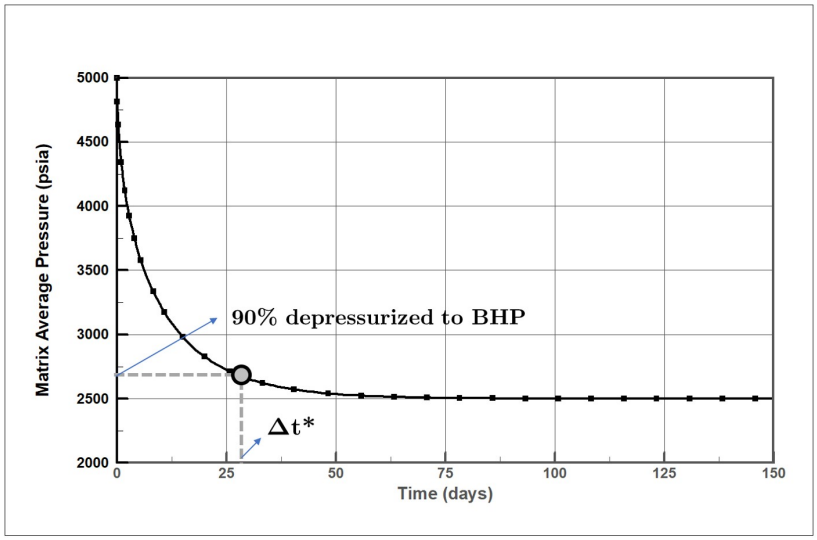

(a) Average matrix pressure profile (P_m)

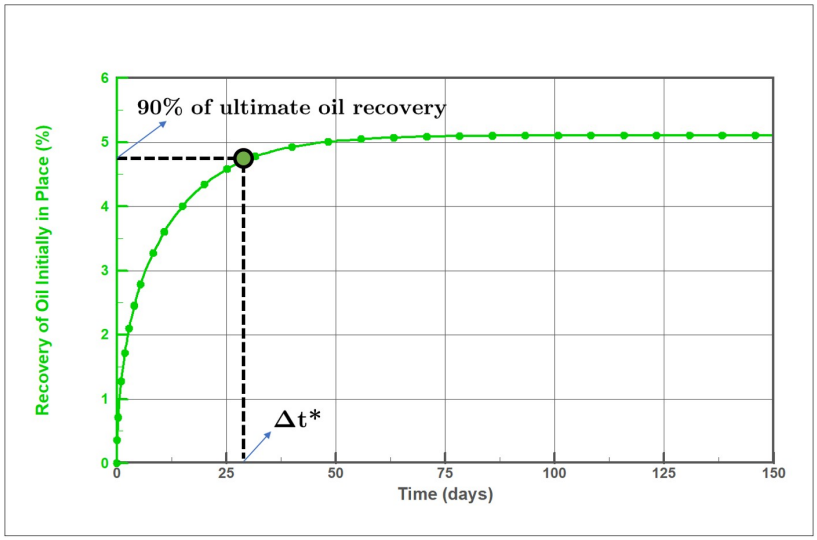

(b) Oil recovery factor profile

Figure 4.17: Δt^* of single-porosity model for $\ell_x = 10$ ft and $k_m = 50$ nd.

It is considered sufficient to have target on depleting the matrix block by almost 90% before reaching BHP, that is also to say 90% of ultimate oil recovery. In this study, the time to reach this condition is named as Δt^*. For instance, using the previous single matrix DPM block (ℓ_x=ℓ_y=10 ft & k_m=50 nd), as seen in Figure 4.17, it is found that Δt^* is reached after 30 days of production.

If this Δt^* is presumed adequate to represent the optimum time to depressurize 90% of matrix block to minimum BHP, then the same amount of time should also work in the case of pressurize matrix pressure. Therefore, the cycle time of huff-n-puff is specified by analyzing Δt^* for multiple cases that depend on the applied properties to the model which are matrix permeability and fracture spacing. Figure 4.18 summarizes the results of Δt^*. As the matrix block becomes bigger and matrix permeability becomes smaller, the longer time it takes to reach Δt^* and vice versa.

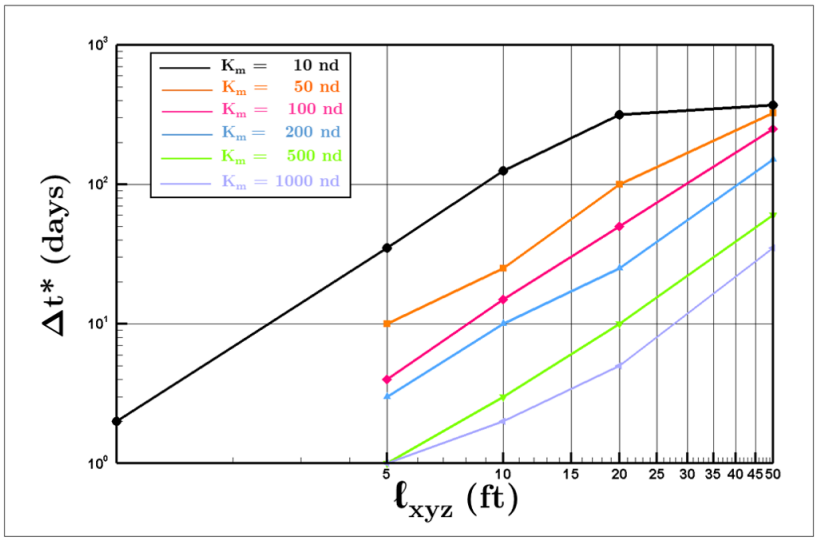

Figure 4.18: Δt* for various fracture spacing and matrix permeability.

Chapter 5

Huff-n-Puff Gas EOR Performance

The exertion of either black-oil and EOS run may not have major affection to the performance during depletion phase. However, it may have completely different behavior when injection is introduced to the model. In this chapter, both black-oil and EOS run are compared. DPM and SPM simulate single matrix block of 10x10x40 ft dimension with matrix permeability of 50 nd. In addition to general properties depicted in Table 3.3, this chapter utilizes Table 3.6 and Table 3.7 as simulation input.

5.1 Single-Porosity Model

Matrix grid blocks number sensitivity

This analysis should always be undertaken regardless of whether it has been done before or not, deeming that the input may have been altered. The matrix grid blocks number is varied from the least of 1x1 to the maximum of 75x75 and the results can be found in Appendix C. One could agree that smaller grid blocks size yields less error, considering that the discretization error is proportional to second order of block size.

From previous analysis in Chapter 4, having 10x10 matrix grid blocks is considered sufficient for depletion phase. Nonetheless, this differs as assured in Figure 5.1 and Figure 5.2, for black oil and EOS run, respectively. Evidently, the recovered oil from 10x10 matrix grid blocks number has enormous differences with 75x75 matrix grid blocks number. Despite the similarity of pressure profile throughout the simulation time, both cases have solely the same production profile during first 60 days before the injection begins. Smaller grid blocks number implies to larger block size, therefore, more oil is in contact with injected gas in the matrix fracture interface. This phenomenon yields *false mixing* between gas that is being injected and the original reservoir oil attributable to dispersion numerical error.

This false mixing evokes more oil being vaporized by gas resulting in higher cumulative injected gas along with higher recovered oil. One should expect over optimistic results than it should be if this erroneous approach is utilized. It may generate better agreement with DPM results, but for the wrong reason. Similar profiles also occur in EOS run.

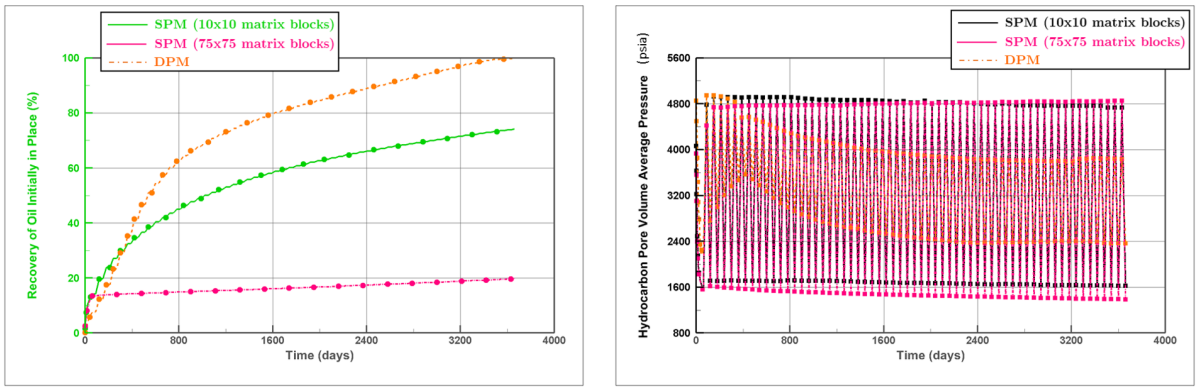

(a) Oil recovery factor profile

(b) Average reservoir pressure profile

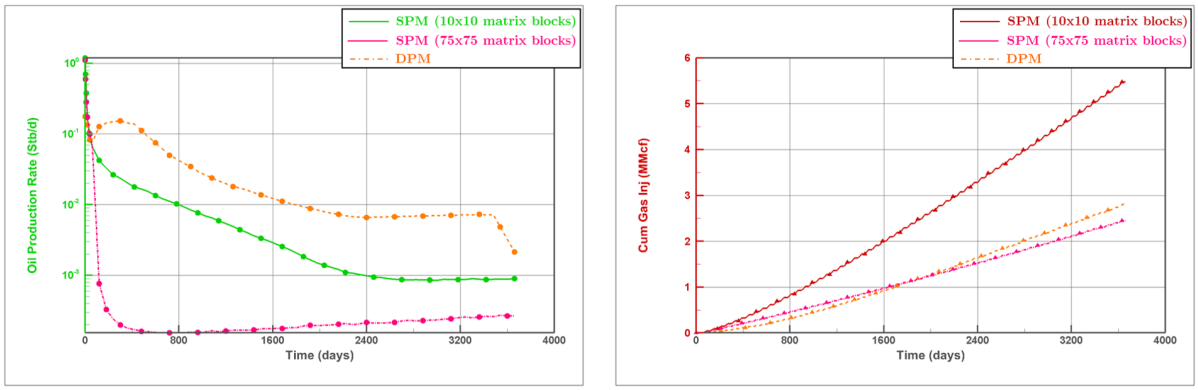

(c) Oil production rate profile

(d) Cumulative injected gas profile

Figure 5.1: Performance comparison between 10x10 and 75x75 matrix grid blocks with black oil simulation

A slice of the model is taken away for studying the saturation profile in correspond to distance (either along the $x-$ or $y-$direction). Such decision allows one to have better understanding what happened in the matrix block, knowing the fact that the mechanism in SPM follows streamline from any point at the edges towards the center of the matrix cell.

Figure 5.3 and 5.4 illustrate oil and gas saturation profile for the case of 10x10 and 75x75 matrix grid blocks, respectively. Comparing these two figures, the discrepancies are spot from the first cycle. More gas is accumulated in the first 0.5 ft near the interface matrix and fracture in 10x10 matrix grid blocks case. It becomes even more extensive after 10 years of injection process reaching 2.5 ft. On the other hand, having 75x75 matrix grid blocks, allowing the gas to move only slightly towards the center of the matrix for over 10 years period of injection phase. The distinction of these two cases indicates more false oil and gas mixing in smaller grid block size, that is creating larger area of miscible gas front.

One should assure that this error is removed such that the result is *dispersion free* by increasing grid blocks number as large as possible until the result becomes convergent. Changing the matrix grid blocks number into 75x75 from 10x10 can reduce the recovered oil by almost 60%. Then again, the maximum that this model can run is only up to 75x75 matrix grid blocks, but it is believed that increasing the grid blocks number more than

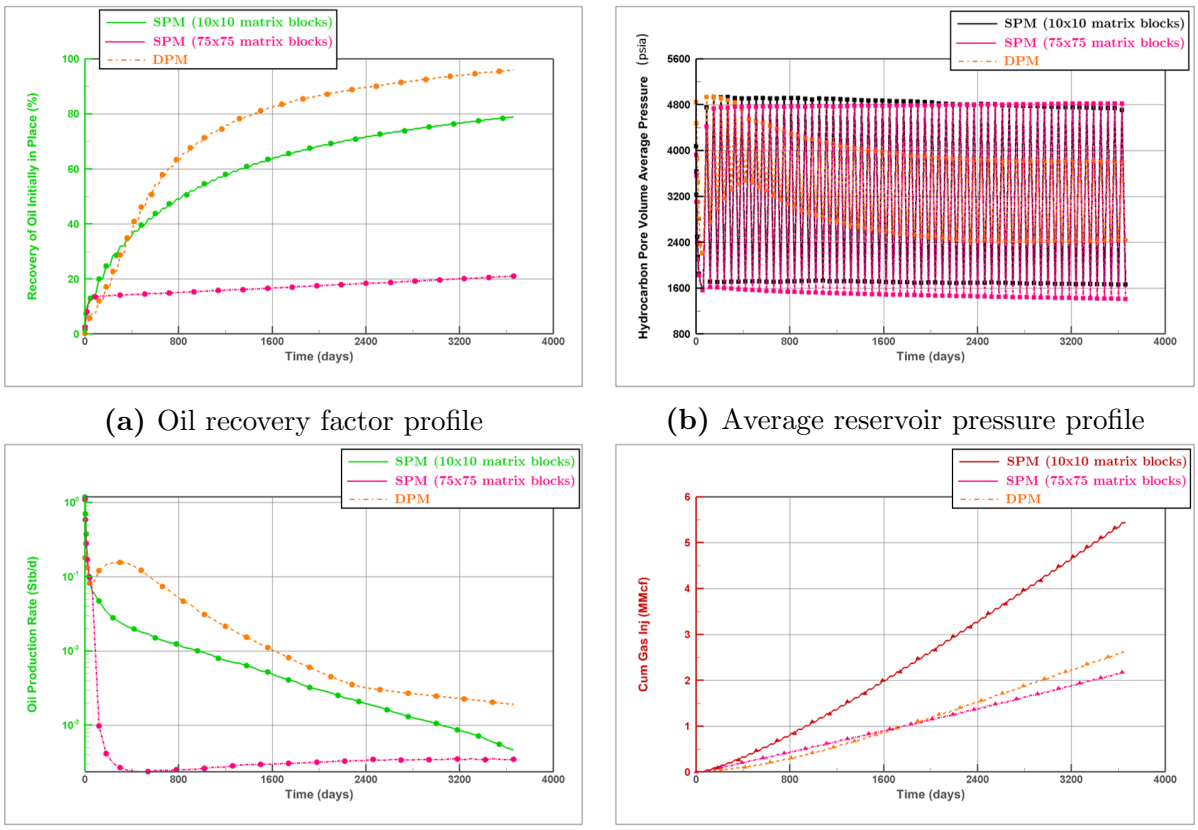

(a) Oil recovery factor profile

(b) Average reservoir pressure profile

(c) Oil production rate profile

(d) Cumulative injected gas profile

Figure 5.2: Performance comparison between 10x10 and 75x75 matrix grid blocks with EOS simulation

this may reduce the produced oil even more. The tremendous difference indicates how the dispersion numerical can escort to incorrect findings.

The relationship of oil recovery factor after 10 years of production with matrix grid blocks number is portrayed in Figure 5.5. Both black oil and EOS run have similar trend denoted in this figure. The recovery factor decreases as the number of matrix grid blocks increases and is consistent to a study by Coats et al. (2009). They concluded that such dispersivity is scale-dependent and reflects conformance (areal and vertical sweep efficiency) that one should eliminate prior to numerical study.

The oil is fully recovered when using 2x2 matrix grid blocks. Having single matrix grid block surprisingly, reduce the recovered oil, as it needs more time than 30 days to charge the pressure along the matrix block and to produce the oil towards the fracture cells. Increasing matrix grid blocks to even higher number such that $\lim_{x\to\infty} 1/N_x = 0$ may result in no increment in oil recovery from injection phase. It is speculated that the only recovered oil is coming from the depletion phase, which in this case during the first 60 days.

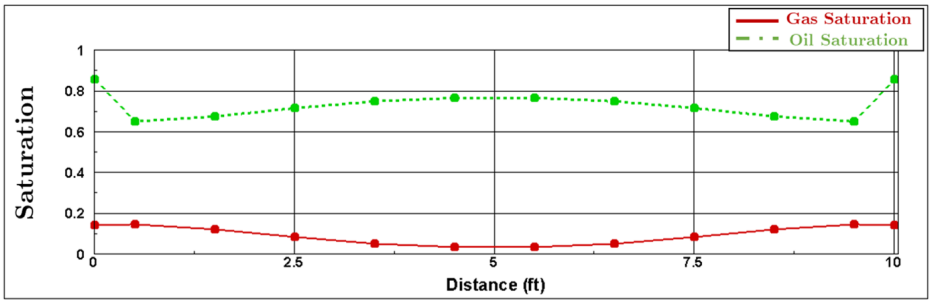

(a) After depletion period (Day 60)

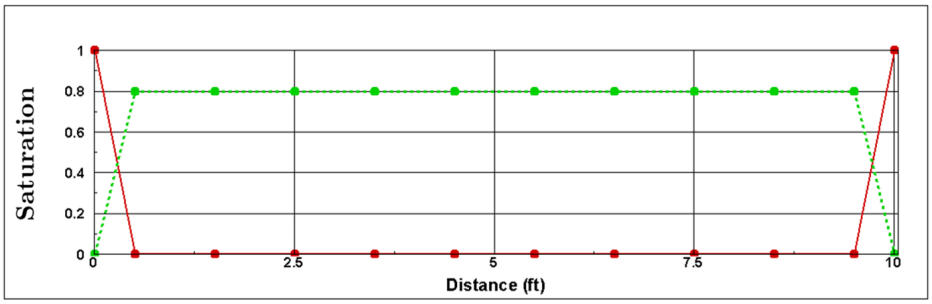

(b) After first injection cycle (Day 90)

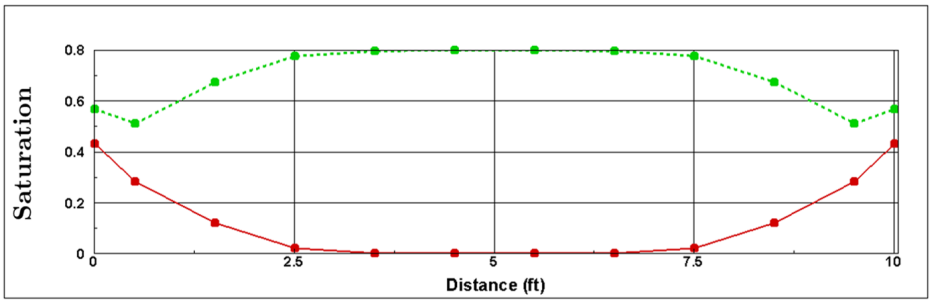

(c) After first production cycle (Day 120)

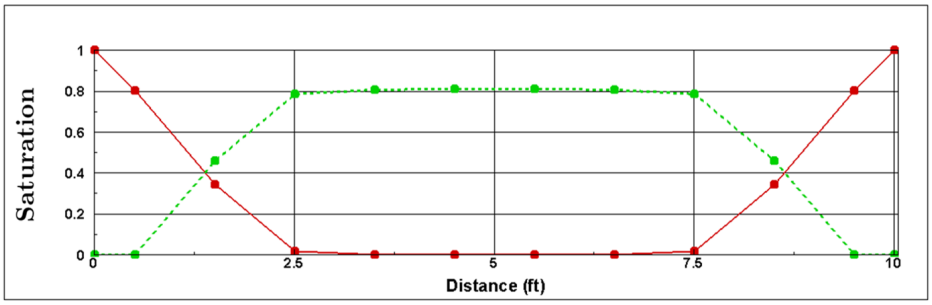

(d) After last injection cycle (Day 3630)

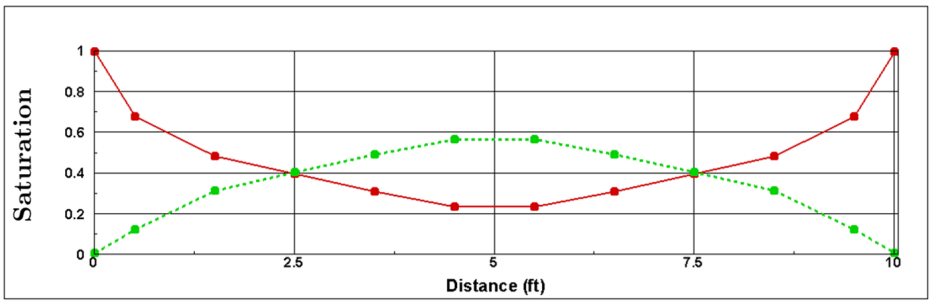

(e) After last production cycle (Day 3660)

Figure 5.3: Oil and gas saturation profile along matrix grid blocks of 10

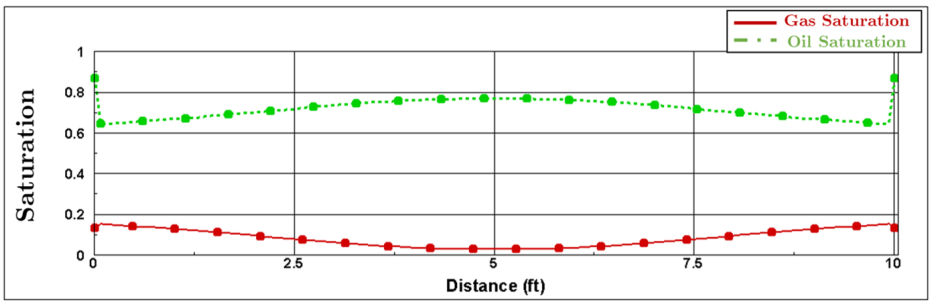

(a) After depletion period (Day 60)

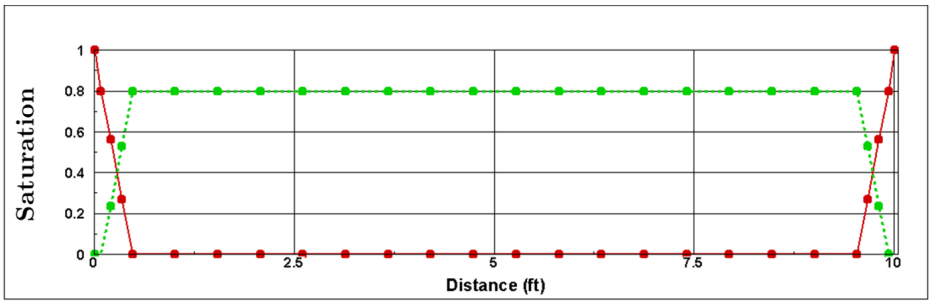

(b) After first injection cycle (Day 90)

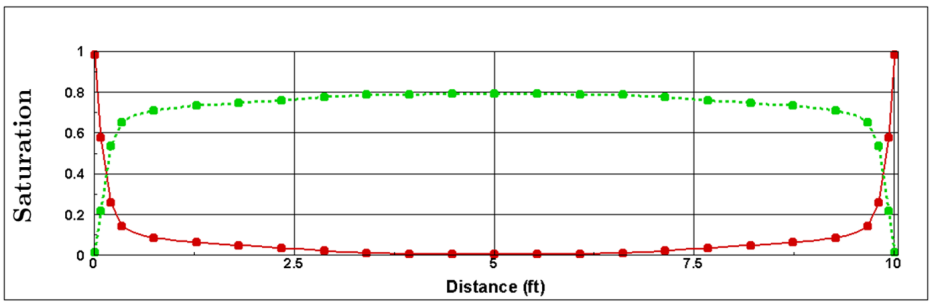

(c) After first production cycle (Day 120)

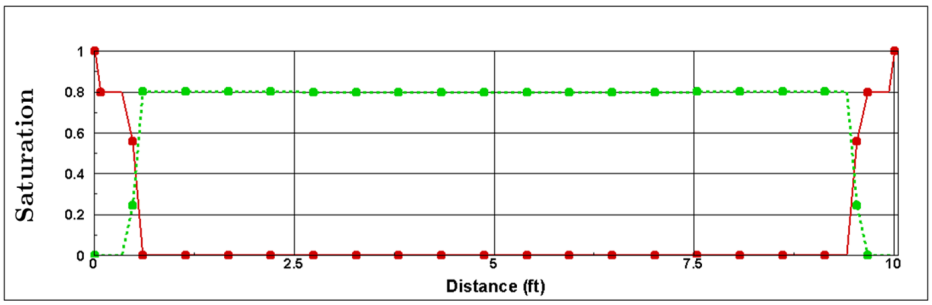

(d) After last injection cycle (t = 3630 days)

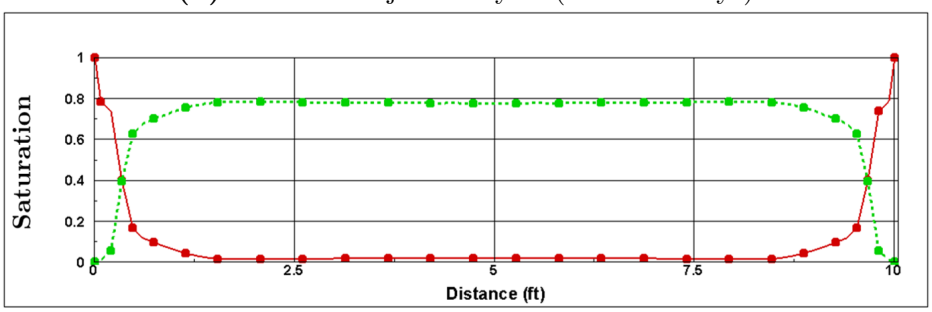

(e) After last production cycle (Day 3660)

Figure 5.4: Oil and gas saturation profile along matrix grid blocks of 75

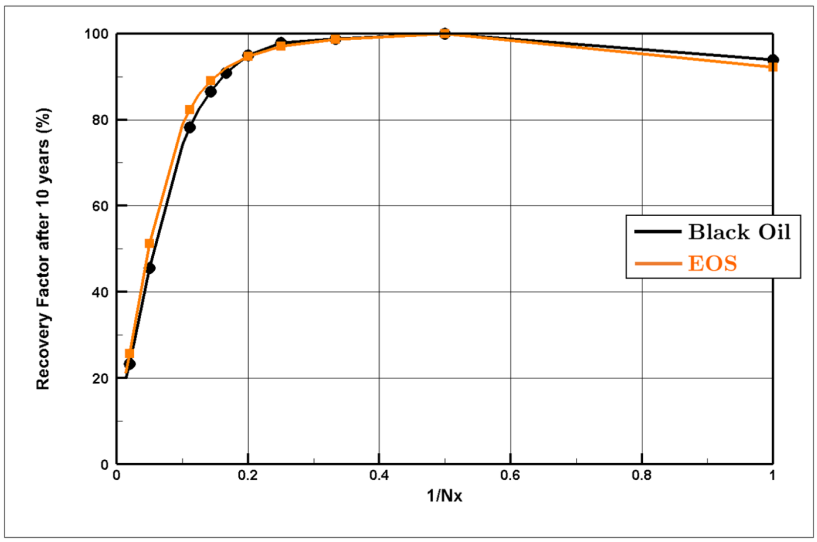

Figure 5.5: Recovery factor after 10 years of injection as a function of matrix block number.

5.2 Dual-Porosity Model

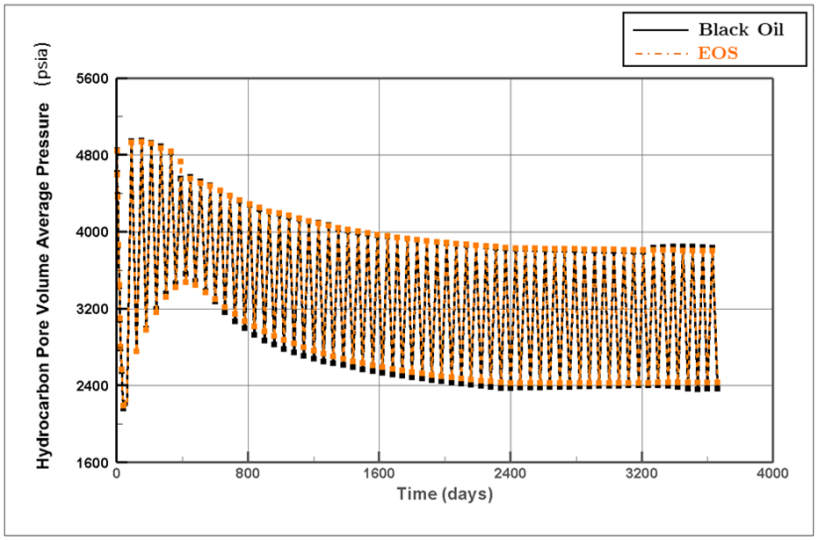

Figure 5.6: Pressure profile comparison of black oil and EOS run.

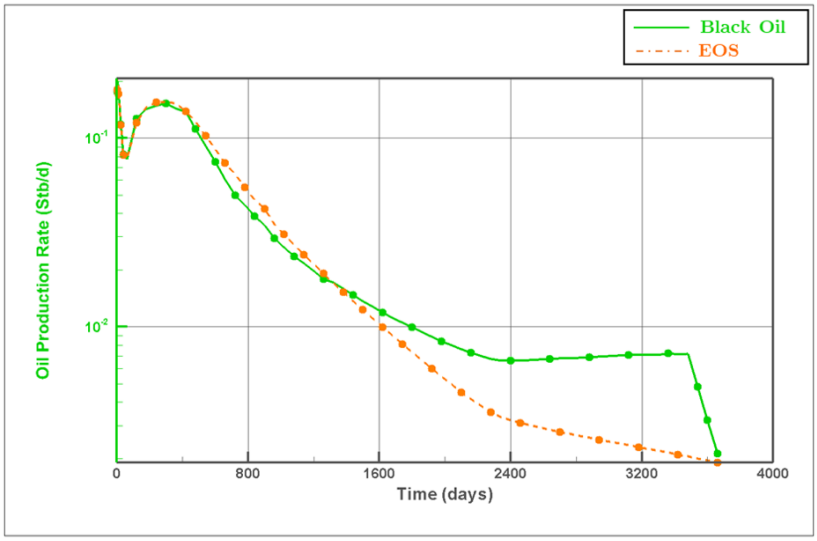

Figure 5.7: Oil production rate profile comparison of black oil and EOS run.

During depletion phase, as mentioned in Chapter 4, both black oil and EOS run show identical results for dual-porosity model. Yet, both runs are compared again to capture any difference behavior in huff-n-puff gas EOR phase. Noticeably, the pressure response for both runs are quite similar as depicted in Figure 5.6.

It is found that at the end of simulation, EOS run has less recovered oil while black oil reaches 100% as denoted in Figure 5.8. This is due to black oil assumption that has only three components. Injecting gas allows gas flow into the matrix. The gas then becomes sufficiently enriched in intermediate components due to vaporization at high pressure such that displacing oil (Whitson & Brulé, 2000). In black oil run, the oil will always be produced as long as there is still oil left inside the block. On the contrary, in

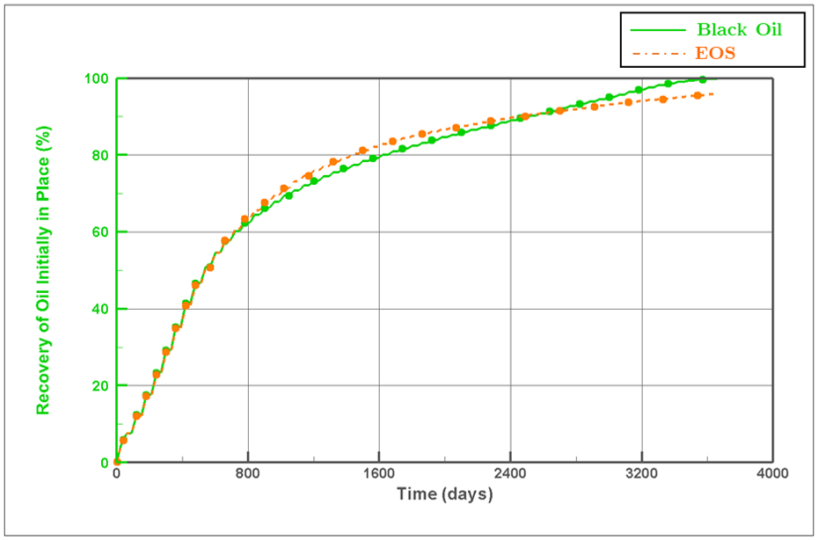

Figure 5.8: Recovery factor profile comparison of black oil and EOS run.

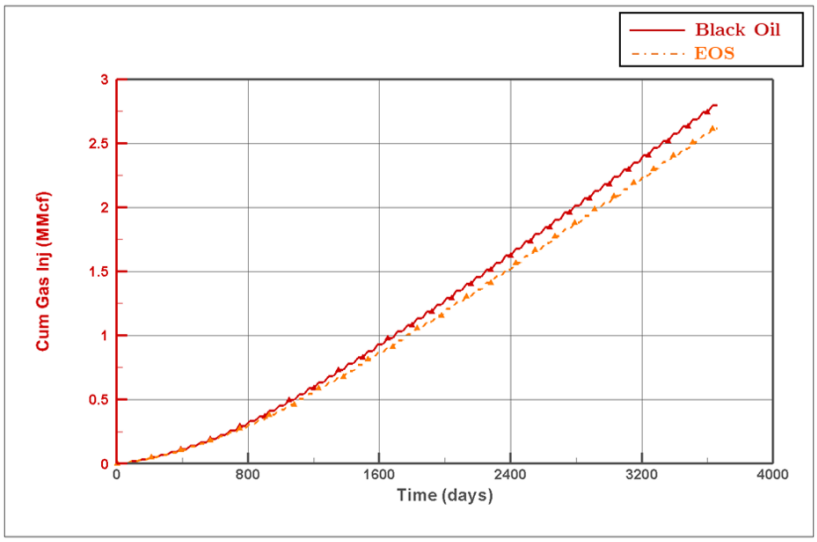

Figure 5.9: Cumulative injected gas profile comparison of black oil and EOS run.

EOS run, at first the oil that becomes vaporized is the leaner components leaving the heavier components in the matrix. As oil production continues, more lean components from the remaining oil leave such that the remaining oil becomes heavier than previously. The production stops when remaining oil cannot be acquired anymore because it is too heavy. Accordingly, higher cumulative injected gas of black oil run compared to EOS run as shown in Figure 5.9. More injected gas implies more oil being swept away from the matrix cells to flow towards the well.

Having less CPU time may be preferable, but it may not be subtle if it obliterates the valid results. Thus, EOS run is carried for further analysis. Yet, black oil run is still undertaken and the results could be found in Appendix C.

5.3 Single- vs Dual-Porosity Model

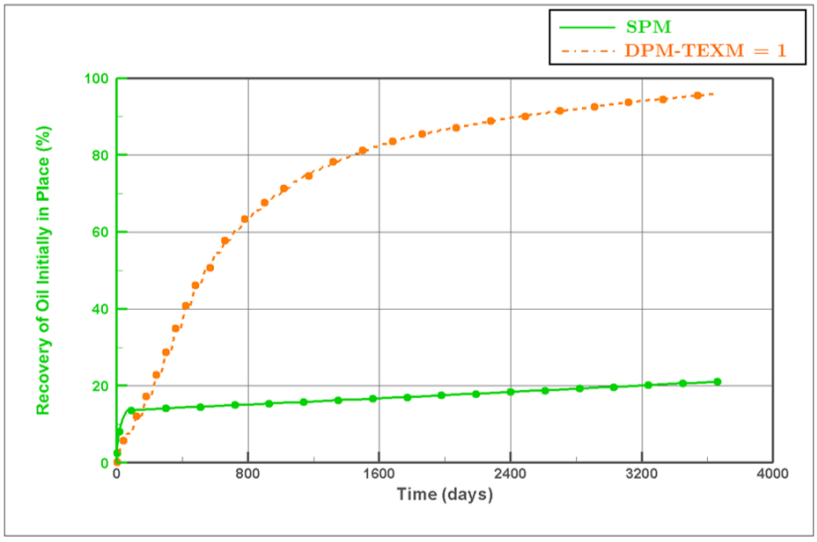

Figure 5.10: Recovery factor profile comparison after 10 years of injection phase.

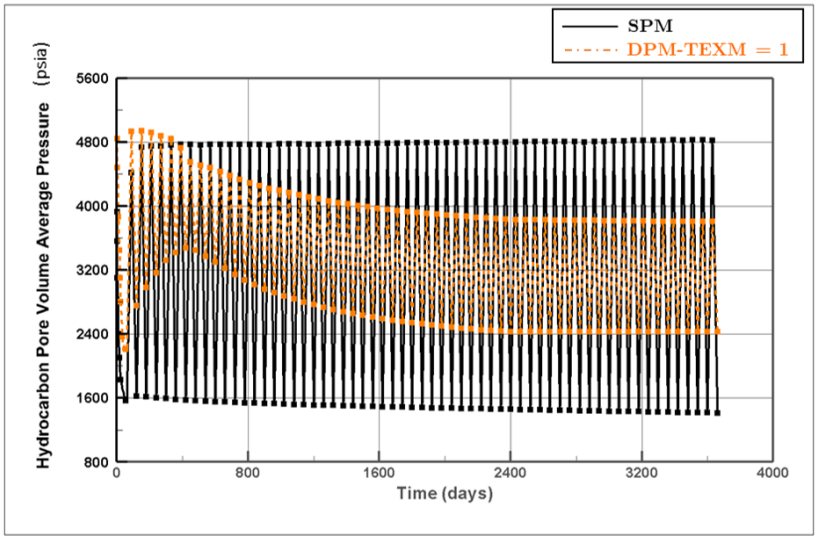

Figure 5.11: Pressure profile comparison after 10 years of injection phase.

Tight unconventional reservoirs have very low permeability, consequently, injecting gas into matrix could take longer time as the fluid hardly to flow. Additionally, the gas, as a matter of fact, pushing the oil further away from fracture cells. There may be some of the oil that becomes miscible with the injected gas, allowing vaporization to the mechanism. This vaporization becomes notable as it determines the incremental of recovery. The more contacts between gas and oil, the more vaporization occurs. During production cycle, the well produces injected gas back together with some of the oil being vaporized.

In SPM, the gas injection affects the outermost of matrix cells first, then move towards the center of matrix cells over time. It allows only small part of oil being in contact with

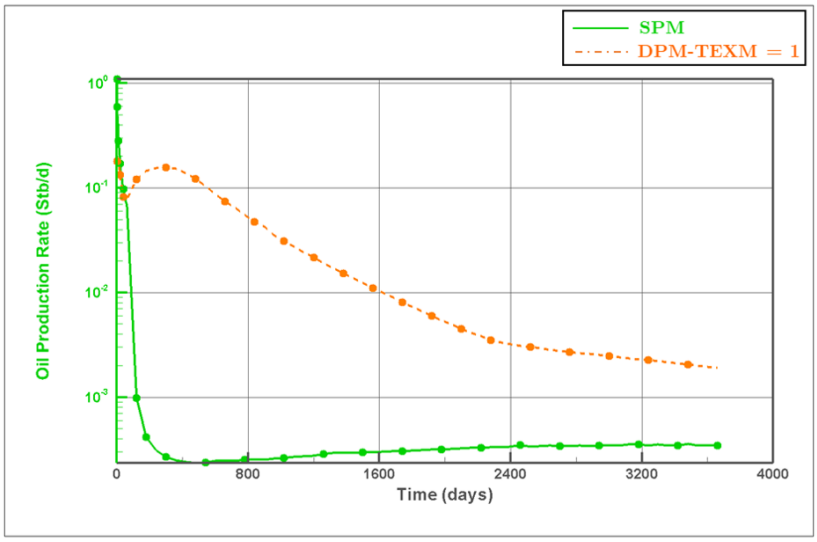

Figure 5.12: Oil production rate profile comparison after 10 years of injection phase.

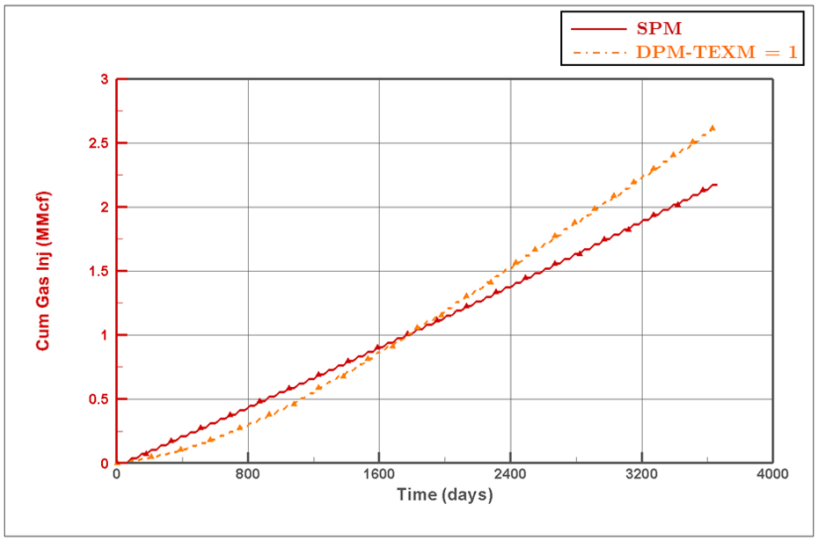

Figure 5.13: Cumulative injected gas profile comparison after 10 years of injection phase.

gas, resulting in small oil being recovered. On the contrary, DPM has an immense recovery that reaches 95% of the total oil in place as depicted in Figure 5.10.

As mentioned previously, DPM assumption is *pseudosteady-state* flow where the pressure changes constant with time throughout the entire block. Once the injection is initiated, unlike SPM, the injected gas is in contact to all of the fluid inside the matrix block. This is confirmed by noticing the constant slope of recovered oil. Although, it is quite higher in the early time compared to later time due to decreasing pressure below bubble point (Figure 5.11), yet both have steady trendline. Having gas evolved from oil also results in decreasing of oil production rate substantially, considering that more gas coming towards the wellbore. Figure 5.12 shows the oil production rate profile. Another prominent result is the fact that the discrepancy between cumulative injected gas generated by DPM and SPM is significant, given the considerable gap in recovered oil, as shown in Figure 5.13. It proves that in SPM, the injected gas does not flow further into

the matrix to produce more oil along with it. In other words, the gas enters the matrix cells to only a small extent.

Modifying TEX by utilizing a multiplier is worth to try, as in the depletion phase doing it so is considered successful. The idea is to have smaller TEX that is reducing the oil rate to get more similar result to SPM.

Looking at Figure 5.14, one needs to reduce TEX by a factor of 8 times to have similar total oil recovery factor at the end of the simulation. Saturation profile is depicted in Figure 5.15. Having TEX multiplier of 8 times smaller results in the movement of oil and gas that are very slow, such one might barely notice the difference of saturation profile initially and after 10 years of injection phase. On the other hand, oil saturation decreases from 0.79 at the end of depletion phase to 0.04 at the end of last production cycle for default Sensor calculated TEX, before applying any modification. Thus, changing in TEX value could results in a considerable different performance. Even though that the total oil recovery factor at the end of the simulation is almost similar to SPM, clearly the results are for wrong reason.

Evidently, DPM cannot seize the performance profiles of SPM properly, even with modifying TEX as portrayed in Figure 5.14 to 5.18. In other words, reducing TEX by a factor of 8 yields oil recovery factor that coincidentally fits SPM at the end of simulation. Hence, it is highly likely that DPM would obtain a misleading result that is over optimistic. DPM will never sufficient in replicating the genuine result of SPM when gas injection is introduced to the model.

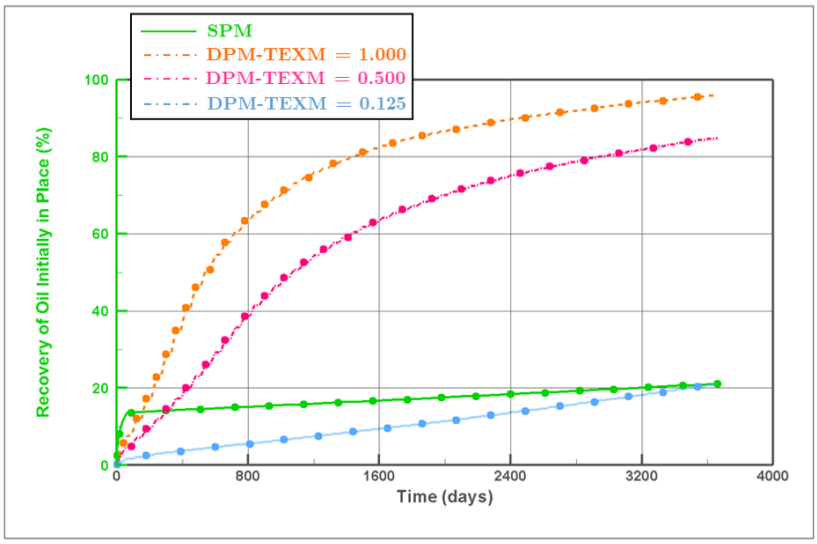

Figure 5.14: Recovery factor profile comparison after 10 years of injection phase after applying modification on TEX.

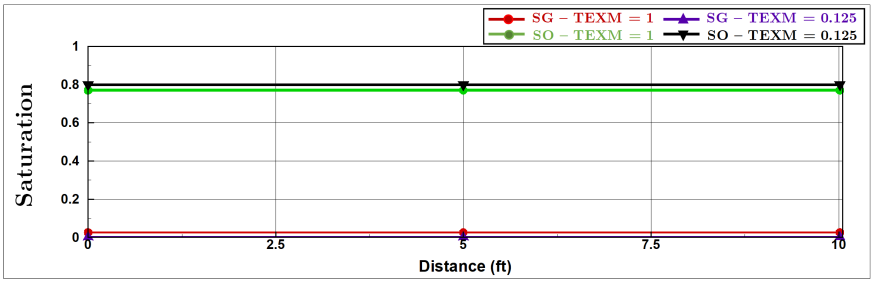

(a) After depletion period (Day 60)

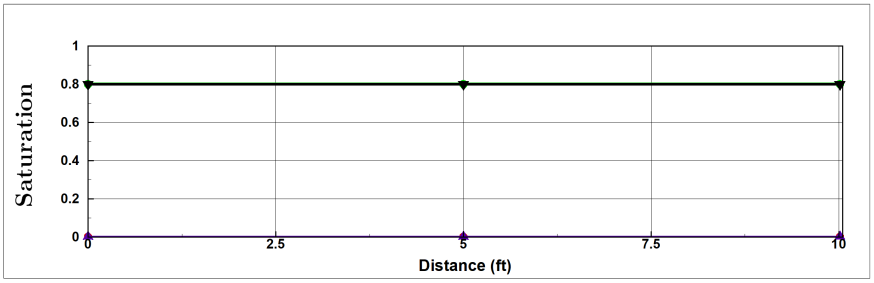

(b) After first injection cycle (Day 90)

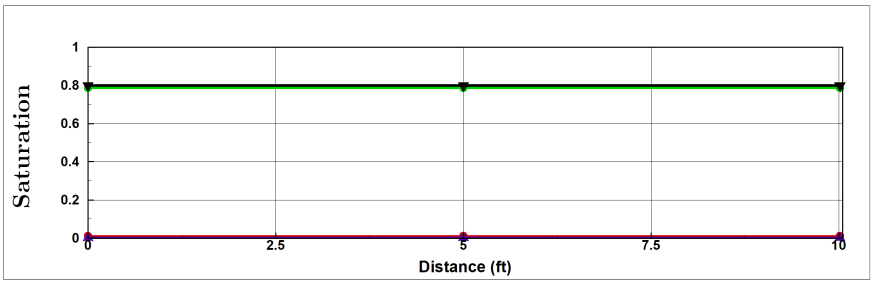

(c) After first production cycle (Day 120)

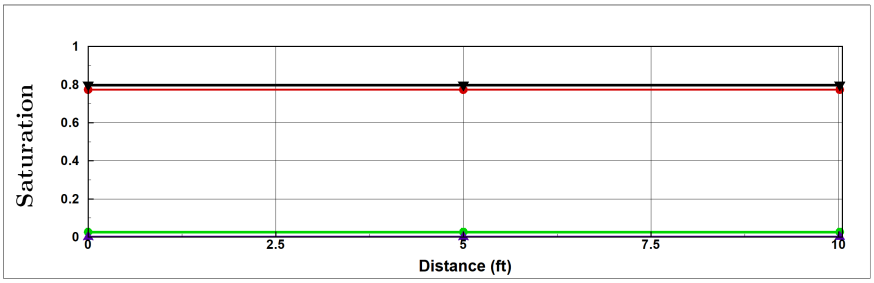

(d) After last injection cycle (Day 3630)

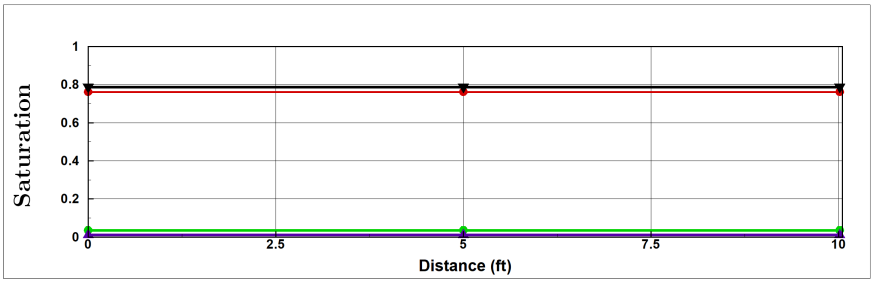

(e) After last production cycle (Day 3660)

Figure 5.15: Oil and gas saturation of DPM with default Sensor calculated TEX (circle) and after being modified by TEX multiplier of 0.125 (triangle)

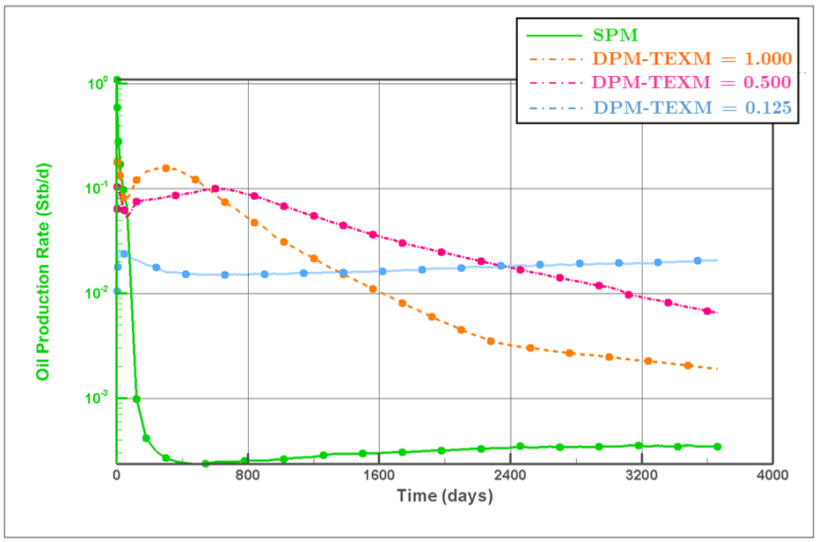

Figure 5.16: Oil production rate profile comparison after 10 years of injection phase after applying modification on TEX.

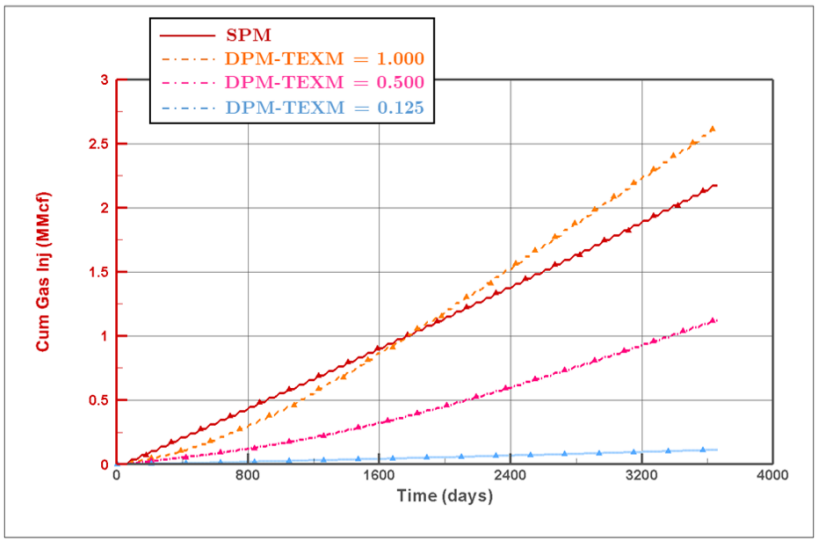

Figure 5.17: Cumulative injected gas profile comparison after 10 years of injection phase after applying modification on TEX.

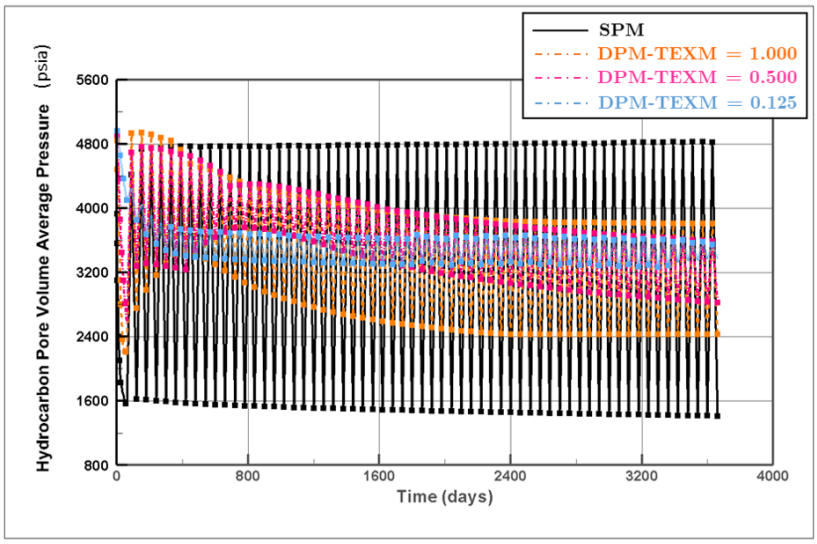

Figure 5.18: Pressure profile comparison after 10 years of injection phase after applying modification on TEX.

Chapter 6

Conclusions

1. Obtaining the optimum number of matrix grid block in SPM is important to shun numerical dispersion error. Having larger grid blocks number can eliminate such error, yet larger CPU time should be expected to compensate it. The optimum number when injection is introduced to the model differ than when it is absent.
2. Matrix-fracture exchange transmissibilities (TEX) defines the performance of DPM between matrix and fracture cells. TEX is mainly a function of the smallest fracture spacing together with matrix permeability. Modifying this value in DPM might be necessary to get better agreement with SPM.
3. Employing DPM in the reservoir simulation reduce CPU time considerably, particularly in larger and complex model. However, careful consideration should be taken prior the decision to choose this model to assure that the results are reliable.
4. SPM captures transient flow in the early time and subsequently reaching PSS flow. The injected gas is in contact with the outermost of matrix cell and over time, it moves further towards the center of matrix.
5. Fluid flow in DPM follows PSS flow where the pressure decreases at the same constant rate uniformly. It allows the injected gas mixes with all of the oil inside the matrix during injection and production process.
6. Black oil run is exerted for depletion phase due to lower CPU time and giving almost equivalent performance to EOS run.
7. For depletion phase, the results of DPM is interchangeably with SPM as no modification is needed, if and only if the fracture spacing is very small and matrix permeability is very high. Larger TEX is expected when having larger fracture spacing along with smaller matrix permeability such that modifications with higher multiplier factor should be implemented.
8. Cyclic time is appointed according to the time during depletion phase to depressurize matrix about 90% from initial reservoir pressure to BHP.
9. The smaller matrix grid blocks number in SPM leads to false faster pressure charging and gas-oil mixing during gas injection phase.

10. Vaporization is the key to determine how much oil can be recovered when gas injection is introduced. The more injected gas contacts oil, the more vaporization takes place.
11. Implementing huff-n-puff gas EOR in tight unconventionals results in very small incremental of recovered oil.
12. EOS run renders less oil production as the heavier oil are left in the matrix and cannot be retrieved. It gives more reasonable approach as what would be found in the real data.
13. DPM yields overoptimistic performances compared to SPM during gas injection phase. Modifying TEX is highly unlikely to get more similar performance to the SPM.
14. DPM might be a credible approach for depletion phase in tight unconventionals. Nevertheless, introducing DPM in huff-n-puff gas EOR might mislead the results that one finds it to be unattainable.

Nomenclature

Acronyms

DPM	=	dual porosity modeling
EOR	=	enhanced oil recovery
EOS	=	equation-of-state
HnP	=	Huff-n-Puff
IAM	=	integrated asset management
SPM	=	single porosity modeling
SRV	=	shattered rock volume
VLE	=	vertical lift equilibrium

Symbols

ΔP	=	upstream and downstream pressure difference, psia
ΔP_f	=	pressure drop along the fracture cells, psia
Δx	=	grid block size along the x-direction, ft
Δy	=	grid block size along the y-direction, ft
Δz	=	grid block size along the z-direction, ft
ℓ_x	=	fracture spacing along the x-direction, ft
ℓ_y	=	fracture spacing along the y-direction, ft
ℓ_z	=	fracture spacing along the z-direction, ft
μ	=	oil viscosity, cP
μ_w	=	water viscosity, cP
ω	=	acentric factor
ϕ_f	=	fracture porosity, fraction
ϕ_m	=	matrix porosity, fraction
ρ_w	=	water density, lb/ft^3

σ = shape factor, 1/ft^2, or interfacial tension, dynes/cm

A = model area, ft^2

B_w = water formation volume factor, rb/stb

BHP_{prod} = minimum bottom hole pressure during production, psia

c_w = water compressibility, 1/psi

c_f = formation compressibility, 1/psi

$DELX$ = grid block size along the x-direction, ft

$DELY$ = grid block size along the y-direction, ft

$DELZ$ = grid block size along the z-direction, ft

DT = SENSOR time step, days

DT_{inj} = injection cycle period, days

DT_{prod} = production cycle period, days

DT_{soak} = soak cycle period, days

f_w = fracture width, mD

H = model thickness, ft

H_{SPM} = SPM thickness, ft

H_{SRV} = SRV thickness, ft

k_f = fracture permeability, mD

k_m = matrix permeability, mD

k_t = total permeability, mD

k_x = matrix permeability along the x-direction, mD

k_{ro} = oil relative permeability

k_{th} = total permeability along the horizontal direction, mD

k_{tv} = total permeability along the vertical direction, mD

L = model length, ft

L_{SPM} = SPM length, ft

L_{SRV} = SRV length, ft

M = molecular weight, lbm/lbm-mol

N_c = number of components

N_m = matrix grid block number

N_x = grid block number along the x-direction

N_y = grid block number along the y-direction

N_z = grid block number along the z-direction

N_{xm} = matrix block number along the x-direction of SPM

N_{ym} = matrix block number along the y-direction of SPM

N_{zm} = matrix block number along the z-direction of SPM

p_c = critical pressure, psia

P_F = fracture grid block pressure, psia

P_M = matrix grid block pressure, psia

P_{avg} = average reservoir pressure, psia

P_{cgo} = gas-oil capillary pressure, psia

P_{inj} = injection pressure, psia

P_{Ri} = initial reservoir pressure, psia

Q = oil production rate, bbl/d

q_o = oil production rate, rb/d

S_{org} = residual oil saturation, fraction

T_c = critical temperature, ^{o}R

T_{dpl} = depletion period, days

T_{inj} = HnP gas EOR period, days

T_R = reservoir temperature, ^{o}F

TEX = matrix-fracture exchange coefficient, rb-cp/d-psi

V_{bl} = grid block volume, ft^3

W = model width, ft

W_{SPM} = SPM width, ft

W_{SRV} = SRV width, ft

Z_c = critical compressibility factor

References

Cheng, Y. (2010, January 1). Impact of Water Dynamics in Fractures on the Perfrmance of Hydraulically Fractured Wells in Gas Shale Reservoirs. *Society of Petroleum Engineers*. doi: 10.2118/127863-PA

Coats, K. H. (1980, October 1). An Equation of State Compositional Model. *Society of Petroleum Engineers*. doi: 10.2118/8284-PA

Coats, K. H. (1989). Implicit Compositional Simulation of Single-Porosity and Dual-Porosity Reservoirs. *Society of Petroleum Engineers*. doi: 10.2118/18427-MS

Coats, K. H., Dempsey, J. R., & Henderson, J. H. (1971). The Use of Vertical Equilibrium in Two-Dimensional Simulation of Three-Dimensional Reservoir Performance. *Society of Petroleum Engineers*. doi: 10.2118/2797-PA

Coats, K. H., Whitson, C. H., & Thomas, K. (2009, February 1). Modeling Conformance as Dispersion. *Society of Petroleum Engineers*. doi: 10.2118/90390-PA

Coats Engineering, Inc. (2011). *Sensor Manual* [Book]. Coats Engineering, Inc.

Coats Engineering, Inc. (2016). *About Sensor.* Retrieved from `http://www.coatsengineering.com/sensor_reservoir_simulator.htm`

Free Software Foundation, Inc. (2017). *The GNU Awk User's Guide.* Retrieved from `https://www.gnu.org/software/gawk/manual/gawk.html`

Golf-Racht, T. V. (1982). *Fundamentals of Fractured Reservoir Engineering* (Vol. 12). Amsterdam, The Netherlands: Elsevier.

Hu, H., Whitson, C. H., & Yuanchang, Q. (1991, January 1). A Study of Recovery Mechanisms in a Nitrogen Diffusion Experiment. *Society of Petroleum Engineers*.

Kanfar, M. S., Ghaderi, S. M., Clarkson, C. R., Reynolds, M. M., & Hetherington, C. (2017). A Modeling Study of EOR Potential for CO2 Huff-n-Puff in Tight Oil Reservoirs - Example from Bakken Formation. *Society of Petroleum Engineers*. doi: 10.2118/185026-MS

Kazemi, H., Eker, I., Torcuk, M. A., & Kurtoglu, B. (2015). Performance Analysis of Unconventional Shale Reservoirs. In *Fundamentals of gas shale reservoirs* (First ed., p. 277-294). John Wiley Sons, Inc. doi: 10.1002/9781119039228

Kazemi, H., Merrill, L., Porterfield, K., & Zeman, P. (1976, December 1). The Behavior of Naturally Fractured Reservoirs. *Society of Petroleum Engineers*. doi: 10.2118/5719-PA

Kurtoglu, B. (2013). *Integrated Reservoir Characterization and Modeling in Support of Enhanced Oil Recovery for Bakken* (PhD thesis). Colorado School of Mines.

Petrostreamz AS. (2016). *Pipe-It.* Retrieved 1 November 2017, from `http://petrostreamz.com/pipeit/`

Reiss, L. H. (1980). *The Reservoir Engineering Aspects of Fractured Formations*. Paris, France: Technip.

Shoaib, S., & Hoffman, B. T. (2009). CO2 Flooding the Elm Coulee Field. *Society of Petroleum Engineers*. doi: 10.2118/123176-MS

Stalkup, F. I. (1984). *Miscible Behavior* (Vol. 8). Richardson, Texas: Monograph Series, SPE.

Tecplot, Inc. (2018). *Tecplot RS Reservoir Simulation Visualization & Analysis Software.* Retrieved from `https://www.tecplot.com/products/tecplot-rs/`

Thomas, W. R., Helms, L. W., Driggers, T. K., Trice, D. W., & Thomas, G. L. (2016, May 6). *EOG Resources (EOG) Earnings Call* [Meeting minutes]. Retrieved from `https://seekingalpha.com/article/3972422-eog-resources-eog-william-r-thomas-q1-2016-results-earnings-call-transcript?page=1`

Uleberg, K., & Kleppe, J. (1996). *Dual Porosity, Dual Permeability Formulation for Fractured Reservoir Simulation.*

U.S. Energy Information Administration. (2018a, February 6). *Annual Energy Outlook 2018 with projections to 2050.* Retrieved 27 May 2018, from `https://www.eia.gov/outlooks/aeo/pdf/AEO2018.pdf`

U.S. Energy Information Administration. (2018b, October 13). *U.s. Crude Oil and Natural Gas Proved Reserves, Year-end 2016.* Retrieved 27 May 2018, from `https://www.eia.gov/naturalgas/crudeoilreserves/`

Warren, J., & Root, P. (1963, September 1). The Behavior of Naturally Fractured Reservoirs. *Society of Petroleum Engineers*. doi: 10.2118/426-PA

Whitson, C. H., & Brulé, M. R. (2000). *Phase Behavior* (Vol. 20). Richardson, Texas: Monograph Series, SPE.

Yu, W., Lashgari, H., & Sepehrnoori, K. (2014). Simulation Study of CO2 Huff-n-Puff Process in Bakken Tight Oil Reservoirs. *Society of Petroleum Engineers*. doi: 10.2118/169575-MS

Yusra, I. (2017). *Huff-n-Puff EOR in Hydraulically-Fractured Tight Unconventional Reservoirs* (Tech. Rep.). Trondheim, Norway: Norwegian University of Science and Technology.

Zick, A. A. (1986, January 1). A Combined Condensing/Vaporizing Mechanism in the Displacement of Oil by Enriched Gases. *Society of Petroleum Engineers*. doi: 10.2118/15493-MS

Zou, C., Yang, Z., & Cui, J. (2013, February). Formation mechanism, geological characteristics and development strategy of nonmarine shale oil in China. *Petroleum Exploration and Development*, *4*, 15-27. doi: 10.1016/S1876-3804(13)60002-6

Appendix A

Black Oil PVT Table

```
   BLACK OIL PVT DATA
   ------------------

   STOCK TANK OIL:
      SP. GR.      0.6177  WATER = 1.0
      LBS/CU FT    38.562
      DEG API      97.577
      MOL. WT.    108.254
   GAS:
      SP. GR.      0.6481  AIR = 1.0
      LBS/SCF    0.049489
      MOL. WT.     18.775

   SATURATED DATA
   --------------
  PSAT    BO      RS      VISO      rs       BG     VISG    IFT
  psia  rb/stb scf/stb     cp   stb/mmcf   rb/scf    cp   dyne/cm
-------------------------------------------------------------------
 500.0  1.0796    93.0   0.280    0.1642 0.005931  0.0127  8.3177
 800.0  1.1088   156.7   0.269    0.2418 0.003617  0.0131  6.9970
1100.0  1.1394   224.4   0.256    0.5110 0.002576  0.0136  5.7995
1400.0  1.1720   297.0   0.243    1.0478 0.001990  0.0142  4.7326
1700.0  1.2070   375.7   0.229    1.8853 0.001617  0.0150  3.7997
2000.0  1.2449   461.4   0.214    3.0651 0.001363  0.0159  2.9992
2302.9  1.2869   556.3   0.200    4.6712 0.001178  0.0170  2.3187

   UNDERSATURATED DATA
   -------------------
  PSAT     P      BO       VISO         BG      VISG
  psia   psia   rb/stb      cp        rb/scf     cp
-----------------------------------------------
 500.0   500.0  1.0796        0.280 0.005931  0.0127
         800.0  1.0753        0.289 0.003608  0.0131
        1100.0  1.0713        0.297 0.002565  0.0136
        1400.0  1.0676        0.305 0.001979  0.0142
        1700.0  1.0641        0.313 0.001608  0.0150
        2000.0  1.0609        0.321 0.001356  0.0159
        2302.9  1.0578        0.328 0.001173  0.0170
        2600.0  1.0549        0.336 0.001041  0.0181
        2900.0  1.0522        0.343 0.000938  0.0193
```

	3300.0	1.0488	0.352	0.000834	0.0209
	3800.0	1.0448	0.363	0.000740	0.0230
	5000.0	1.0365	0.389	0.000602	0.0279
800.0	800.0	1.1088	0.269	0.003617	0.0131
	1100.0	1.1041	0.278	0.002573	0.0136
	1400.0	1.0997	0.286	0.001986	0.0142
	1700.0	1.0956	0.294	0.001615	0.0150
	2000.0	1.0918	0.302	0.001362	0.0159
	2302.9	1.0882	0.310	0.001179	0.0169
	2600.0	1.0848	0.318	0.001045	0.0179
	2900.0	1.0816	0.325	0.000942	0.0191
	3300.0	1.0776	0.335	0.000838	0.0207
	3800.0	1.0730	0.347	0.000743	0.0228
	5000.0	1.0634	0.373	0.000603	0.0276
1100.0	1100.0	1.1394	0.256	0.002576	0.0136
	1400.0	1.1342	0.265	0.001989	0.0142
	1700.0	1.1294	0.273	0.001617	0.0150
	2000.0	1.1249	0.281	0.001364	0.0158
	2302.9	1.1206	0.290	0.001181	0.0168
	2600.0	1.1167	0.297	0.001047	0.0179
	2900.0	1.1130	0.305	0.000944	0.0191
	3300.0	1.1083	0.315	0.000839	0.0207
	3800.0	1.1030	0.327	0.000744	0.0227
	5000.0	1.0919	0.354	0.000604	0.0275
1400.0	1400.0	1.1720	0.243	0.001990	0.0142
	1700.0	1.1662	0.251	0.001618	0.0150
	2000.0	1.1609	0.259	0.001365	0.0158
	2302.9	1.1559	0.267	0.001181	0.0168
	2600.0	1.1513	0.275	0.001048	0.0179
	2900.0	1.1470	0.283	0.000944	0.0191
	3300.0	1.1416	0.293	0.000839	0.0207
	3800.0	1.1354	0.305	0.000744	0.0227
	5000.0	1.1227	0.333	0.000604	0.0275
1700.0	1700.0	1.2070	0.229	0.001617	0.0150
	2000.0	1.2007	0.237	0.001364	0.0159
	2302.9	1.1947	0.245	0.001181	0.0169
	2600.0	1.1894	0.253	0.001047	0.0180
	2900.0	1.1843	0.260	0.000944	0.0191
	3300.0	1.1780	0.270	0.000839	0.0207
	3800.0	1.1708	0.283	0.000744	0.0228
	5000.0	1.1562	0.311	0.000604	0.0276
2000.0	2000.0	1.2449	0.214	0.001363	0.0159
	2302.9	1.2379	0.222	0.001180	0.0169
	2600.0	1.2316	0.230	0.001046	0.0180
	2900.0	1.2256	0.238	0.000943	0.0192
	3300.0	1.2183	0.248	0.000839	0.0208
	3800.0	1.2099	0.260	0.000744	0.0229
	5000.0	1.1930	0.288	0.000604	0.0277
2302.9	2302.9	1.2869	0.200	0.001178	0.0170
	2600.0	1.2794	0.208	0.001045	0.0181
	2900.0	1.2723	0.215	0.000942	0.0193
	3300.0	1.2636	0.225	0.000838	0.0209
	3800.0	1.2539	0.237	0.000743	0.0230
	5000.0	1.2342	0.265	0.000605	0.0279

Appendix B

Depletion Performance Results

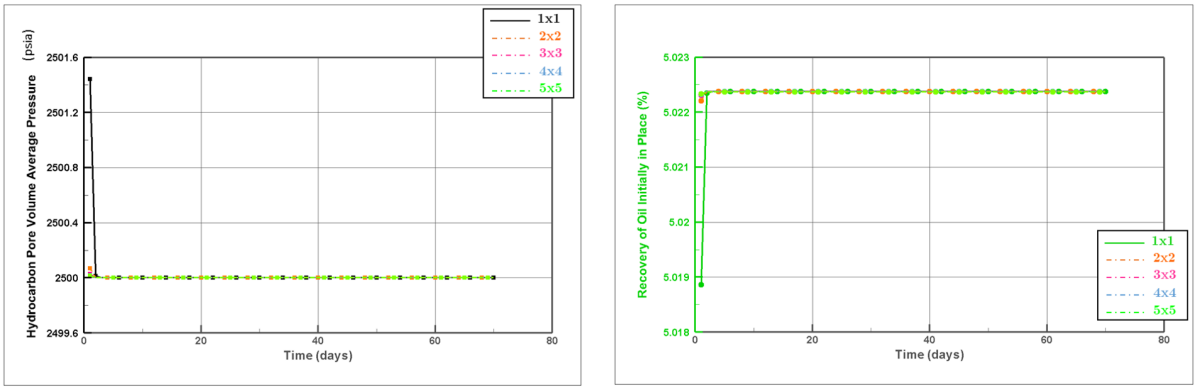

(a) Pressure profile **(b)** Oil recovery factor profile

Figure B.1: SPM - Matrix block number sensitivity - $\ell_x = 1$ ft.

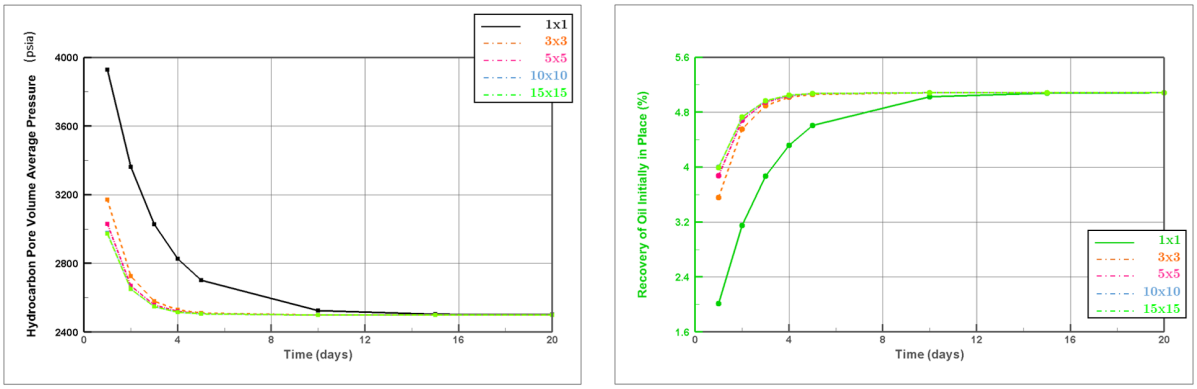

(a) Pressure profile **(b)** Oil recovery factor profile

Figure B.2: SPM - Matrix block number sensitivity - $\ell_x = 5$ ft.

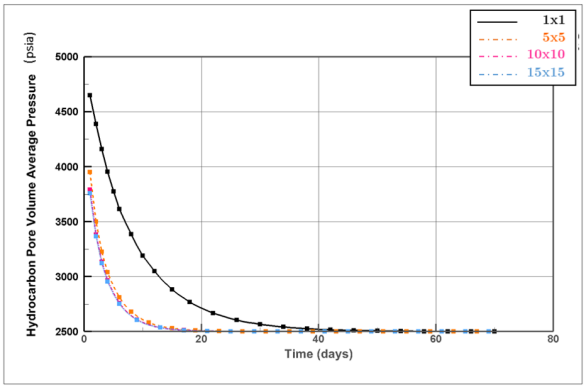

(a) Pressure profile

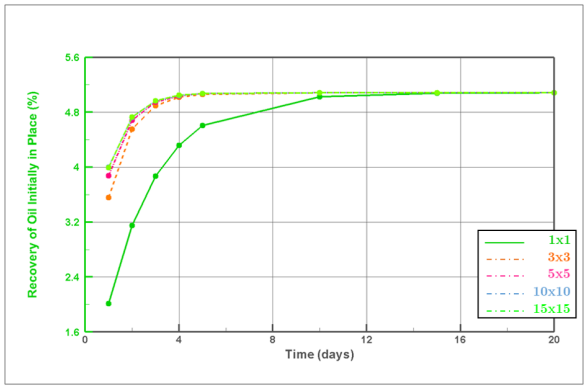

(b) Oil recovery factor profile

Figure B.3: SPM - Matrix block number sensitivity - $\ell_x = 10$ ft.

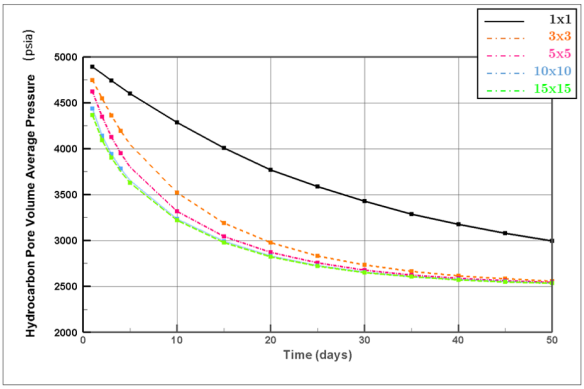

(a) Pressure profile

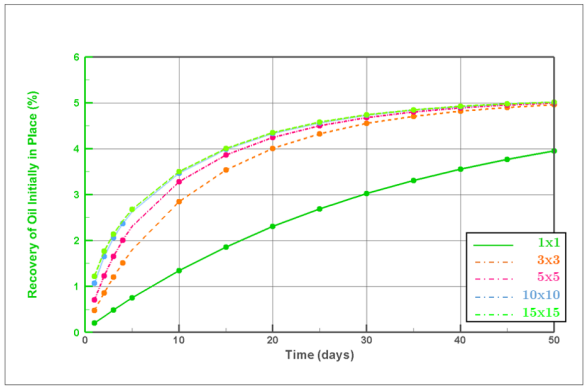

(b) Oil recovery factor profile

Figure B.4: SPM - Matrix block number sensitivity - $\ell_x = 20$ ft.

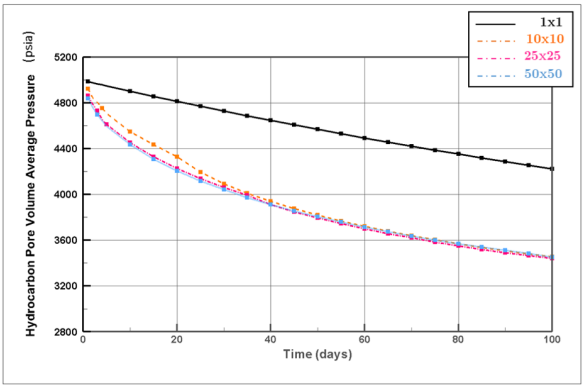

(a) Pressure profile

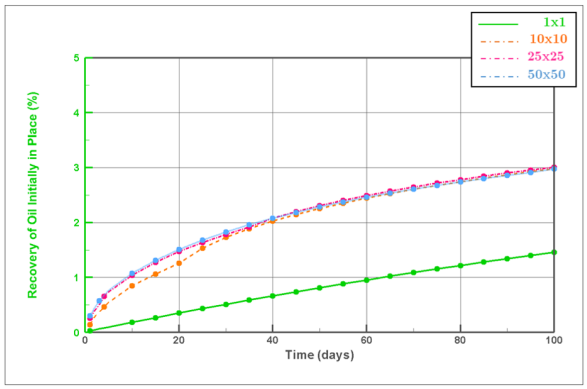

(b) Oil recovery factor profile

Figure B.5: SPM - Matrix block number sensitivity - $\ell_x = 50$ ft.

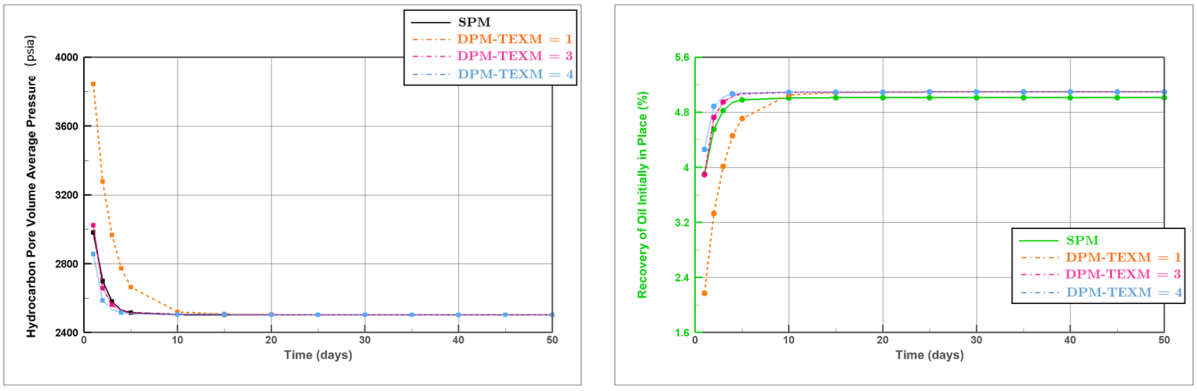

(a) Pressure profile **(b)** Oil recovery factor profile

Figure B.6: Dual-porosity performance profile corresponding to single-porosity by changing TEX multiplier for first block of $\ell_x = 1$ ft and $k_m = 10$ nd.

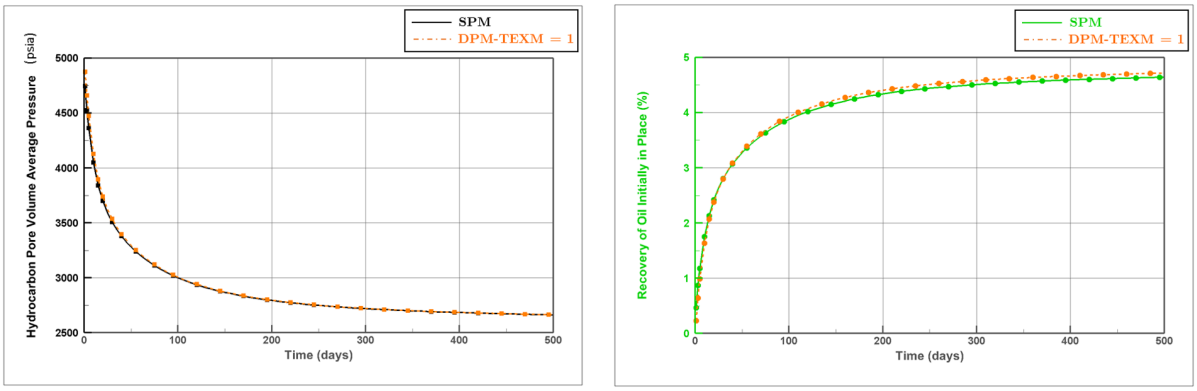

(a) Pressure profile **(b)** Oil recovery factor profile

Figure B.7: Dual-porosity performance profile corresponding to single-porosity by changing TEX multiplier for second block of $\ell_x = 1$ ft and $k_m = 10$ nd.

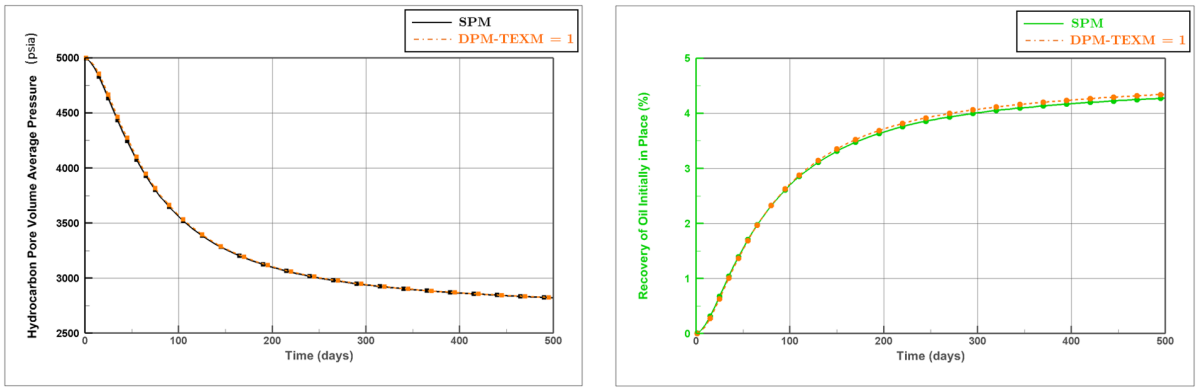

(a) Pressure profile **(b)** Oil recovery factor profile

Figure B.8: Dual-porosity performance profile corresponding to single-porosity by changing TEX multiplier for forth block of $\ell_x = 1$ ft and $k_m = 10$ nd.

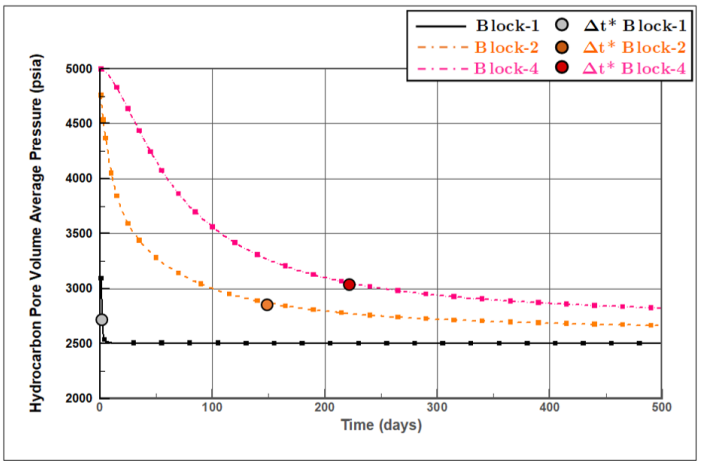

(a) Matrix pressure (P_m) profile

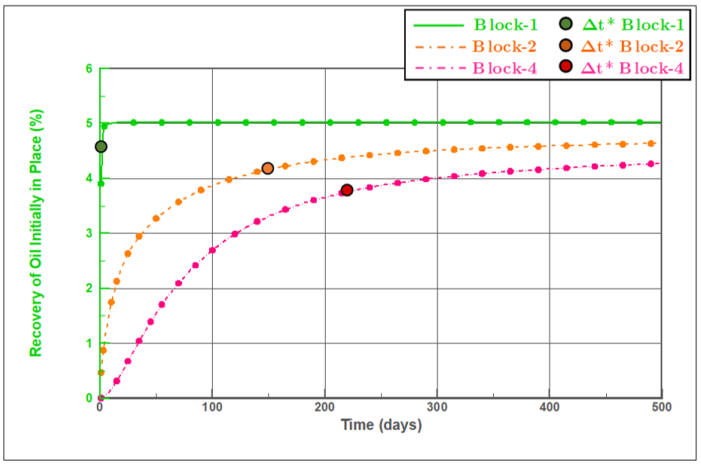

(b) Oil recovery factor profile

Figure B.9: Δt^* of single-porosity model for $\ell_x = 1$ ft and $k_m = 10$ nd.

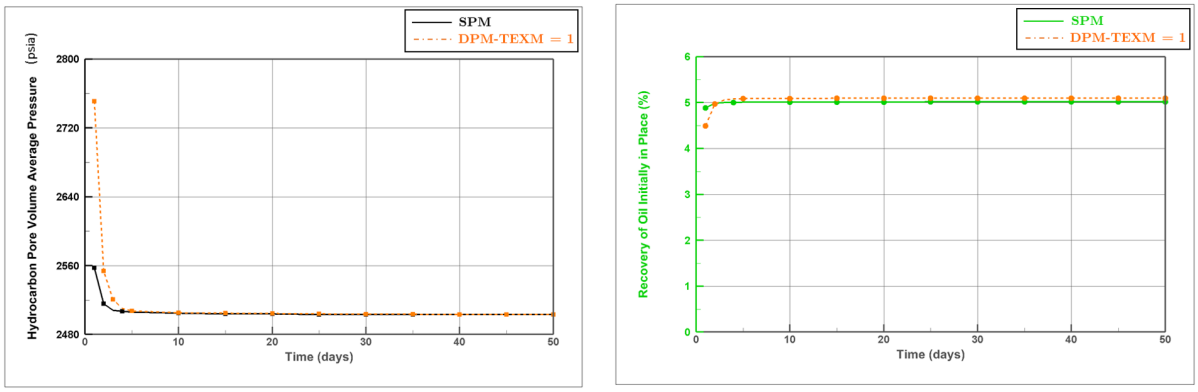

(a) Pressure profile **(b)** Oil recovery factor profile

Figure B.10: Dual-porosity performance profile corresponding to single-porosity by changing TEX multiplier for first block of $\ell_x = 1$ ft and $k_m = 50$ nd.

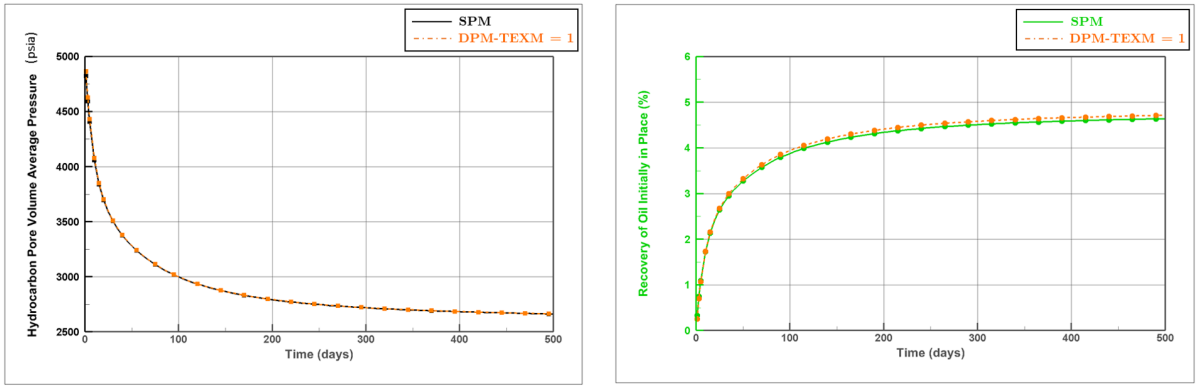

(a) Pressure profile **(b)** Oil recovery factor profile

Figure B.11: Dual-porosity performance profile corresponding to single-porosity by changing TEX multiplier for second block of $\ell_x = 1$ ft and $k_m = 50$ nd.

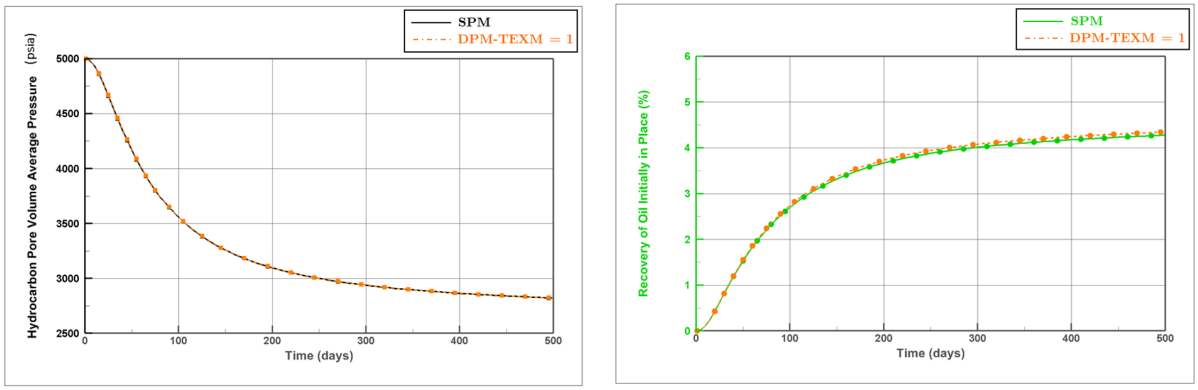

(a) Pressure profile **(b)** Oil recovery factor profile

Figure B.12: Dual-porosity performance profile corresponding to single-porosity by changing TEX multiplier for forth block of $\ell_x = 1$ ft and $k_m = 50$ nd.

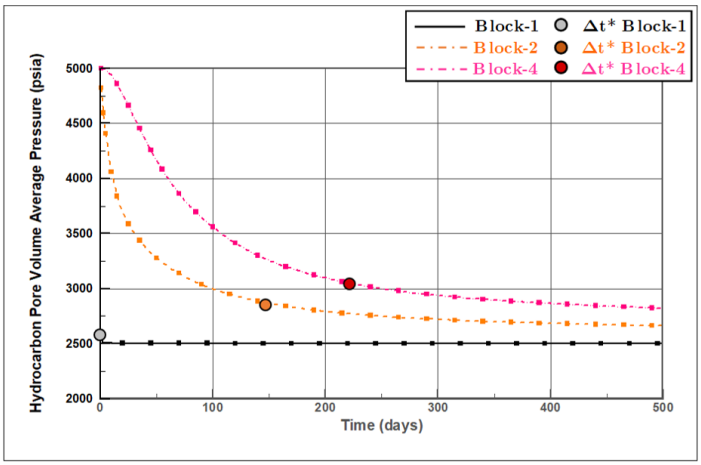

(a) Matrix pressure (P_m) profile

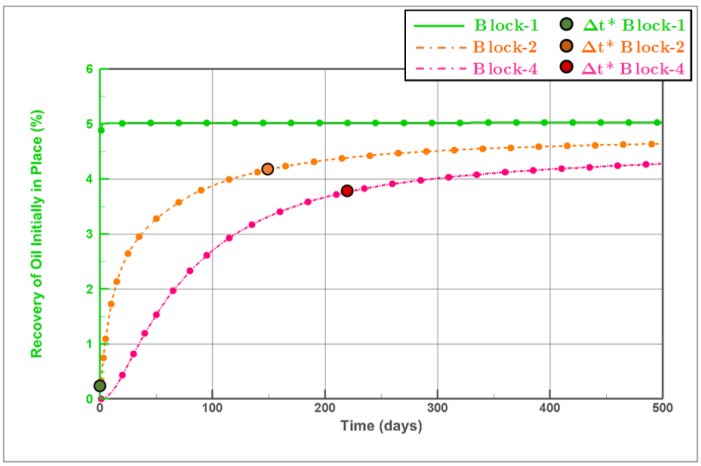

(b) Oil recovery factor profile

Figure B.13: Δt^* of single-porosity model for $\ell_x = 1$ ft and $k_m = 50$ nd.

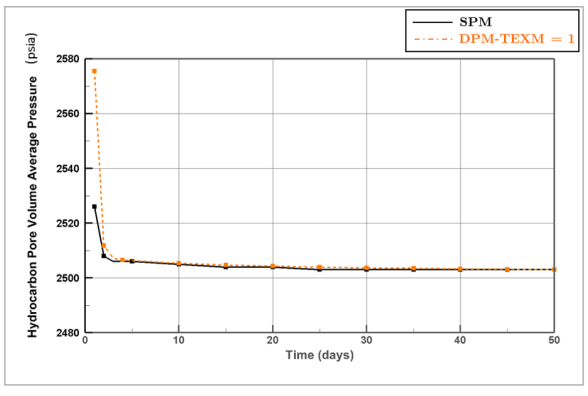

(a) Pressure profile

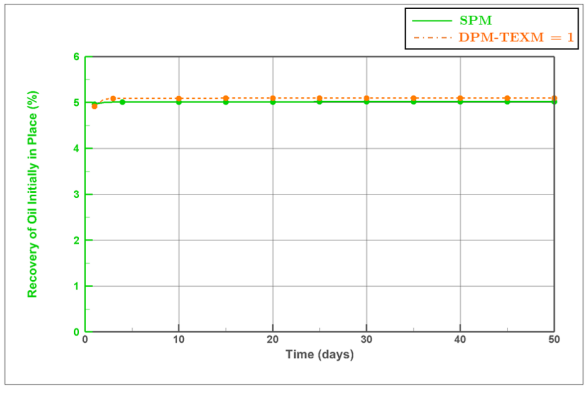

(b) Oil recovery factor profile

Figure B.14: Dual-porosity performance profile corresponding to single-porosity by changing TEX multiplier for first block of $\ell_x = 1$ ft and $k_m = 100$ nd.

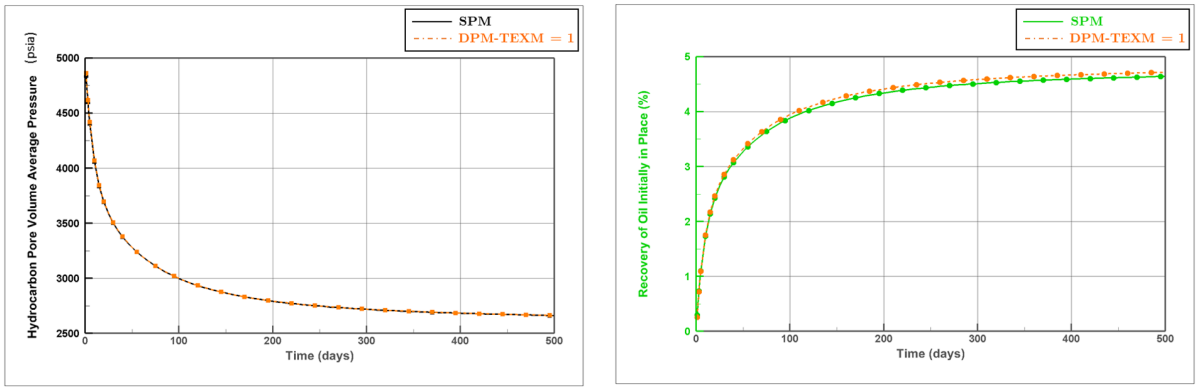

(a) Pressure profile **(b)** Oil recovery factor profile

Figure B.15: Dual-porosity performance profile corresponding to single-porosity by changing TEX multiplier for second block of $\ell_x = 1$ ft and $k_m = 100$ nd.

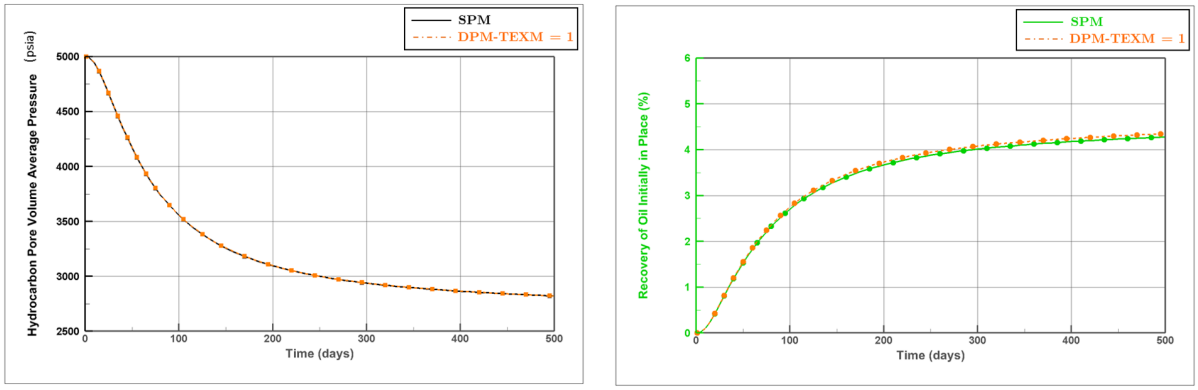

(a) Pressure profile **(b)** Oil recovery factor profile

Figure B.16: Dual-porosity performance profile corresponding to single-porosity by changing TEX multiplier for forth block of $\ell_x = 1$ ft and $k_m = 100$ nd.

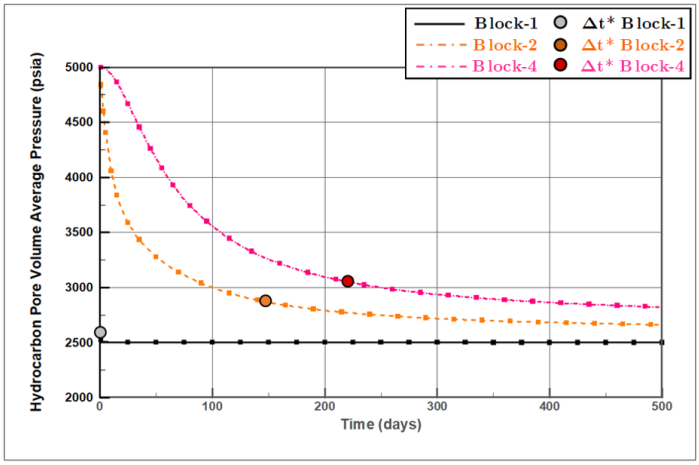

(a) Matrix pressure (P_m) profile

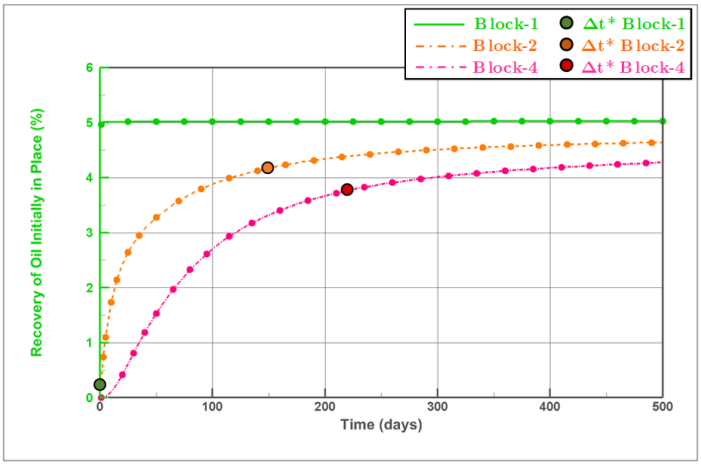

(b) Oil recovery factor profile

Figure B.17: Δt^* of single-porosity model for $\ell_x = 1$ ft and $k_m = 100$ nd.

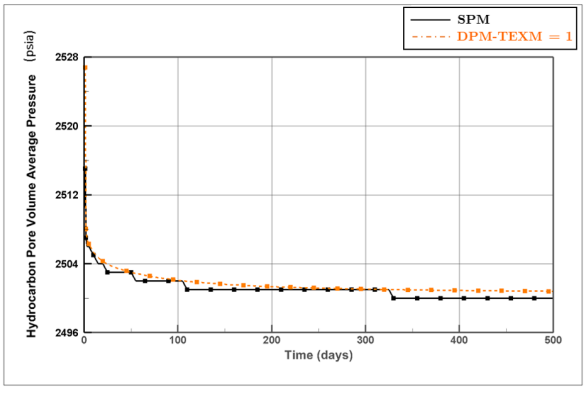

(a) Pressure profile

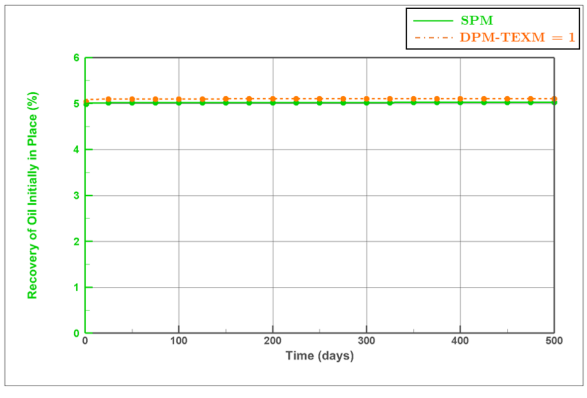

(b) Oil recovery factor profile

Figure B.18: Dual-porosity performance profile corresponding to single-porosity by changing TEX multiplier for first block of $\ell_x = 1$ ft and $k_m = 200$ nd.

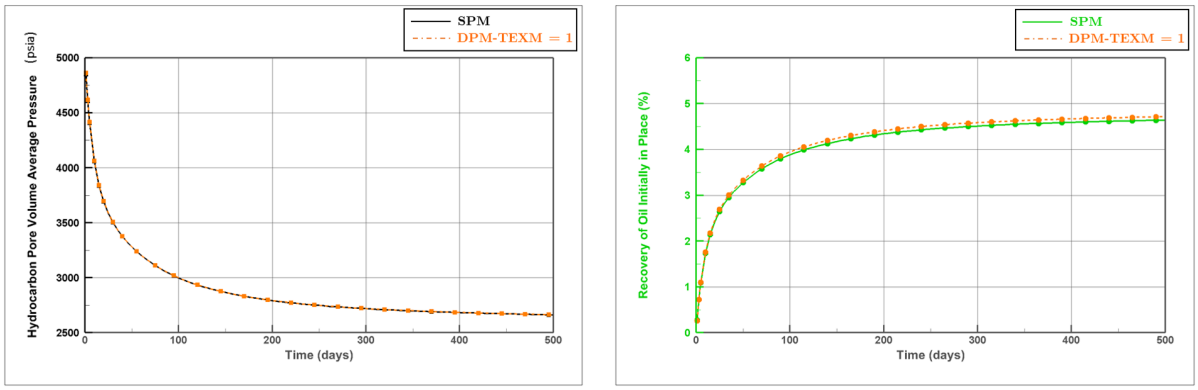

(a) Pressure profile **(b)** Oil recovery factor profile

Figure B.19: Dual-porosity performance profile corresponding to single-porosity by changing TEX multiplier for second block of $\ell_x = 1$ ft and $k_m = 200$ nd.

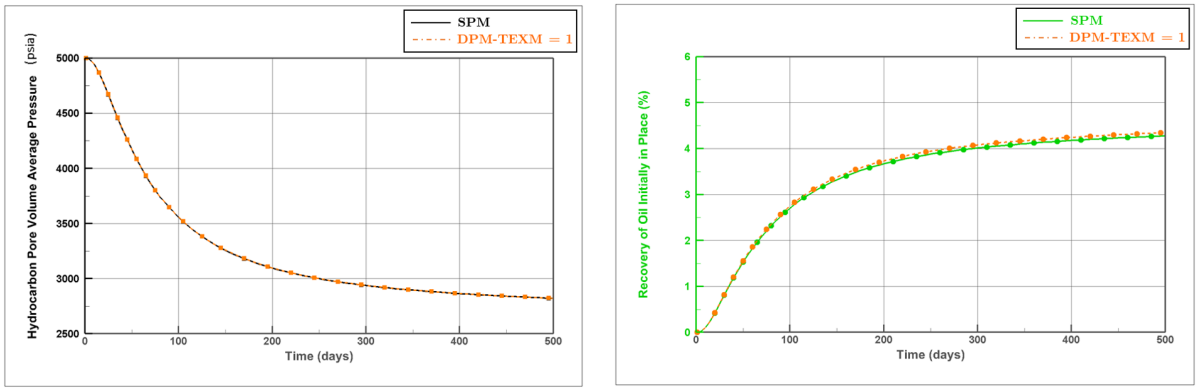

(a) Pressure profile **(b)** Oil recovery factor profile

Figure B.20: Dual-porosity performance profile corresponding to single-porosity by changing TEX multiplier for forth block of $\ell_x = 1$ ft and $k_m = 200$ nd.

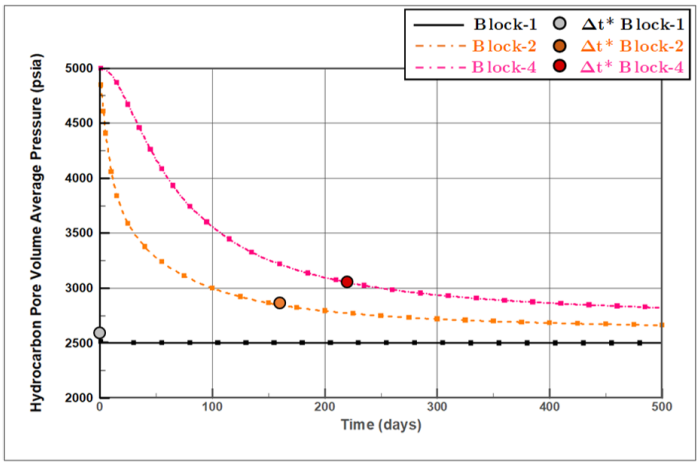

(a) Matrix pressure (P_m) profile

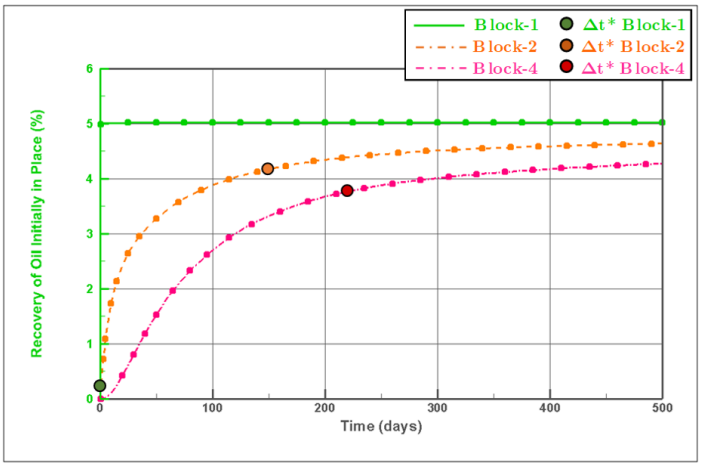

(b) Oil recovery factor profile

Figure B.21: Δt^* of single-porosity model for $\ell_x = 1$ ft and $k_m = 200$ nd.

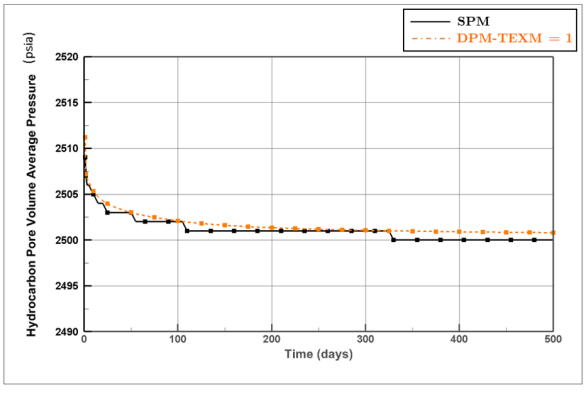

(a) Pressure profile

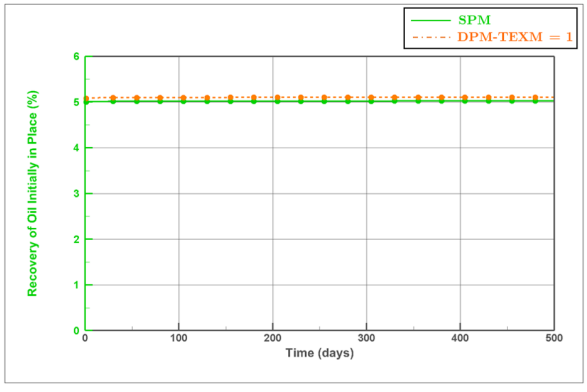

(b) Oil recovery factor profile

Figure B.22: Dual-porosity performance profile corresponding to single-porosity by changing TEX multiplier for first block of $\ell_x = 1$ ft and $k_m = 500$ nd.

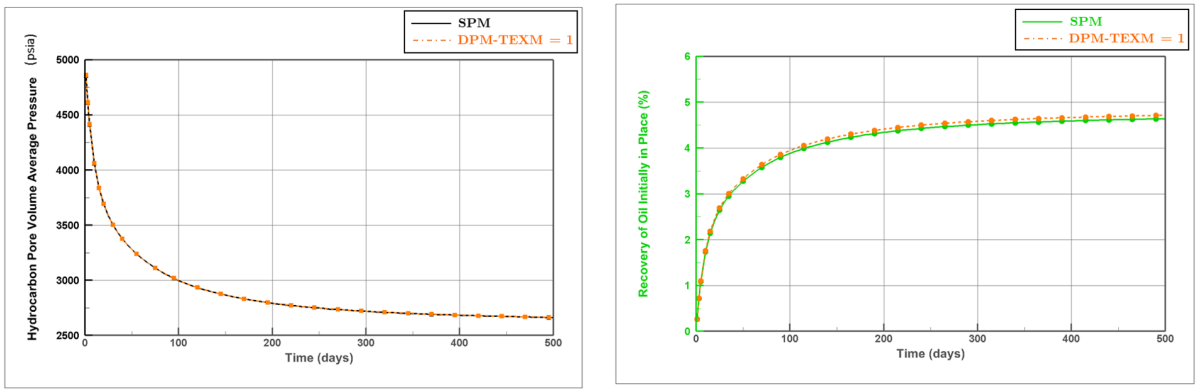

(a) Pressure profile **(b)** Oil recovery factor profile

Figure B.23: Dual-porosity performance profile corresponding to single-porosity by changing TEX multiplier for second block of $\ell_x = 1$ ft and $k_m = 500$ nd.

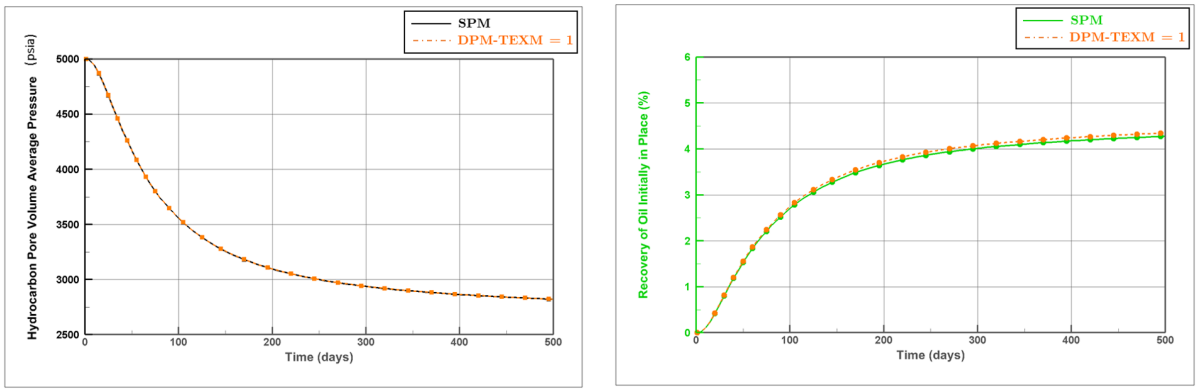

(a) Pressure profile **(b)** Oil recovery factor profile

Figure B.24: Dual-porosity performance profile corresponding to single-porosity by changing TEX multiplier for forth block of $\ell_x = 1$ ft and $k_m = 500$ nd.

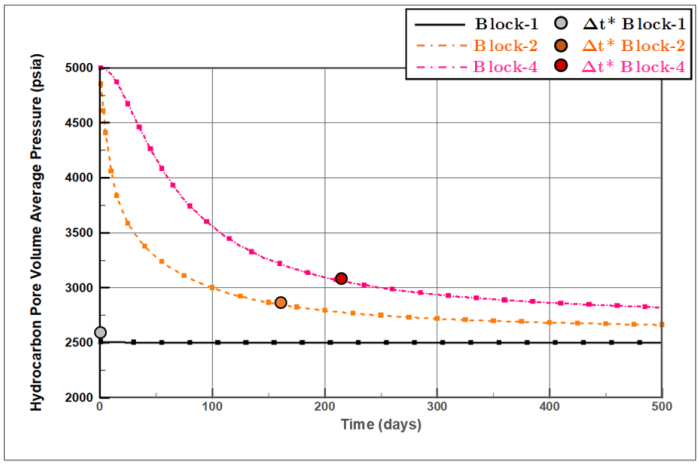

(a) Matrix pressure (P_m) profile

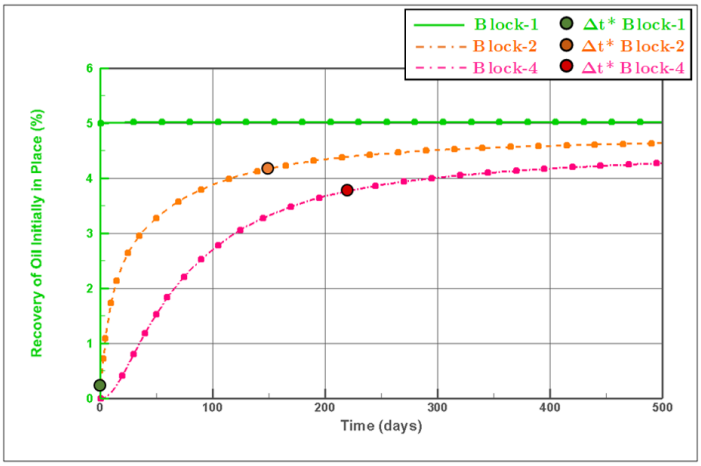

(b) Oil recovery factor profile

Figure B.25: Δt^* of single-porosity model for $\ell_x = 1$ ft and $k_m = 500$ nd.

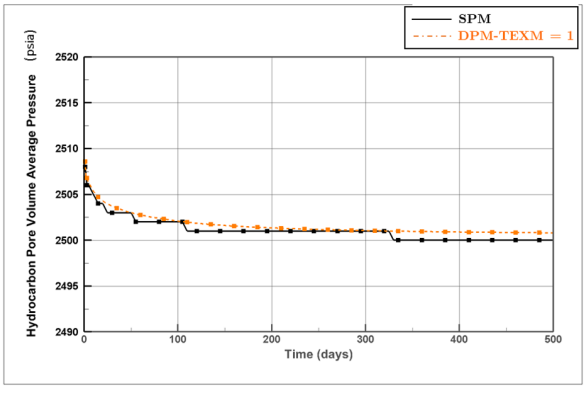

(a) Pressure profile

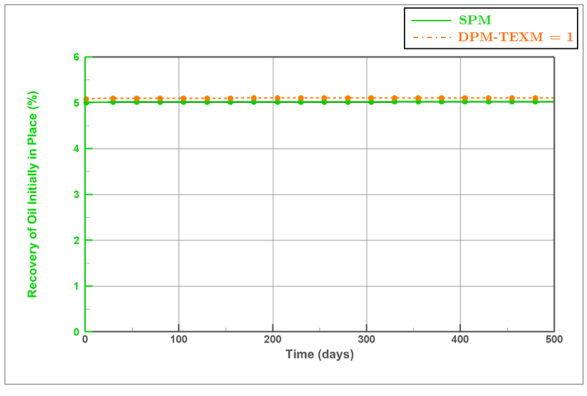

(b) Oil recovery factor profile

Figure B.26: Dual-porosity performance profile corresponding to single-porosity by changing TEX multiplier for first block of $\ell_x = 1$ ft and $k_m = 1000$ nd.

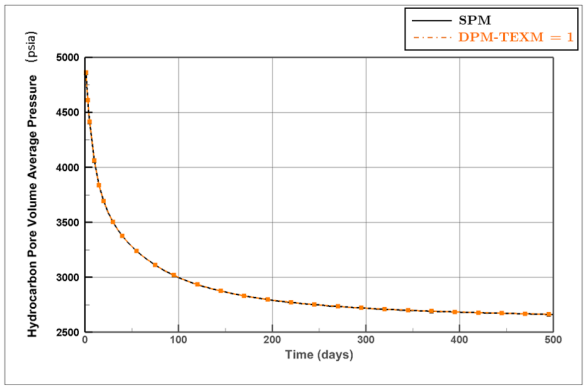

(a) Pressure profile

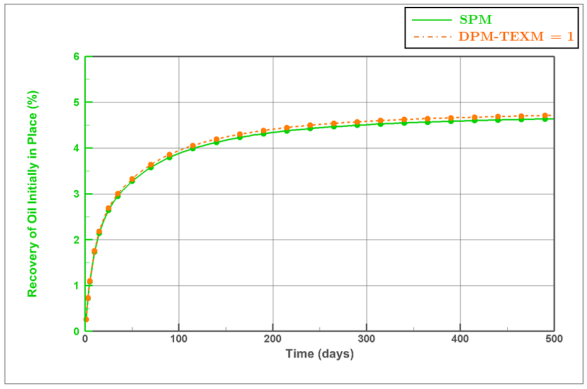

(b) Oil recovery factor profile

Figure B.27: Dual-porosity performance profile corresponding to single-porosity by changing TEX multiplier for second block of $\ell_x = 1$ ft and $k_m = 1000$ nd.

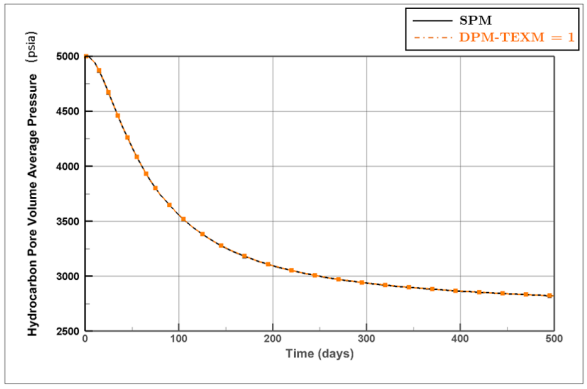

(a) Pressure profile

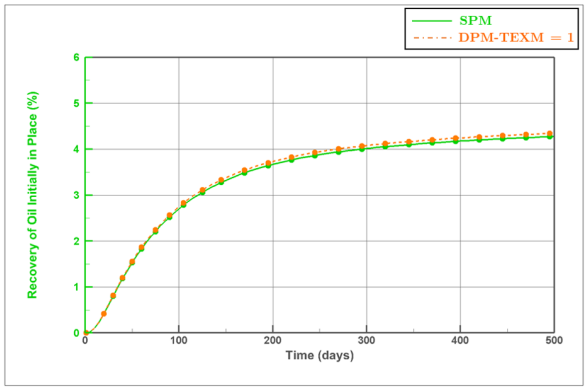

(b) Oil recovery factor profile

Figure B.28: Dual-porosity performance profile corresponding to single-porosity by changing TEX multiplier for forth block of $\ell_x = 1$ ft and $k_m = 1000$ nd.

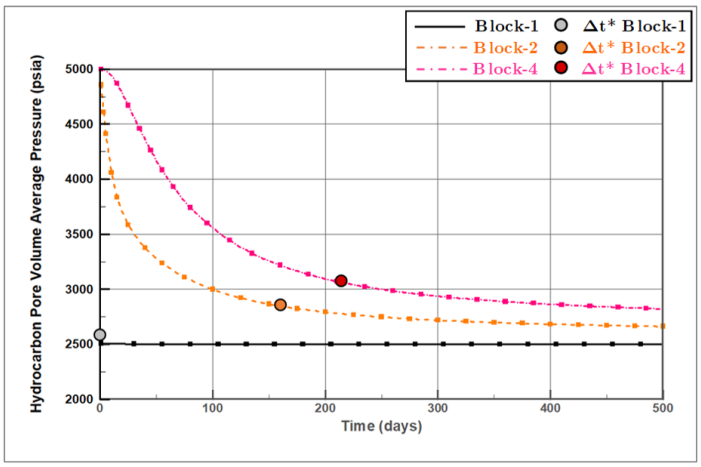

(a) Matrix pressure (P_m) profile

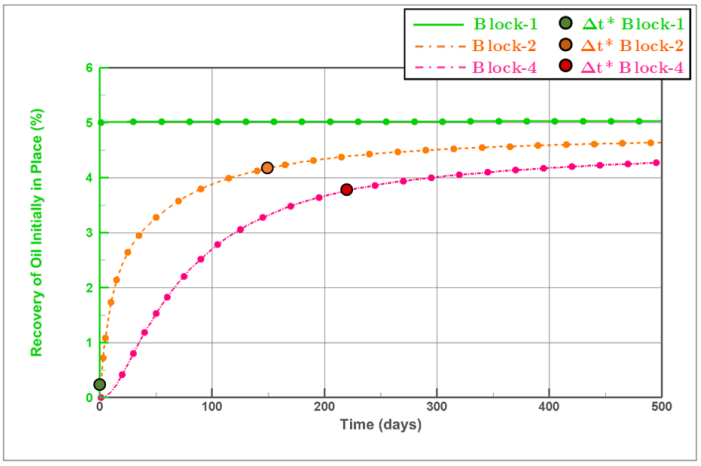

(b) Oil recovery factor profile

Figure B.29: Δt^* of single-porosity model for $\ell_x = 1$ ft and $k_m = 1000$ nd.

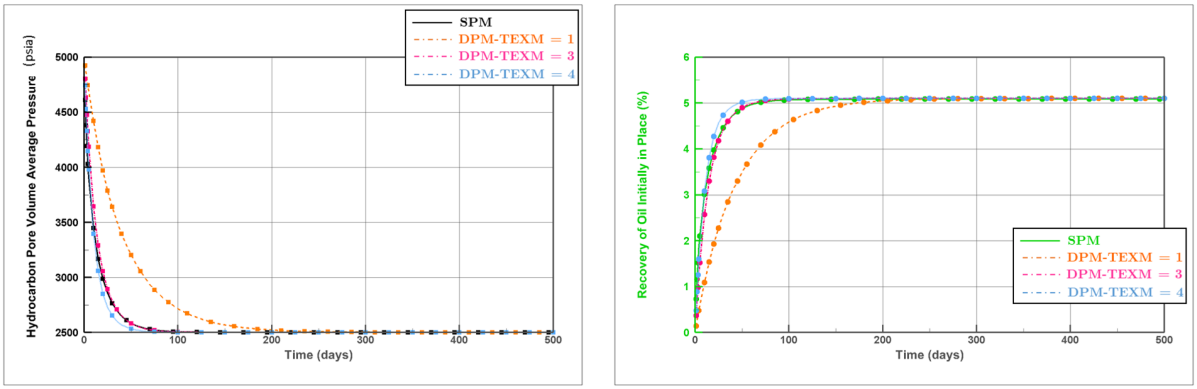

(a) Pressure profile **(b)** Oil recovery factor profile

Figure B.30: Dual-porosity performance profile corresponding to single-porosity by changing TEX multiplier for first block of $\ell_x = 5$ ft and $k_m = 10$ nd.

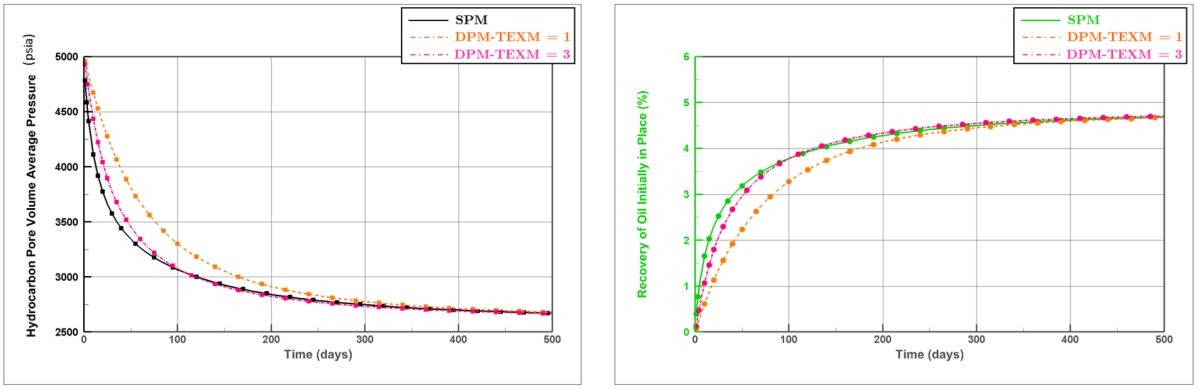

(a) Pressure profile **(b)** Oil recovery factor profile

Figure B.31: Dual-porosity performance profile corresponding to single-porosity by changing TEX multiplier for second block of $\ell_x = 5$ ft and $k_m = 10$ nd.

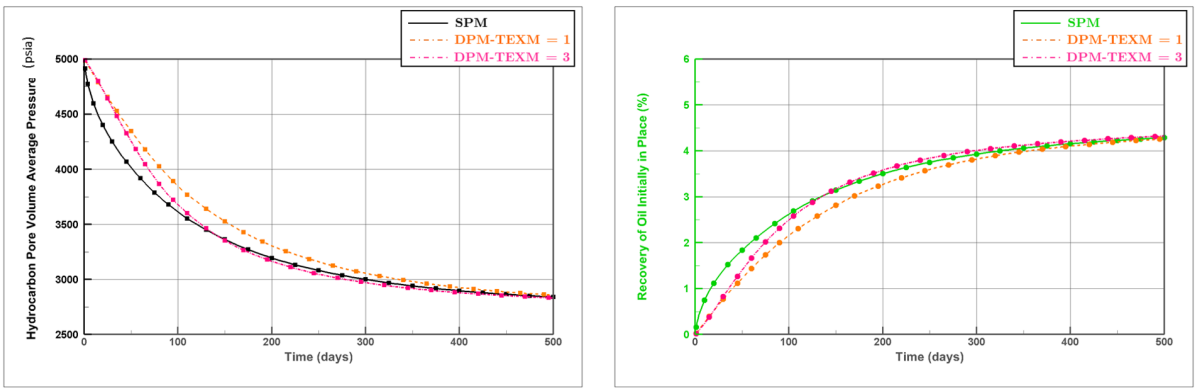

(a) Pressure profile **(b)** Oil recovery factor profile

Figure B.32: Dual-porosity performance profile corresponding to single-porosity by changing TEX multiplier for forth block of $\ell_x = 5$ ft and $k_m = 10$ nd.

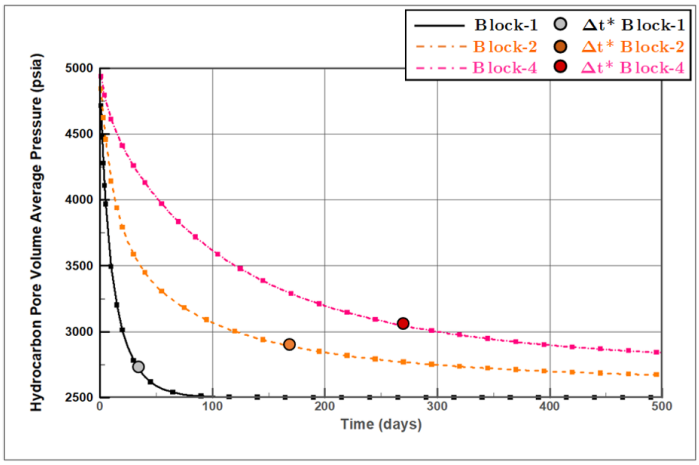

(a) Matrix pressure (P_m) profile

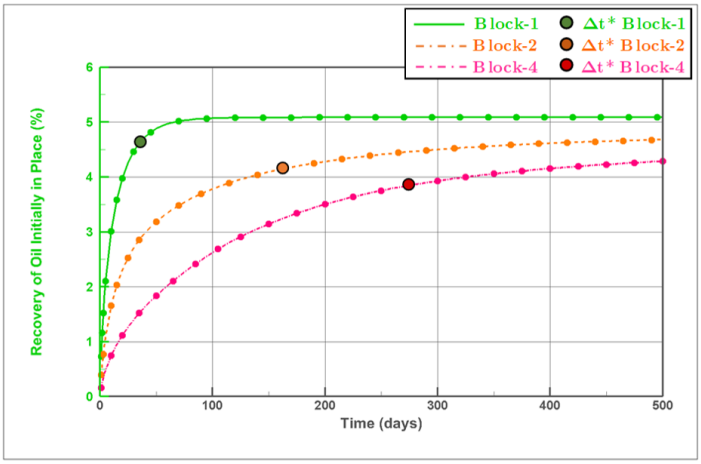

(b) Oil recovery factor profile

Figure B.33: Δt^* of single-porosity model for $\ell_x = 5$ ft and $k_m = 10$ nd.

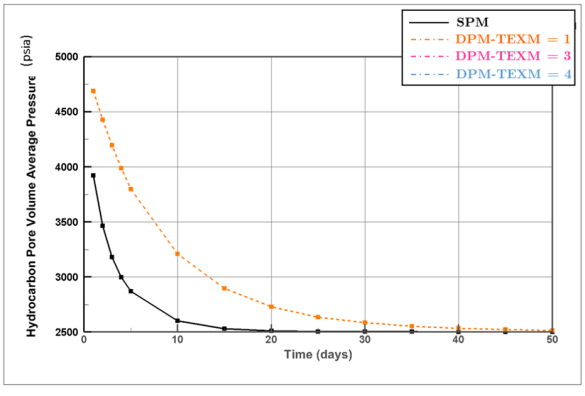

(a) Pressure profile

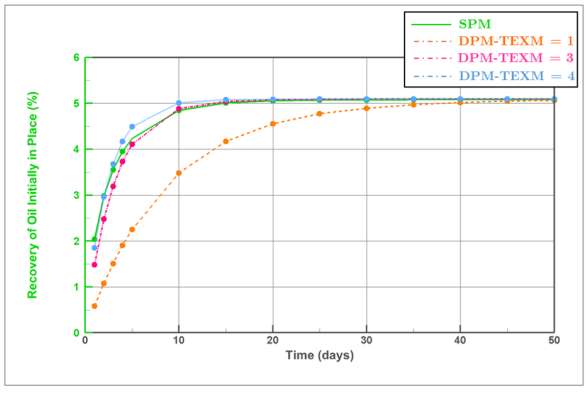

(b) Oil recovery factor profile

Figure B.34: Dual-porosity performance profile corresponding to single-porosity by changing TEX multiplier for first block of $\ell_x = 5$ ft and $k_m = 50$ nd.

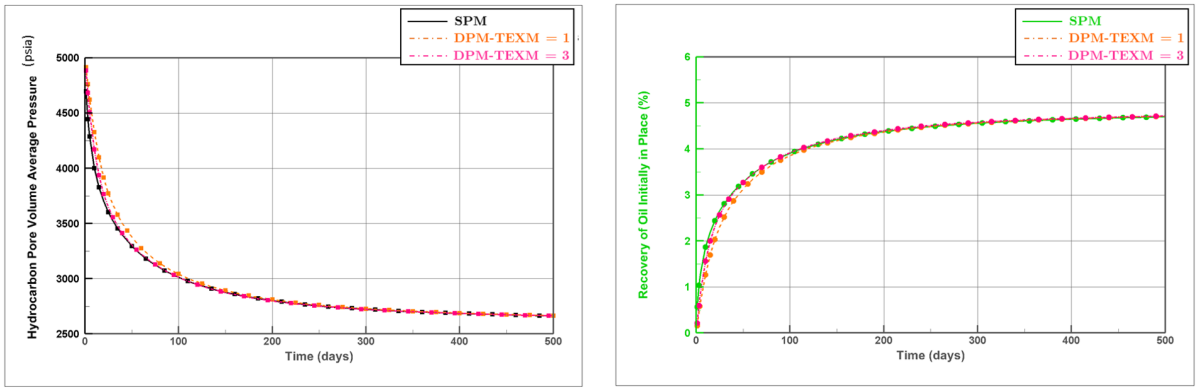

(a) Pressure profile **(b)** Oil recovery factor profile

Figure B.35: Dual-porosity performance profile corresponding to single-porosity by changing TEX multiplier for second block of $\ell_x = 5$ ft and $k_m = 50$ nd.

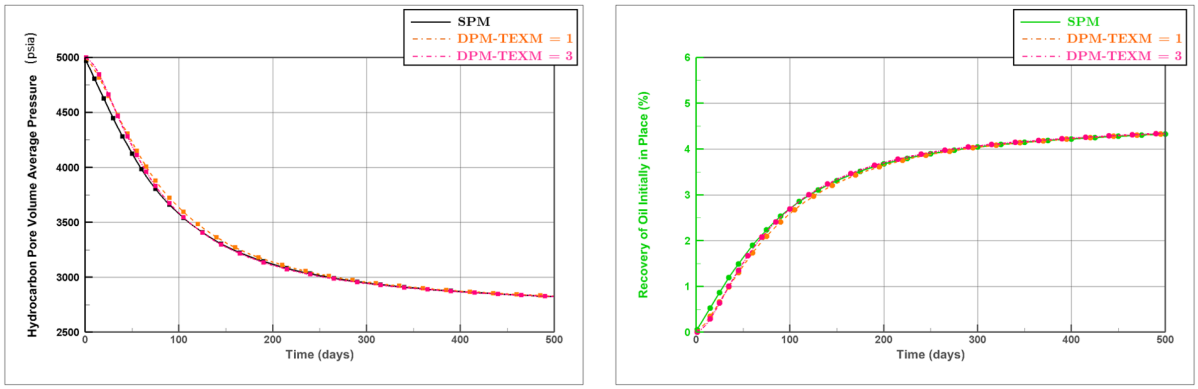

(a) Pressure profile **(b)** Oil recovery factor profile

Figure B.36: Dual-porosity performance profile corresponding to single-porosity by changing TEX multiplier for forth block of $\ell_x = 5$ ft and $k_m = 50$ nd.

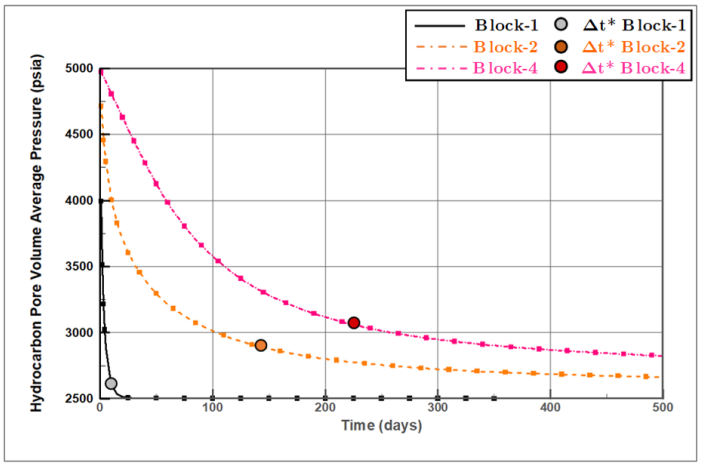

(a) Matrix pressure (P_m) profile

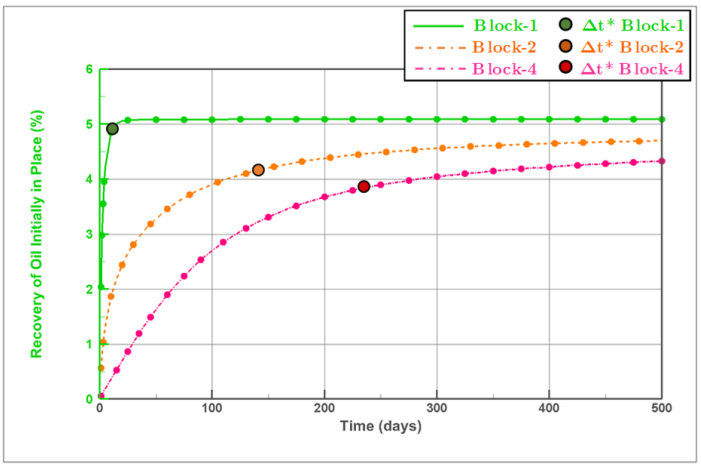

(b) Oil recovery factor profile

Figure B.37: Δt^* of single-porosity model for $\ell_x = 5$ ft and $k_m = 50$ nd.

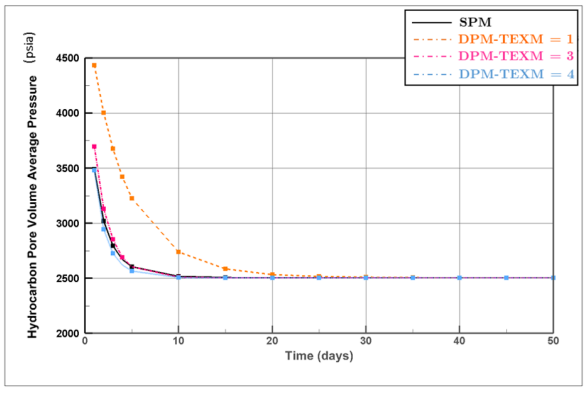

(a) Pressure profile

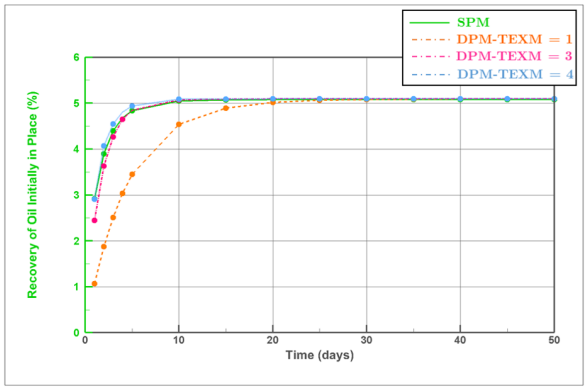

(b) Oil recovery factor profile

Figure B.38: Dual-porosity performance profile corresponding to single-porosity by changing TEX multiplier for first block of $\ell_x = 5$ ft and $k_m = 100$ nd.

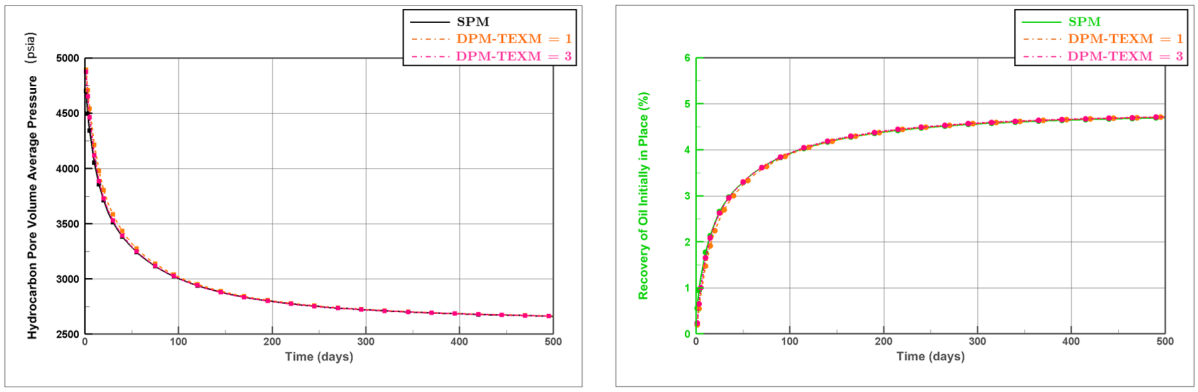

(a) Pressure profile **(b)** Oil recovery factor profile

Figure B.39: Dual-porosity performance profile corresponding to single-porosity by changing TEX multiplier for second block of $\ell_x = 5$ ft and $k_m = 100$ nd.

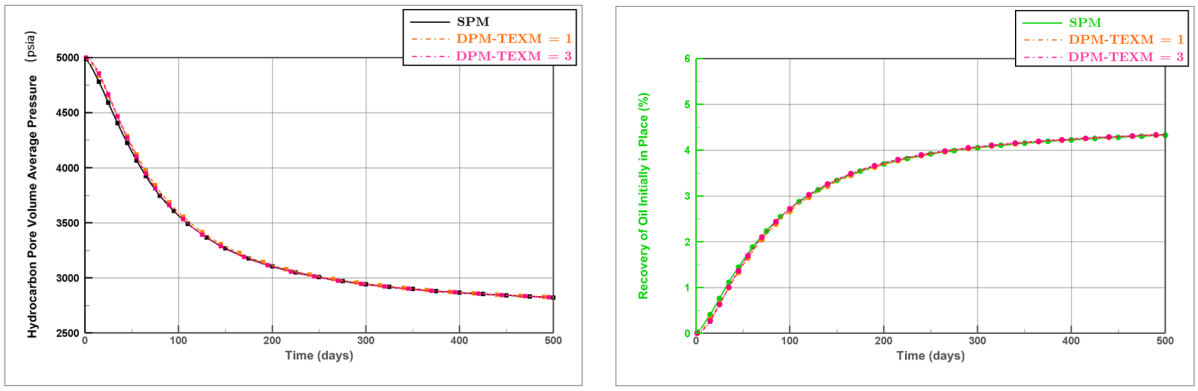

(a) Pressure profile **(b)** Oil recovery factor profile

Figure B.40: Dual-porosity performance profile corresponding to single-porosity by changing TEX multiplier for forth block of $\ell_x = 5$ ft and $k_m = 100$ nd.

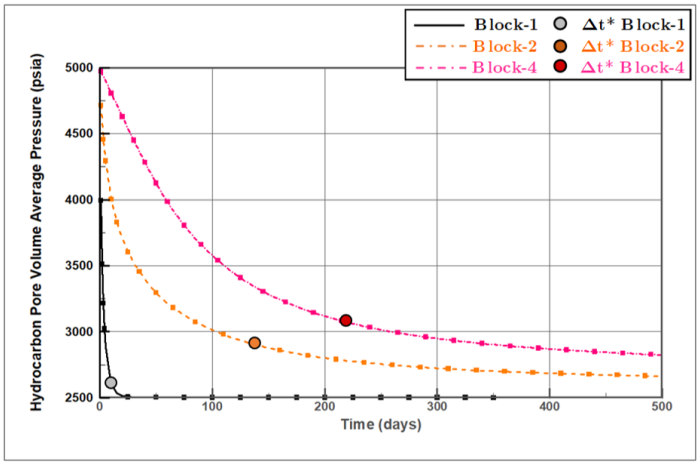

(a) Matrix pressure (P_m) profile

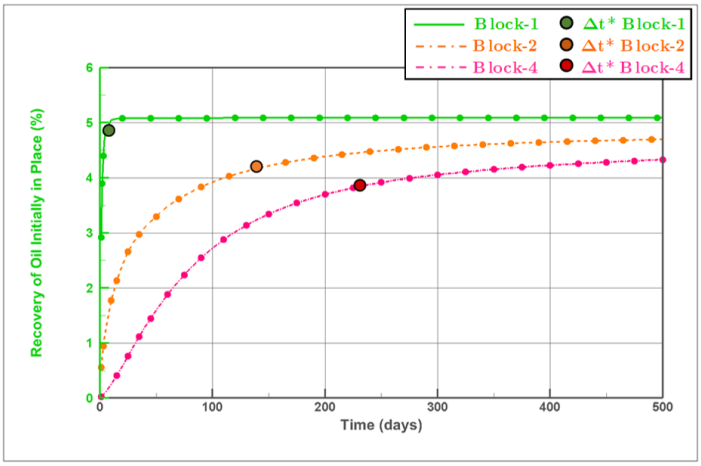

(b) Oil recovery factor profile

Figure B.41: Δt^* of single-porosity model for $\ell_x = 5$ ft and $k_m = 100$ nd.

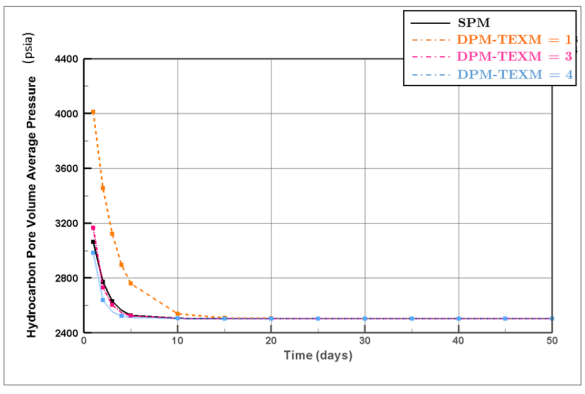

(a) Pressure profile

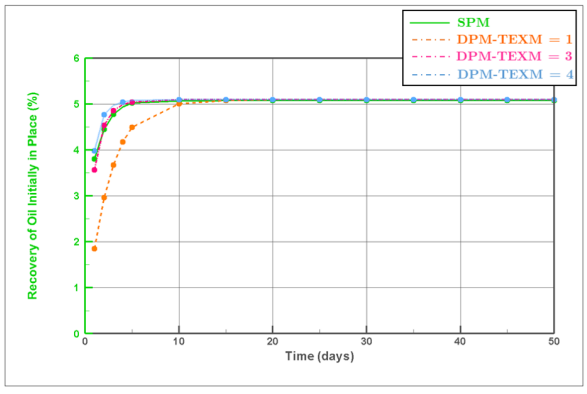

(b) Oil recovery factor profile

Figure B.42: Dual-porosity performance profile corresponding to single-porosity by changing TEX multiplier for first block of $\ell_x = 5$ ft and $k_m = 200$ nd.

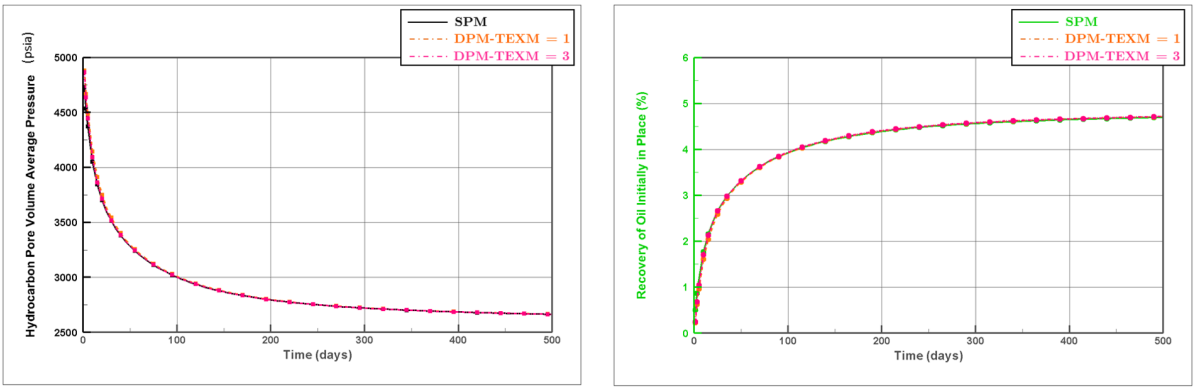

(a) Pressure profile **(b)** Oil recovery factor profile

Figure B.43: Dual-porosity performance profile corresponding to single-porosity by changing TEX multiplier for second block of $\ell_x = 5$ ft and $k_m = 200$ nd.

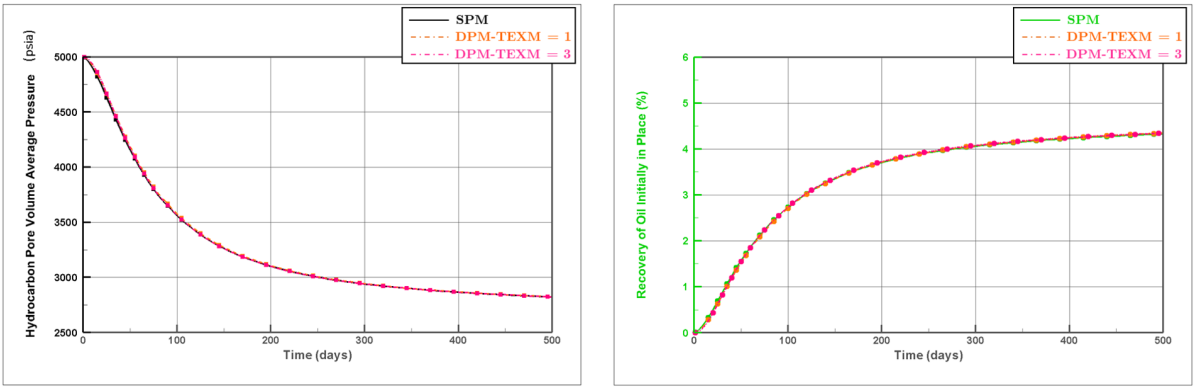

(a) Pressure profile **(b)** Oil recovery factor profile

Figure B.44: Dual-porosity performance profile corresponding to single-porosity by changing TEX multiplier for forth block of $\ell_x = 5$ ft and $k_m = 200$ nd.

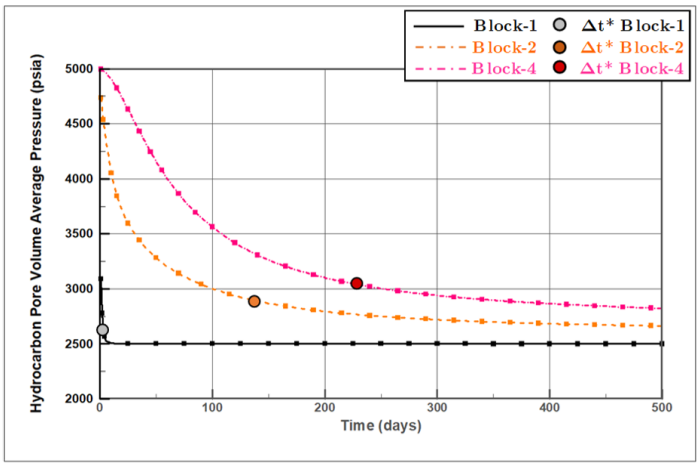

(a) Matrix pressure (P_m) profile

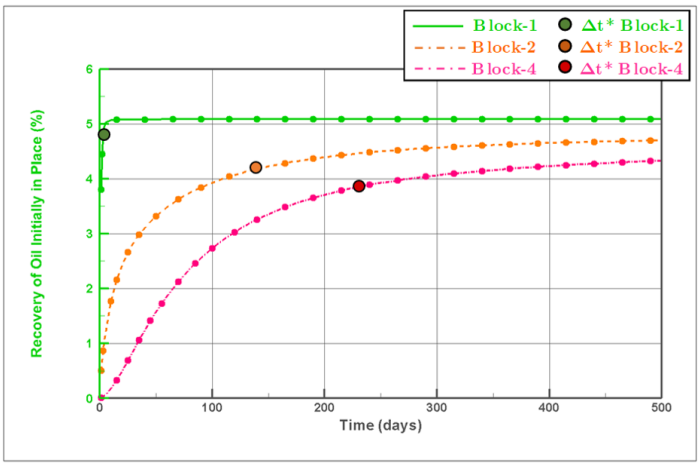

(b) Oil recovery factor profile

Figure B.45: Δt^* of single-porosity model for $\ell_x = 5$ ft and $k_m = 200$ nd.

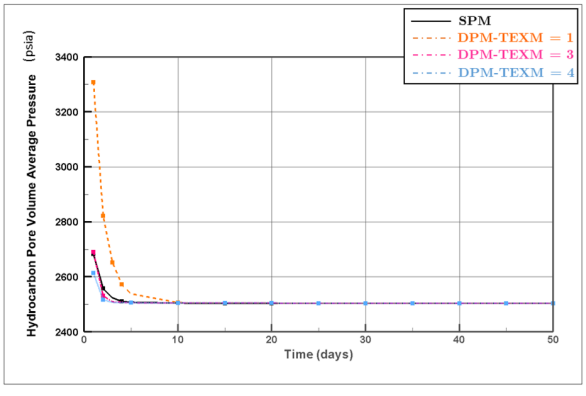

(a) Pressure profile

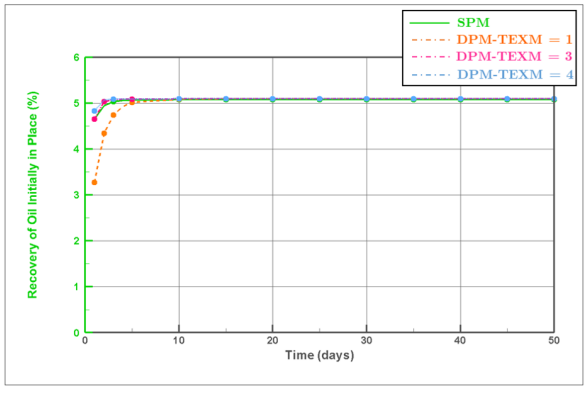

(b) Oil recovery factor profile

Figure B.46: Dual-porosity performance profile corresponding to single-porosity by changing TEX multiplier for first block of $\ell_x = 5$ ft and $k_m = 500$ nd.

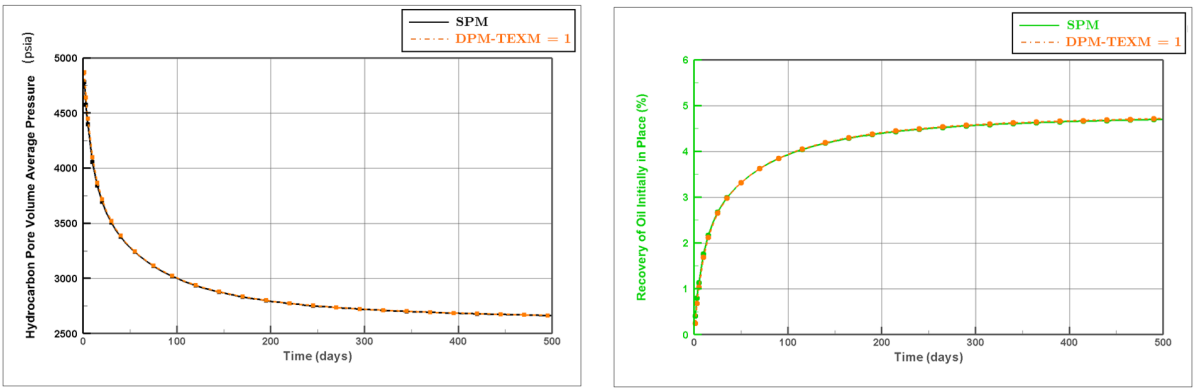

(a) Pressure profile **(b)** Oil recovery factor profile

Figure B.47: Dual-porosity performance profile corresponding to single-porosity by changing TEX multiplier for second block of $\ell_x = 5$ ft and $k_m = 500$ nd.

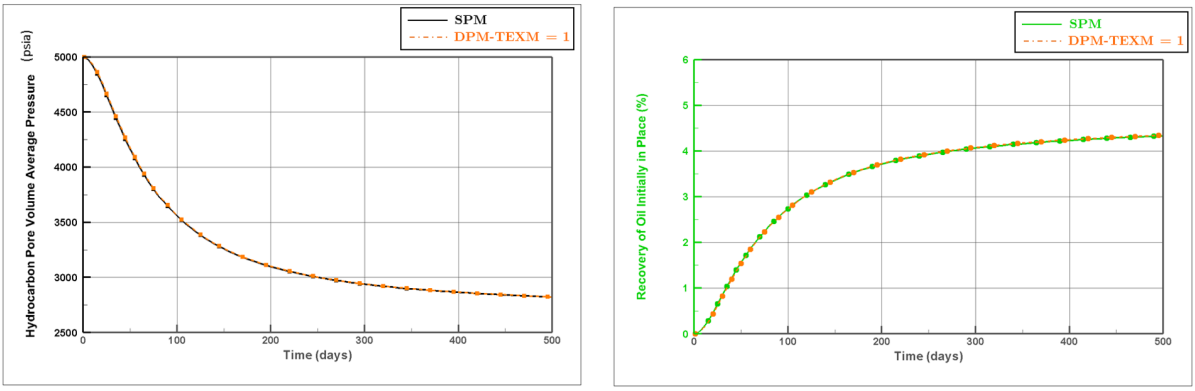

(a) Pressure profile **(b)** Oil recovery factor profile

Figure B.48: Dual-porosity performance profile corresponding to single-porosity by changing TEX multiplier for forth block of $\ell_x = 5$ ft and $k_m = 500$ nd.

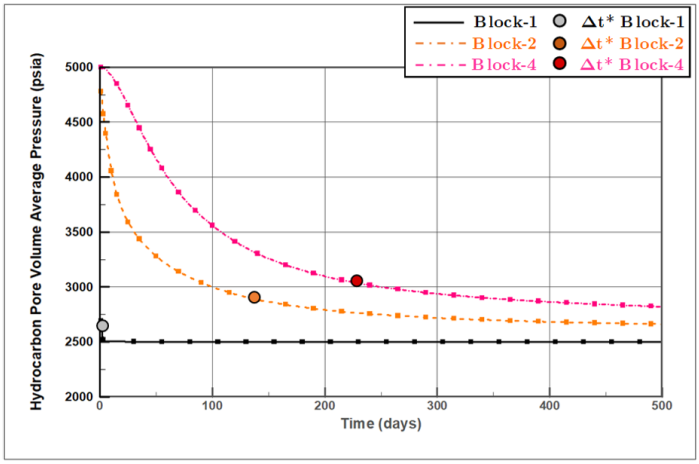

(a) Matrix pressure (P_m) profile

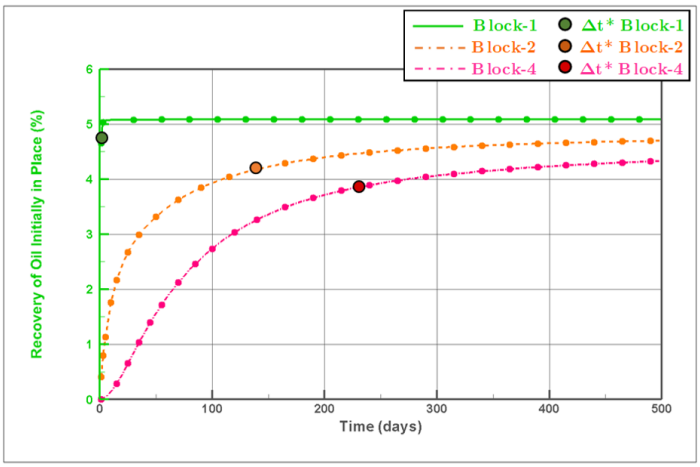

(b) Oil recovery factor profile

Figure B.49: Δt^* of single-porosity model for $\ell_x = 5$ ft and $k_m = 500$ nd.

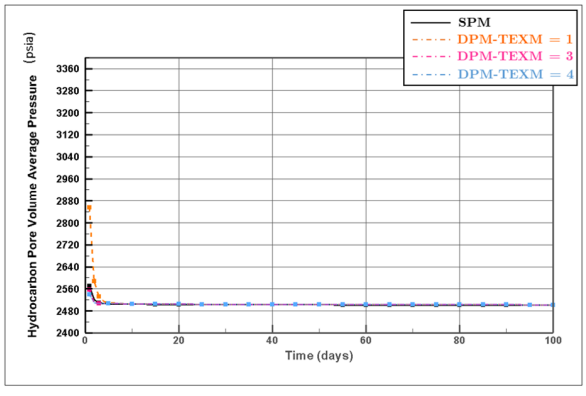

(a) Pressure profile

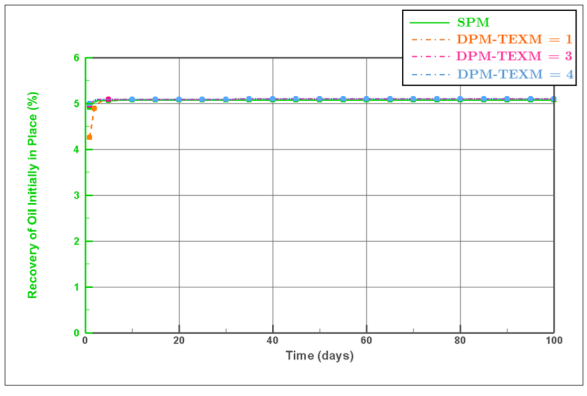

(b) Oil recovery factor profile

Figure B.50: Dual-porosity performance profile corresponding to single-porosity by changing TEX multiplier for first block of $\ell_x = 5$ ft and $k_m = 1000$ nd.

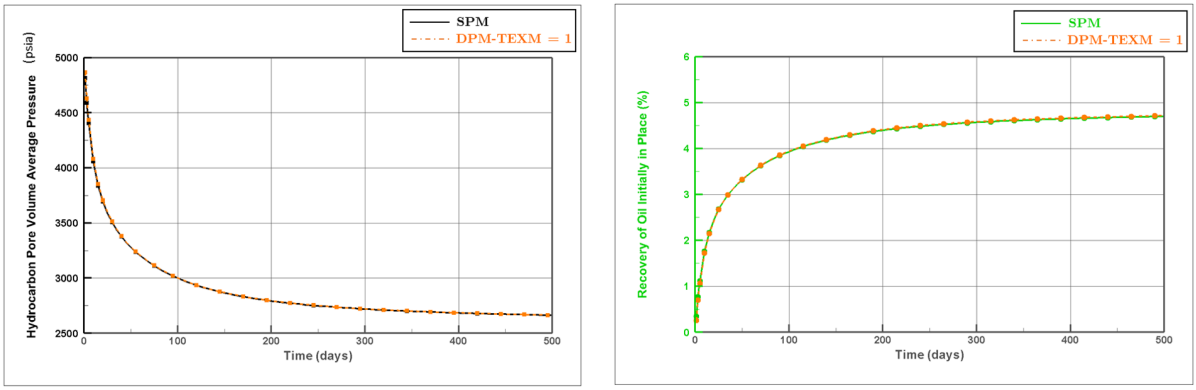

(a) Pressure profile **(b)** Oil recovery factor profile

Figure B.51: Dual-porosity performance profile corresponding to single-porosity by changing TEX multiplier for second block of $\ell_x = 5$ ft and $k_m = 1000$ nd.

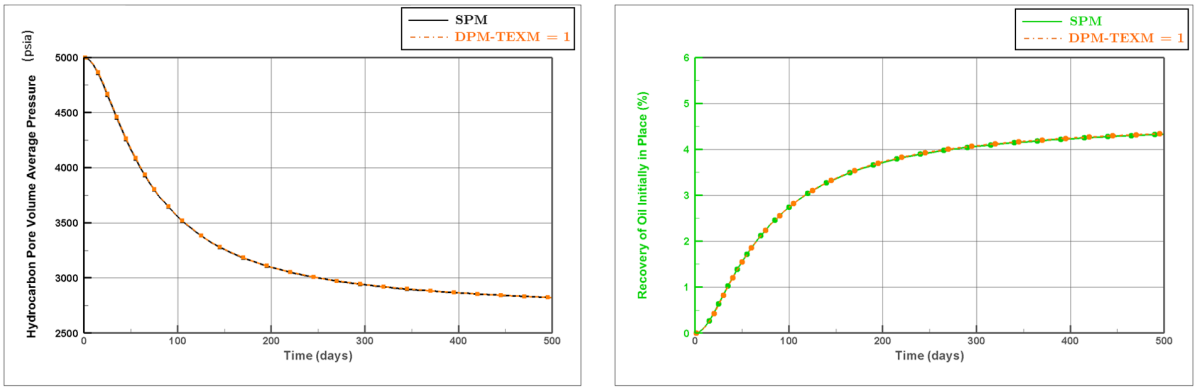

(a) Pressure profile **(b)** Oil recovery factor profile

Figure B.52: Dual-porosity performance profile corresponding to single-porosity by changing TEX multiplier for forth block of $\ell_x = 5$ ft and $k_m = 1000$ nd.

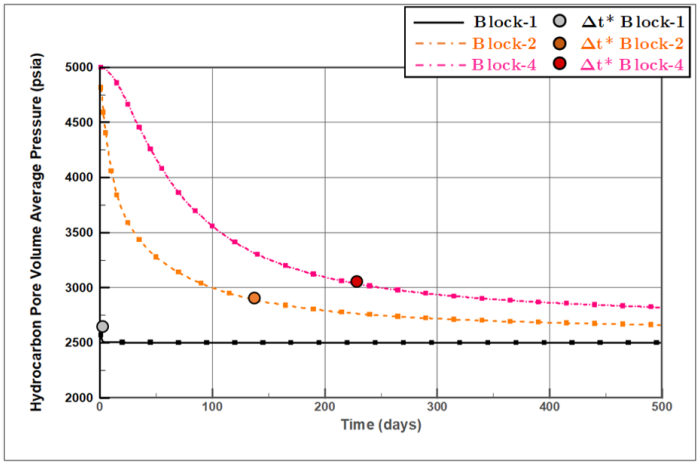

(a) Matrix pressure (P_m) profile

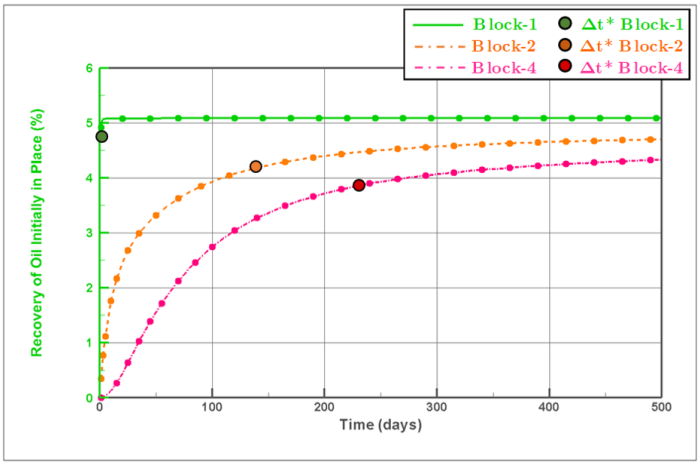

(b) Oil recovery factor profile

Figure B.53: Δt^* of single-porosity model for $\ell_x = 5$ ft and $k_m = 1000$ nd.

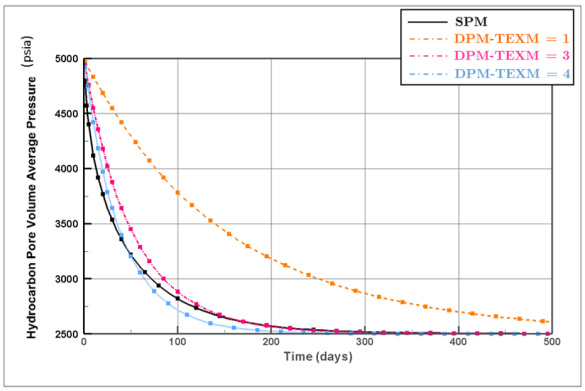

(a) Pressure profile

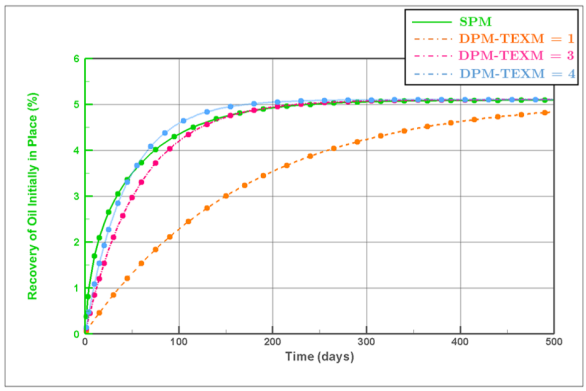

(b) Oil recovery factor profile

Figure B.54: Dual-porosity performance profile corresponding to single-porosity by changing TEX multiplier for first block of $\ell_x = 10$ ft and $k_m = 10$ nd.

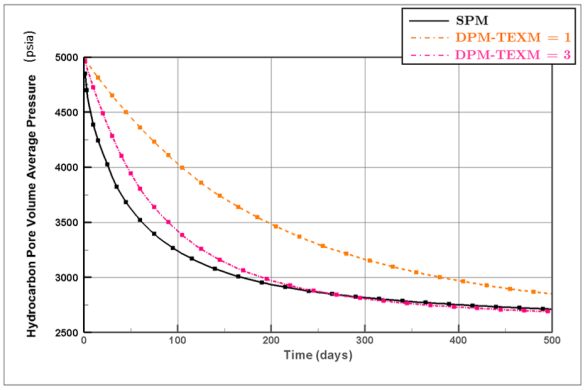

(a) Pressure profile

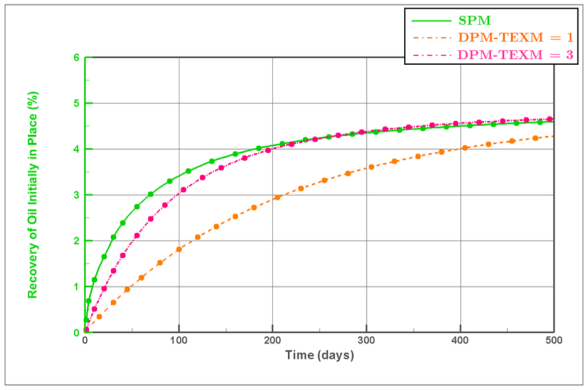

(b) Oil recovery factor profile

Figure B.55: Dual-porosity performance profile corresponding to single-porosity by changing TEX multiplier for second block of $\ell_x = 10$ ft and $k_m = 10$ nd.

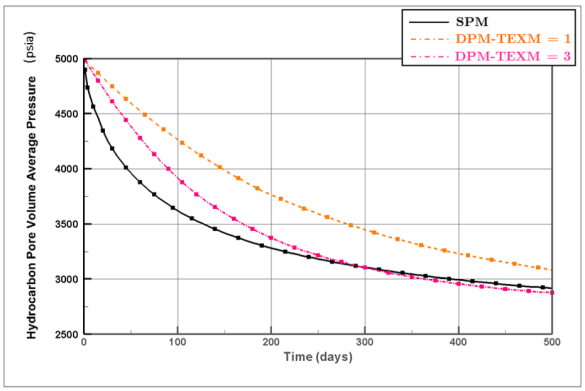

(a) Pressure profile

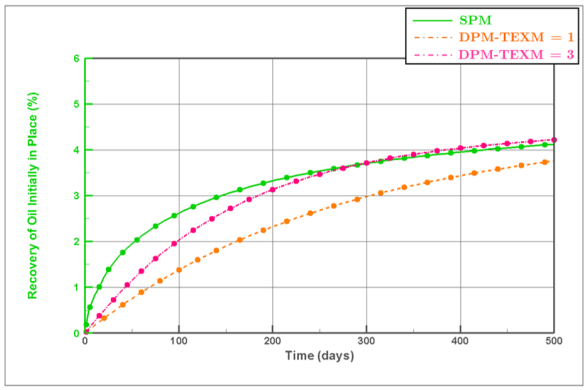

(b) Oil recovery factor profile

Figure B.56: Dual-porosity performance profile corresponding to single-porosity by changing TEX multiplier for forth block of $\ell_x = 10$ ft and $k_m = 10$ nd.

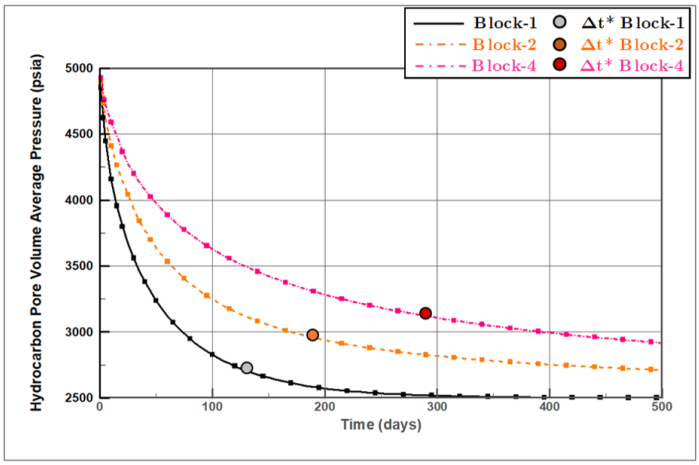

(a) Matrix pressure (P_m) profile

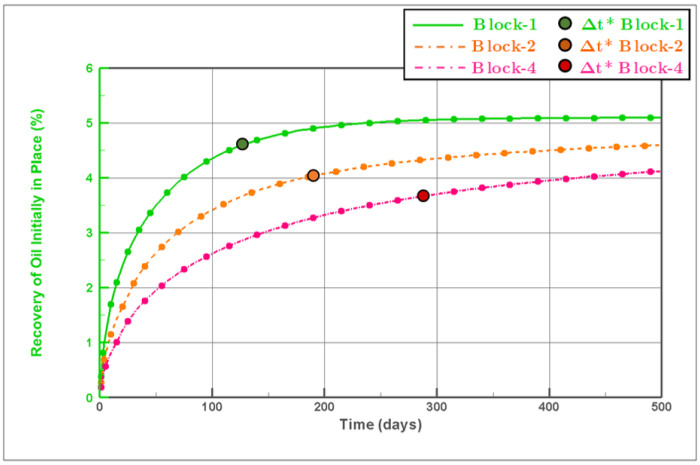

(b) Oil recovery factor profile

Figure B.57: Δt^* of single-porosity model for $\ell_x = 10$ ft and $k_m = 10$ nd.

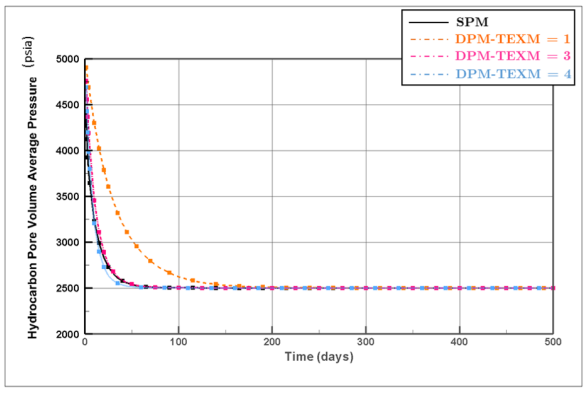

(a) Pressure profile

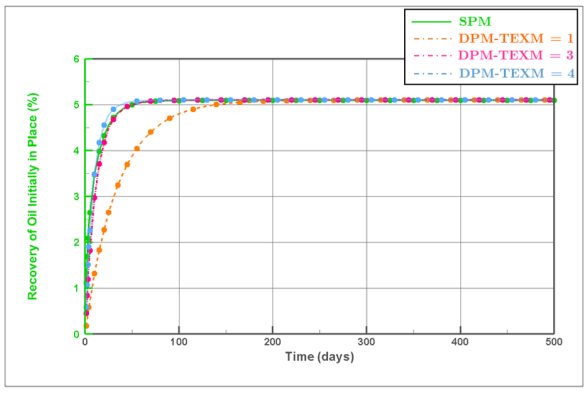

(b) Oil recovery factor profile

Figure B.58: Dual-porosity performance profile corresponding to single-porosity by changing TEX multiplier for first block of $\ell_x = 10$ ft and $k_m = 50$ nd.

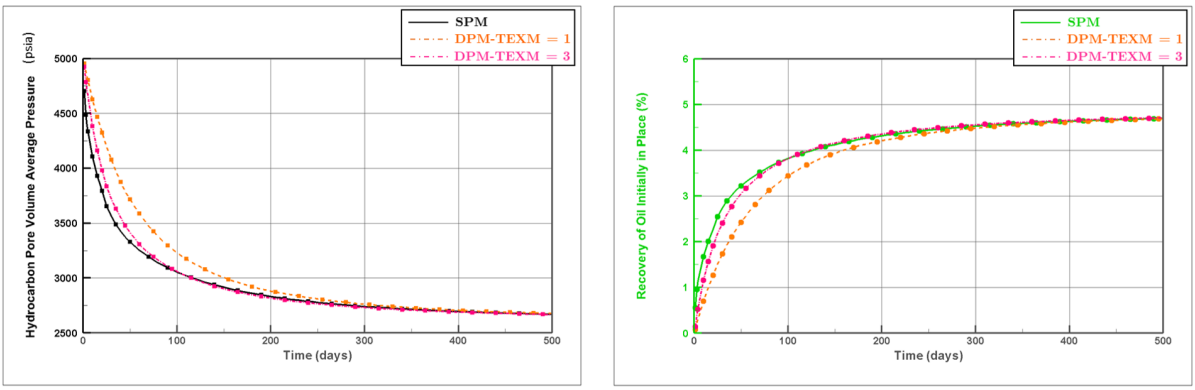

(a) Pressure profile **(b)** Oil recovery factor profile

Figure B.59: Dual-porosity performance profile corresponding to single-porosity by changing TEX multiplier for second block of $\ell_x = 10$ ft and $k_m = 50$ nd.

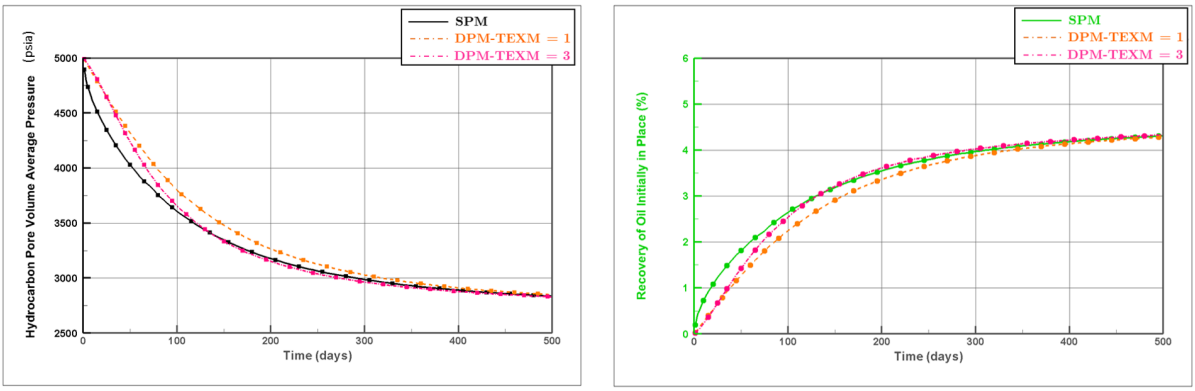

(a) Pressure profile **(b)** Oil recovery factor profile

Figure B.60: Dual-porosity performance profile corresponding to single-porosity by changing TEX multiplier for forth block of $\ell_x = 10$ ft and $k_m = 50$ nd.

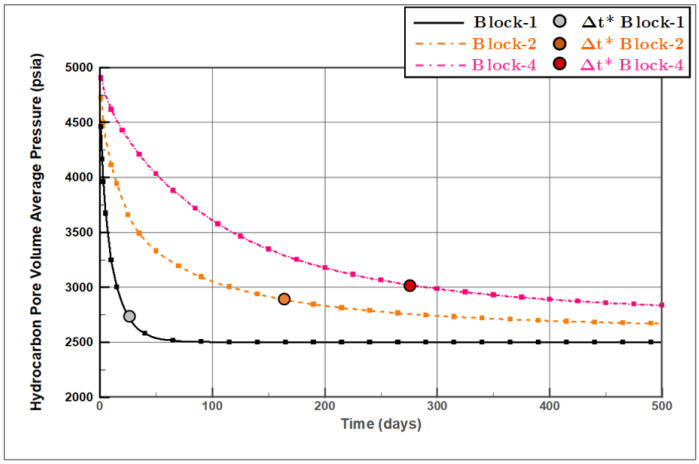

(a) Matrix pressure (P_m) profile

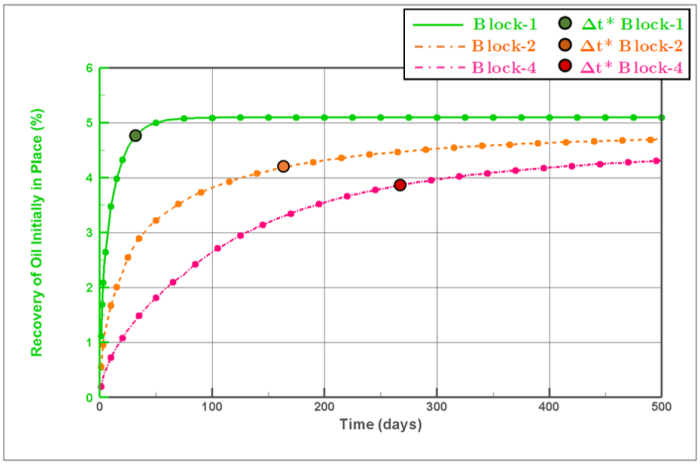

(b) Oil recovery factor profile

Figure B.61: Δt^* of single-porosity model for $\ell_x = 10$ ft and $k_m = 50$ nd.

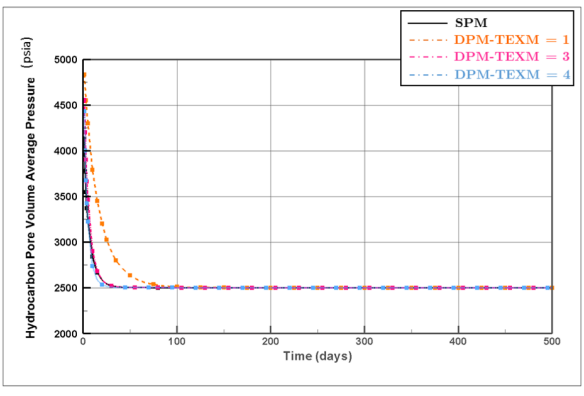

(a) Pressure profile

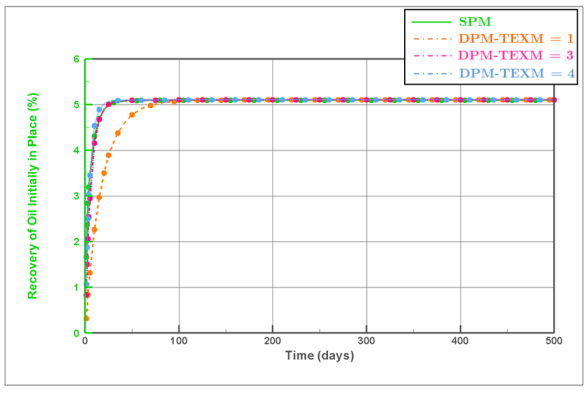

(b) Oil recovery factor profile

Figure B.62: Dual-porosity performance profile corresponding to single-porosity by changing TEX multiplier for first block of $\ell_x = 10$ ft and $k_m = 100$ nd.

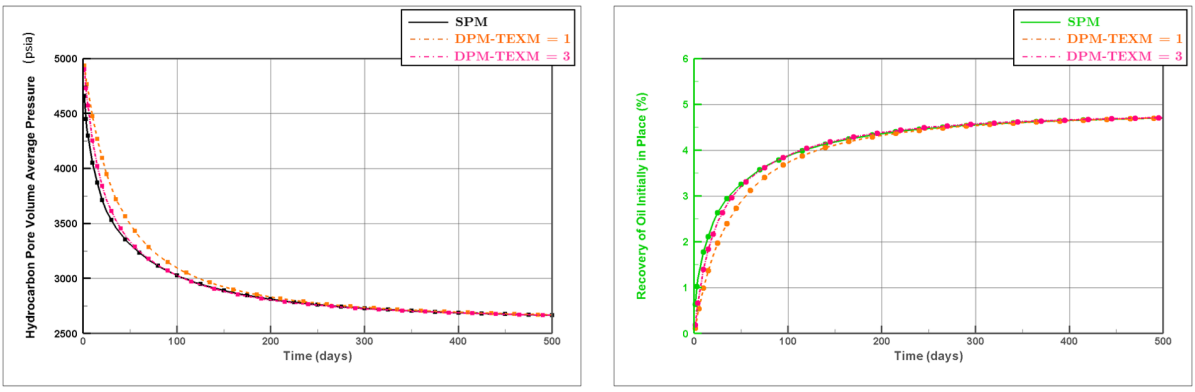

(a) Pressure profile **(b)** Oil recovery factor profile

Figure B.63: Dual-porosity performance profile corresponding to single-porosity by changing TEX multiplier for second block of $\ell_x = 10$ ft and $k_m = 100$ nd.

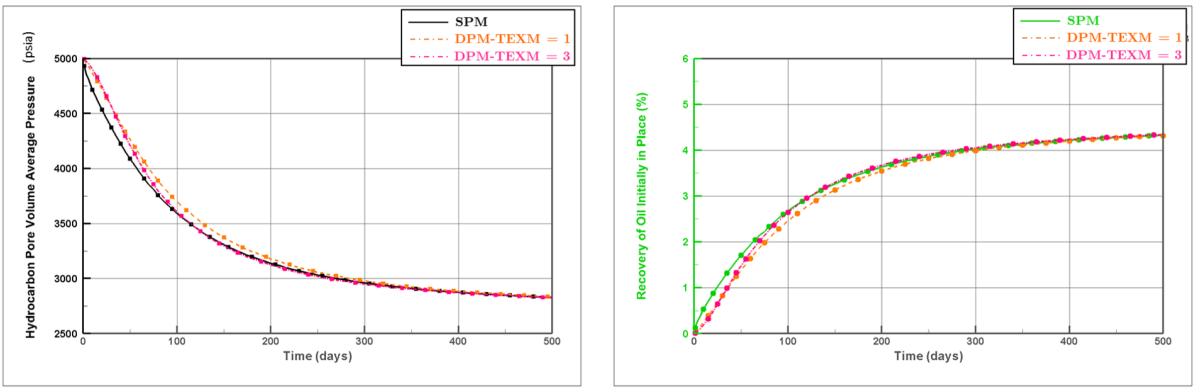

(a) Pressure profile **(b)** Oil recovery factor profile

Figure B.64: Dual-porosity performance profile corresponding to single-porosity by changing TEX multiplier for forth block of $\ell_x = 10$ ft and $k_m = 100$ nd.

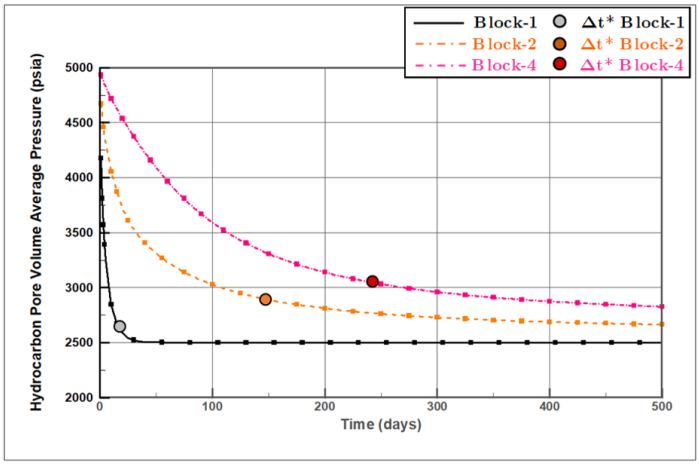

(a) Matrix pressure (P_m) profile

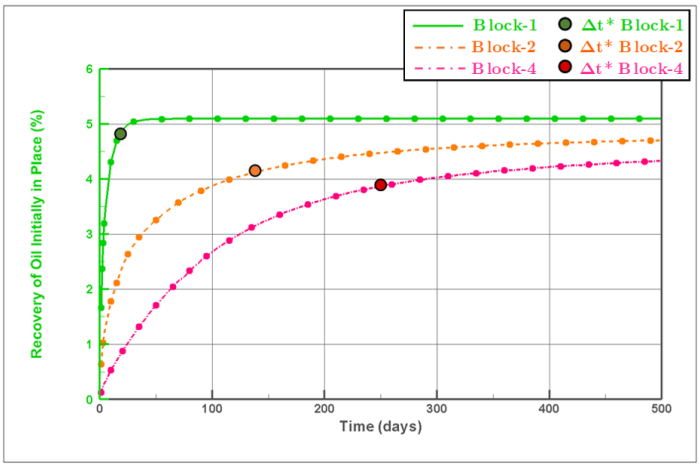

(b) Oil recovery factor profile

Figure B.65: Δt^* of single-porosity model for $\ell_x = 10$ ft and $k_m = 100$ nd.

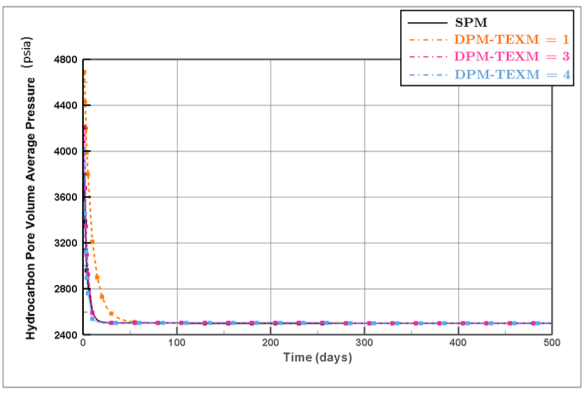

(a) Pressure profile

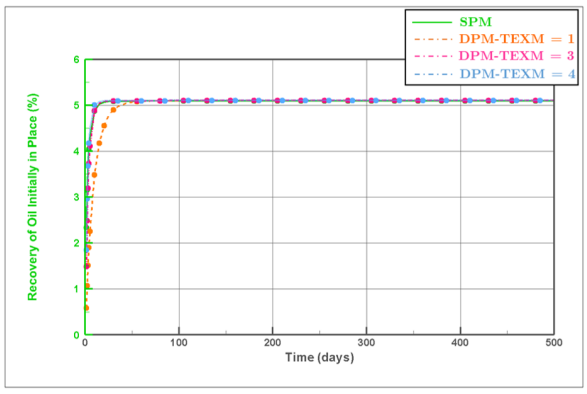

(b) Oil recovery factor profile

Figure B.66: Dual-porosity performance profile corresponding to single-porosity by changing TEX multiplier for first block of $\ell_x = 10$ ft and $k_m = 200$ nd.

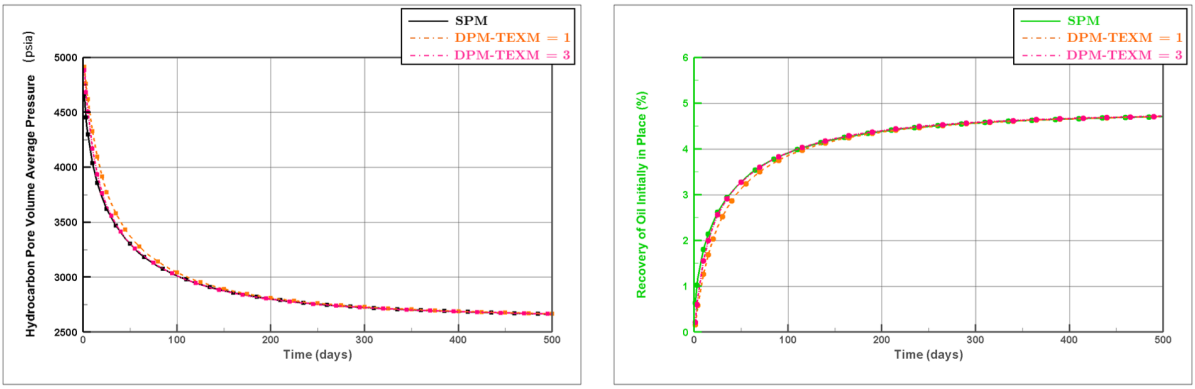

(a) Pressure profile **(b)** Oil recovery factor profile

Figure B.67: Dual-porosity performance profile corresponding to single-porosity by changing TEX multiplier for second block of $\ell_x = 10$ ft and $k_m = 200$ nd.

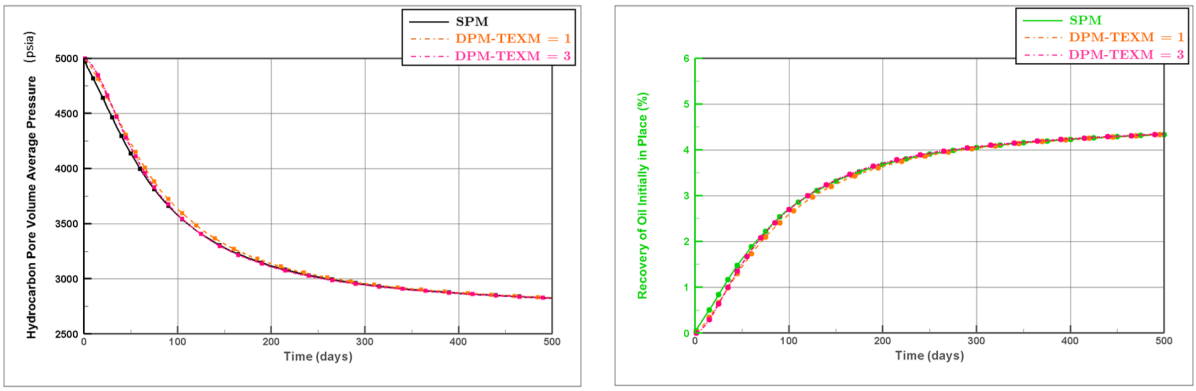

(a) Pressure profile **(b)** Oil recovery factor profile

Figure B.68: Dual-porosity performance profile corresponding to single-porosity by changing TEX multiplier for forth block of $\ell_x = 10$ ft and $k_m = 200$ nd.

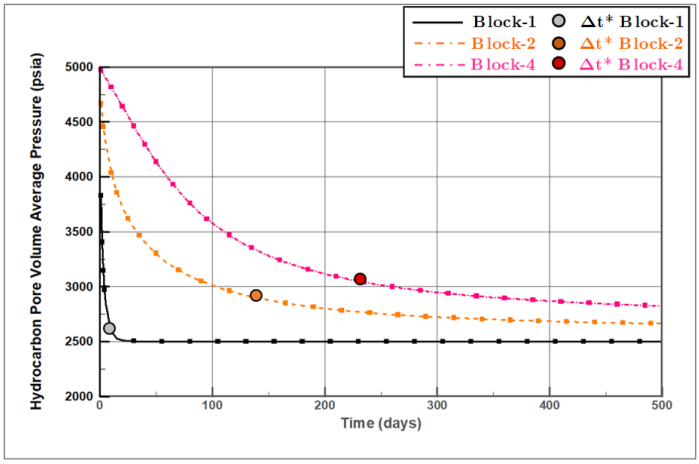

(a) Matrix pressure (P_m) profile

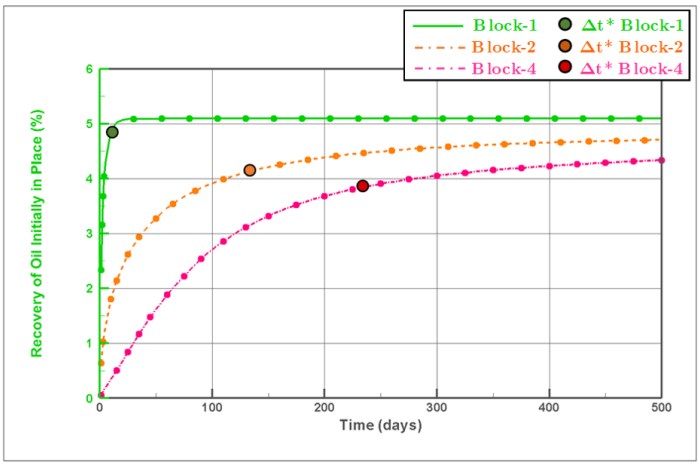

(b) Oil recovery factor profile

Figure B.69: Δt^* of single-porosity model for $\ell_x = 10$ ft and $k_m = 200$ nd.

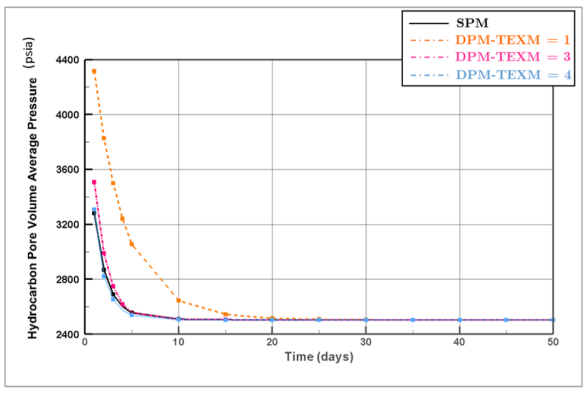

(a) Pressure profile

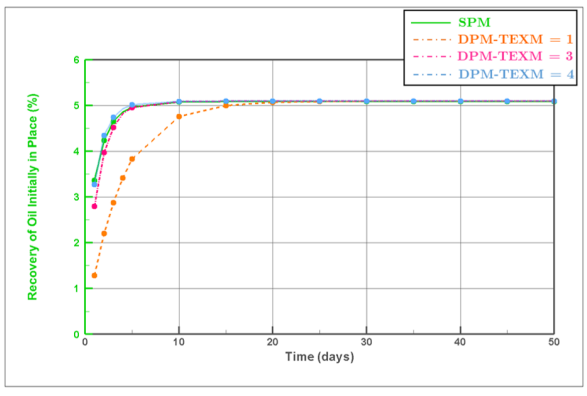

(b) Oil recovery factor profile

Figure B.70: Dual-porosity performance profile corresponding to single-porosity by changing TEX multiplier for first block of $\ell_x = 10$ ft and $k_m = 500$ nd.

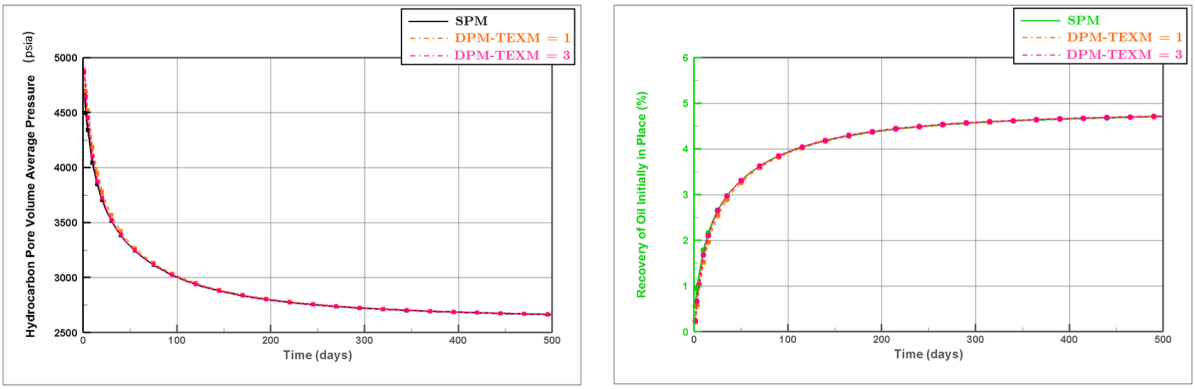

(a) Pressure profile **(b)** Oil recovery factor profile

Figure B.71: Dual-porosity performance profile corresponding to single-porosity by changing TEX multiplier for second block of $\ell_x = 10$ ft and $k_m = 500$ nd.

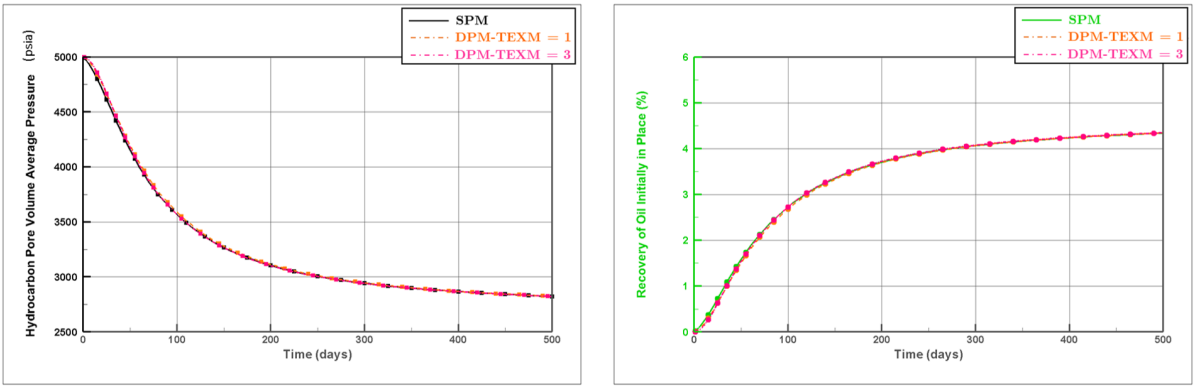

(a) Pressure profile **(b)** Oil recovery factor profile

Figure B.72: Dual-porosity performance profile corresponding to single-porosity by changing TEX multiplier for forth block of $\ell_x = 10$ ft and $k_m = 500$ nd.

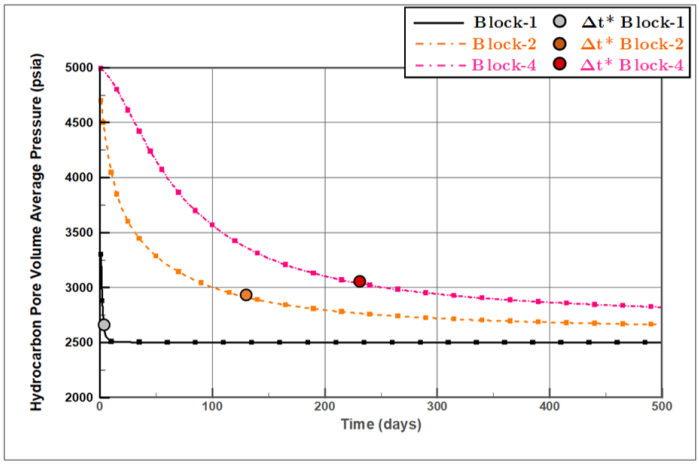

(a) Matrix pressure (P_m) profile

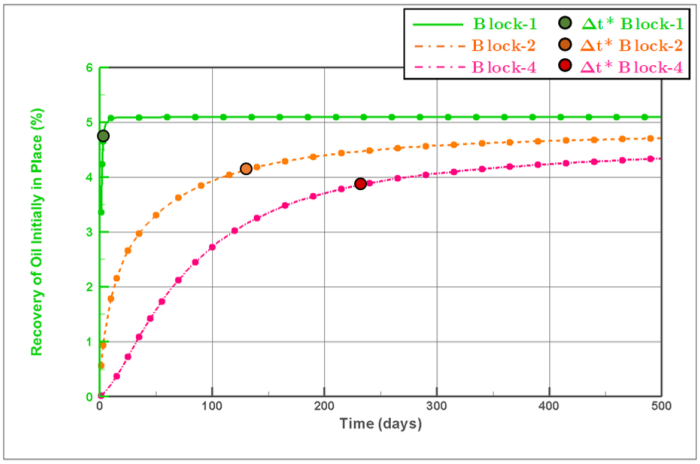

(b) Oil recovery factor profile

Figure B.73: Δt^* of single-porosity model for $\ell_x = 10$ ft and $k_m = 500$ nd.

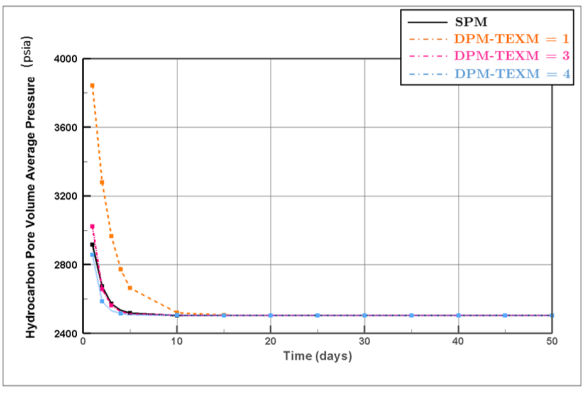

(a) Pressure profile

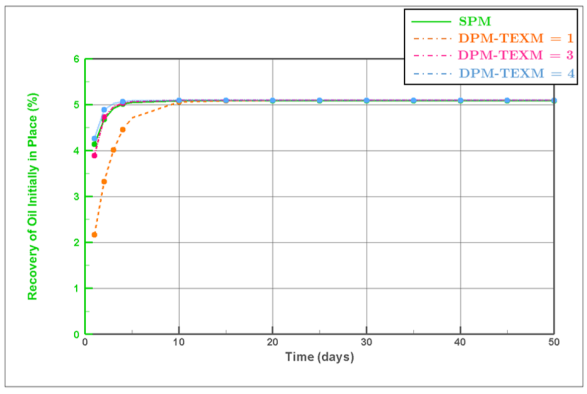

(b) Oil recovery factor profile

Figure B.74: Dual-porosity performance profile corresponding to single-porosity by changing TEX multiplier for first block of $\ell_x = 10$ ft and $k_m = 1000$ nd.

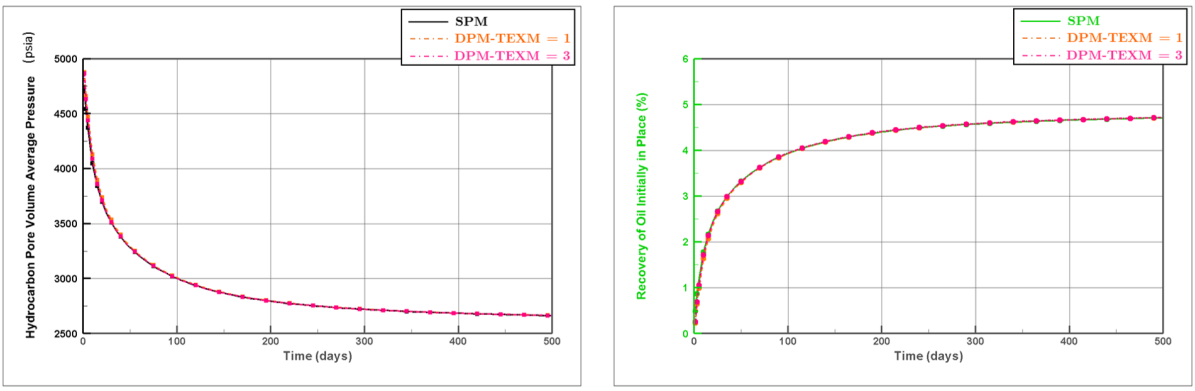

(a) Pressure profile **(b)** Oil recovery factor profile

Figure B.75: Dual-porosity performance profile corresponding to single-porosity by changing TEX multiplier for second block of $\ell_x = 10$ ft and $k_m = 1000$ nd.

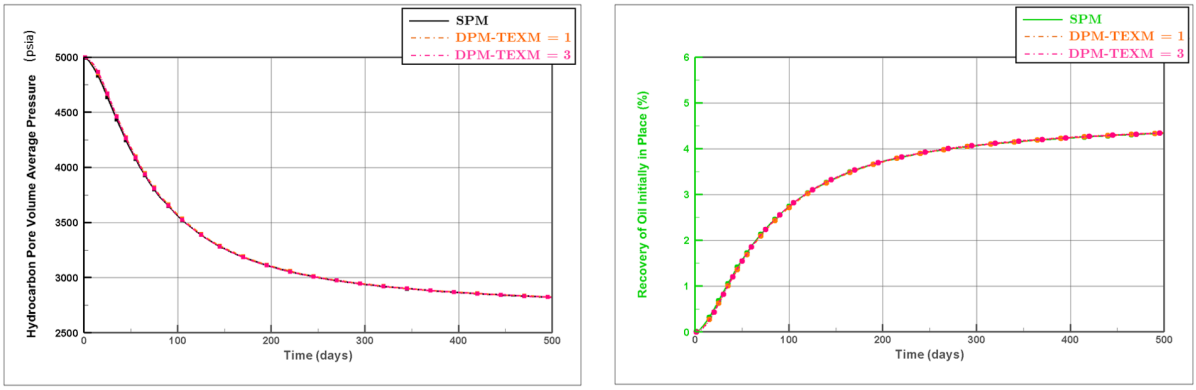

(a) Pressure profile **(b)** Oil recovery factor profile

Figure B.76: Dual-porosity performance profile corresponding to single-porosity by changing TEX multiplier for forth block of $\ell_x = 10$ ft and $k_m = 1000$ nd.

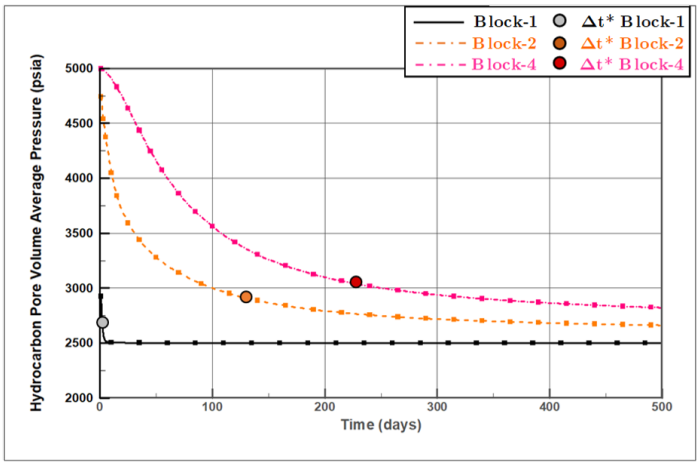

(a) Matrix pressure (P_m) profile

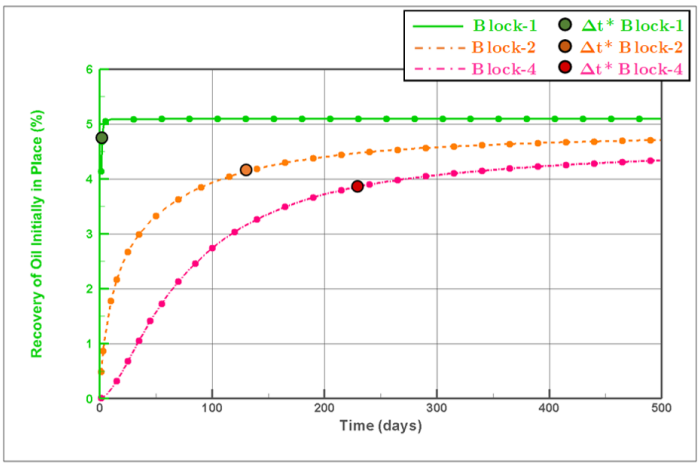

(b) Oil recovery factor profile

Figure B.77: Δt^* of single-porosity model for $\ell_x = 10$ ft and $k_m = 1000$ nd.

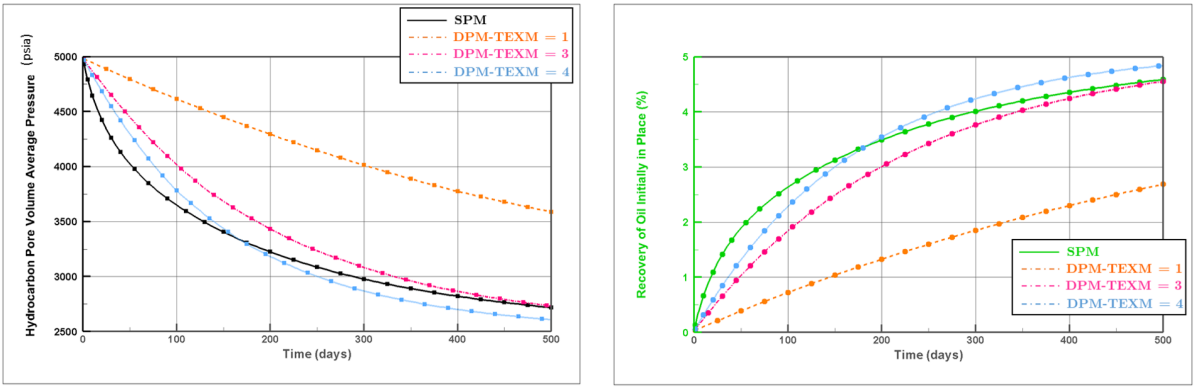

(a) Pressure profile **(b)** Oil recovery factor profile

Figure B.78: Dual-porosity performance profile corresponding to single-porosity by changing TEX multiplier for first block of $\ell_x = 20$ ft and $k_m = 10$ nd.

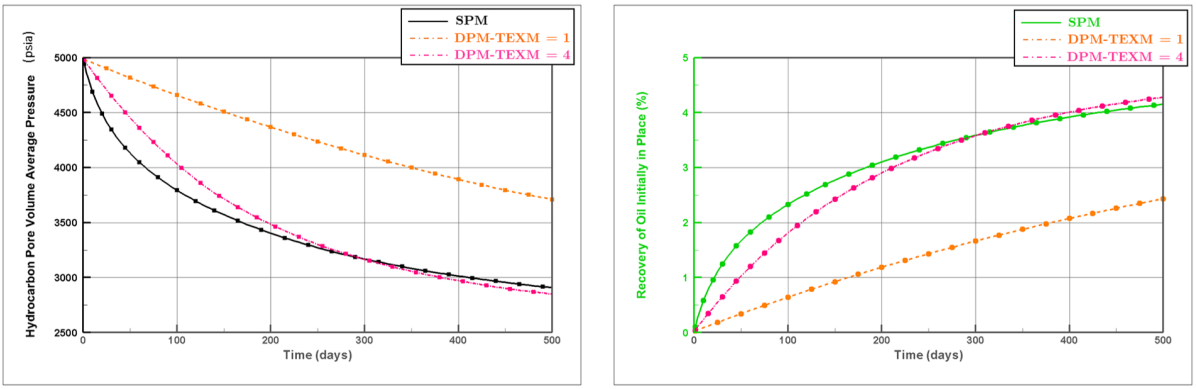

(a) Pressure profile **(b)** Oil recovery factor profile

Figure B.79: Dual-porosity performance profile corresponding to single-porosity by changing TEX multiplier for second block of $\ell_x = 20$ ft and $k_m = 10$ nd.

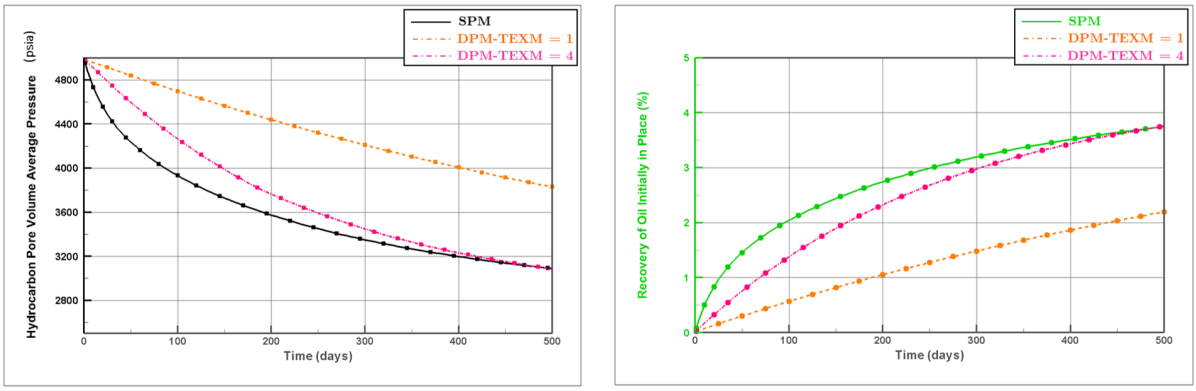

(a) Pressure profile **(b)** Oil recovery factor profile

Figure B.80: Dual-porosity performance profile corresponding to single-porosity by changing TEX multiplier for forth block of $\ell_x = 20$ ft and $k_m = 10$ nd.

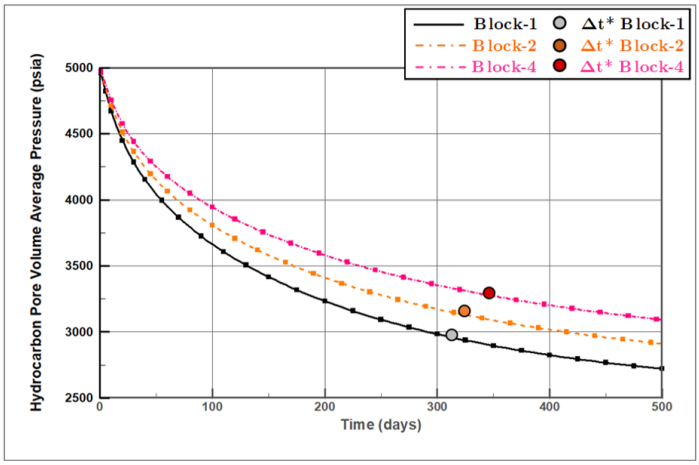

(a) Matrix pressure (P_m) profile

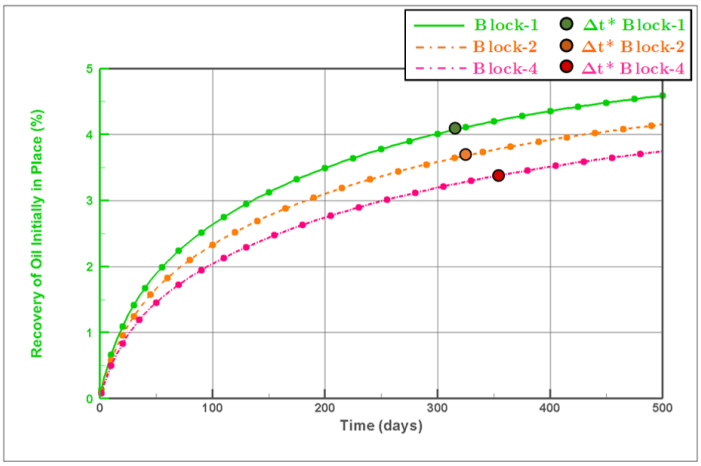

(b) Oil recovery factor profile

Figure B.81: Δt^* of single-porosity model for $\ell_x = 20$ ft and $k_m = 10$ nd.

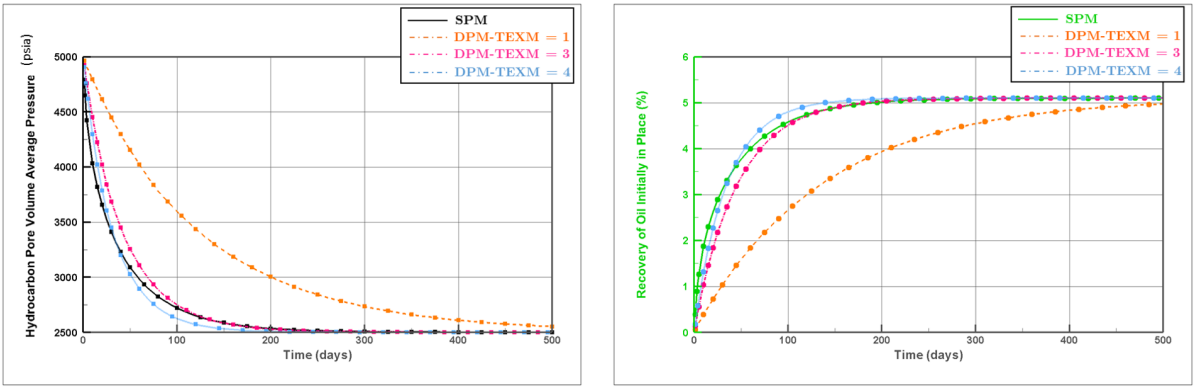

(a) Pressure profile **(b)** Oil recovery factor profile

Figure B.82: Dual-porosity performance profile corresponding to single-porosity by changing TEX multiplier for first block of $\ell_x = 20$ ft and $k_m = 50$ nd.

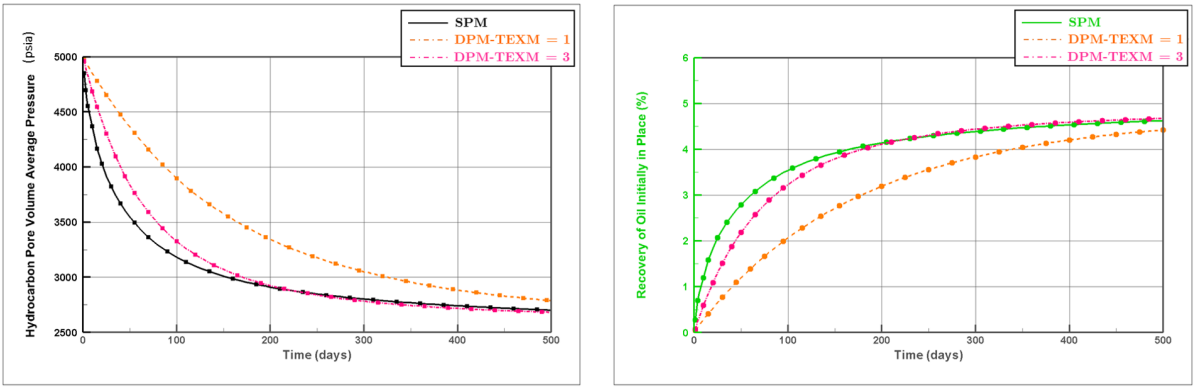

(a) Pressure profile **(b)** Oil recovery factor profile

Figure B.83: Dual-porosity performance profile corresponding to single-porosity by changing TEX multiplier for second block of $\ell_x = 20$ ft and $k_m = 50$ nd.

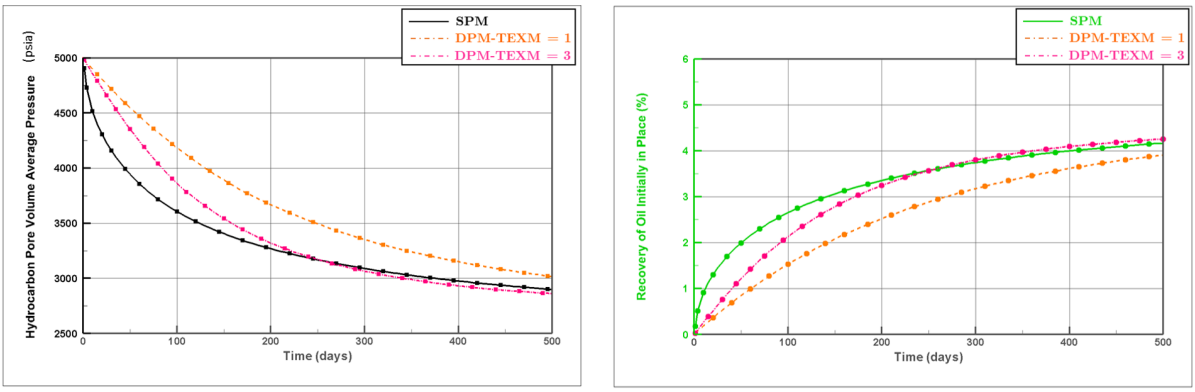

(a) Pressure profile **(b)** Oil recovery factor profile

Figure B.84: Dual-porosity performance profile corresponding to single-porosity by changing TEX multiplier for forth block of $\ell_x = 20$ ft and $k_m = 50$ nd.

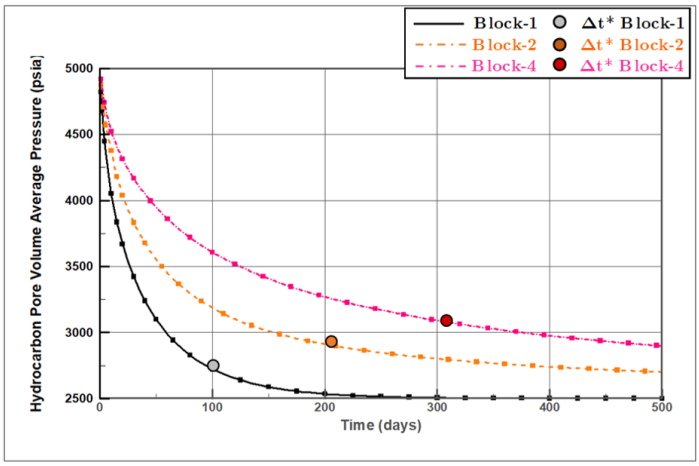

(a) Matrix pressure (P_m) profile

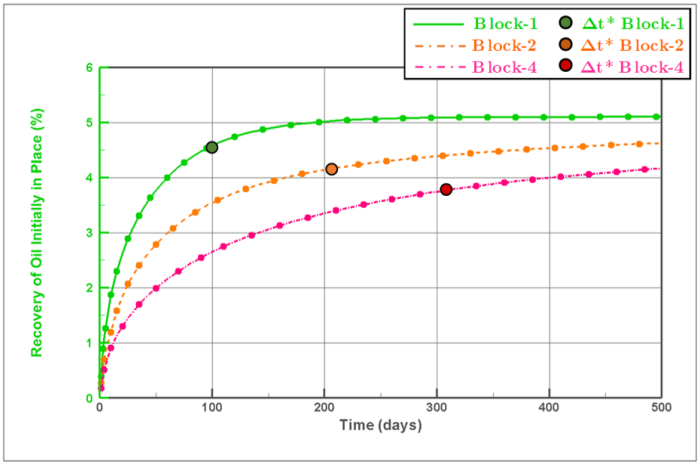

(b) Oil recovery factor profile

Figure B.85: Δt^* of single-porosity model for $\ell_x = 20$ ft and $k_m = 50$ nd.

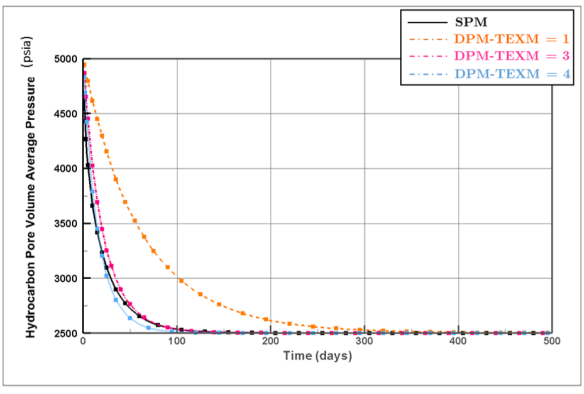

(a) Pressure profile

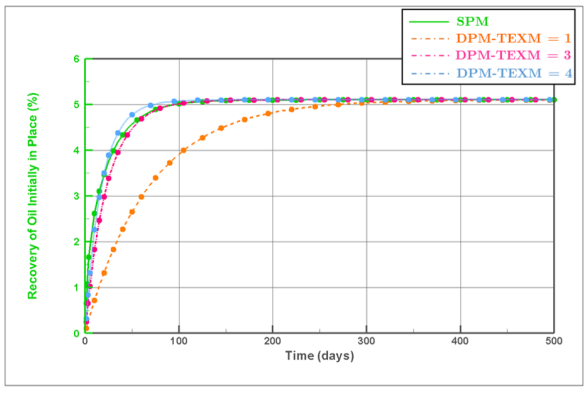

(b) Oil recovery factor profile

Figure B.86: Dual-porosity performance profile corresponding to single-porosity by changing TEX multiplier for first block of $\ell_x = 20$ ft and $k_m = 100$ nd.

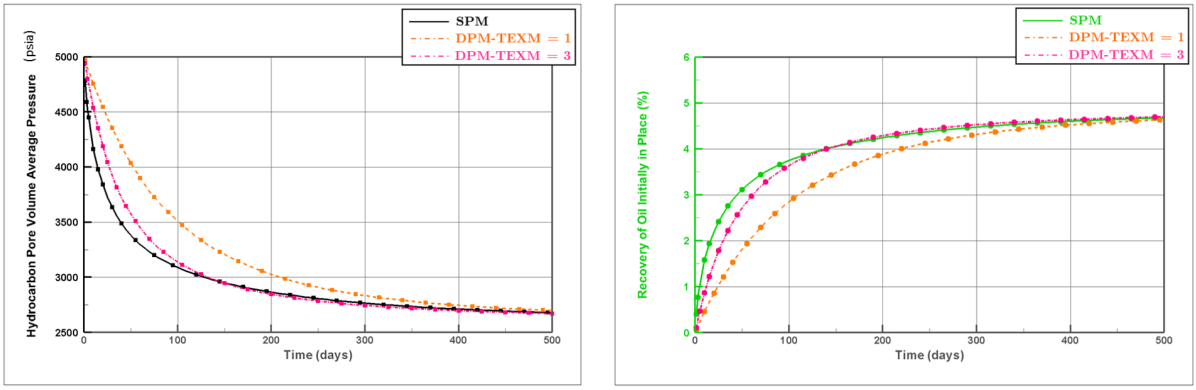

(a) Pressure profile **(b)** Oil recovery factor profile

Figure B.87: Dual-porosity performance profile corresponding to single-porosity by changing TEX multiplier for second block of $\ell_x = 20$ ft and $k_m = 100$ nd.

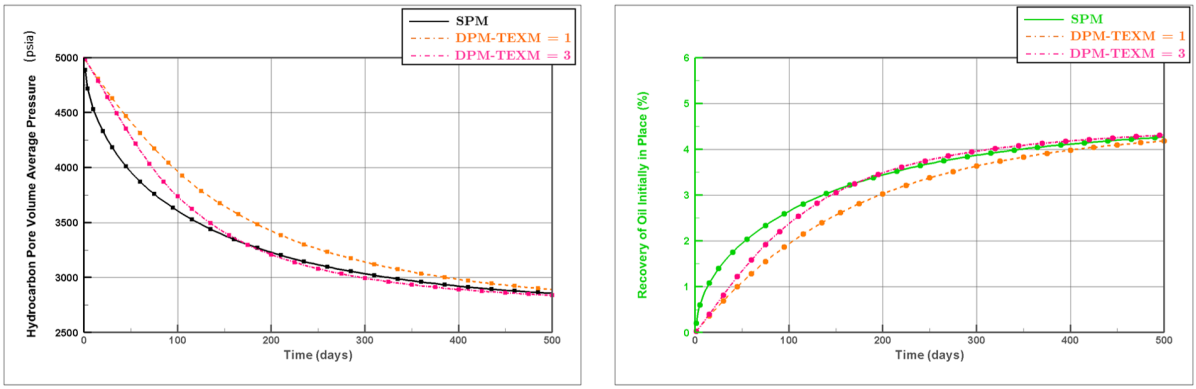

(a) Pressure profile **(b)** Oil recovery factor profile

Figure B.88: Dual-porosity performance profile corresponding to single-porosity by changing TEX multiplier for forth block of $\ell_x = 20$ ft and $k_m = 100$ nd.

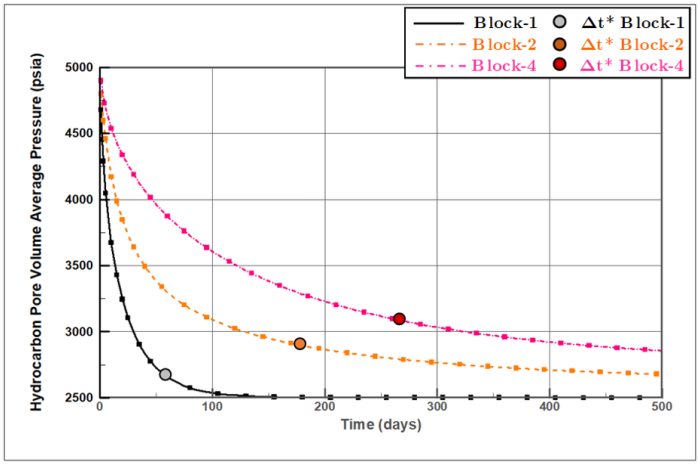

(a) Matrix pressure (P_m) profile

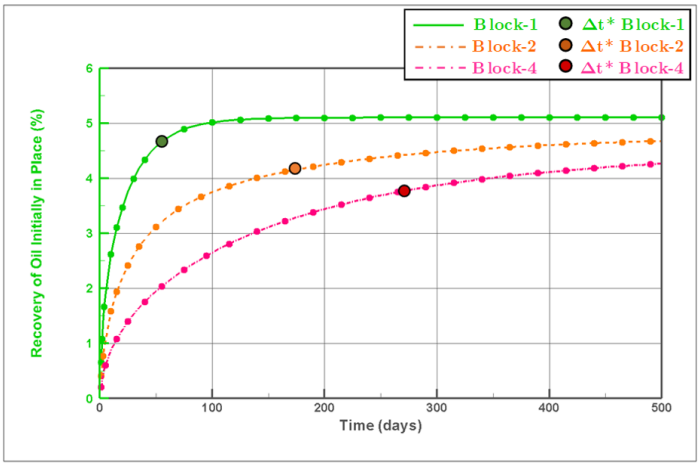

(b) Oil recovery factor profile

Figure B.89: Δt^* of single-porosity model for $\ell_x = 20$ ft and $k_m = 100$ nd.

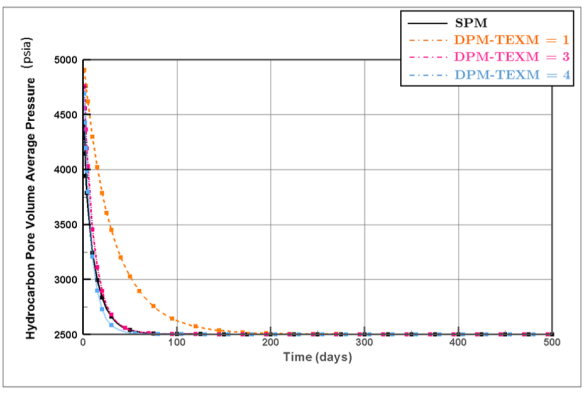

(a) Pressure profile

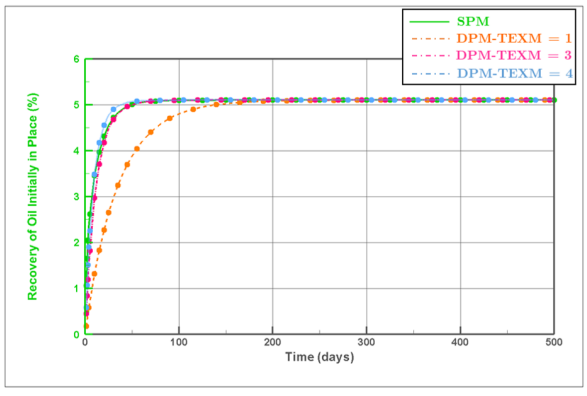

(b) Oil recovery factor profile

Figure B.90: Dual-porosity performance profile corresponding to single-porosity by changing TEX multiplier for first block of $\ell_x = 20$ ft and $k_m = 200$ nd.

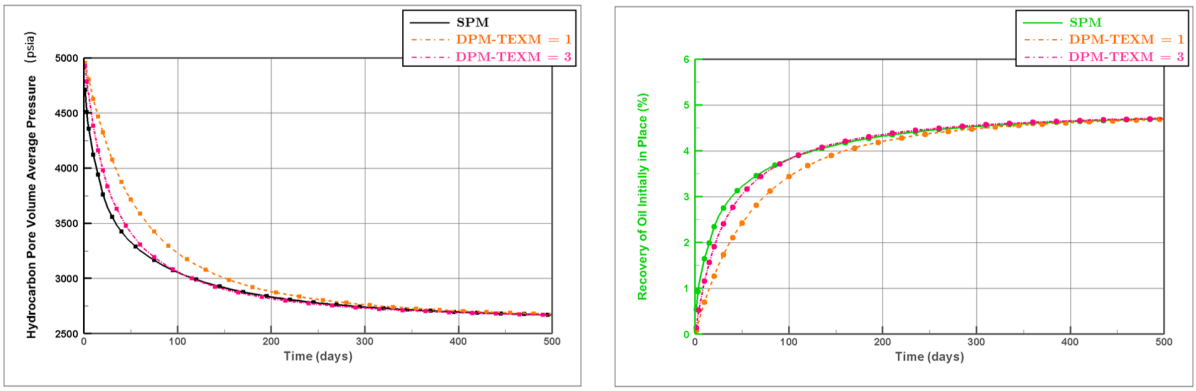

(a) Pressure profile **(b)** Oil recovery factor profile

Figure B.91: Dual-porosity performance profile corresponding to single-porosity by changing TEX multiplier for second block of $\ell_x = 20$ ft and $k_m = 200$ nd.

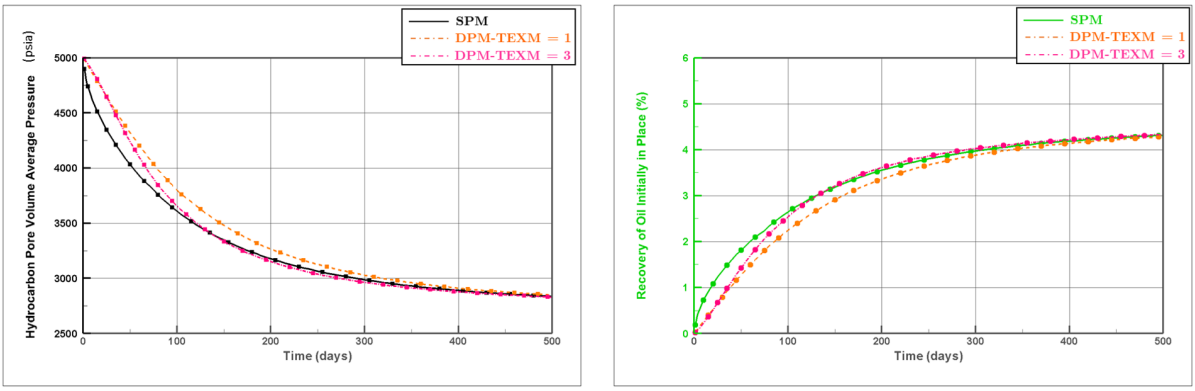

(a) Pressure profile **(b)** Oil recovery factor profile

Figure B.92: Dual-porosity performance profile corresponding to single-porosity by changing TEX multiplier for forth block of $\ell_x = 10$ ft and $k_m = 200$ nd.

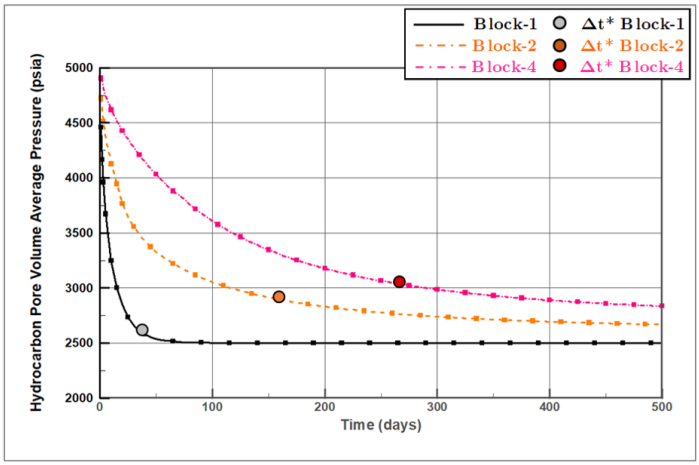

(a) Matrix pressure (P_m) profile

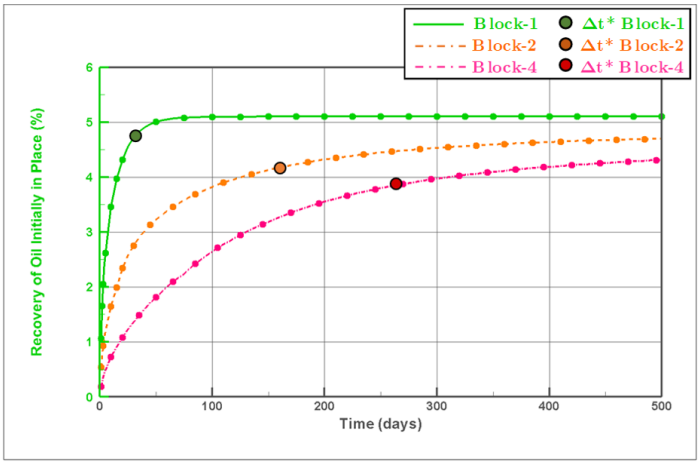

(b) Oil recovery factor profile

Figure B.93: Δt^* of single-porosity model for $\ell_x = 20$ ft and $k_m = 200$ nd.

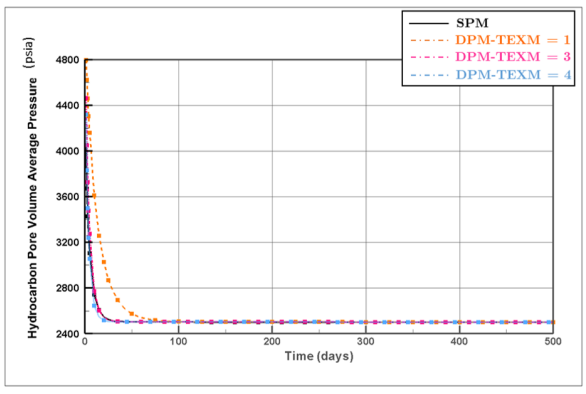

(a) Pressure profile

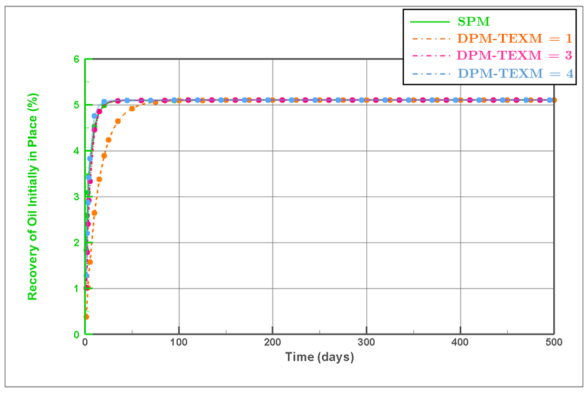

(b) Oil recovery factor profile

Figure B.94: Dual-porosity performance profile corresponding to single-porosity by changing TEX multiplier for first block of $\ell_x = 20$ ft and $k_m = 500$ nd.

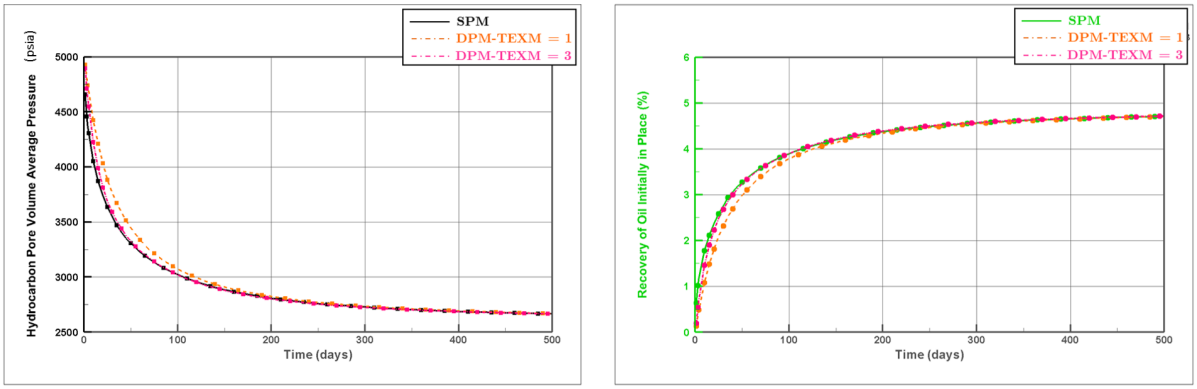

(a) Pressure profile **(b)** Oil recovery factor profile

Figure B.95: Dual-porosity performance profile corresponding to single-porosity by changing TEX multiplier for second block of $\ell_x = 20$ ft and $k_m = 500$ nd.

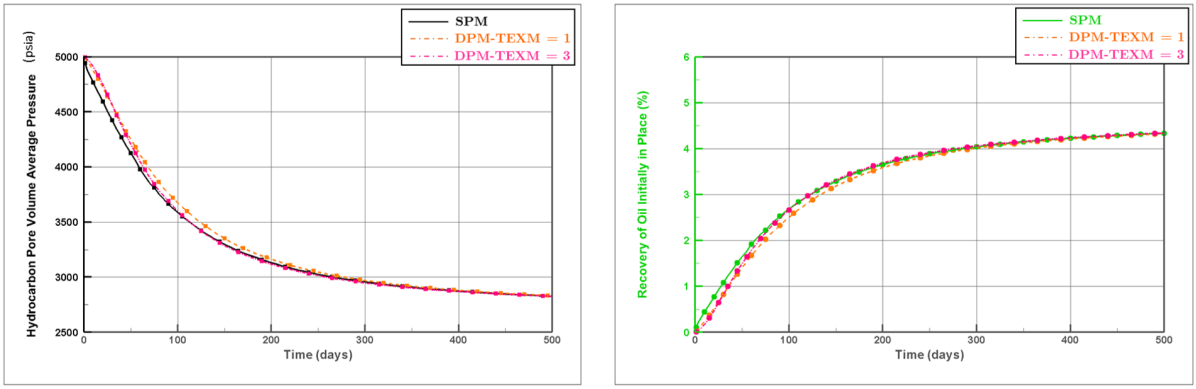

(a) Pressure profile **(b)** Oil recovery factor profile

Figure B.96: Dual-porosity performance profile corresponding to single-porosity by changing TEX multiplier for forth block of $\ell_x = 20$ ft and $k_m = 500$ nd.

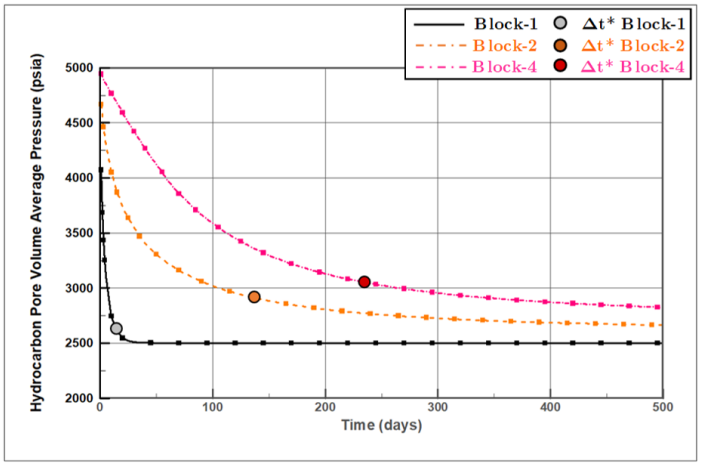

(a) Matrix pressure (P_m) profile

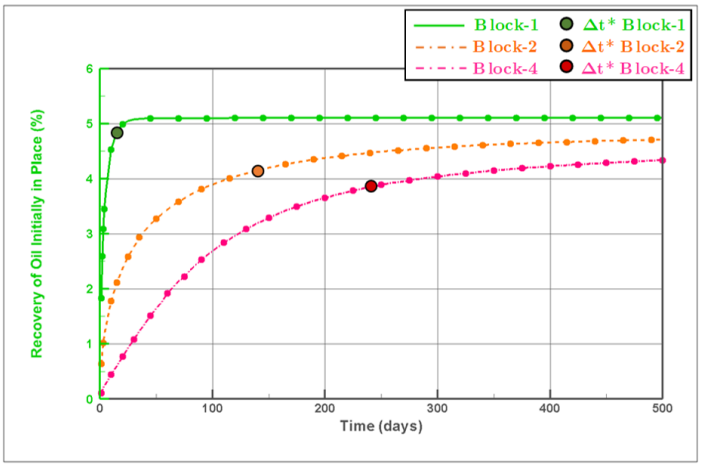

(b) Oil recovery factor profile

Figure B.97: Δt^* of single-porosity model for $\ell_x = 20$ ft and $k_m = 500$ nd.

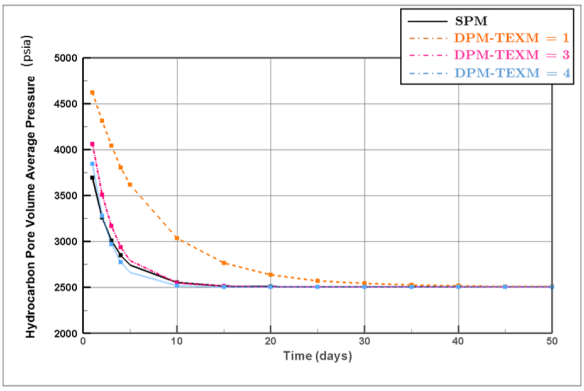

(a) Pressure profile

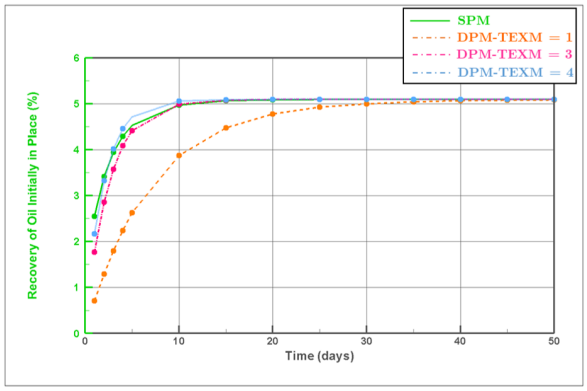

(b) Oil recovery factor profile

Figure B.98: Dual-porosity performance profile corresponding to single-porosity by changing TEX multiplier for first block of $\ell_x = 20$ ft and $k_m = 1000$ nd.

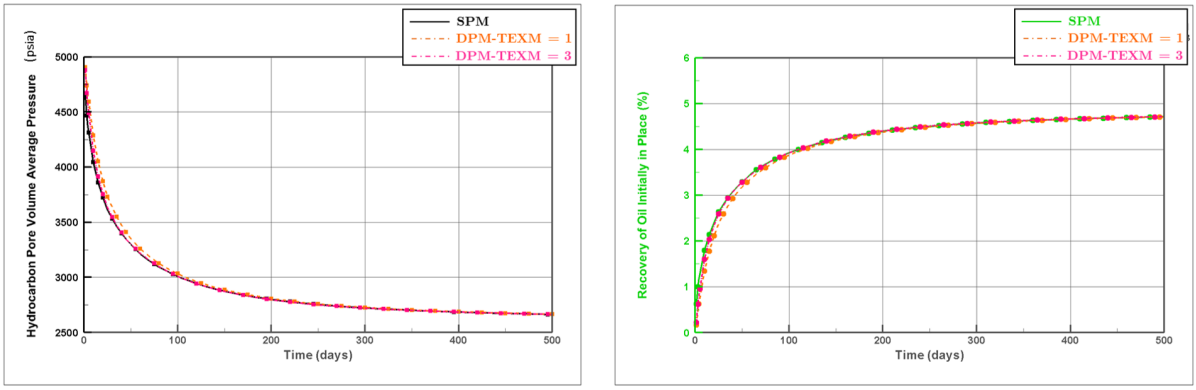

(a) Pressure profile **(b)** Oil recovery factor profile

Figure B.99: Dual-porosity performance profile corresponding to single-porosity by changing TEX multiplier for second block of $\ell_x = 20$ ft and $k_m = 1000$ nd.

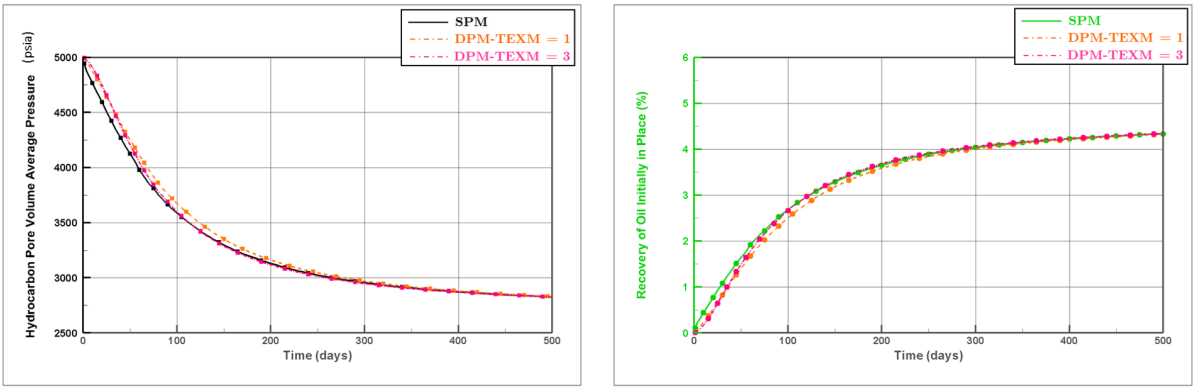

(a) Pressure profile **(b)** Oil recovery factor profile

Figure B.100: Dual-porosity performance profile corresponding to single-porosity by changing TEX multiplier for forth block of $\ell_x = 20$ ft and $k_m = 1000$ nd.

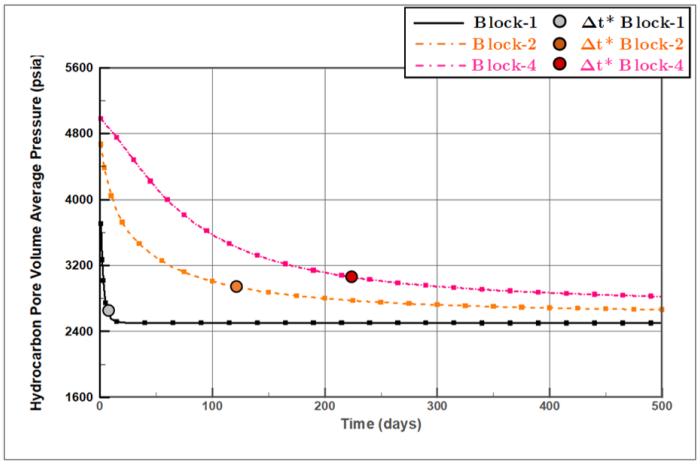

(a) Matrix pressure (P_m) profile

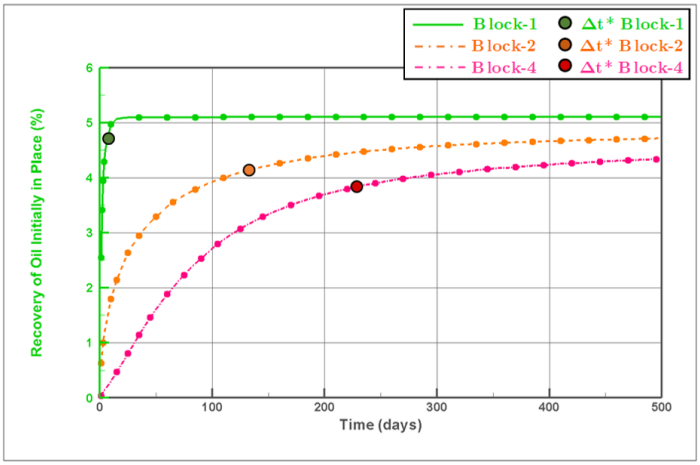

(b) Oil recovery factor profile

Figure B.101: Δt^* of single-porosity model for $\ell_x = 20$ ft and $k_m = 1000$ nd.

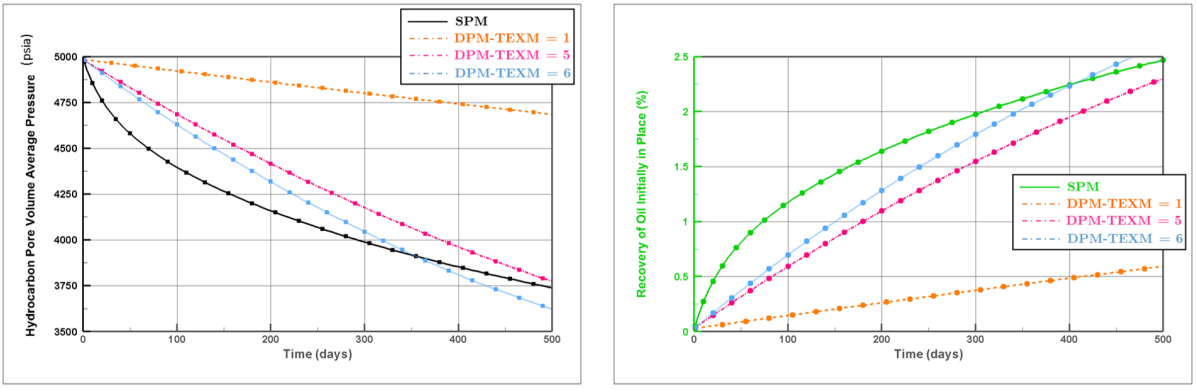

(a) Pressure profile **(b)** Oil recovery factor profile

Figure B.102: Dual-porosity performance profile corresponding to single-porosity by changing TEX multiplier for first block of $\ell_x = 50$ ft and $k_m = 10$ nd.

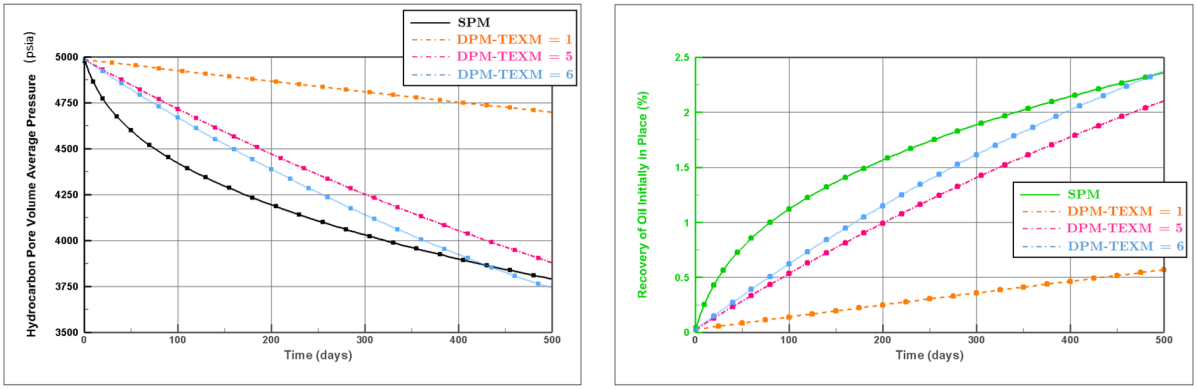

(a) Pressure profile **(b)** Oil recovery factor profile

Figure B.103: Dual-porosity performance profile corresponding to single-porosity by changing TEX multiplier for second block of $\ell_x = 50$ ft and $k_m = 10$ nd.

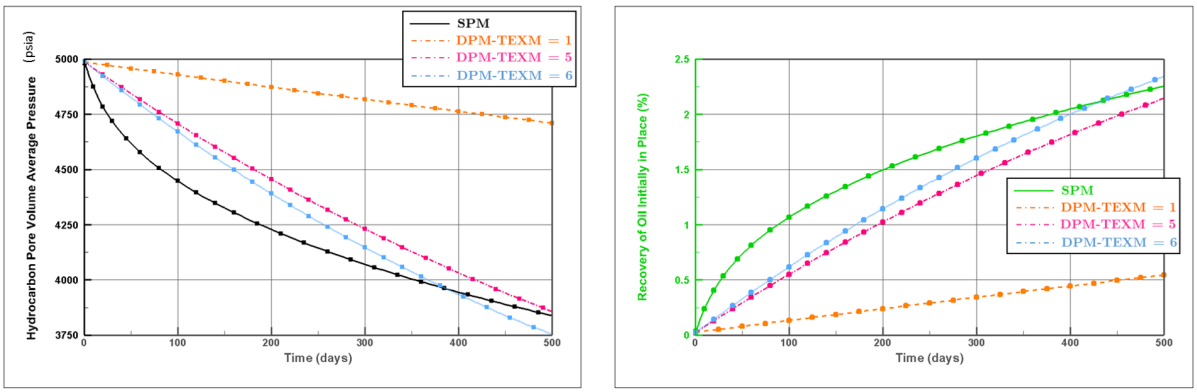

(a) Pressure profile **(b)** Oil recovery factor profile

Figure B.104: Dual-porosity performance profile corresponding to single-porosity by changing TEX multiplier for forth block of $\ell_x = 50$ ft and $k_m = 10$ nd.

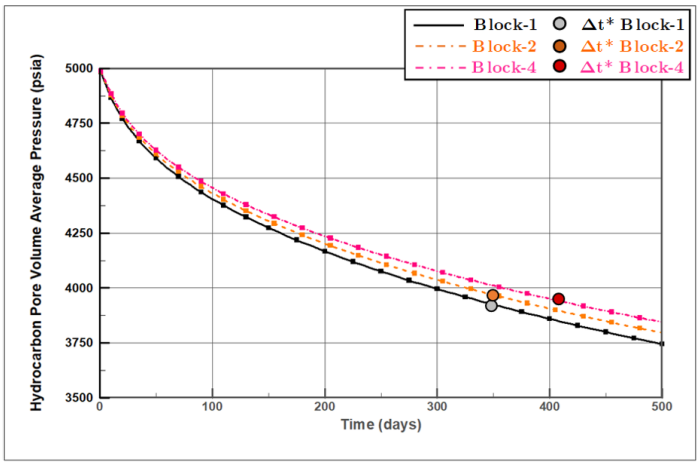

(a) Matrix pressure (P_m) profile

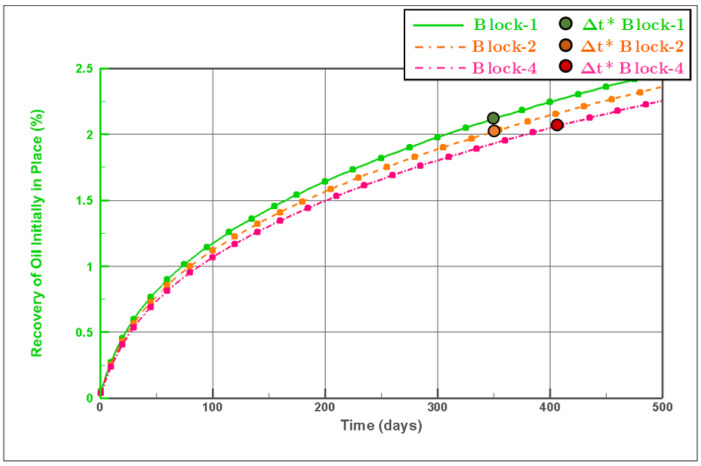

(b) Oil recovery factor profile

Figure B.105: Δt^* of single-porosity model for $\ell_x = 50$ ft and $k_m = 10$ nd.

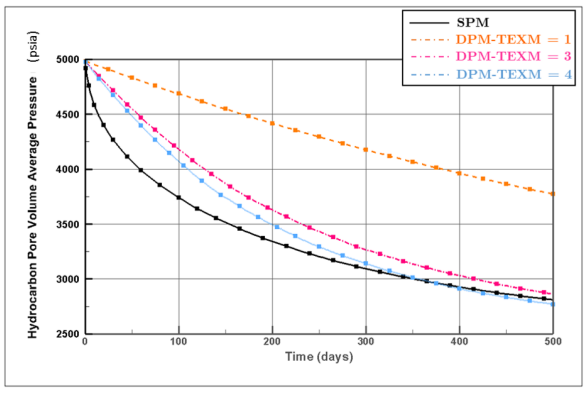

(a) Pressure profile

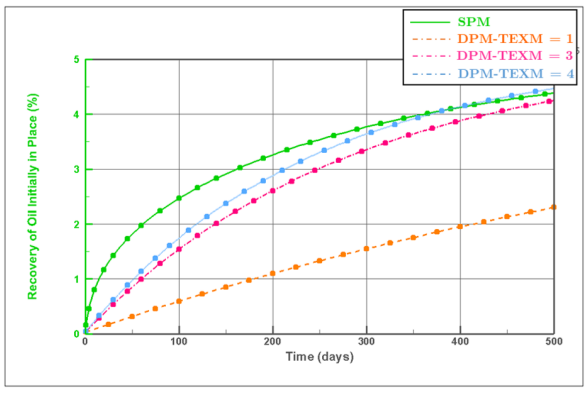

(b) Oil recovery factor profile

Figure B.106: Dual-porosity performance profile corresponding to single-porosity by changing TEX multiplier for first block of $\ell_x = 50$ ft and $k_m = 50$ nd.

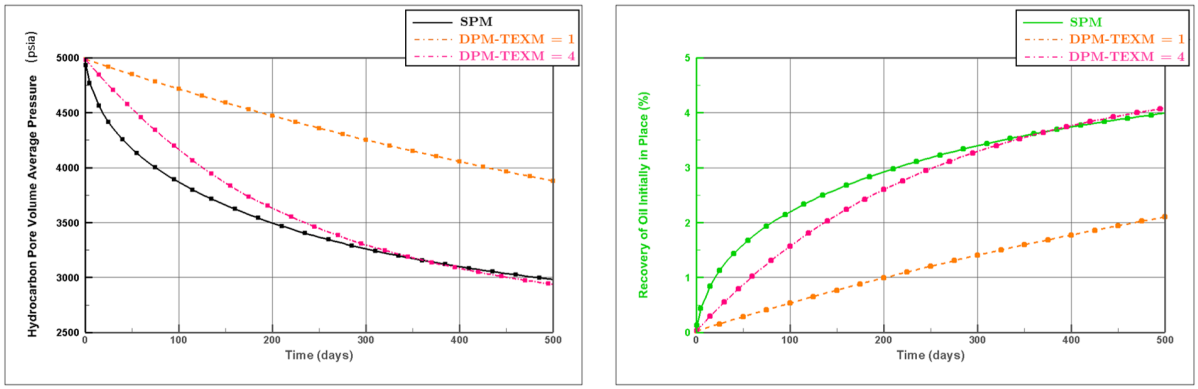

(a) Pressure profile **(b)** Oil recovery factor profile

Figure B.107: Dual-porosity performance profile corresponding to single-porosity by changing TEX multiplier for second block of $\ell_x = 50$ ft and $k_m = 50$ nd.

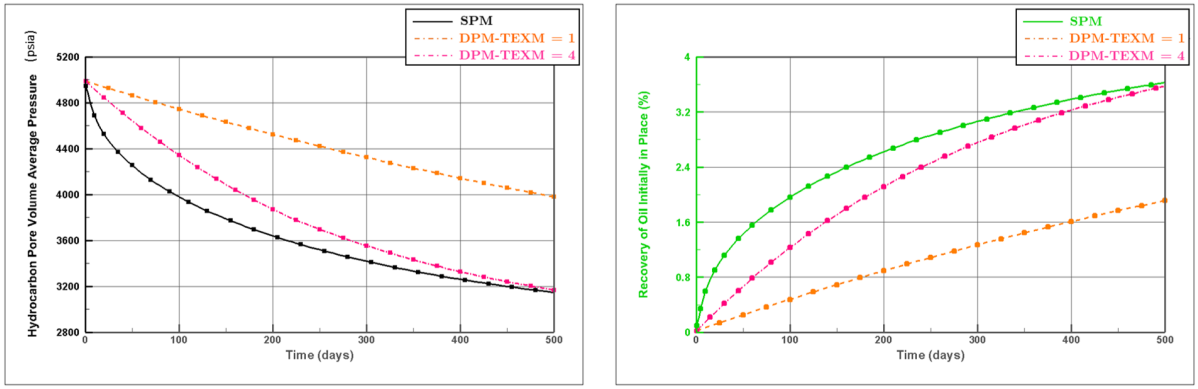

(a) Pressure profile **(b)** Oil recovery factor profile

Figure B.108: Dual-porosity performance profile corresponding to single-porosity by changing TEX multiplier for forth block of $\ell_x = 50$ ft and $k_m = 50$ nd.

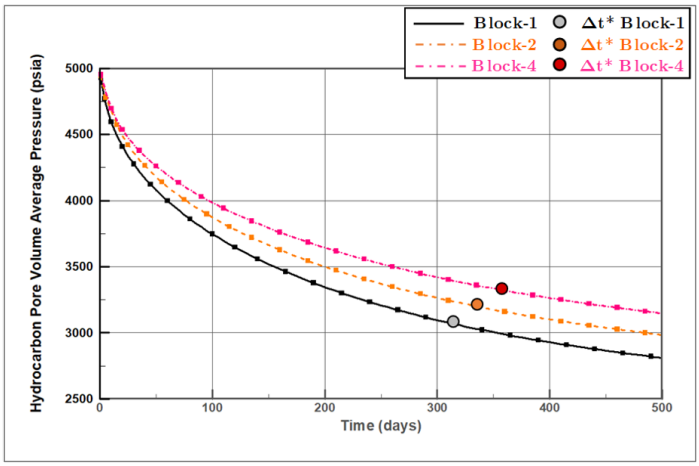

(a) Matrix pressure (P_m) profile

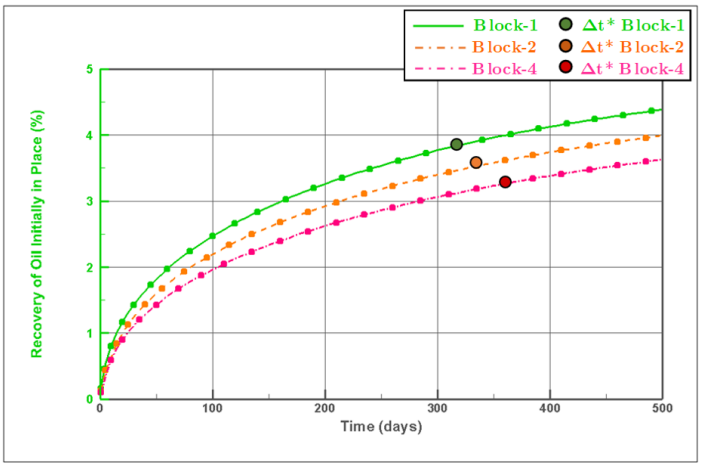

(b) Oil recovery factor profile

Figure B.109: Δt^* of single-porosity model for $\ell_x = 50$ ft and $k_m = 50$ nd.

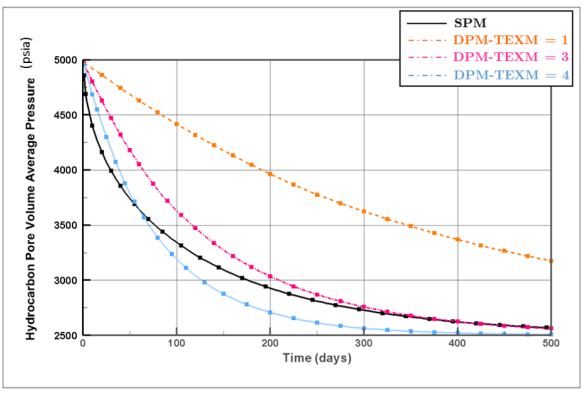

(a) Pressure profile

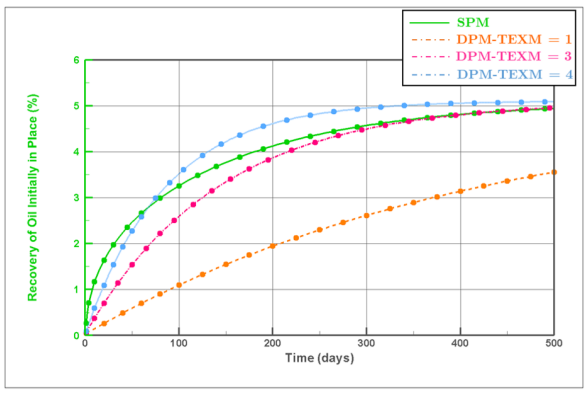

(b) Oil recovery factor profile

Figure B.110: Dual-porosity performance profile corresponding to single-porosity by changing TEX multiplier for first block of $\ell_x = 50$ ft and $k_m = 100$ nd.

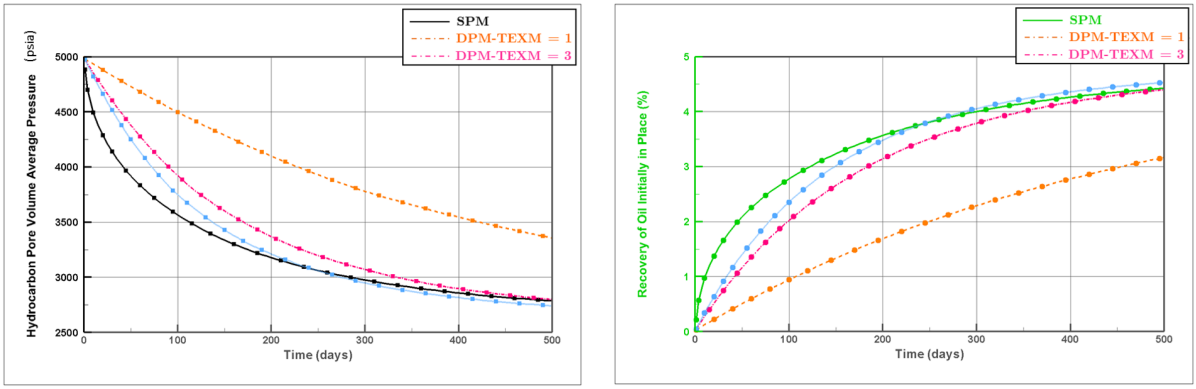

(a) Pressure profile **(b)** Oil recovery factor profile

Figure B.111: Dual-porosity performance profile corresponding to single-porosity by changing TEX multiplier for second block of $\ell_x = 50$ ft and $k_m = 100$ nd.

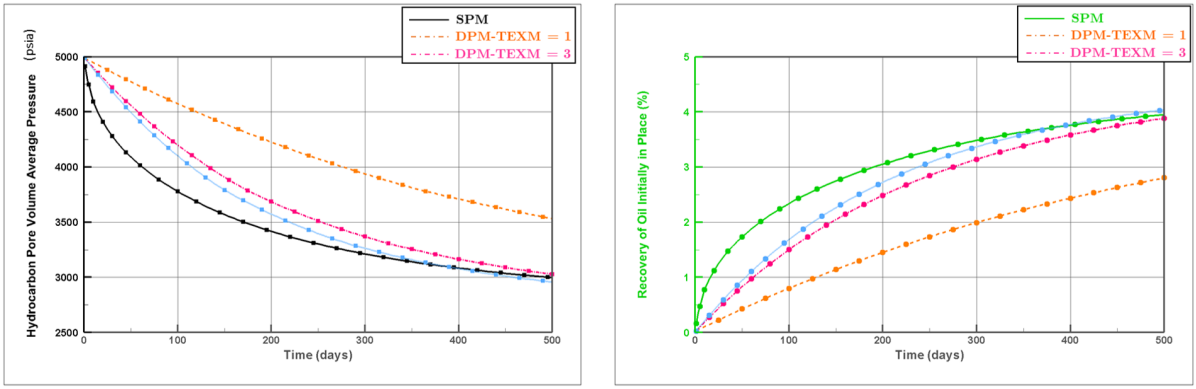

(a) Pressure profile **(b)** Oil recovery factor profile

Figure B.112: Dual-porosity performance profile corresponding to single-porosity by changing TEX multiplier for forth block of $\ell_x = 50$ ft and $k_m = 100$ nd.

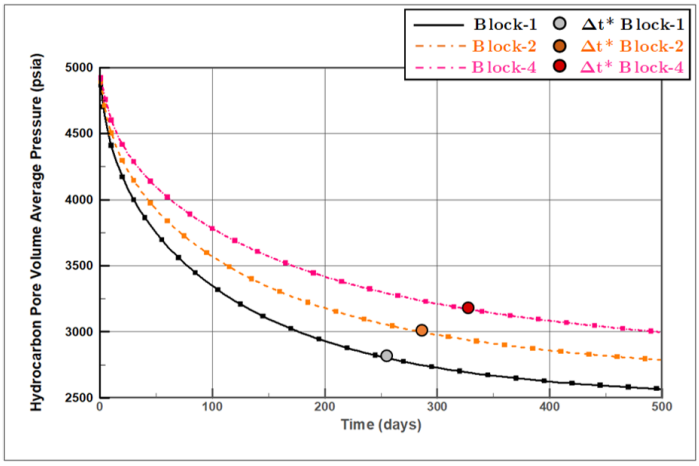

(a) Matrix pressure (P_m) profile

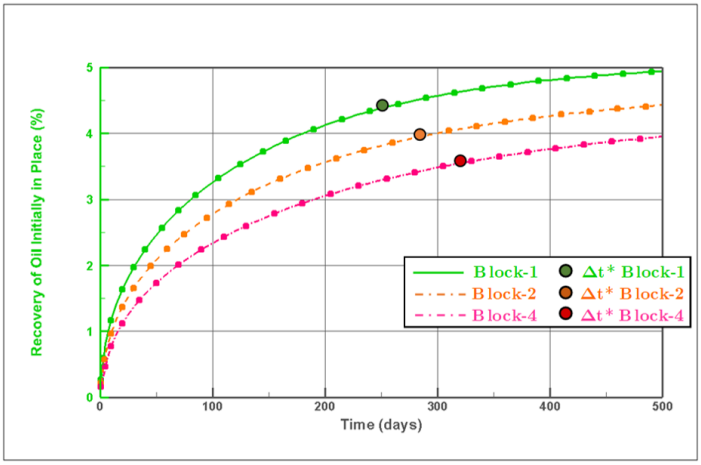

(b) Oil recovery factor profile

Figure B.113: Δt^* of single-porosity model for $\ell_x = 50$ ft and $k_m = 100$ nd.

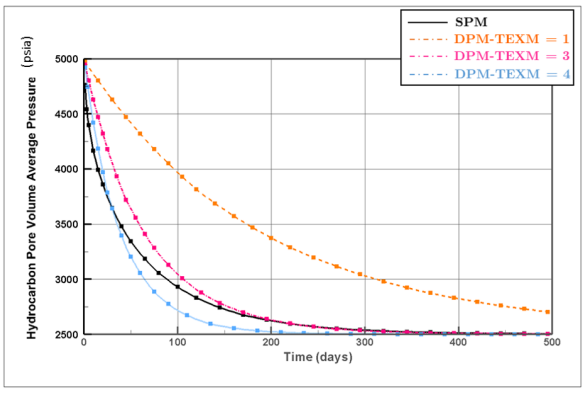

(a) Pressure profile

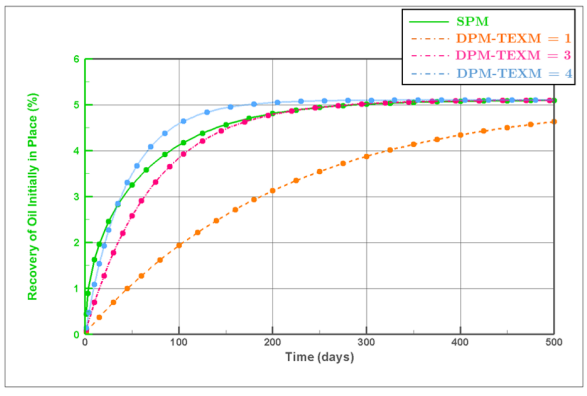

(b) Oil recovery factor profile

Figure B.114: Dual-porosity performance profile corresponding to single-porosity by changing TEX multiplier for first block of $\ell_x = 50$ ft and $k_m = 200$ nd.

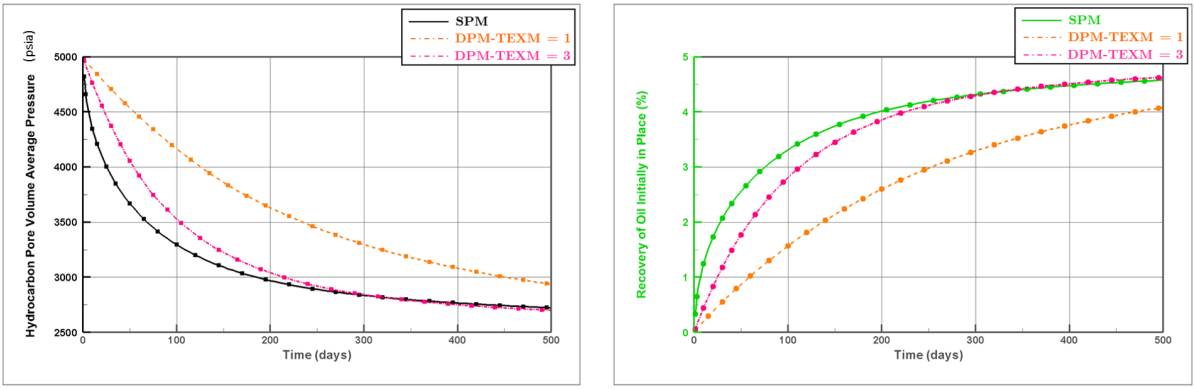

(a) Pressure profile **(b)** Oil recovery factor profile

Figure B.115: Dual-porosity performance profile corresponding to single-porosity by changing TEX multiplier for second block of $\ell_x = 50$ ft and $k_m = 200$ nd.

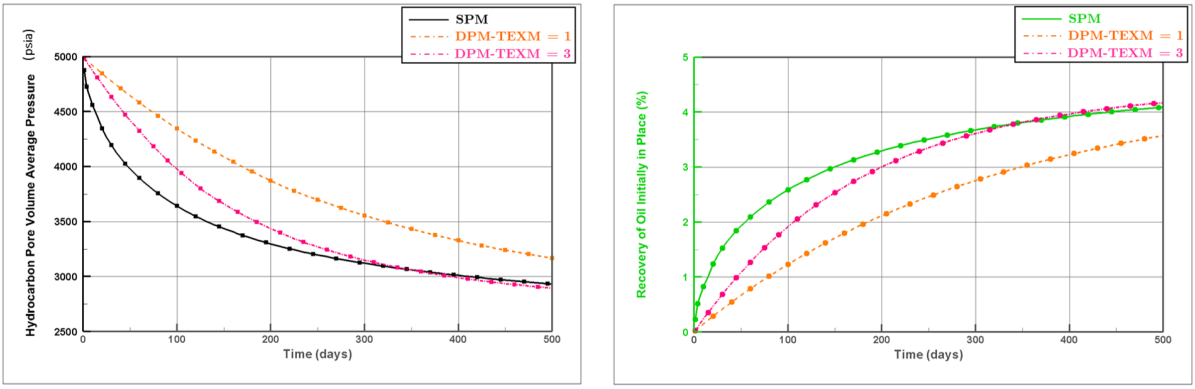

(a) Pressure profile **(b)** Oil recovery factor profile

Figure B.116: Dual-porosity performance profile corresponding to single-porosity by changing TEX multiplier for forth block of $\ell_x = 50$ ft and $k_m = 200$ nd.

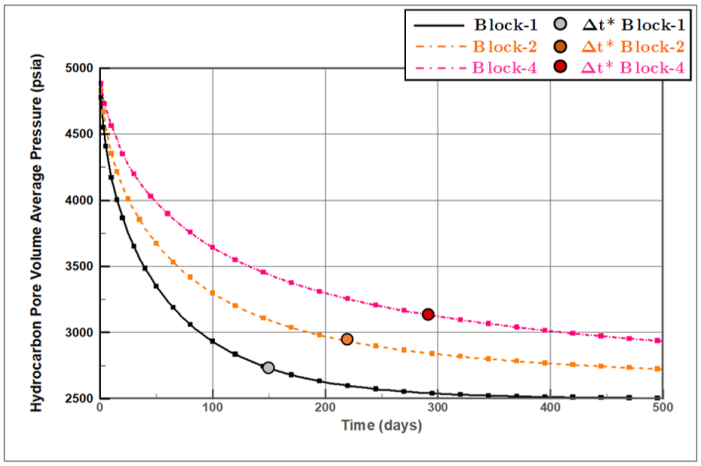

(a) Matrix pressure (P_m) profile

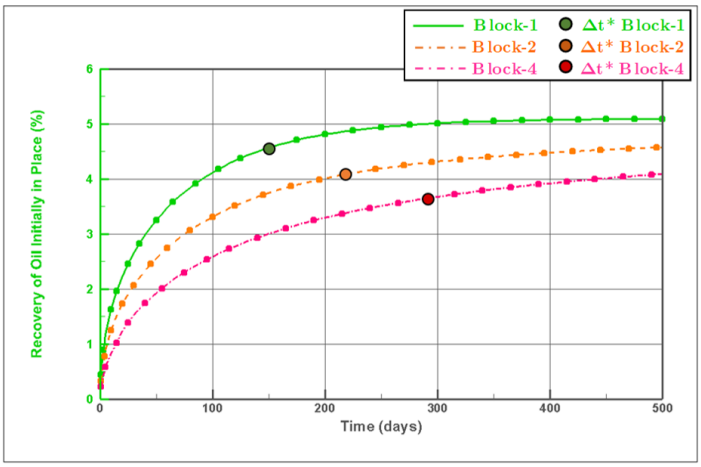

(b) Oil recovery factor profile

Figure B.117: Δt^* of single-porosity model for $\ell_x = 50$ ft and $k_m = 200$ nd.

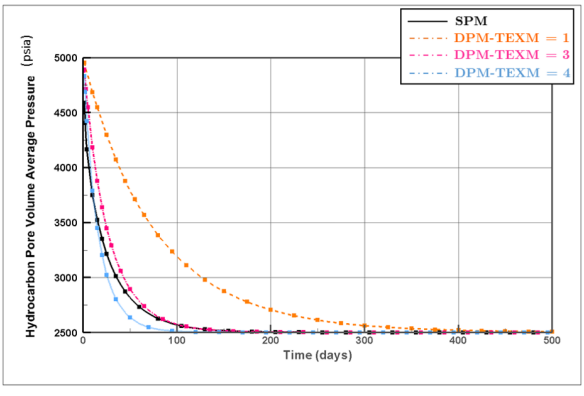

(a) Pressure profile

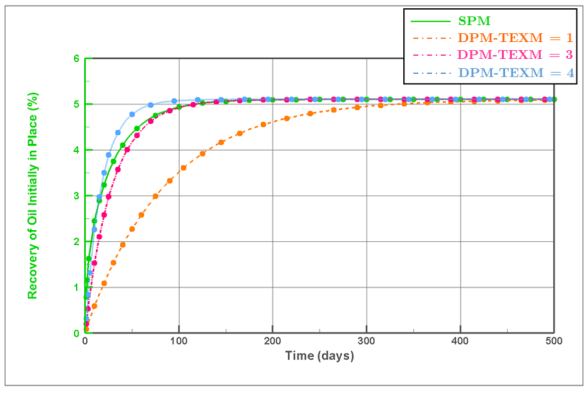

(b) Oil recovery factor profile

Figure B.118: Dual-porosity performance profile corresponding to single-porosity by changing TEX multiplier for first block of $\ell_x = 50$ ft and $k_m = 500$ nd.

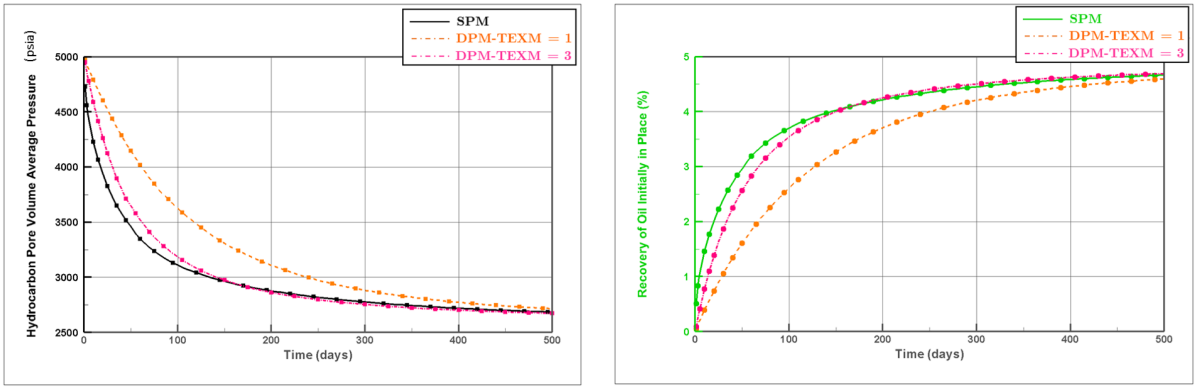

(a) Pressure profile **(b)** Oil recovery factor profile

Figure B.119: Dual-porosity performance profile corresponding to single-porosity by changing TEX multiplier for second block of $\ell_x = 50$ ft and $k_m = 500$ nd.

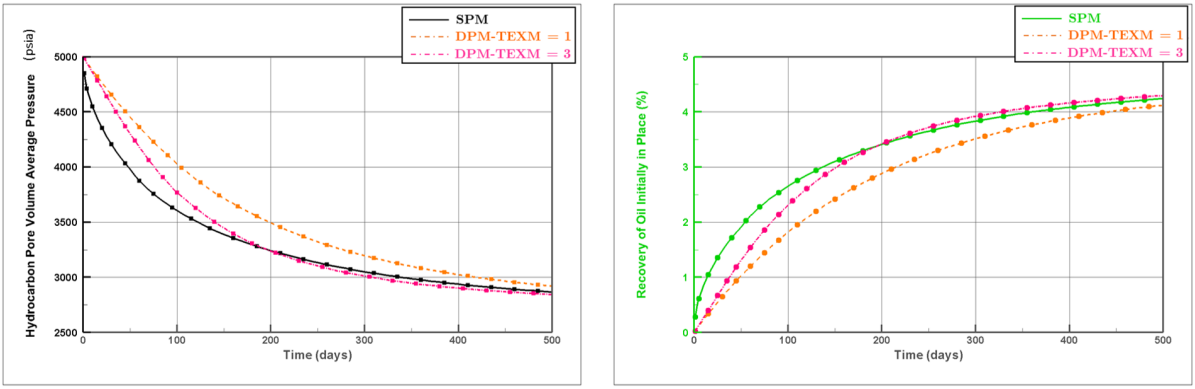

(a) Pressure profile **(b)** Oil recovery factor profile

Figure B.120: Dual-porosity performance profile corresponding to single-porosity by changing TEX multiplier for forth block of $\ell_x = 50$ ft and $k_m = 500$ nd.

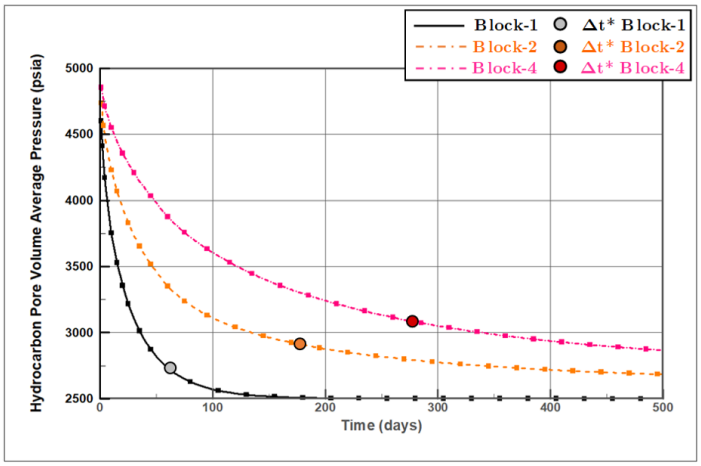

(a) Matrix pressure (P_m) profile

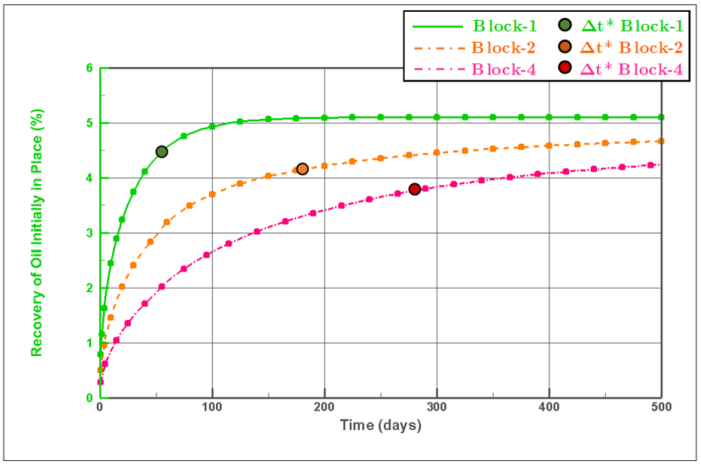

(b) Oil recovery factor profile

Figure B.121: Δt^* of single-porosity model for $\ell_x = 50$ ft and $k_m = 500$ nd.

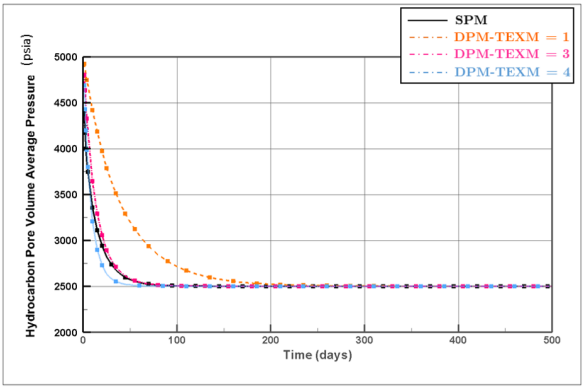

(a) Pressure profile

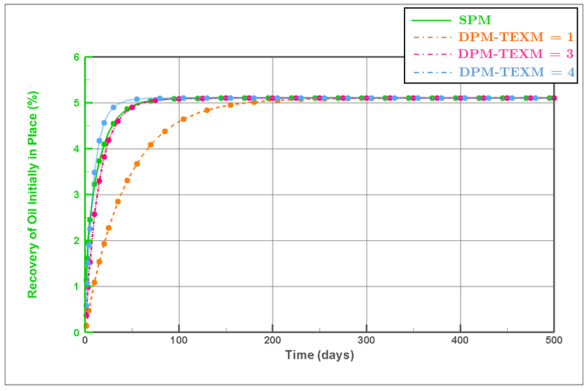

(b) Oil recovery factor profile

Figure B.122: Dual-porosity performance profile corresponding to single-porosity by changing TEX multiplier for first block of $\ell_x = 50$ ft and $k_m = 1000$ nd.

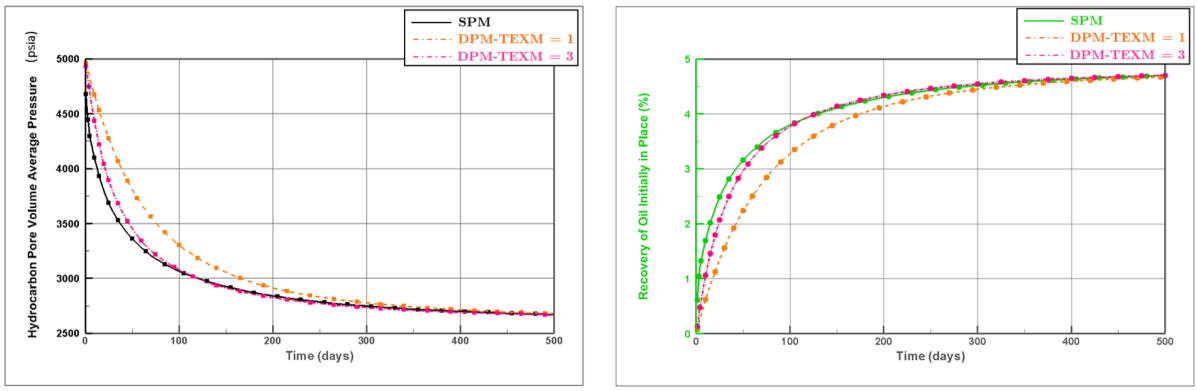

(a) Pressure profile **(b)** Oil recovery factor profile

Figure B.123: Dual-porosity performance profile corresponding to single-porosity by changing TEX multiplier for second block of $\ell_x = 50$ ft and $k_m = 1000$ nd.

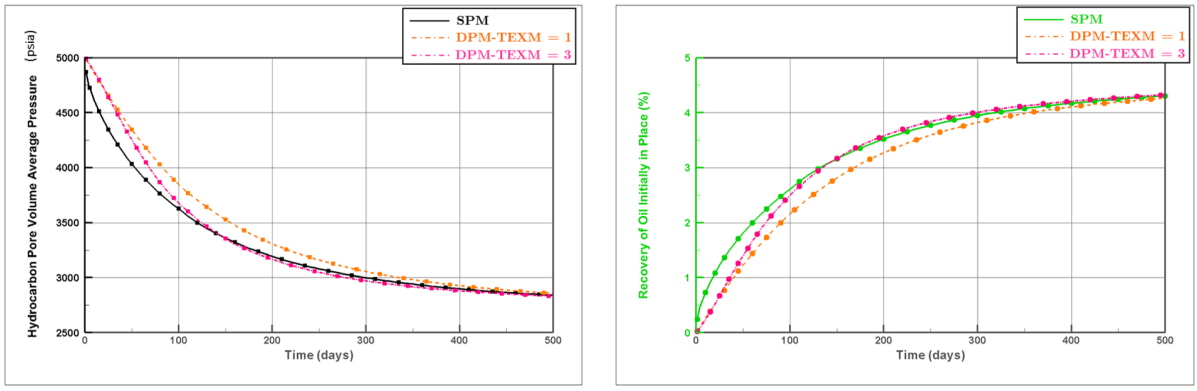

(a) Pressure profile **(b)** Oil recovery factor profile

Figure B.124: Dual-porosity performance profile corresponding to single-porosity by changing TEX multiplier for forth block of $\ell_x = 50$ ft and $k_m = 1000$ nd.

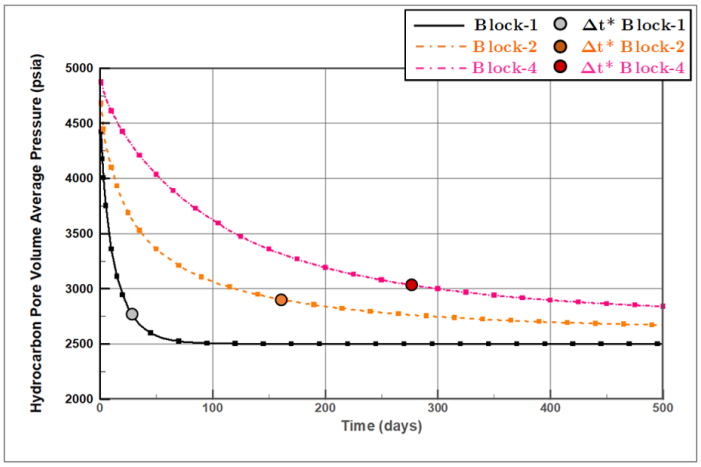

(a) Matrix pressure (P_m) profile

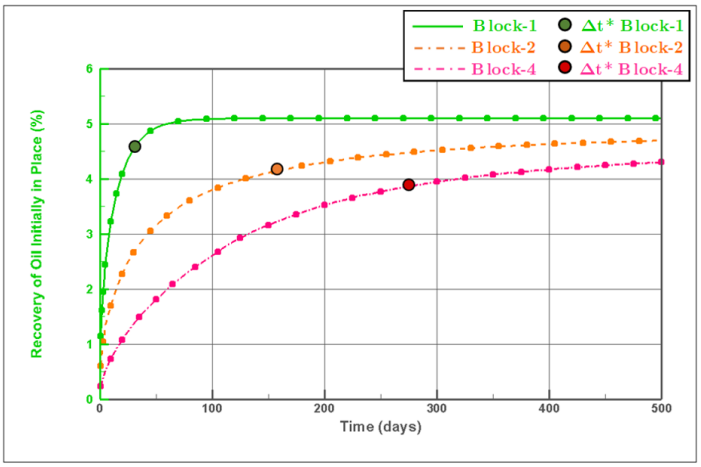

(b) Oil recovery factor profile

Figure B.125: Δt^* of single-porosity model for $\ell_x = 50$ ft and $k_m = 1000$ nd.

Table B.1: SPM vs DPM Comparison Summary of Depletion Phase - $\ell_x = 1$ ft $\ell_x = 5$ ft

$\ell_x = 1$ ft					$\ell_x = 5$ ft				
K_m (nd)	Block	$\Delta t*$ (days)	TEXM	TEX $\left(\frac{rb-cp}{d-psi}\right)$	K_m (nd)	Block	$\Delta t*$ (days)	TEXM	TEX $\left(\frac{rb-cp}{d-psi}\right)$
10	1	2	3	1.1E-1	10	1	35	3	4.3E-3
	2	150	1	3.6E-2		2	165	3	4.3E-3
	4	220	1	3.6E-2		4	280	3	4.3E-3
50	1	0	1	1.8E-1	50	1	10	3	2.2E-2
	2	150	1	1.8E-1		2	145	3	2.2E-2
	4	220	1	1.8E-1		4	240	3	2.2E-2
100	1	0	1	3.6E-1	100	1	4	3	4.3E-2
	2	150	1	3.6E-1		2	140	3	4.3E-2
	4	220	1	3.6E-1		4	235	3	4.3E-2
200	1	0	1	7.2E-1	200	1	3	3	8.6E-2
	2	150	1	7.2E-1		2	140	3	8.6E-2
	4	220	1	7.2E-1		4	235	3	8.6E-2
500	1	0	1	1.8E0	500	1	1	3	2.2E-1
	2	150	1	1.8E0		2	140	1	7.2E-2
	4	220	1	1.8E0		4	235	1	7.2E-2
1000	1	0	1	3.6E0	1000	1	1	3	4.3E-1
	2	150	1	3.6E0		2	140	1	1.4E-1
	4	220	1	3.6E0		4	235	1	1.4E-1

Table B.2: SPM vs DPM Comparison Summary of Depletion Phase - $\ell_x = 10$ ft $\ell_x = 20$ ft

$\ell_x = 10$ ft					$\ell_x = 20$ ft				
K_m (nd)	Block	$\Delta t*$ (days)	TEXM	TEX $\left(\frac{rb-cp}{d-psi}\right)$	K_m (nd)	Block	$\Delta t*$ (days)	TEXM	TEX $\left(\frac{rb-cp}{d-psi}\right)$
10	1	125	3	1.1E-3	10	1	315	3	2.7E-4
	2	195	3	1.1E-3		2	320	4	3.6E-4
	4	290	3	1.1E-3		4	350	4	3.6E-4
50	1	25	3	5.4E-3	50	1	100	3	1.4E-3
	2	160	3	5.4E-3		2	205	3	1.4E-3
	4	270	3	5.4E-3		4	305	3	1.4E-3
100	1	15	3	1.1E-2	100	1	50	3	2.7E-3
	2	145	3	1.1E-2		2	175	3	2.7E-3
	4	250	3	1.1E-2		4	270	3	2.7E-3
200	1	10	3	2.2E-2	200	1	25	3	5.4E-3
	2	140	3	2.2E-2		2	160	3	5.4E-3
	4	240	3	2.2E-2		4	265	3	5.4E-3
500	1	3	3	5.4E-2	500	1	10	3	1.4E-2
	2	135	3	5.4E-2		2	145	3	1.4E-2
	4	235	3	5.4E-2		4	245	3	1.4E-2
1000	1	2	3	1.1E-1	1000	1	5	3	2.7E-2
	2	135	1	3.6E-2		2	140	3	2.7E-2
	4	230	1	3.6E-2		4	235	3	2.7E-2

Table B.3: SPM vs DPM Comparison Summary of Depletion Phase - $\ell_x = 50$ ft

$\ell_x = 50$ ft				
K_m (nd)	Block	$\Delta t*$ (days)	TEXM	TEX $\left(\frac{rb-cp}{d-psi}\right)$
10	1	370	5	7.2E-5
	2	365	6	8.7E-5
	4	405	6	8.7E-5
50	1	325	3	2.5E-4
	2	345	4	2.9E-4
	4	360	4	2.9E-4
100	1	250	3	4.3E-4
	2	290	3	4.3E-4
	4	325	3	4.3E-4
200	1	150	3	8.6E-4
	2	210	3	8.6E-4
	4	295	3	8.6E-4
500	1	60	3	2.2E-3
	2	185	3	2.2E-3
	4	280	3	2.2E-3
1000	1	35	3	4.3E-3
	2	160	3	4.3E-3
	4	275	3	4.3E-3

Appendix C

Huff-n-Puff Gas EOR Performance Results

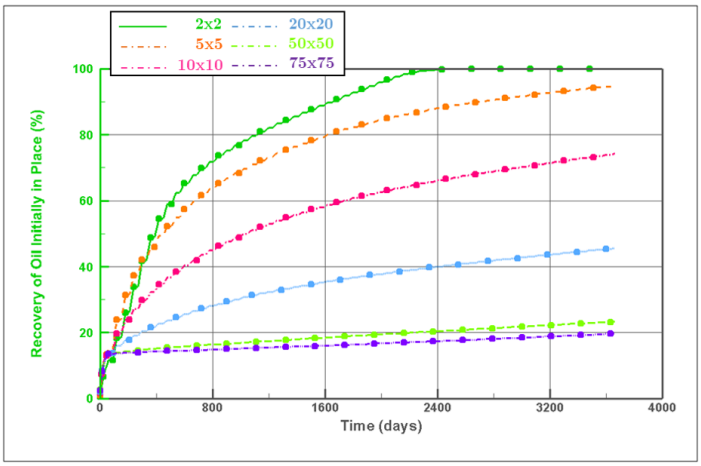

(a) Oil recovery factor profile

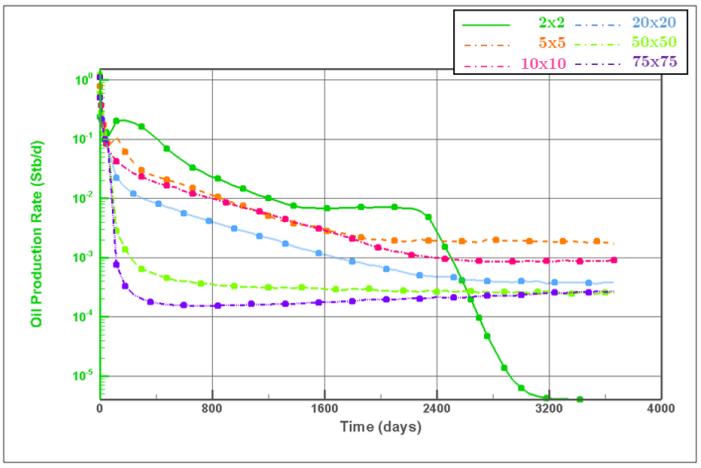

(b) Oil production rate profile

Figure C.1: Matrix block number sensitivity of injection performance with black oil simulation

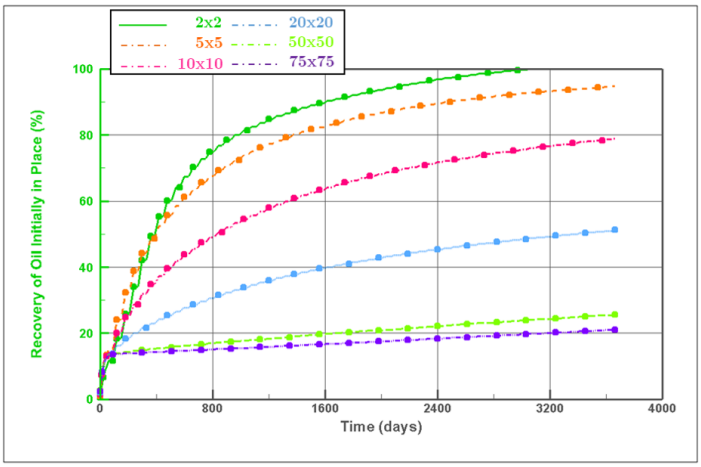

(a) Oil recovery factor profile

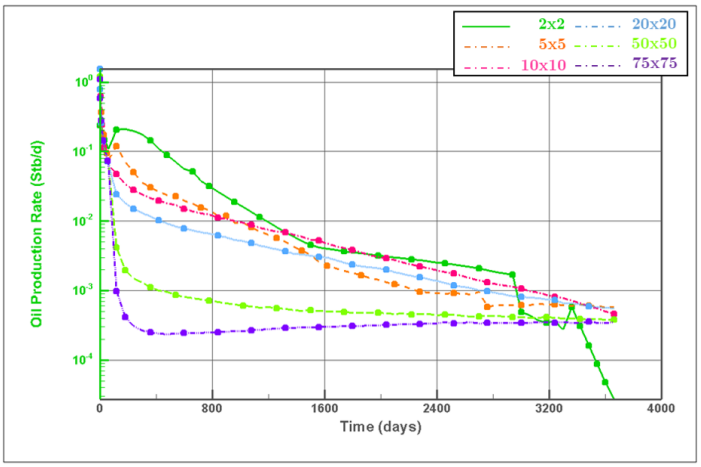

(b) Oil production rate profile

Figure C.2: Matrix block number sensitivity of injection performance with EOS simulation

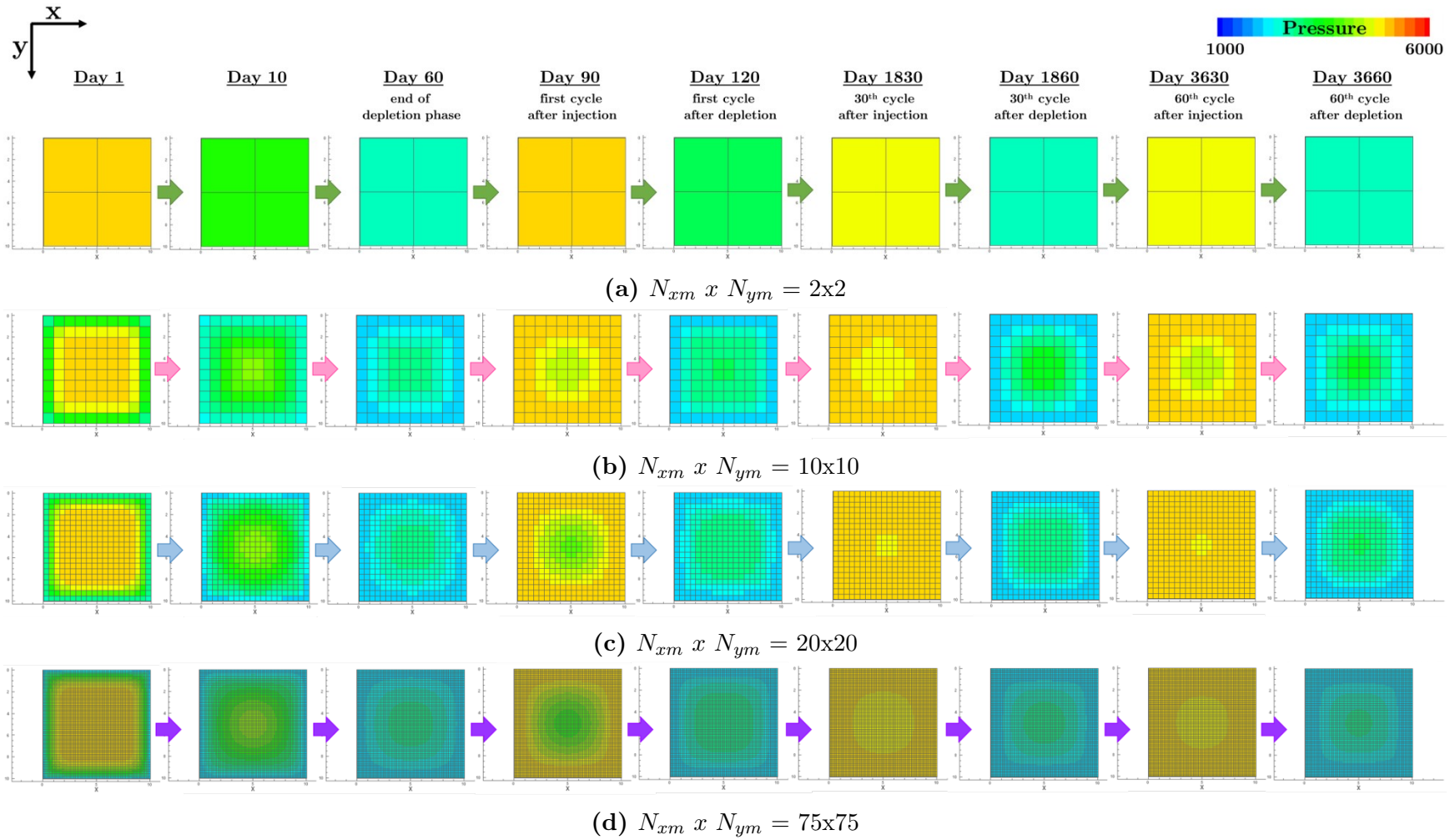

(a) N_{xm} x N_{ym} = 2x2

(b) N_{xm} x N_{ym} = 10x10

(c) N_{xm} x N_{ym} = 20x20

(d) N_{xm} x N_{ym} = 75x75

Figure C.3: Matrix block number sensitivity with black oil simulation - Pressure response in 2D.

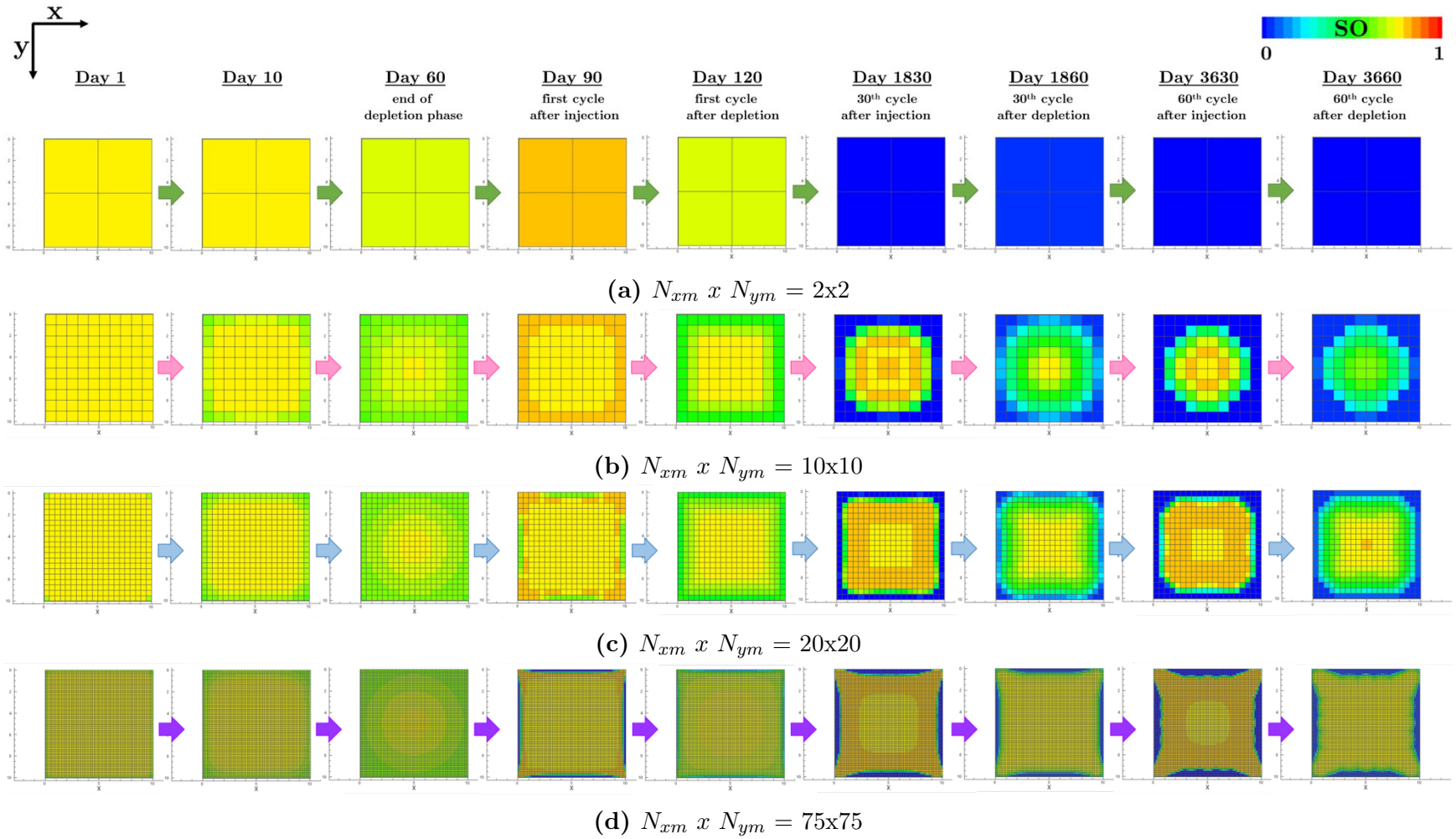

(a) N_{xm} x N_{ym} = 2x2

(b) N_{xm} x N_{ym} = 10x10

(c) N_{xm} x N_{ym} = 20x20

(d) N_{xm} x N_{ym} = 75x75

Figure C.4: Matrix block number sensitivity with black oil simulation - Oil saturation response in 2D.

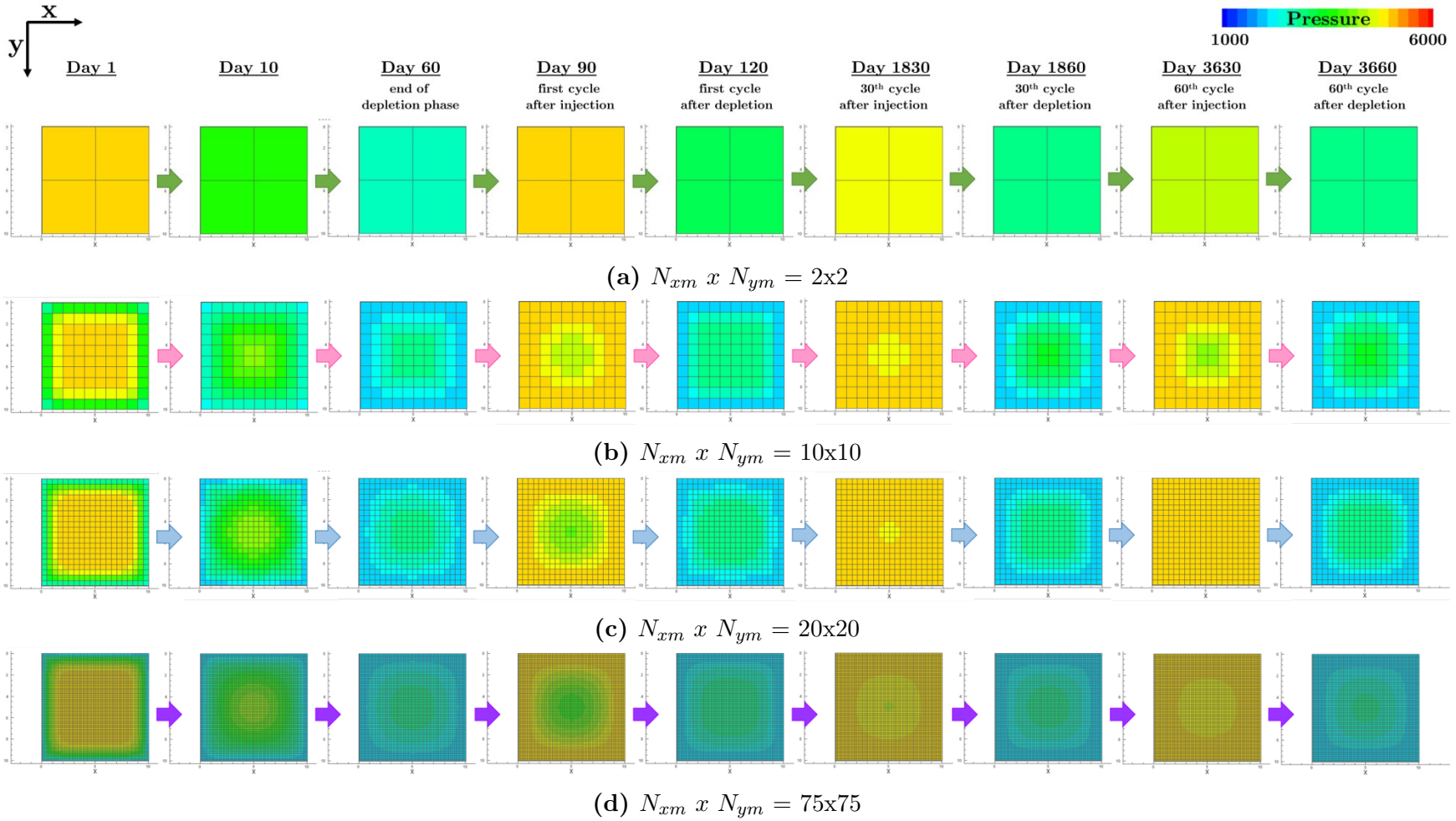

(a) N_{xm} x N_{ym} = 2x2

(b) N_{xm} x N_{ym} = 10x10

(c) N_{xm} x N_{ym} = 20x20

(d) N_{xm} x N_{ym} = 75x75

Figure C.5: Matrix block number sensitivity with EOS simulation - Pressure response in 2D.

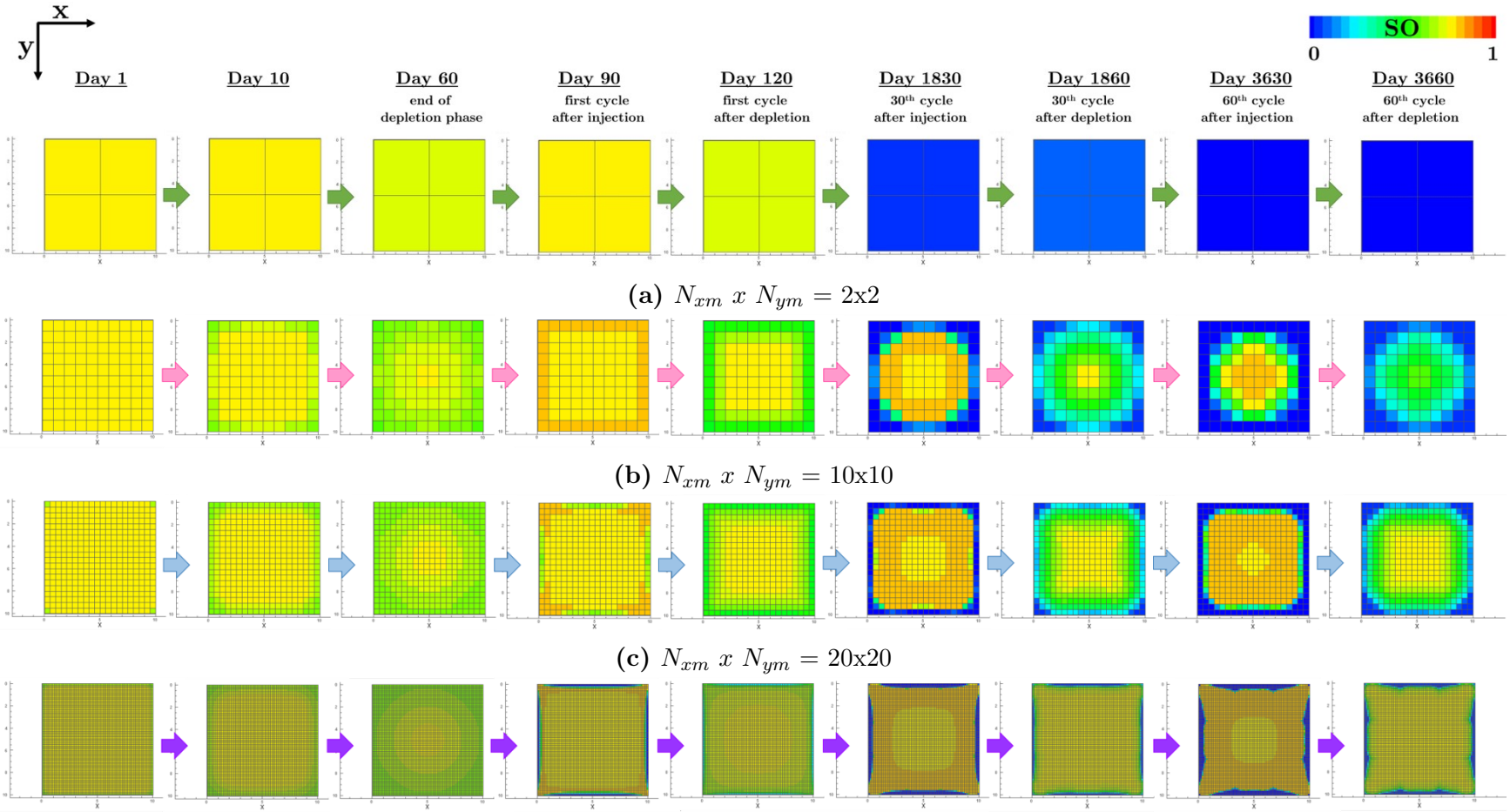

(a) $N_{xm}\ x\ N_{ym}$ = 2x2

(b) $N_{xm}\ x\ N_{ym}$ = 10x10

(c) $N_{xm}\ x\ N_{ym}$ = 20x20

(d) $N_{xm}\ x\ N_{ym}$ = 75x75

Figure C.6: Matrix block number sensitivity with EOS simulation - Oil saturation response in 2D.

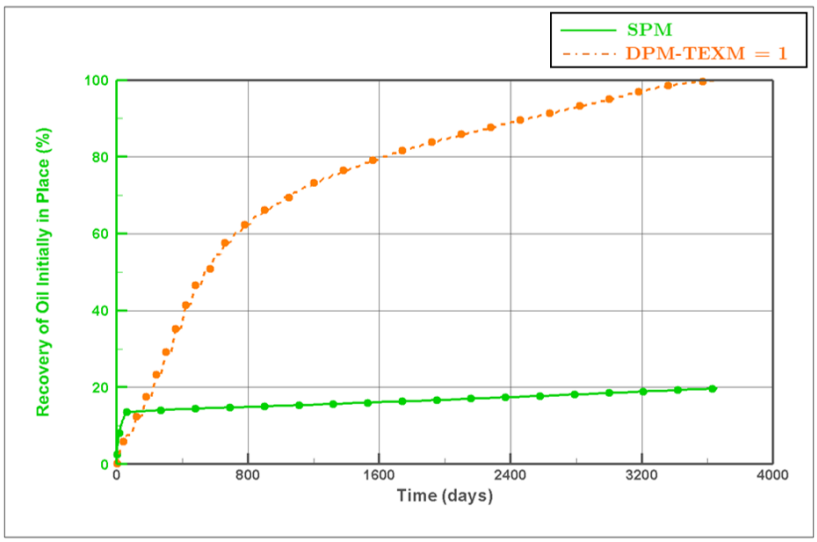

Figure C.7: Recovery factor profile comparison after 10 years of gas injection.

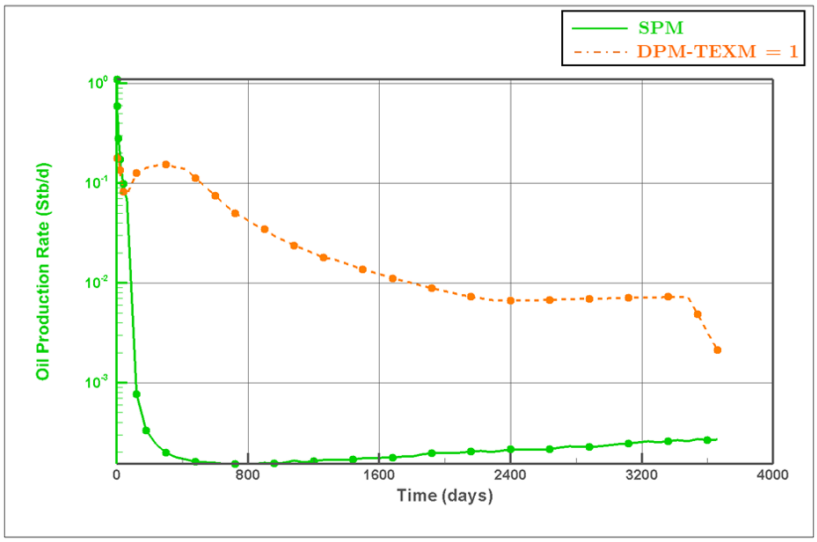

Figure C.8: Oil production rate profile comparison after 10 years of gas injection.

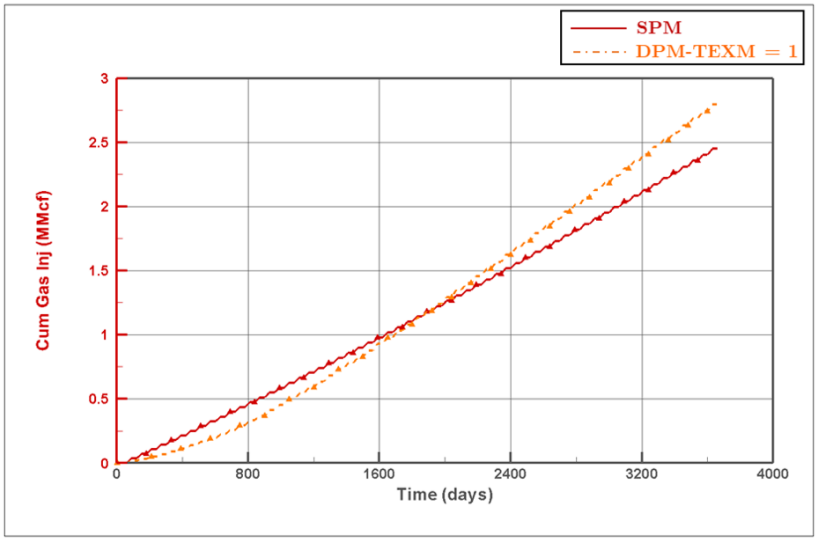

Figure C.9: Cumulative injected gas profile comparison after 10 years of gas injection.

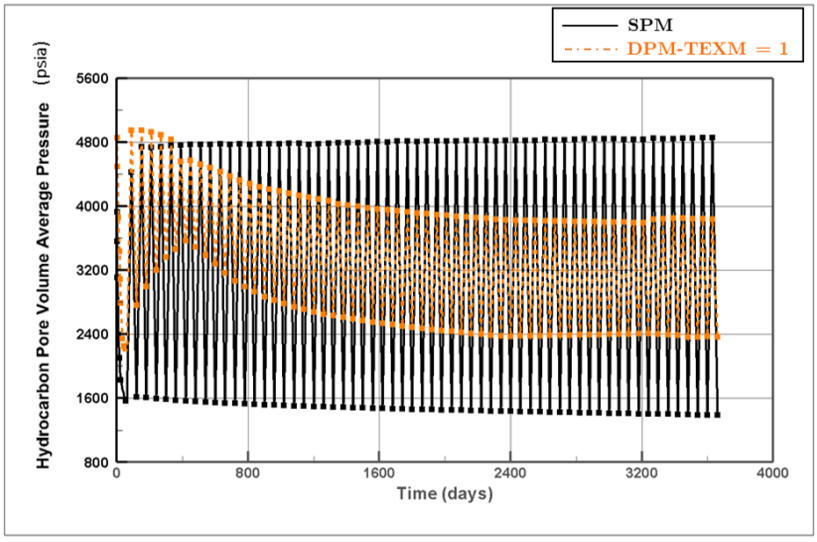

Figure C.10: Pressure profile comparison after 10 years of gas injection.

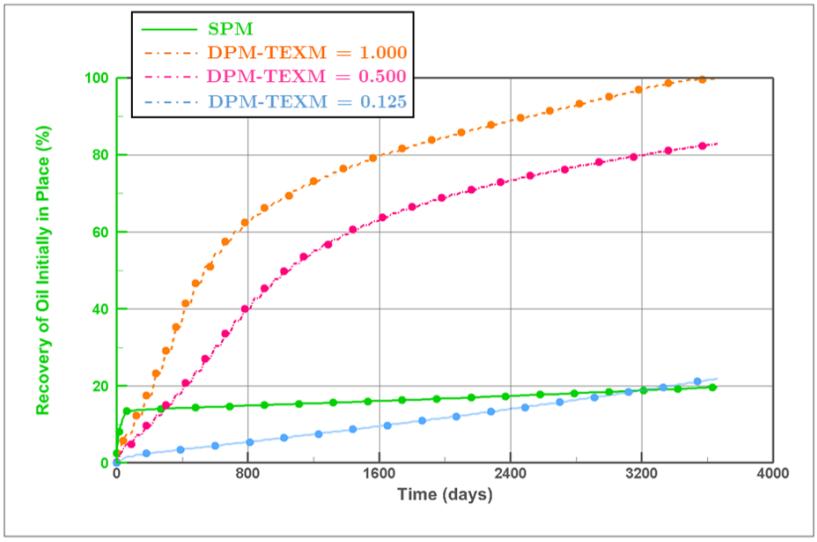

Figure C.11: Recovery factor profile comparison after 10 years of gas injection after applying modification on TEX.

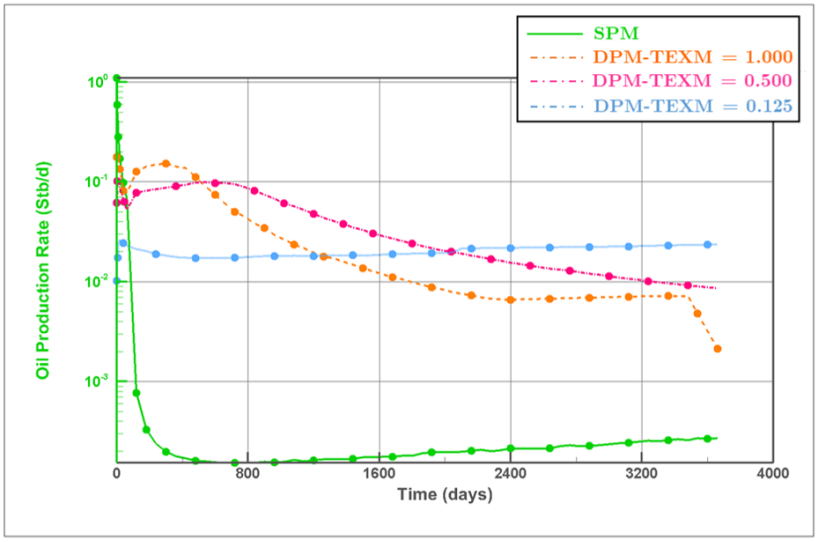

Figure C.12: Oil production rate profile comparison after 10 years of gas injection after applying modification on TEX.

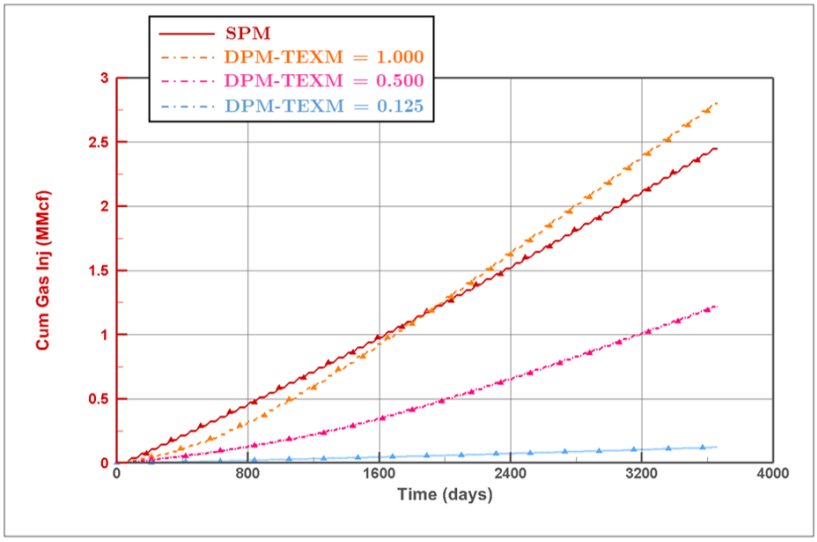

Figure C.13: Cumulative injected gas profile comparison after 10 years of gas injection after applying modification on TEX.

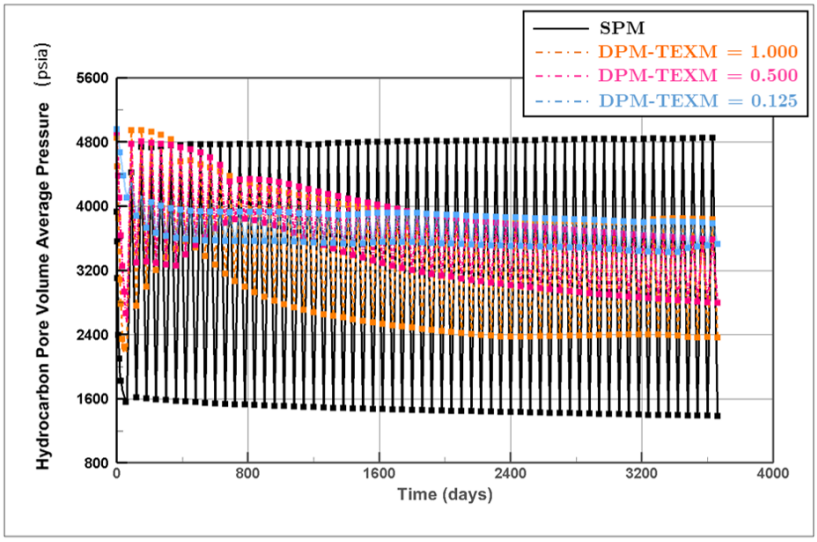

Figure C.14: Pressure profile comparison after 10 years of gas injection after applying modification on TEX.

Appendix D

Sensor Input Files

Example SENSOR SPM and DPM input files, the performances are shown in Figure B.58.

D.1 Single-Porosity Modeling

```
TITLE
Single Porosity Model
ENDTITLE

GRID 12 12 1
IMPLICIT
PRINTREG 0
PRINTKR
MAPSPRINT 1 P PSAT SG SO SW GG GO KX KY KZ ROCKTYPE POROS PV HCPV TX TY
TZ REGION
MAPSFILE P SAT SG SO SW KX KY KZ ROCKTYPE POROS PV HCPV TX TY TZ REGION
MISC 1.01 3.E-6 63.05228 .5 4E-6 2718

KRANALYTICAL 1 !  matrix
   .2  .3  .1 0.
  1   1   1
  1.5 1.5 1.5 1.5
KRANALYTICAL 2 !  fracture
  0   0   0   0
  1   1   1
  1   1   1   1

C SKIP ! Uncomment this if EOS run is desired
BLACKOIL 1 7 12
PRESSURES 500 800 1100 1400 1700 2000 2302 2600 2900 3300 3800 5000 6000
7000
RESERVOIR FLUID
  0.  .5 .03 .07 .2 .15 .05
C SEPARATOR ! Default
C   14.7 60.
ENDBLACKOIL
C SKIPEND ! Uncomment this if EOS run is desired
```

```
PVTEOS
  160
 CPT      PC        TC         MW       PCHOR       AC      ZCRIT
  CO2  1071.3310  548.4600  44.0100  78.0000 .2250000 .274077
  C1    667.8000  343.0000  16.0400  71.0000 .0130000 .290000
  C3    616.3000  665.7000  44.1000 151.0000 .1524000 .277000
  C6    436.9000  913.4000  86.1800 271.0000 .3007000 .264000
  C10   304.0000 1111.8000 142.2900 431.0000 .4885000 .257000
  C15   200.0000 1270.0000 206.0000 631.0000 .6500000 .245000
  C20   162.0000 1380.0000 282.0000 831.0000 .8500000 .235000
BIN
  .1 .1 .1 .1 .100 .100
     .0 .0 .0 .050 .050
        .0 .0 .005 .005
           .0 .000 .000
              .000 .000
                   .000

POROS XVAR
  1 10*0.2 1
MOD
  1 12 1  1  1 1 = 1
  1 12 12 12 1 1 = 1
KX XVAR
  0.02 10*5e-005 0.02
MOD
  1 12 1  1  1 1 = 0.02
  1 12 12 12 1 1 = 0.02
KY EQUALS KX
KZ EQUALS KX
DEPTH CON CENTER
  5000
THICKNESS ZVAR
  40
DELX XVAR
  0.01 10*1 0.01
DELY YVAR
  0.01 10*1 0.01
REGION CON
  3
ROCKTYPE XVAR
  2 10*1 2
MOD
  1  12 1  1 1 1 = 1
  12 12 12 1 1 1 = 1

INITIAL 1
C SKIP ! Uncomment this if EOS run is desired
DEPTH PSATBP
  5000 2302.9
C SKIPEND ! Uncomment this if EOS run is desired
SKIP ! Comment this if EOS run is desired
DEPTH
  5000.  2302 0.  .5 .03 .07 .2 .15 .05 !  Depth psat zi
SKIPEND ! Comment this if EOS run is desired
```

```
PINIT 5000
ZINIT 5000
ENDINIT !**end of Initial Data**

C**start of Recurrent Data**
WELL
  I J K PI
 PROD
  1  1  1 1
  1  2  1 1
  1  3  1 1
  1  4  1 1
  1  5  1 1
  1  6  1 1
  1  7  1 1
  1  8  1 1
  1  9  1 1
  1  10 1 1
  1  11 1 1
  1  12 1 1
  2  1  1 1
  2  12 1 1
  3  1  1 1
  3  12 1 1
  4  1  1 1
  4  12 1 1
  5  1  1 1
  5  12 1 1
  6  1  1 1
  6  12 1 1
  7  1  1 1
  7  12 1 1
  8  1  1 1
  8  12 1 1
  9  1  1 1
  9  12 1 1
  10 1  1 1
  10 12 1 1
  11 1  1 1
  11 12 1 1
  12 1  1 1
  12 2  1 1
  12 3  1 1
  12 4  1 1
  12 5  1 1
  12 6  1 1
  12 7  1 1
  12 8  1 1
  12 9  1 1
  12 10 1 1
  12 11 1 1
  12 12 1 1

C SKIP ! Uncomment this for depletion phase
 INJ1
  1  1  1 1
```

```
  1  2  1 1
  1  3  1 1
  1  4  1 1
  1  5  1 1
  1  6  1 1
  1  7  1 1
  1  8  1 1
  1  9  1 1
  1  10 1 1
  1  11 1 1
  1  12 1 1
  2  1  1 1
  2  12 1 1
  3  1  1 1
  3  12 1 1
  4  1  1 1
  4  12 1 1
  5  1  1 1
  5  12 1 1
  6  1  1 1
  6  12 1 1
  7  1  1 1
  7  12 1 1
  8  1  1 1
  8  12 1 1
  9  1  1 1
  9  12 1 1
  10 1  1 1
  10 12 1 1
  11 1  1 1
  11 12 1 1
  12 1  1 1
  12 2  1 1
  12 3  1 1
  12 4  1 1
  12 5  1 1
  12 6  1 1
  12 7  1 1
  12 8  1 1
  12 9  1 1
  12 10 1 1
  12 11 1 1
  12 12 1 1
C SKIPEND ! Uncomment this for depletion phase
WELLTYPE
  PROD 6 !  RBOIL
  INJ -2 !  Comment this for depletion phase
BHP
  PROD 2500
  INJ 2500 !  Comment this for depletion phase
RATE
  PROD 1000000
  INJ -1 !  Comment this for depletion phase
MAPSFREQ 1
MAPSFILEFREQ 1
DT 0.001
```

```
TIME 60 5
C END ! Uncomment this for depletion phase

C Cycle = 1 ================================================
BHP
  PROD 5000
  INJ 5000
RATE
  PROD -1
  INJ 1000000
MAPSFREQ 1
MAPSFILEFREQ 1
DT 0.001
TIME 90
BHP
  PROD 1000
  INJ 1000
RATE
  PROD 1000000
  INJ -1
MAPSFREQ 1
MAPSFILEFREQ 1
DT 0.001
TIME 120

C Cycle = 2 ================================================
BHP
  PROD 5000
  INJ 5000
RATE
  PROD -1
  INJ 1000000
MAPSFREQ 1
MAPSFILEFREQ 1
DT 0.001
TIME 150
BHP
  PROD 1000
  INJ 1000
RATE
  PROD 1000000
  INJ -1
MAPSFREQ 1
MAPSFILEFREQ 1
DT 0.001
TIME 180
```

•
•
•

```
C Cycle = 60 ===============================================
BHP
  PROD 5000
  INJ 5000
RATE
```

```
  PROD -1
  INJ 1000000
MAPSFREQ 1
MAPSFILEFREQ 1
DT 0.001
TIME 3630
BHP
  PROD 1000
  INJ 1000
RATE
  PROD 1000000
  INJ -1
MAPSFREQ 1
MAPSFILEFREQ 1
DT 0.001
TIME 3660
END
```

D.2 Dual-Porosity Modeling

```
TITLE
Dual Porosity Model
ENDTITLE

GRID 4 50 2
DUAL 1
LX CON
10
LY CON
10
PRINTREG 0
PRINTKR
MAPSPRINT 1 P PSAT SG SO SW GG GO KX KY KZ ROCKTYPE POROS PV HCPV TX TY
TZ REGION
MAPSFILE P SAT SG SO SW KX KY KZ ROCKTYPE POROS PV HCPV TX TY TZ REGION
TEX
MISC 1.01 3.E-6 63.05228 .5 4E-6 2718

KRANALYTICAL 1 !  matrix
   .2  .3  .1 0.
  1   1   1
  1.5 1.5 1.5 1.5
KRANALYTICAL 2 !  fracture
  0   0   0   0
  1   1   1
  1   1   1   1

C SKIP ! Uncomment this if EOS run is desired
BLACKOIL 1 7 12
PRESSURES 500 800 1100 1400 1700 2000 2302 2600 2900 3300 3800 5000 6000
7000
RESERVOIR FLUID
  0.  .5 .03 .07 .2 .15 .05
C SEPARATOR ! Default
```

```
C   14.7 60.
ENDBLACKOIL
C SKIPEND ! Uncomment this if EOS run is desired

PVTEOS
  160
 CPT      PC        TC         MW       PCHOR       AC      ZCRIT
  CO2  1071.3310  548.4600  44.0100  78.0000 .2250000 .274077
  C1    667.8000  343.0000  16.0400  71.0000 .0130000 .290000
  C3    616.3000  665.7000  44.1000 151.0000 .1524000 .277000
  C6    436.9000  913.4000  86.1800 271.0000 .3007000 .264000
  C10   304.0000 1111.8000 142.2900 431.0000 .4885000 .257000
  C15   200.0000 1270.0000 206.0000 631.0000 .6500000 .245000
  C20   162.0000 1380.0000 282.0000 831.0000 .8500000 .235000
BIN
  .1 .1 .1 .1 .100 .100
     .0 .0 .0 .050 .050
        .0 .0 .005 .005
           .0 .000 .000
              .000 .000
                   .000

POROS ZVAR
  0.2 0.001
KX ZVAR
  5e-005 0.02
KY EQUALS KX
KZ EQUALS KX
DEPTH CON CENTER
  5000
THICKNESS CON
  40
DELX CON
  50
DELY CON
  200
REGION ZVAR
  1 2
MOD
  1 1 1 1 1 2 = 3
ROCKTYPE ZVAR
  1 2
CTEX CON ! Change to new TEX after applying multiplier
C   0.001802

INITIAL NOVE
C SKIP ! Uncomment this if EOS run is desired
DEPTH PSATBP
  5000 2302.9
C SKIPEND ! Uncomment this if EOS run is desired
SKIP ! Comment this if EOS run is desired
DEPTH
  5000.  2302 0.  .5 .03 .07 .2 .15 .05 !  Depth psat zi
SKIPEND ! Comment this if EOS run is desired
PINIT 5000
ZINIT 5000
```

```
ENDINIT !**end of Initial Data**

C**start of Recurrent Data**
WELL
  I1 I2 J1 J2 K1 K2 PI
 PROD
  1 1 1 1 2 2 1
C SKIP ! Uncomment this for depletion phase
 INJ
  1 1 1 1 2 2 1
C SKIPEND ! Uncomment this for depletion phase
WELLTYPE
  PROD 6 !  RBOIL
  INJ -2 !  Comment this for depletion phase
BHP
  PROD 2500
  INJ 2500 !  Comment this for depletion phase
RATE
  PROD 1000000
  INJ -1 !  Comment this for depletion phase
MAPSFREQ 1
MAPSFILEFREQ 1
DT 0.001
TIME 60 5
C END ! Uncomment this for depletion phase

C Cycle = 1 ================================================
BHP
  PROD 5000
  INJ 5000
RATE
  PROD -1
  INJ 1000000
MAPSFREQ 1
MAPSFILEFREQ 1
DT 0.001
TIME 90
BHP
  PROD 1000
  INJ 1000
RATE
  PROD 1000000
  INJ -1
MAPSFREQ 1
MAPSFILEFREQ 1
DT 0.001
TIME 120

C Cycle = 2 ================================================
BHP
  PROD 5000
  INJ 5000
RATE
  PROD -1
  INJ 1000000
MAPSFREQ 1
```

```
MAPSFILEFREQ 1
DT 0.001
TIME 150
BHP
  PROD 1000
  INJ 1000
RATE
  PROD 1000000
  INJ -1
MAPSFREQ 1
MAPSFILEFREQ 1
DT 0.001
TIME 180
```

•
•
•

```
C Cycle = 60 ================================================
BHP
  PROD 5000
  INJ 5000
RATE
  PROD -1
  INJ 1000000
MAPSFREQ 1
MAPSFILEFREQ 1
DT 0.001
TIME 3630
BHP
  PROD 1000
  INJ 1000
RATE
  PROD 1000000
  INJ -1
MAPSFREQ 1
MAPSFILEFREQ 1
DT 0.001
TIME 3660
END
```